

8-2015

## Structure and Composition of Postsynaptic Densities

Madeline Farley

Follow this and additional works at: [https://digitalcommons.library.tmc.edu/utgsbs\\_dissertations](https://digitalcommons.library.tmc.edu/utgsbs_dissertations)



Part of the [Developmental Neuroscience Commons](#), [Molecular and Cellular Neuroscience Commons](#),  
and the [Structural Biology Commons](#)

---

### Recommended Citation

Farley, Madeline, "Structure and Composition of Postsynaptic Densities" (2015). *The University of Texas MD Anderson Cancer Center UTHealth Graduate School of Biomedical Sciences Dissertations and Theses (Open Access)*. 603.

[https://digitalcommons.library.tmc.edu/utgsbs\\_dissertations/603](https://digitalcommons.library.tmc.edu/utgsbs_dissertations/603)

This Dissertation (PhD) is brought to you for free and open access by the The University of Texas MD Anderson Cancer Center UTHealth Graduate School of Biomedical Sciences at DigitalCommons@TMC. It has been accepted for inclusion in The University of Texas MD Anderson Cancer Center UTHealth Graduate School of Biomedical Sciences Dissertations and Theses (Open Access) by an authorized administrator of DigitalCommons@TMC. For more information, please contact [digitalcommons@library.tmc.edu](mailto:digitalcommons@library.tmc.edu).

# STRUCTURE AND COMPOSITION OF POSTSYNAPTIC DENSITIES

A

DISSERTATION

Presented to the Faculty of  
The University of Texas  
Health Science Center at Houston  
and  
The University of Texas  
MD Anderson Cancer Center  
Graduate School of Biomedical Sciences  
in Partial Fulfillment  
of the Requirements  
for the Degree of  
DOCTOR OF PHILOSOPHY

by

Madeline M. Farley, B.S

Houston, Texas

August, 2015

## **Acknowledgements**

First I want to thank my entire family, as they have certainly been the biggest force helping to guide me through life. My mother always put my education first and raised me to be an independent thinker standing on my own two feet. My father has always been so proud to call me his spawn, always answered all of my random phone calls and passed to me his love of trivia. I also want to thank my stepparents, Dave and Cynthia, for stepping into the role of parent and putting us kids first. Dave has always been ready for lengthy life discussions on the porch and specifically helped me to realize how much I would enjoy graduate school and ultimately academia. I also want to thank my siblings Adrienne, Conner, Brittany, Nikki and DJ for being great company and constantly providing learning opportunities for their big sister. I specifically want to thank Adrienne for always giving me a run for my money. Most importantly I want to thank my loving husband Josh for being my best friend, balancing out my crazy, supporting me through 6 years of graduate school and always believing in me, even when I doubted myself.

I am extremely fortunate to have such a large group of friends and owe them thanks for years of friendship. Specifically I want to thank Julia Reynolds for guiding me through my first research experience, introducing me to my husband and for 10 years of friendship. I also want to thank Monica Gireud, my running buddy, and Dayne Goss for being lifelong partners in crime with Josh and me. I will always be grateful for Elisa Vesely and our late night science discussions, always accompanied by a bottle of wine. Also, I would like to thank Brittany Parker Kerrigan for our many lunch dates and Natalie Sirisaengtaksin for being my trivia bud and always offering illustrator support.

Lastly I am thankful for all the Neuroscience Program students I have had the pleasure of knowing and for Amanda Williamson, the best program coordinator possible.

Next I want like to thank the many teachers and mentors I have had throughout my academic career, including the faculty at Louisiana School for Math, Science and the Arts and my college advisor Dr. Joshua Lawrence. I also want to thank my supervisory committee Dr. Andy Bean, Dr. Jack Waymire, Dr. John Putkey and Dr. Jun Liu for years of mentoring and guidance. I am so grateful for the welcoming acceptance into the Waxham lab family by Dr. Hugo Sanabria, Dr. Sally Kim and Dr. Andy Hudmon. Dr. Mathew Swulius graciously trained me during my first year in the Waxham lab and always sends wisdom my way. I must certainly thank Dr. Laurel Hoffman for all of the cakes as well as countless scientific and non-scientific conversations; it was so very helpful to have someone who has been in my shoes to bounce ideas off of everyday.

Most importantly I want to thank my Ph.D. advisor Dr. Neal Waxham. Words truly cannot express how thankful I am to have been trained and mentored by such a caring and thoughtful scientist. I am so very thankful for all of Neal's wisdom and time, which have helped me to mature immensely during my time in the lab. As I leave the Waxham lab I can only hope that Neal will continue to be proud of my growth as a scientist. Finally, I have to thank the TMC parking garages, especially garage 3, for always taking my hard-earned money.



# STRUCTURE AND COMPOSITION OF POSTSYNAPTIC DENSITIES

Madeline Marie Farley, Ph.D.

Supervisory Professor: M. Neal Waxham, Ph.D.

## **Abstract**

Communication between neurons within the brain occurs at chemical synapses and is fundamental for all brain functions. Modulation of the strength of communication is controlled by both presynaptic and postsynaptic mechanisms and is termed synaptic plasticity. One postsynaptic structure postulated to regulate synaptic strength is the postsynaptic density (PSD), a large electron dense protein complex located just below the synaptic membrane. The PSD, which is composed of signaling, scaffold and cytoskeletal proteins, supports and organizes neurotransmitter receptors within the synaptic membrane in addition to bridging signaling with the actin cytoskeletal network. The protein composition and structure of PSDs is known to change in response to synaptic activity and several PSD proteins are implicated in neurological conditions characterized by synaptic dysfunction. However, there is a lack of information regarding the variability of PSD structure and composition from individual PSDs across the brain. In order to address this deficiency, PSDs were isolated from adult rat cerebella, hippocampi and cerebral cortices three brain regions with unique neuronal populations. The structure and composition of morphologically identified PSDs from these regions was then compared through immunogold analysis and electron tomography. Tomographic reconstructions revealed that while the majority of PSDs shared a similar dense protein organization, there were cerebellar PSDs which displayed a latticelike protein organization. PSDs from cortices and cerebellar were

also approximately twice as thick as hippocampal PSDs and thicker than previously reported measurements. This suggests that the PSD extends further into the postsynaptic spine than previously appreciated, presumably facilitating interactions with the spine cytoskeletal network. Immunogold analysis of PSD scaffold proteins suggested that the underlying PSD scaffold is quite variable across the brain, and even within brain regions. Additionally, an immunogold analysis of two key molecules documented to play roles in synaptic plasticity, CaMKII and the proteasome, supported their potential role in structural modifications of the PSD. Together, these results indicate that PSDs exhibit remarkable diversity in their composition and morphology, presumably as a reflection of the unique functional demands placed on different synapses.

## Table of Contents

<b>Acknowledgments</b> .....	<b>ii</b>
<b>Abstract</b> .....	<b>iv</b>
<b>Table of Contents</b> .....	<b>vi</b>
<b>List of Illustrations</b> .....	<b>x</b>
<b>List of Tables</b> .....	<b>xiv</b>
<b>Chapter 1. Introduction</b> .....	<b>1</b>
1.1. <i>Chemical Synapses</i> .....	1
1.2. <i>The Postsynaptic Density</i> .....	5
1.2.1. <i>Major Proteins of the Postsynaptic Density</i> .....	5
1.2.1.1. <i>CaMKII</i> .....	6
1.2.1.2. <i>PSD-95</i> .....	8
1.2.1.3. <i>SAP102</i> .....	10
1.2.1.4. <i>Shank Proteins</i> .....	11
1.2.1.5. <i>Homer</i> .....	13
1.2.1.6. <i>NMDA-type Glutamate Receptors</i> .....	14
1.2.1.7. <i>Actin and <math>\alpha</math>-Actinin</i> .....	15
1.2.2. <i>PSD Morphology and Structural Organization</i> .....	19

<b>Chapter 2. Methodology</b>	<b>22</b>
2.1. <i>Isolation of Postsynaptic Densities from Cerebella, Hippocampi, and Cerebral Cortices</i>	22
2.2. <i>Protein Assays, SDS Page and Western Blotting</i>	26
2.3. <i>Immunogold Labeling of Isolated Postsynaptic Densities</i>	30
2.4. <i>Spatial Analysis of Immunogold Labeling</i>	35
2.5. <i>Electron Tomography</i>	38
2.6. <i>Tomographic Reconstruction and Image Processing</i>	39
<b>Chapter 3. Isolation of Postsynaptic Densities from Adult Rat Cerebral Cortices, Hippocampi, and Cerebella</b>	<b>44</b>
3.1. <i>Enrichment of PSDs from Brain Tissue</i>	44
3.2. <i>Gross Morphology of Isolated PSDs from Negative Stain Micrographs</i>	52
3.3. <i>Surface Area of Isolated PSDs from Negative Stain Micrographs</i>	62
<b>Chapter 4. Morphology of Postsynaptic Densities from Adult Rat Cerebella, Hippocampi, and Cerebral Cortices</b>	<b>64</b>
4.1. <i>PSD Morphology from Negative Stain Electron Tomography</i>	64
4.2. <i>PSD Morphology from Cryo Electron Tomography</i>	76
4.3. <i>Protein-to-Volume Ratios of Isolated PSDs</i>	78
4.4. <i>PSD Thickness from Tomographic Reconstructions</i>	79

<b>Chapter 5. Protein Composition of Postsynaptic Densities from Adult Rat Cerebella, Hippocampi, and Cerebral Cortices</b>	<b>90</b>
5.1. <i>PSD Protein Staining Patterns</i>	90
5.2. <i>Immunogold Labeling of Major PSD Proteins</i>	93
5.2.1. <i>Scaffold Proteins within and across PSD Groups</i>	101
5.2.2. <i>Signaling Molecules within and across PSD Groups</i>	103
5.2.3. <i>Neurotransmitter Receptors within and across PSD Groups</i>	105
5.2.4. <i>Proteasome within and across PSD Groups</i>	106
5.2.5. <i>Additional Trends across PSD Groups</i>	106
5.3. <i>Spatial Analysis of Gold Labeling</i>	113
<b>Chapter 6. Discussion</b>	<b>119</b>
<b>Appendix 1. Insights into the Dynamic PSD Structure</b>	<b>139</b>
A.1.1. <i>Introduction</i>	139
A.1.2. <i>Additional Methodology</i>	143
A.1.2.1. <i>Preparation of Hippocampal Slices and Chemical Induction of Neuronal Activity</i>	143
A.1.2.2. <i>Isolation of Postsynaptic Densities from Forebrains at Postnatal Days 2, 7, 14, 21, and 60</i>	143
A.1.2.3. <i>Western Blotting and Immunogold Labeling</i>	145

<i>A.1.3. Results</i>	148
<i>A.1.3.1. Hippocampal Slice PSDs</i>	148
<i>A.1.3.2. PSDs during Development</i>	156
<i>A.1.4. Discussion</i>	161
<b>Appendix 2. CaMKII Isoforms Differentially Impact the Structure of Actin Cytoskeleton</b>	<b>165</b>
<i>A.2.1. Introduction</i>	165
<i>A.2.2. Methodology</i>	169
<i>A.2.3. Results</i>	169
A.2.3.1. Actin Filaments are Bundled Similarly by $\delta$ CaMKII and $\beta$ CaMKII	169
A.2.3.2. $\gamma$ CaMKII Uniquely Bundles Actin Filaments	170
<i>A.2.4. Discussion</i>	174
<b>Bibliography</b>	<b>175</b>
<b>Vita</b>	<b>200</b>

## List of Illustrations

<b>Fig. 1.1.</b> Synapses in Thin Sectioned Neuronal Tissue.....	3
<b>Fig. 1.2.</b> Overview of Chemical Transmission.....	4
<b>Fig. 1.3.</b> Summary of Major PSD Protein Interactions.....	17
<b>Fig. 1.4.</b> Organization of Major PSD Proteins.....	18
<b>Fig. 2.1.</b> Dissection of Adult Rat Cerebellum, Hippocampi and Cortices.....	24
<b>Fig. 2.2.</b> Isolation of PSDs from Cortices, Hippocampi, and Cerebella.....	25
<b>Fig. 2.3.</b> Western Blots against PSD Proteins.....	29
<b>Fig. 2.4.</b> Immunogold Labeling.....	34
<b>Fig. 2.5.</b> Example Ripley's K Function Analysis.....	37
<b>Fig. 2.6.</b> Grid Preparation and Differential Filtering of a Tomographic Reconstruction .....	42
<b>Fig. 3.1.</b> Isolation of Postsynaptic Densities.....	48
<b>Fig. 3.2.</b> Loss of Presynaptic Elements and Enrichment of Postsynaptic Elements .....	49
<b>Fig. 3.3.</b> Electron Micrographs of Synaptic Junctions and PSDs.....	50
<b>Fig. 3.4.</b> Protein Profiles of Homogenate, Synaptosome and PSD fractions.....	51
<b>Fig. 3.5.</b> Low Magnification Micrograph of Negatively Stained Cortical PSDs.....	56
<b>Fig. 3.6.</b> Low Magnification Micrograph of Negatively Stained Hippocampal PSDs .....	57

<b>Fig. 3.7.</b> <i>Low Magnification Micrograph of Negatively Stained Cerebellar PSDs</i> .....	58
<b>Fig. 3.8.</b> <i>High Magnification Micrographs of Negatively Stained Cortical PSDs</i> .....	59
<b>Fig. 3.9.</b> <i>High Magnification Micrographs of Negatively Stained Hippocampal PSDs</i> .....	60
<b>Fig. 3.10.</b> <i>High Magnification Micrographs of Negatively Stained Cerebellar PSDs</i> .....	61
<b>Fig. 3.11.</b> <i>Distribution of PSD Surface Areas</i> .....	63
<b>Fig. 4.1.</b> <i>Negative Stain Tomographic Reconstructions of PSDs Isolated from Adult Rat Cortices, Hippocampi, and Cerebella</i> .....	69
<b>Fig. 4.2.</b> <i>Tomographic Reconstructions of Negatively Stained Cortical PSDs</i> .....	70
<b>Fig. 4.3.</b> <i>Tomographic Reconstructions of Negatively Stained Hippocampal PSDs</i> .....	71
<b>Fig. 4.4.</b> <i>Tomographic Reconstructions of Negatively Stained Cerebellar PSDs with Dense Morphology</i> .....	72
<b>Fig. 4.5.</b> <i>Tomographic Reconstructions of Negatively Stained Cerebellar PSDs with Granular Morphology</i> .....	73
<b>Fig. 4.6.</b> <i>Tomographic Reconstructions of Negatively Stained Cerebellar PSDs with Lacy Morphology</i> .....	74
<b>Fig. 4.7.</b> <i>Fine Morphology of Isolated PSDs from Negative Stain Tomographic Reconstructions</i> .....	75



<b>Fig. 4.8.</b> <i>Tomographic Reconstructions of Cryo-Preserved Cortical PSDs</i> .....	82
<b>Fig. 4.9.</b> <i>Tomographic Reconstructions of Cryo-Preserved Hippocampal PSDs</i> .....	83
<b>Fig. 4.10.</b> <i>Tomographic Reconstructions of Cryo-Preserved Cerebellar PSDs with Dense Morphology</i> .....	84
<b>Fig. 4.11.</b> <i>Tomographic Reconstructions of Cryo-Preserved Cerebellar PSDs with Granular Morphology</i> .....	85
<b>Fig. 4.12.</b> <i>Tomographic Reconstructions of Cryo-Preserved Cerebellar PSDs with Lacy Morphology</i> .....	86
<b>Fig. 4.13.</b> <i>PSD Protein-to-Volume Ratios Measured from Cryo Tomographic Reconstructions</i> .....	87
<b>Fig. 5.1.</b> <i>Comparison of Isolated PSD Protein Profiles</i> .....	92
<b>Fig. 5.2.</b> <i>PSDs Immunogold Labeled for Scaffolds: <math>\alpha</math>-Actinin, Actin, PSD-95 and Homer</i> .....	96
<b>Fig. 5.3.</b> <i>PSDs Immunogold Labeled for Scaffolds: SAP102, Shank1, Shank2, and Shank3</i> .....	97
<b>Fig. 5.4.</b> <i>PSDs Immunogold Labeled for <math>Ca^{2+}</math> Signaling Proteins</i> .....	98
<b>Fig. 5.5.</b> <i>PSDs Immunogold Labeled for Neurotransmitter Receptors</i> .....	99
<b>Fig. 5.6.</b> <i>PSDs Immunogold Labeled for the Proteasome</i> .....	100
<b>Fig. 5.7.</b> <i>Bar Graph of Immunogold Labeling Results</i> .....	109
<b>Fig. 5.8.</b> <i>Percentage of Total Immunogold Labeling</i> .....	112

<b>Fig. 5.9.</b> <i>PSDs Immunogold Labeled for PSD-95</i> .....	116
<b>Fig. 5.10.</b> <i>Ripley's K Function Analysis of Random and Non-Random Gold Distribution</i> .....	117
<b>Fig. 6.1.</b> <i>Proposed Organization of PSD Scaffolds from Cortical, Hippocampal and Cerebellar PSDs</i> .....	138
<b>Fig. A.1.1.</b> <i>Model for Activity-induced Structural Reorganization of the PSD by the Ubiquitin Proteasome System</i> .....	142
<b>Fig. A.1.2.</b> <i>Isolation of PSDs from Forebrains throughout Development</i> .....	146
<b>Fig. A.1.3.</b> <i>Histograms of Control and TEA Treated Hippocampal Slice PSD Surface Areas</i> .....	153
<b>Fig. A.1.4.</b> <i>Preliminary Average Labeling Densities for RPT6 on Developmental PSDs</i> .....	159
<b>Fig. A.1.5.</b> <i>Western Blots Illustrating the Developmental Profiles for Select PSD Proteins</i> .....	160
<b>Fig. A.2.1.</b> <i>Domain Map of CaMKII Isoforms</i> .....	168
<b>Fig. A.2.2.</b> <i>Structural Analysis of Actin Bundles Formed in the Presence of the <math>\beta</math> and <math>\delta</math> Isoforms of CaMKII</i> .....	172
<b>Fig. A.2.3.</b> <i>Structure of Layered <math>\gamma</math>CaMKII Bundle</i> .....	173

## List of Tables

<b>Table 1.1.</b> <i>Major PSD Proteins</i> .....	16
<b>Table 2.1.</b> <i>Antibody Information for all Primary Antibodies Used</i> .....	32
<b>Table 2.2.</b> <i>Antibody Information for all Secondary Antibodies Used</i> .....	33
<b>Table 2.3.</b> <i>Differential Filtering of a Tomographic Reconstruction</i> .....	43
<b>Table 4.1.</b> <i>PSD Surface Area, Thickness and Protein-to-Volume Ratio Measured from Cryo Tomographic Reconstructions</i> .....	88
<b>Table 4.2.</b> <i>PSD Surface Area and Thickness Compared from Cryo and Negative Stain Tomographic Reconstructions</i> .....	89
<b>Table 5.1.</b> <i>Summary of Immunogold labeling Experiments</i> .....	108
<b>Table 5.2.</b> <i>Immunogold Labeling Densities Compared Across Regions</i> .....	110
<b>Table 5.3.</b> <i>Fractions of PSDs with Gold Labeling above Background</i> .....	111
<b>Table 5.4.</b> <i>Summary of Gold Distribution Data by Ripley's K Function Analysis</i> .....	118
<b>Table A.1.1.</b> <i>Antibody Information for all Primary Antibodies Used</i> .....	147
<b>Table A.1.2.</b> <i>Preliminary Immunogold Labeling for Hippocampal Slice PSDs treated with TEA and Controls</i> .....	154
<b>Table A.1.3.</b> <i>Preliminary Immunogold Labeling for Control and TEA Treated PSDs Isolated from Hippocampal Slices</i> .....	155

**Table A.1.4.** *Preliminary Immunogold Labeling for RPT6 on Developmental PSDs*

..... 158

## Chapter 1. Introduction

### 1.1. *Chemical Synapses*

The mammalian brain is composed of billions of neurons which communicate at synapses, the site of contact between two neurons where information is physically passed from one neuron to another in the form of chemicals or electrical charge. Synapses were directly visualized by electron microscopy in the mid-twentieth century and this work established the basic ultrastructure of chemical synapses (Palay, 1956, Gray, 1959b). These studies revealed that presynaptic processes are frequently found in close opposition to postsynaptic membranes of dendritic spines. These early studies describe dendritic spine heads as approximately 2  $\mu\text{m}$  long with the dendritic neck as narrow as 100 nm and often containing a spine apparatus (Gray, 1959b). The presynaptic process, which often contained mitochondria (Palay, 1956, Gray, 1959b) and vesicles between 20-65 nm (Palay, 1956), has been described as approximately 1  $\mu\text{m}$  in diameter with the presynaptic neck between 200 nm and 300 nm in diameter (Gray, 1959b). Figure 1.1 is a micrograph of thin sectioned neuronal tissue in which dendritic spines are evident; several presynaptic terminals, filled with synaptic vesicles, can be seen in close opposition to postsynaptic spines and the area between the presynaptic and postsynaptic membranes, termed synaptic cleft, is visible. The synaptic cleft is approximately 20-30 nm in width and electron dense material sits between the two synaptic membranes (Palay, 1956, Gray, 1959b). Just below the postsynaptic membrane is a larger electron dense band termed the postsynaptic density (PSD) (Gray, 1959b), also evident in Figure 1.1, which on average extends approximately 46 nm into the postsynaptic spine and is believed to be present in the majority of excitatory chemical synapses (Gray, 1959a).

Chemical synapses are categorized as either excitatory or inhibitory depending on the type of neurotransmitters released. The majority of synapses, and the synapses focused on in this work, release the excitatory neurotransmitter glutamate (Sheng and Hoogenraad, 2007). During synaptic transmission, illustrated in Figure 1.2, presynaptic action potentials result in an influx of calcium ( $\text{Ca}^{2+}$ ) into the presynaptic terminal, which results in the fusion of synaptic vesicles with the plasma membrane and release of glutamate into the synaptic cleft (Sheng and Hoogenraad, 2007). Glutamate can then bind glutamate receptors on the postsynaptic membrane, including  $\alpha$ -amino-3-hydroxy-5-methyl-4-isoxazolepropionic acid receptors (AMPA receptors) and N-methyl-D-aspartic acid receptors (NMDARs), resulting in a postsynaptic influx of sodium ions that depolarize the postsynaptic cell (Figure 1.2) (Sheng and Hoogenraad, 2007). Depolarization above a specific voltage threshold results in a significant increase in postsynaptic  $\text{Ca}^{2+}$  through NMDARs, which triggers a cascade of postsynaptic signaling resulting in long-term potentiation (LTP) or long-term depression (LTD), two models of learning which represent the long lasting changes associated with learning and memory (Sheng and Kim, 2002). The strength of synaptic transmission is important for brain function including learning and memory (Malenka and Bear, 2004, Sheng and Hoogenraad, 2007). Activity-dependent alterations in the strength of communication between neurons is the basis of information storage, and the strength of neuronal communication depends on the number of synapses and strength of synaptic transmission (Chklovskii et al., 2004, Sheng and Hoogenraad, 2007), that can be modulated by both presynaptic and postsynaptic mechanisms, termed synaptic plasticity (Sheng and Kim, 2002).

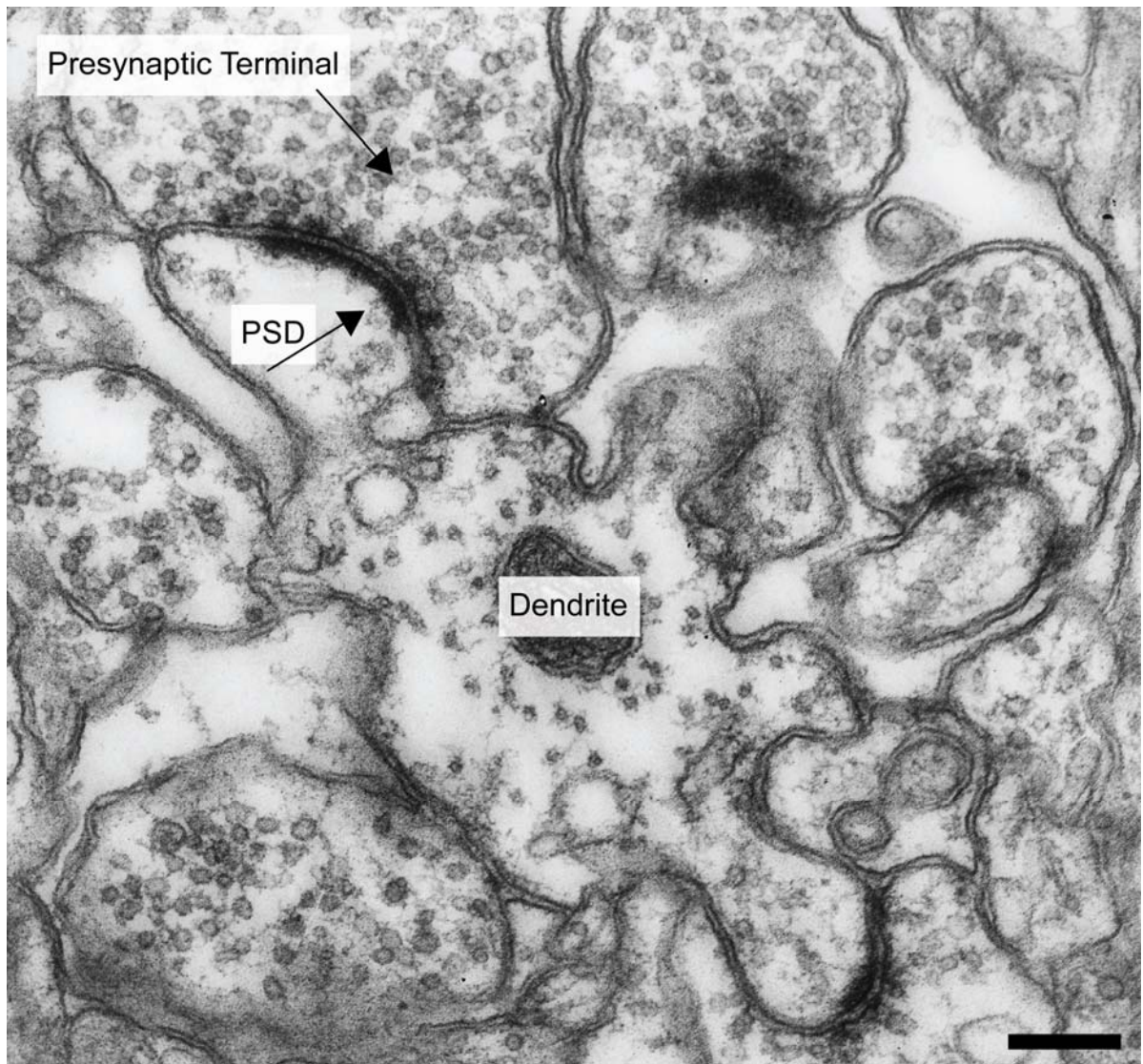


**Figure 1.1.** *Synapses in Thin Sectioned Neuronal Tissue.*

Cross-section through dendritic spines from a micrograph of thin sectioned neuronal tissue. Included in this micrograph are several examples of presynaptic terminals and postsynaptic densities (PSD). Adapted with permission from: Synapse Web, Kristen M. Harris, PI, <http://synapses.clm.utexas.edu/>. Micrograph by J. Spacek. Scale bar = 500 nm.

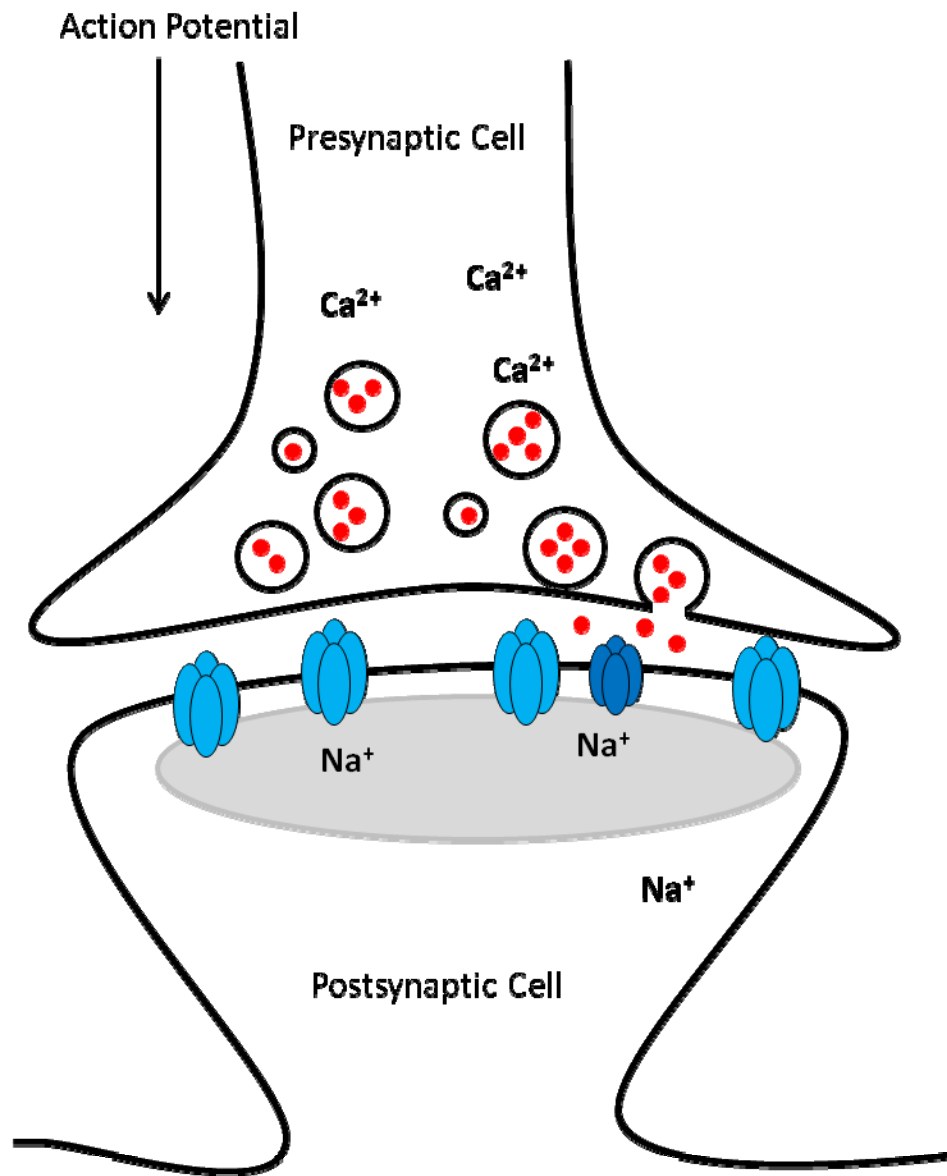


**Figure 1.2.** *Overview of Chemical Transmission.*

Action potentials in the presynaptic cell drive  $\text{Ca}^{2+}$  ions into the presynaptic compartment, which results in the fusion of synaptic vesicles with the plasma membrane and release of neurotransmitter glutamate into the synaptic cleft. Once in the synaptic cleft, glutamate can bind and activate AMPARs and NMDARs on the postsynaptic membrane, increasing postsynaptic sodium levels.



## 1.2. *The Postsynaptic Density*

PSDs were first described as electron-dense synaptic specializations present at all mature glutamatergic synapses (Palay, 1956, Gray, 1959b, Cotman et al., 1974), as discussed above and shown in Figure 1.1 and in Figure 1.2 as the gray postsynaptic oval structure. PSDs are approximately 100-500 nm in diameter, 40-60 nm thick, have an average mass of 1 GDa and are composed of hundreds of proteins including signaling, scaffolding and cytoskeletal proteins, as well as neurotransmitter receptors (Cotman et al., 1974, Chen et al., 2005, Collins et al., 2006, Dosemeci et al., 2007). PSDs function to support and organize the neurotransmitter receptors located in the synaptic plasma membrane and to form functional protein modules bridging neurotransmitter receptors with cytoplasmic signaling proteins that are crucial for synaptic transmission and are implicated in disorders of neurologic dysfunction (Kim and Sheng, 2004, Sheng and Kim, 2011).

### 1.2.1. *Major Proteins of The Postsynaptic Density*

Proteomic analyses of postsynaptic density fractions have identified a long list of proteins that are associated with PSDs (Jordan et al., 2004, Li et al., 2004, Peng et al., 2004, Yoshimura et al., 2004, Collins et al., 2005, Cheng et al., 2006, Dosemeci et al., 2006, Dosemeci et al., 2007) with a consensus of approximately 400 proteins including a variety of signaling, cytoskeletal and scaffolding molecules as well as an array of receptors and channels (Collins et al., 2005). Semiquantitative measurements of protein complexes from PSD fractions that were affinity-purified for the major PSD scaffold protein PSD-95, revealed 288 PSD proteins (Dosemeci et al., 2007). Included in the 50 most abundant were, in order;  $\text{Ca}^{2+}$ /calmodulin-dependent protein kinase II

(CaMKII), PSD-95, actin, Shank3, Homer, Shank1, Shank2, NMDAR subunit NR2b, SAP102, NMDAR subunit NR1, and  $\alpha$ -actinin (Dosemeci et al., 2007). The proposed functions, protein-protein interactions and implications in neurologic dysfunction for these PSD proteins are discussed below. Table 1.1 summarizes the molecular weight (kDa), relevant protein interactions and the estimated number of each protein within an average PSD for these PSD proteins, while Figure 1.3 illustrates the relevant protein interactions in a stick model and Figure 1.4 models a possible organization for these proteins within PSDs. (For reviews on PSD proteins see (Kennedy, 2000, Okabe, 2007, Sheng and Hoogenraad, 2007)).

#### 1.2.1.1. *CaMKII*

The major PSD protein CaMKII (Kennedy et al., 1983), which is estimated to represent 2-6% of the total mass of the PSD (Chen et al., 2005), is a holoenzyme composed of 12 subunits of varying ratios of  $\alpha$ CaMKII and  $\beta$ CaMKII, two isoforms of CaMKII, organized into two stacked rings of 6 subunits each (Kolodziej et al., 2000, Gaertner et al., 2004a, Swulius and Waxham, 2008). CaMKII is postulated to be a crucial element in NMDAR-dependent LTP, a form of synaptic plasticity (Malenka et al., 1989, Fink and Meyer, 2002, Lisman et al., 2002, Colbran and Brown, 2004, Lisman et al., 2012), and in structurally organizing the PSD (Lin and Redmond, 2009, Hell, 2014). CaMKII translocates to PSDs in animal models of ischemia (Aronowski et al., 1992, Kolb et al., 1995) and in response to NMDAR activation (Strack et al., 1997, Shen and Meyer, 1999) and high levels of potassium (Dosemeci et al., 2001). CaMKII can self-associate (Hudmon et al., 2005) and  $\alpha$ CaMKII directly binds NMDAR subunits,

transmembrane protein densin-180, actin binding protein  $\alpha$ -actinin, synGAP (Colbran, 2004) and the proteasome (Bingol et al., 2010, Djakovic et al., 2012), while  $\beta$ CaMKII can bind  $\alpha$ -actinin and actin (Colbran, 2004). Immunogold labeling experiments on isolated PSDs determined that within PSDs, CaMKII is typically located 25 nm underneath the synaptic face clustering toward the cytoplasmic edge (Petersen et al., 2003), and although there are variable concentrations of CaMKII within PSDs (Petersen et al., 2003), it is approximated that 80 holoenzymes exist within each PSD (Chen et al., 2005). Imaging of isolated PSDs by electron tomography has allowed visual identification of the holoenzymes (Fera et al., 2012), which are barrel shaped and approximately 20 nm in diameter and height (Kolodziej et al., 2000), within individual PSD structures.

After activation of CaMKII by  $\text{Ca}^{2+}$ -bound calmodulin, CaMKII can autophosphorylate and remain activate until dephosphorylated (Miller and Kennedy, 1986, Swulius and Waxham, 2008). The  $\alpha$ CaMKII and  $\beta$ CaMKII isoforms have differential affinities for  $\text{Ca}^{2+}$ /CaM (Gaertner et al., 2004b) and effects on synaptic transmission (Thiagarajan et al., 2002). The active kinase can phosphorylate many PSD proteins (Dosemeci and Jaffe, Yoshimura et al., 2002), including the proteasome (Djakovic et al., 2012), synGAP, a Ras GTPase-activating protein (Oh et al., 2004), the NR2 subunits of the NMDAR (Omkumar et al., 1996, Strack and Colbran, 1998), AMPAR subunits, and scaffolds PSD-95, Homer (Yoshimura et al., 2002), GKAP and Shank (Dosemeci and Jaffe), often significantly increasing their activity level. In response to NMDAR activation,  $\beta$ CaMKII, which binds monomeric and filamentous actin, modifies the synaptic actin network by regulating actin polymerization and structure (Okamoto et al., 2007, Sanabria et al., 2009, Hoffman et al., 2013),

suggesting a role for  $\beta$ CaMKII in synaptic maturation by regulating synaptic cytoskeletal structure (Fink et al., 2003). In further support of CaMKII's importance in synaptic function, inhibitory phosphorylation of CaMKII blocks LTP (Elgersma et al., 2002, Lisman et al., 2012), a form of synaptic plasticity and CaMKII has been implicated in several neurological diseases characterized by synaptic dysfunction including Angelman syndrome (Weeber et al., 2003, van Woerden et al., 2007) and Parkinson's disease (Picconi et al., 2004). For a review of CaMKII's role in PSDs see (Hell, 2014).

#### 1.2.1.2. *PSD-95*

PSD-95 is a scaffold protein, which contains a PDZ domain allowing self-association and formation of multiprotein complexes. Other scaffolds within the PSD-95 family include PSD-93, SAP102, and SAP97. PSD-95 is believed to organize the postsynaptic density by bridging signaling molecules with receptors at the synaptic membrane, including both AMPARs and NMDARs. PSD-95 can interact with a variety of proteins through its PDZ domain including NMDAR subunits, potassium channels, synGAP, neuroligin a trans-synaptic protein which helps align the presynaptic and postsynaptic membranes, and stargazin proteins which bind AMPARs at the synaptic membrane. PSD-95 can also bind GKAP, another PSD scaffold protein that bridges PSD-95 and Shank, due to a SH3 domain (Kim and Sheng, 2004, Zheng et al., 2011). Proteomic analysis by mass spectrometry measured PSD-95 to be three times more abundant than scaffolds GKAP and Shank combined (Peng et al., 2004), while another study estimates that PSD-95 comprises 2.3% of total PSD mass, with approximately

300 copies of PSD-95 per PSD (Chen et al., 2005), further confirming PSD-95's status as the major PSD scaffold.

Within PSDs, PSD-95 is located approximately 10-20 nm underneath the synaptic membrane as determined by immunogold labeling experiments on thin sectioned neuronal tissue (Valtschanoff and Weinberg, 2001) and by tomography of isolated PSDs (Petersen et al., 2003, DeGiorgis et al., 2006, Chen et al., 2008, Chen et al., 2011). When present in PSDs the scaffold is in an extended conformation forming a layer of vertical filaments approximately 10-20 nm from the postsynaptic membrane (Chen et al., 2008), presumably bridging glutamate receptors with proteins further inside the PSD (Chen et al., 2011). Additionally PSD-95 levels within PSDs increase throughout development (Swulius et al., 2010) appearing to replace the PDZ scaffold SAP102 (Sans et al., 2000, Petralia et al., 2005).

Mice lacking PSD-95 have alterations in spatial learning and both LTP and LTD, two NMDAR-dependent forms of plasticity (Migaud et al., 1998). Overexpression of PSD-95 resulted in increased number of AMPARs, dependent on palmitoylation of PSD-95, and enhanced AMPAR signaling (El-Husseini et al., 2000). Palmitoylation of PSD-95, the addition of a palmitate moiety, is crucial for accumulation of PSD-95 in synapses (Craven et al., 1999), and depalmitoylation of PSD-95 is required for glutamate driven endocytosis of AMPARs (El-Husseini et al., 2002). PSD-95 is also degraded by the ubiquitin proteasome system in response to activation of NMDARs, and results in the internalization of AMPARs (Colledge et al., 2003). Additionally, soluble amyloid beta (A $\beta$ ), implicated in Alzheimer's disease as a cause of synaptic dysfunction, has been shown to induce PSD-95 degradation through activation of NMDARs (Roselli et al., 2005). While the exact functions of PSD-95 are not entirely

clear, there is overwhelming evidence that PSD-95 is crucial for organization of glutamate receptors and synaptic transmission, by influencing synaptic size and strength.

#### 1.2.1.3. *SAP102*

SAP102, as mentioned above, is also a scaffold in the PDZ domain containing PSD-95 family (Kim and Sheng, 2004, Zheng et al., 2011). SAP102 is highly abundant early in development, decreasing in concentration as PSD-95 increases significantly throughout postnatal development in both hippocampal tissue (Sans et al., 2000) and PSDs (Petrulia et al., 2005). The developmental switch between SAP102 and PSD-95 mimics a switch in NMDAR subunits from NR2b in early postnatal hippocampal tissue to NR2a (Sans et al., 2000, Petrulia et al., 2005), suggesting preferred binding between SAP102 and NR2b, and PSD-95 and NR2a. These results are supported by co-immunoprecipitation experiments in adult hippocampal tissue (Sans et al., 2000). SAP102 is composed of three PDZ domains, a SH3 and a GK domain, same as PSD-95, allowing SAP102 to interact with NMDAR subunits, potassium channels, synGAP, neuroligin, stargazin, and GKAP (Kim and Sheng, 2004, Zheng et al., 2011). SAP102 helps establish early postsynaptic organization through interactions with NR2b and GKAP which forms a complex with scaffolds SAP102, Shank and Homer (Petrulia et al., 2005, Zheng et al., 2011). SAP102 is more mobile than PSD-95 in PSDs and this was attributed to association with the highly mobile actin network through the SH3 or GK domains (Zheng et al., 2010), presumably through interactions with GKAP. Additionally SAP102 and PSD-95 appear to differentially interact with and regulate glutamate receptors; overexpression of PSD-95 leads to increases in functional

synaptic AMPARs (El-Husseini et al., 2000). In contrast, functional increases in NMDARs result from overexpression of SAP102 (Zheng et al., 2011).

#### *1.2.1.4. Shank Proteins*

The Shank family of proteins, comprised of Shank1, Shank2 and Shank3, are also believed to function as PSD scaffolds, containing a SH3 domain and a PDZ domain among others (Sheng and Kim, 2000). The Shank family interacts with PSD scaffolds GKAP and Homer through their PDZ and SH3 domains (Sheng and Kim, 2000, Kim and Sheng, 2004). All three scaffolds are expressed in the brain with varying abundance and expression patterns (Boeckers et al., 1999a, Boeckers et al., 1999b, Sheng and Kim, 2000) and are enriched in PSDs (Lim et al., 1999, Naisbitt et al., 1999). It is estimated that the ratio of PSD-95: GKAP: Shank: Homer is approximately 6: 2: 2: 1 in forebrain PSDs, with Shank2 as the most abundant Shank in forebrain PSDs and Shank1 the least abundant (Cheng et al., 2006). In addition to interacting with PSD scaffolds GKAP and Homer, Shank proteins can also directly bind some metabotropic glutamate receptors (mGluRs) (Tu et al., 1999), several actin binding proteins including cortactin which binds F-actin (Du et al., 1998), other Shank proteins (Sheng and Kim, 2000), and GRIP which interacts with AMPARs (Sheng and Kim, 2000). Through interactions with PSD-95, Homer and GRIP, Shank can indirectly form protein complexes with NMDARs, mGluRs, and AMPARs and presumably bridge together these protein modules through Shank-Shank interactions (Sheng and Kim, 2000), which are hypothesized to form the core structural framework of the PSD (Baron et al., 2006). Similar to scaffolds PSD-95 (Colledge et al., 2003) and GKAP, Shanks are also targeted and degraded by the ubiquitin proteasome system (Ehlers, 2003).

Shank can also indirectly interact with the actin network through cortactin, further supporting the notion that Shanks form the PSD core bridging receptor protein modules to the cytoskeletal network. Immunogold labeling experiments on thin sectioned neuronal tissue determined Shank to be located within PSDs approximately 24 nm underneath the synaptic membrane (Valtschanoff and Weinberg, 2001) and significantly more Shank is detected by immunogold labeling on the cytoplasmic face compared to the synaptic face (Petersen et al., 2003). Overexpression of Shank alters spine morphology and induces recruitment of F-actin to spines further suggesting that Shank functionally connects synaptic activity to the spine cytoskeleton (Sala et al., 2001).

The importance of Shank in synaptic function is highlighted by several studies which have implicated Shank in neurological disorders and diseases such as autism spectrum disorders (Durand et al., 2007, Moessner et al., 2007, Gauthier et al., 2009, Berkel et al., 2010, Arons et al., 2012, Sato et al., 2012) and Alzheimer's disease (Gong et al., 2009, Roselli et al., 2009, Pham et al., 2010, Grabrucker et al., 2011b, Grabrucker et al., 2011d). Mutations in each of the three Shank proteins have been associated with autism spectrum disorders (Durand et al., 2007, Moessner et al., 2007, Gauthier et al., 2009, Kumar and Christian, 2009, Berkel et al., 2010, Grabrucker et al., 2011c, Sato et al., 2012). Autism spectrum disorder related mutations in Shank1 and Shank2 are believed to caused synaptic dysfunction through their influence on spine morphology and glutamate receptor signaling, while mutations in Shank3 disrupt transsynaptic singling via neuroligin (Arons et al., 2012). Shank protein-protein interaction are also heavily regulated by synaptic zinc levels and zinc is required for Shank to associate with PSDs (Baron et al., 2006, Grabrucker et al., 2011a).



Intriguingly zinc deficiencies in the brain have been associated with problems in learning and memory (Takeda, 2000) and many other neurological disorders including Parkinson's disease and Down's syndrome (Grabrucker et al., 2011b). Alzheimer's disease associated A $\beta$  can sequester synaptic zinc and application of soluble A $\beta$  has been shown to decrease synaptic levels of Shank (Roselli et al., 2009, Grabrucker et al., 2011d) and Homer, and is associated with a reduction of PSD size (Roselli et al., 2009). This is an interesting finding given the reductions in synaptic zinc (Suh et al., 2000) and Shank (Pham et al., 2010) in the hippocampi of human Alzheimer's disease patients.

#### 1.2.1.5. *Homer*

Homer, the binding partner of Shank proteins, is enriched in the brain and in PSDs (Xiao et al., 1998). Homer can bind the PSD scaffold Shank, mGluRs, IP3 receptors, and other Homer molecules forming multimers (Tu et al., 1998, Xiao et al., 1998). In fact, the mesh-like structure formed by Homer-Shank interactions is believed to form the core scaffold of the PSD (Hayashi et al., 2009). Homer is believed to assist in regulating synaptic Ca<sup>2+</sup>, spine morphology and synaptic transmission through interactions with mGluRs (Foa and Gasperini, 2009). Interestingly, the effects of Shank overexpression on spine morphology and F-actin translocation, described previously, are dependent upon Homer, presumably mediated by the ability of Homer to regulate intracellular Ca<sup>2+</sup> levels through direct interactions with mGluRs and IP3 receptors (Sala et al., 2001). Homer knockout mice are deficient in formation of fear memories (Inoue et al., 2009) and Homer has also been implicated in Fragile X and Alzheimer's disease, among other pathologic conditions (Foa and Gasperini, 2009). Within

forebrain PSDs, it is estimated that for every two Shank molecules there is one Homer molecule (Cheng et al., 2006) and Homer, like Shank, lies closer to the cytoplasmic PSD face (Petrálie et al., 2005).

#### 1.2.1.6. *NMDA-type Glutamate Receptors*

NMDARs are glutamate receptors that allow  $\text{Ca}^{2+}$  to enter the postsynaptic compartment in response to synaptic depolarization. Activation of NMDARs can trigger LTP or LTD, two forms of long lasting changes in synaptic plasticity associated with learning and memory (Sheng and Kim, 2002). The receptors are composed of four subunits, two NR1 subunits and two NR2 subunits all of which are enriched in PSDs (Al-Hallaq et al., 2001, Lee et al., 2001, Okabe, 2007, Sorokina et al., 2011). The NR2 subunits NR2a and NR2b, which accounts for approximately 1% of the total PSD protein (Okabe, 2007), can directly bind PDZ proteins in the PSD-95 family (Sorokina et al., 2011). NR2 subunits also bind CaMKII, situating the  $\text{Ca}^{2+}$ -dependent kinase in a favorable position to receive  $\text{Ca}^{2+}$  flowing through open NMDAR channels (Strack and Colbran, 1998, Kennedy, 2000). NR1 subunits can also bind calmodulin, the  $\text{Ca}^{2+}$  binding protein required for activation of CaMKII, further highlighting the connection between NMDARs and the CaMKII pathway. NR1 and NR2b subunits can also directly bind  $\alpha$ -actinin, bridging NMDARs to the actin network as  $\alpha$ -actinin binds actin (Wyszynski et al., 1997). Intriguingly, NMDAR knockout mice had no observable defect in either synaptic morphology or protein composition (Okabe, 2007), although activation of NMDAR results in phosphorylation of over 100 PSD proteins (Coba et al., 2009, Sheng and Kim, 2011). Immunogold studies on synapses (Racca et al., 2000) and

proteomic analysis of PSD fractions (Cheng et al., 2006) suggest that approximately 10 NMDARs are present in individual synapses.

#### *1.2.1.7. Actin and $\alpha$ -Actinin*

Actin is highly enriched in spines and is thought to contribute to spine size and morphology, molecular transport, and anchoring of the PSD and neurotransmitter receptors (Cingolani and Goda, 2008, Schoenenberger et al., 2011). Actin directly binds  $\beta$ CaMKII,  $\alpha$ -actinin and cortactin (Okabe, 2007);  $\alpha$ -actinin bridges actin to NMDARs (Wyszynski et al., 1997),  $\alpha$ CaMKII and  $\beta$ CaMKII (Okabe, 2007), while cortactin links actin to the Shank/GKAP/PSD-95 scaffold complex through Shank (Du et al., 1998, Naisbitt et al., 1999, Kim and Sheng, 2004, Okabe, 2007). Actin exists in a monomeric form, G-actin, and a filamentous form, F-actin, both of which interact with  $\beta$ CaMKII which in turn regulates actin polymerization and F-actin bundling in an activity-dependent manner (Okamoto et al., 2007, Sanabria et al., 2009, Hoffman et al., 2013). Treadmilling of PSD associated actin is believed to organize the internal PSD structure which is highly dynamic (Blanpied et al., 2008, Kerr and Blanpied, 2012); depolymerization of F-actin reduced synaptic NMDARs and AMPARs (Allison et al., 1998) as well as the mobility of PSD scaffolds PSD-95, GKAP, Shank and Homer (Kuriu et al., 2006). Given that  $\beta$ CaMKII modulates actin binding and F-actin structure in response to calcium influxes through NMDARs (Okamoto et al., 2007, Sanabria et al., 2009, Hoffman et al., 2013), presumably the internal organization of the PSDs is also regulated by CaMKII in an activity-dependent manner.

	Type of PSD Protein	Molecular Weight	Relevant Binding Partners	Estimated Copies within PSD
<b><math>\alpha</math>CaMKII</b>	Signaling	55 kDa	NR2 $\alpha$ -actinin proteasome $\alpha$ CaMKII	$\approx$ 80 Mixed Holoenzymes
<b><math>\beta</math>CaMKII</b>	Signaling	60 kDa	G-actin F-actin $\alpha$ -actinin	
<b>PSD-95</b>	Scaffold	95 kDa	GKAP NR2 stargazin	$\approx$ 300
<b>SAP102</b>	Scaffold	105 kDa	neuroligin PSD-95 SAP102	x
<b>Shank1</b>	Scaffold	120-240 kDa	GKAP Homer	$\approx$ 150
<b>Shank2</b>	Scaffold	160 kDa	cortactin Shank	
<b>Shank3</b>	Scaffold	190 kDa	mGluRs neuroligin	
<b>Homer</b>	Scaffold	45 kDa	mGluRs Shank Homer	$\approx$ 50
<b>Actin</b>	Scaffold	42 kDa	$\beta$ CaMKII $\alpha$ -actinin cortactin	x
<b><math>\alpha</math>-actinin</b>	Scaffold	100 kDa	actin $\alpha$ CaMKII $\beta$ CaMKII NR1 NR2	x
<b>NR1</b>	Receptor	105 kDa	$\alpha$ -actinin CaM	$\approx$ 10 - 20 NMDARs
<b>NR2b</b>	Receptor	166 kDa	$\alpha$ CaMKII PSD-95 SAP102 $\alpha$ -actinin	

**Table 1.1. Major PSD Proteins.**

For review of PSD protein interactions see (Sheng and Kim, 2000, Kim and Sheng, 2004, Okabe, 2007, Sheng and Hoogenraad, 2007, Foa and Gasperini, 2009) and for estimated copies within PSDs see (Cheng et al., 2006, Okabe, 2007, Sheng and Hoogenraad, 2007).

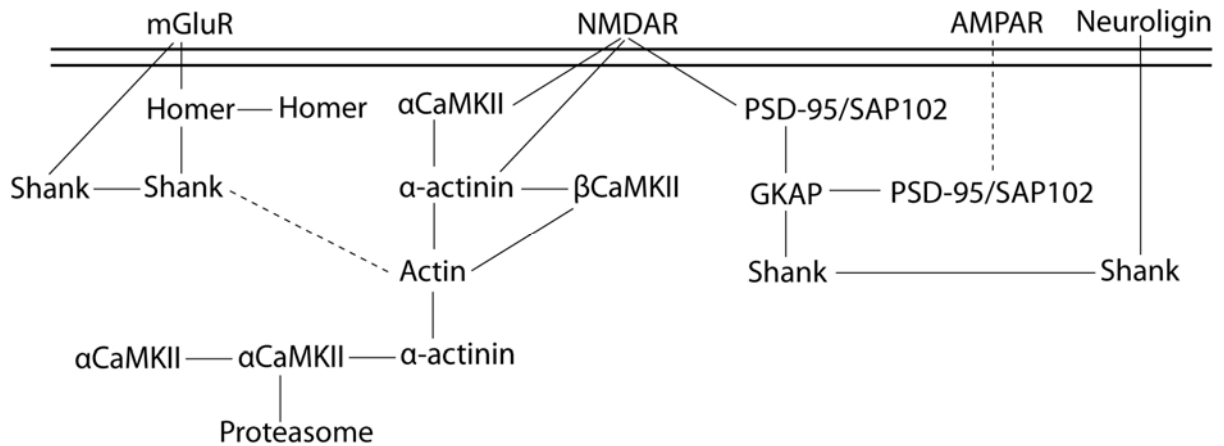


**Figure 1.3.** *Summary of Major PSD Protein Interactions.*

Summary of the major protein interactions for the PSD proteins described in this chapter and referenced through this dissertation. Solid lines indicate direct interactions, while dashed lines indicate indirect interactions. The double line just below the NMDAR and AMPAR represents the synaptic plasma membrane. For review of PSD protein interactions see (Sheng and Kim, 2000, Kim and Sheng, 2004, Okabe, 2007, Sheng and Hoogenraad, 2007, Foa and Gasperini, 2009).

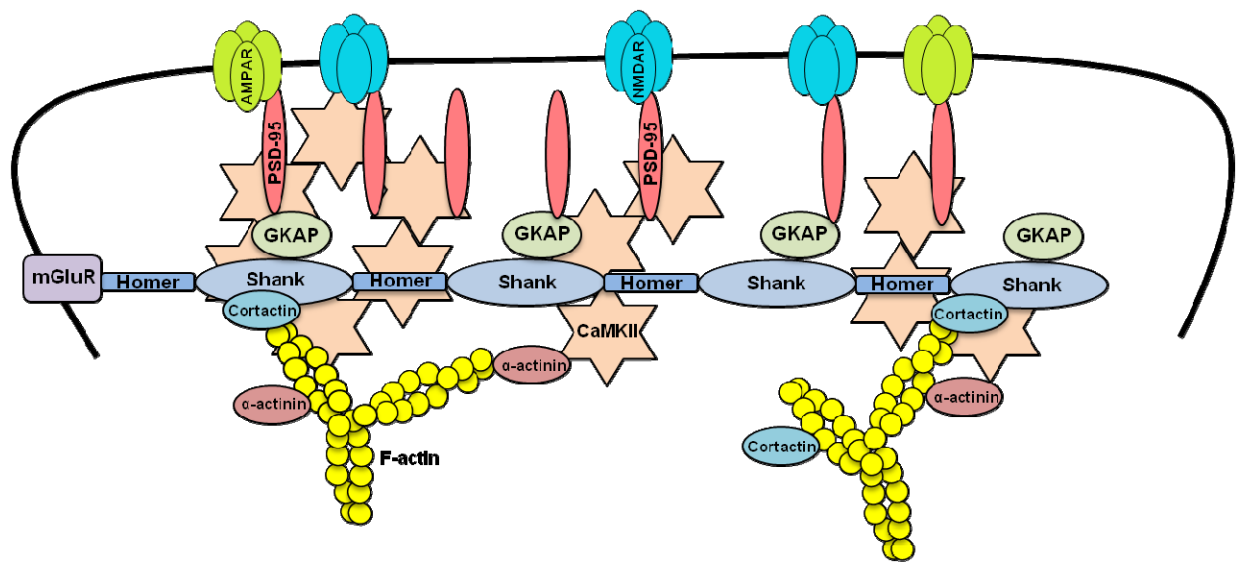


**Figure 1.4.** *Organization of Major PSD Proteins.*

Possible organization of key PSD proteins based on protein interactions and estimated location within PSDs (Sheng and Kim, 2011).

### 1.2.2. PSD Morphology and Structural Organization

PSD morphology has been described from thin sectioned neuronal tissue (Palay, 1956, Gray, 1959b, a, 1961, Cohen and Siekevitz, 1978, Harris et al., 1992) as well as from biochemically isolated PSDs, which are morphologically consistent with PSDs in the native synaptic environment (Cotman et al., 1974, Cohen et al., 1977, Matus and Taff-Jones, 1978, Carlin et al., 1980, Petersen et al., 2003). Historically PSDs have been described as dense cup-shaped structures between 0.2-1  $\mu\text{m}$  in diameter and approximately 60 nm thick composed of smaller but poorly resolved particles (Cotman et al., 1974, Cohen et al., 1977, Cohen and Siekevitz, 1978), with a distinct cleft and cytoplasmic faces (Petersen et al., 2003). More recently, through the use of cryo and stain electron tomography, protein substructures of filamentous and globular proteins have been resolved (Swulius et al., Chen et al., 2008, Fera et al., 2012, Swulius et al., 2012). Isolated PSDs have also been treated with various detergents (Matus and Taff-Jones, 1978) and reducing agents (Blomberg et al., 1977) to strip away proteins in order to describe the underlying lattice presumed to be the core scaffold of the PSD.

The morphologic changes in PSDs during synaptic maturation have also been described; early in development PSDs appear to be thin lattices of protein and through development proteins are recruited to the PSD (Swulius et al., 2010), significantly increases the density of the PSD structure (Swulius et al., 2012). Similarly PSD morphology (Dosemeci et al., 2001) and PSD protein composition (Ehlers, 2003) change in response to synaptic activity. PSD composition is dynamically regulated by protein phosphorylation (Dosemeci and Jaffe, Yoshimura et al., 2002, Cheng et al., 2006), palmitoylation (El-Husseini Ael et al., 2002), reorganization (Kuriu et al., 2006,

Blanpied et al., 2008, Tao-Cheng et al., 2010, Zheng et al., 2010, Yang et al., 2011, Kerr and Blanpied, 2012), degradation (Ehlers, 2003, Yi and Ehlers, 2005), synthesis (Steward and Schuman, 2003, Schuman et al., 2006) and recruitment (Strack et al., 1997, Djakovic et al., 2009). These changes in PSD composition and protein organization are hypothesized to modulate synaptic transmission and therefore contribute to learning and memory (Kennedy, 2000). To better understand the PSD composition and eventually how it is dynamically regulated, numerous proteomic studies have been targeted at defining the PSD proteome (Jordan et al., 2004, Li et al., 2004, Peng et al., 2004, Yoshimura et al., 2004, Collins et al., 2005, Cheng et al., 2006, Dosemeci et al., 2007). Compositional changes in PSDs throughout development (Sans et al., 2000, Petralia et al., 2005, Swulius et al., 2010) and in response to activity (Ehlers, 2003) have also been investigated and several groups have also employed immunogold labeling to assess PSD protein organization (Valtschanoff and Weinberg, 2001, Petersen et al., 2003, DeGiorgis et al., 2006, Chen et al., 2008, Swulius et al., 2010), indentifying several PSD proteins which redistributed within PSDs in response to activity (Tao-Cheng et al., 2010, Yang et al., 2011). For reviews on PSD structure see (Okabe, 2007, Sheng and Hoogenraad, 2007, Sheng and Kim, 2011).

However, there is a lack of information regarding the variability of PSD morphology and protein composition across the brain. It is hypothesized that different areas of the brain place unique demands on the process of synaptic transmission and that the PSD protein composition, and therefore PSD structure, likely change across the brain to support these unique demands. Gross differences in morphology have been described between PSDs isolated from cerebral cortices and cerebella from post-mortem canine brains (Carlin et al., 1980); cortical PSDs were thicker while cerebellar



PSDs appeared to be more latticelike in structure (Carlin et al., 1980). Additionally a proteomics study measured 43 PSD proteins which statistically differed in concentration between cortical and cerebellar derived PSD including neurotransmitter receptors, signaling and scaffold molecules (Cheng et al., 2006). However PSDs are heterogeneous, each one is compositionally and structurally unique based on the activation history of that particular synapse. Therefore while proteomic approaches provide valuable information regarding the bulk composition of PSD fractions, a more direct comparison of PSD morphology and protein composition of individual PSDs from across the brain is still needed and is the focus of this dissertation.

## Chapter 2: Methodology

### *2.1. Isolation of Postsynaptic Densities from Cerebella, Hippocampi, and Cerebral Cortices*

PSDs were isolated following a previously reported protocol (Swulius et al., 2010, Swulius et al., 2012), which was adapted from a widely used PSD enrichment procedure (Cohen et al., 1977), in order to remove PSDs from the crowded environment of synapses for morphological and compositional analyses. For a single preparation, brains were removed within 30 seconds of decapitation from nine adult male Sprague-Dawley rats (176-200 g) and placed in an ice-cold isotonic sucrose solution (buffer A) of 0.5 mM HEPES/KOH pH 7.4, 0.32 M sucrose, 1 mM MgCl<sub>2</sub>, 0.5 mM CaCl<sub>2</sub> and 1 µg/ml leupeptin. The cerebella, hippocampi, and cortices were immediately dissected, as shown in Figure 2.1, and separately homogenized in a total volume of 45 ml buffer A with a motor-driven glass/Teflon homogenizer (0.2 mm clearance). All steps of the following protocol were accomplished at 4°C. For each region, homogenates were spun at 1,400 x g for 10 minutes in a JA20 rotor. Supernatants were saved and pellets were resuspended in 12.5 ml buffer A (2 pellets from cortical tissue and 1 pellet each from cerebellar and hippocampal tissue) and spun again at 1,400 x g for 10 minutes. The supernatants were combined and pelleted at 13,800 x g for 10 minutes. The resulting pellets were resuspended and hand homogenized in a second sucrose solution, buffer B, (0.5 mM HEPES/KOH pH 7.4, 0.32 M sucrose and 1 µg/ml leupeptin), applied to sucrose gradients (<12 ml sample in buffer B, 12 ml 1.0 M sucrose, 13 ml 1.4 M sucrose) and spun at 112,000 x g for 120 minutes in a SW32 rotor. The synaptosomal fraction, at the 1.0/1.4 M interface, was collected, diluted in an equal volume of buffer B, and then an equal volume of triton

extraction buffer (5 mM HEPES/KOH pH 7.4, 0.32 M sucrose, 1% TX-100) was added. The sample was homogenized and continuously mixed on a rotator for 15 minutes before being spun at 32,800 x g for 20 minutes. The resulting pellet was suspended in buffer B, applied to a second sucrose gradient (2 ml of sample in buffer B, 2 ml 1.0 M sucrose, 4 ml 1.5 M sucrose, 2 ml 2.1 M sucrose) and spun for 120 minutes at 271,000 x g in a SW41 rotor. The synaptic junction fraction, the interface between the 1.5 M and 2.1 M sucrose, was then brought to 3 ml with 5 mM HEPES/KOH, pH 7.4, before the addition of an equal volume of a triton extraction buffer and rotated for 30 minutes. To produce the PSD fraction, the material was then added to the final sucrose gradient (6 ml sample, 4 ml 1.5 M sucrose, 2 ml 2.1 M sucrose) and spun at 210,000 x g for 20 minutes. The postsynaptic density material at the 1.5/2.1 M interface was then diluted to 5 ml with 5 mM HEPES/KOH pH 7.4, pelleted at 48,500 x g for 15 minutes in a SW55 rotor, resuspended in 300-500  $\mu$ l 20% glycerol in 5 mM HEPES/KOH pH 7.4, and stored as aliquots at -80°C. All spins were performed in either the Avanti® J-E Centrifuge or Optima XPN-80 Ultracentrifuge, both from Beckman Coulter. Gradients were spun with acceleration and deceleration program 1, resulting in a 2 minute acceleration to and deceleration from 170 RPM, respectively. The isolation protocol is summarized in Figure 2.2.

The data described in this dissertation, regarding PSDs from different brain regions, were produced from two independent PSD preparations that each contained the three isolated brain regions from nine rats. It is important to acknowledge that the process of isolating the PSD from the brain has the potential to alter its structure and composition. This limitation should be kept in mind when attempting to place the findings in this dissertation in the context of PSD structure and function *in vivo*.

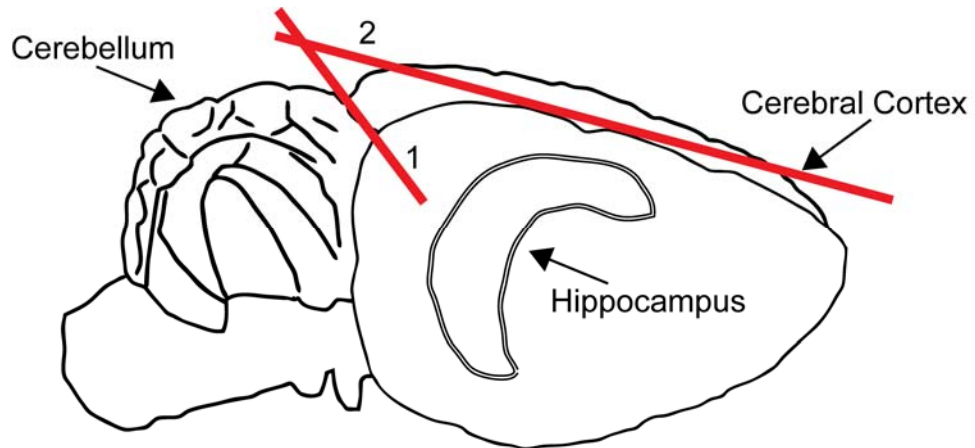


**Figure 2.1.** *Dissection of Adult Rat Cerebellum, Hippocampi and Cortices.*

First, the cerebellum was dissected out by cutting along the plane of the line marked 1, isolating it away from the rest of the forebrain. The two hemispheres of the cortex were then separated by cutting along the plane of the line marked 2 in order to isolate the two hippocampi from the rest of the cerebral cortex.

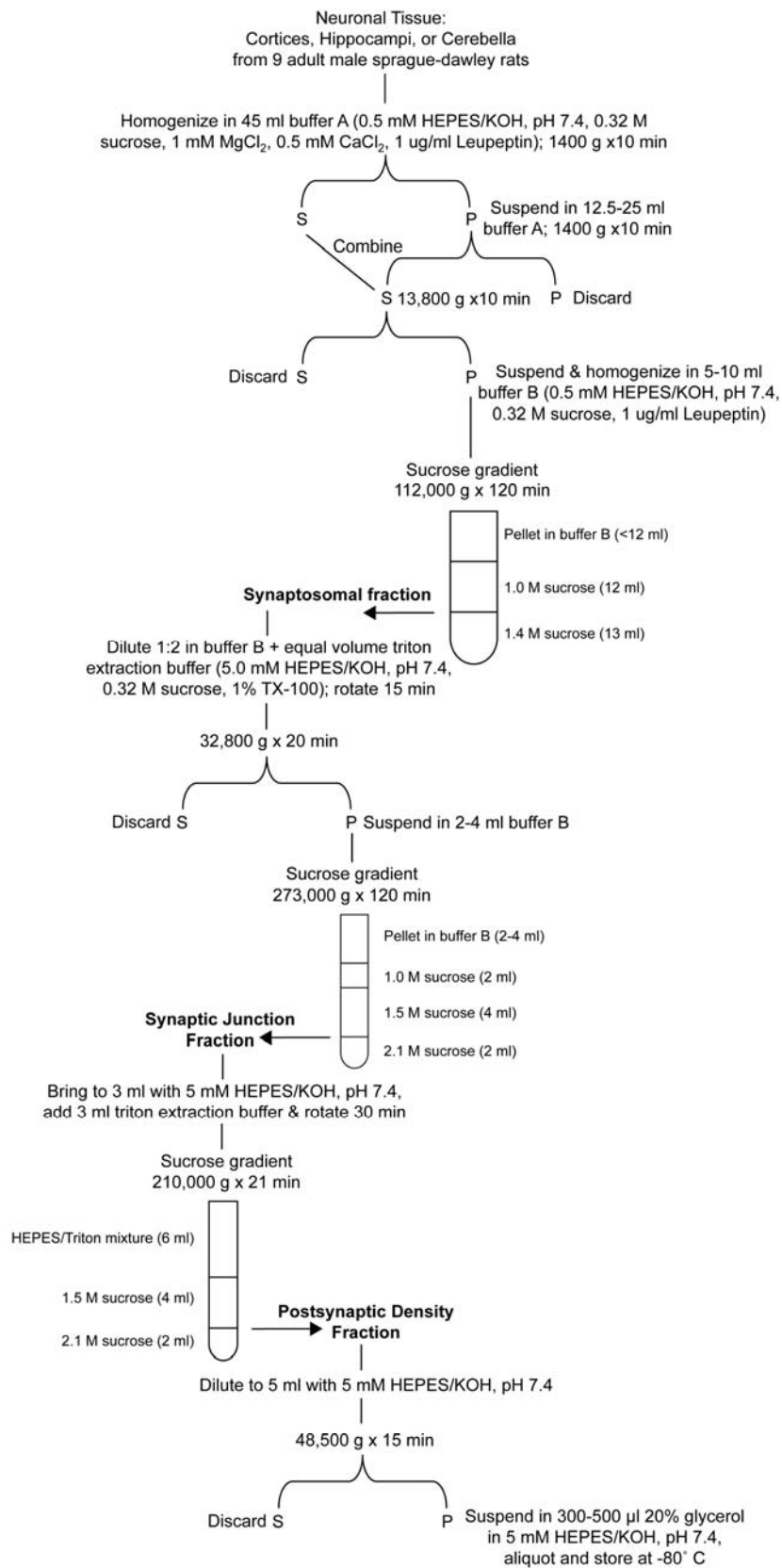


**Figure 2.2.** Isolation of PSDs from Cortices, Hippocampi, and Cerebella.

## *2.2. Protein Assays, SDS Page and Western Blotting*

Protein concentrations were determined in triplicate and averaged using either the Bio-Rad Protein Assay (BIORAD, #500-006) or Pierce BCA Protein Assay Kit (Pierce, #23225), with serial dilutions of BSA standards in buffers matching that of the unknown sample. The Bio-Rad assay is not compatible with detergents, while the Pierce assay is not compatible with glycerol concentrations above 10%.

For protein staining, 3-5 µg of total protein from PSD fractions were separated by SDS-PAGE with 10% polyacrylamide gels. Gels were incubated for 1 hr in excess fixation solution (30% methanol, 7.5% acetic acid) before staining with Amersham Deep Purple Total Protein Stain (GE Healthcare) diluted 1 part stain to 200 parts 100 mM sodium borate, pH 10.5 for 1 hr. After staining, gels were washed for 30 min in wash solution (30% methanol) and then 30 min in fixation solution. After a 5 min rinse in fixation solution, gels were imaged on the Typhoon scanner, using the green laser (532 nm) at 500 PMT and 10 µm resolution; ImageQuant was used to estimate the molecular weight and intensity of each band. All incubations were performed at room temperature on an orbital shaker.

For Western blotting, 5-10 µg of total protein from homogenate, synaptosome, synaptic junction, or PSD fractions from cerebella, hippocampi, cortices, and forebrains were separated by SDS-PAGE with 8%, 10%, or 15% polyacrylamide gels, in running buffer (25 mM Tris Base, 192 mM Glycine, 0.1% SDS). Separated proteins were transferred (transfer buffer: 25 mM Tris Base, 192 mM Glycine, 0.02% SDS, 30% methanol) to nitrocellulose membranes at 4°C for 2 hours at 80 volts and membranes were then incubated in blocking buffer (5% dry milk in wash buffer (10 mM Tris, pH 8.0, 150 mM NaCl, and 0.05% NP40)). Membranes were then incubated in primary

antibodies including  $\alpha$ -actinin (mouse, Sigma, A5044, 1:2500), actin (rabbit, Sigma, A2066, 1:500), PSD-95 (mouse, Thermo-Scientific, MA1-046, 1:2000-5000), Homer (mouse, Santa Cruz, sc-17842, 1:1000), SAP102 (mouse, Neuromab, 75-058, 1:2500), Shank1 (mouse, Neuromab, 75-064, 1:1000), Shank2 (mouse, Neuromab, 75-088, 1:1000), Shank3 (mouse, Neuromab, 75-109, 1:1000),  $\alpha$ CaMKII (mouse, produced in house, 1:2000),  $\beta$ CaMKII (mouse, Invitrogen 13-9800, 1:2000), CaM (mouse, Upstate 05-173, 1:1000), NR1 (mouse, Millipore, MAB363, 1:2500), NR2b (mouse, Millipore, MAB5778, 1:2500), RPT6 (mouse, Enzo Life Science, PW9265, 1:2500) and SV2 (mouse, Developmental Studies Hybridoma Bank, AB 2315387, 1:1000) diluted in blocking buffer, for 1 hour. Primary antibody information is summarized in Table 2.1. Blots were then rinsed twice in wash buffer before a 1 hour incubation in secondary antibodies. Secondary antibodies included HRP anti-mouse (goat, Pierce, 31430, 1:1250-5000), HRP anti-rabbit (goat, Pierce, 31460, 1:2000), or Alexa 488 anti-mouse (goat, Molecular Probes, A-11029, 1:5000). Secondary antibody information is included in Table 2.2. After incubation with secondary antibodies, membranes were rinsed twice with wash buffer prior to imaging on a Typhoon Trio<sup>+</sup> scanner (GE Healthcare), with the green laser (532 nm), a PMT value ranging between 400-550 and a resolution between of at least 50  $\mu$ m. The Pierce<sup>®</sup> ECL 2 system (Thermo Scientific) was used for developing blots incubated with either HRP secondary antibody. This included replacing the wash buffer with 0.1% TWEEN in phosphate buffered saline throughout blot development and a 5 minute incubation in substrate working solution, which contains the substrate to be oxidized by HRP, prior to imaging on a Typhoon Trio<sup>+</sup> scanner (GE Healthcare), with the blue laser (488 nm), a PMT value ranging between 400-550 and a resolution between of at least 50  $\mu$ m.

Western blots were performed for each primary antibody to test specificity on adult forebrain PSD fractions. Each antibody stained the appropriate molecular weight band on the gel and these bands are shown in Figure 2.3. As expected, single bands for  $\alpha$ -actinin, actin, PSD-95, Homer, SAP102, Shank1, Shank2, Shank3,  $\alpha$ CaMKII,  $\beta$ CaMKII, NR1, NR2b, RPT6, and SV2 were detected at 100 kDa, 42 kDa, 95 kDa, 45 kDa, 105 kDa, 205 kDa, 160 kDa, 190 kDa, 55 kDa, 60 kDa, 110 kDa, 170 kDa, 48 kDa, and 95 kDa, respectively.



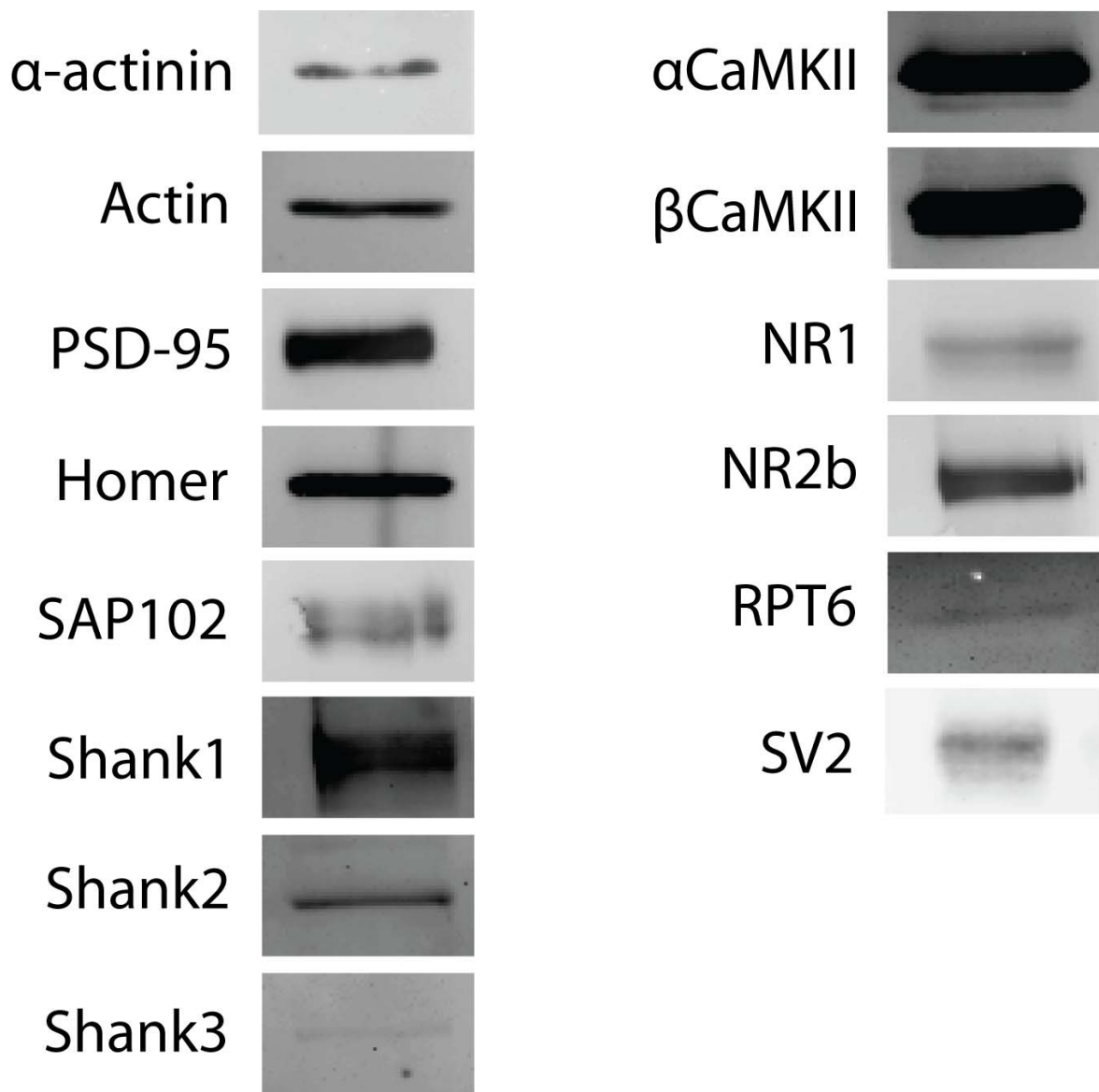


**Figure 2.3.** *Western Blots against PSD Proteins.*

Lanes were loaded with between 5 and 10 ug of adult forebrain PSDs and blots were developed using HRP secondary antibodies and the Pierce<sup>®</sup> ECL 2 system. The SV2 blot was loaded with 8 µg of cortical homogenate, as SV2 is a presynaptic protein not detected in PSD fractions, and was developed with the Alexa 488 goat anti-mouse secondary.

### *2.3. Immunogold Labeling of Isolated Postsynaptic Densities*

Five microliters of PSDs, approximately 0.7  $\mu$ g, were added to freshly glow-discharged formvar/carbon coated copper grids (Ted Pella) for 5 minutes. All steps were performed at room temperature in a humidified chamber. After blotting excess liquid, grids were floated upside down on 35  $\mu$ L drops of blocking buffer (5% BSA in HEPES Buffered Saline: 20 mM HEPES, 150 mM KCL, pH 7.4) for 10 minutes. After blotting, grids were then placed on top of 25  $\mu$ L drops of primary antibody for 30 minutes. Primary and secondary antibodies were diluted to working concentration in blocking buffer. Primary antibodies, summarized in Table 2.1, included those to:  $\alpha$ -actinin (mouse, Sigma, A5044, 1:20), actin (rabbit, Sigma, A2066, 1:20), PSD-95 (mouse, Thermo-Scientific, MA1-046, 1:20), Homer (mouse, Santa Cruz, sc-17842, 1:50), SAP102 (mouse, Neuromab, 75-058, 1:10), Shank1 (mouse, Neuromab, 75-064, 1:20), Shank2 (mouse, Neuromab, 75-088, 1:50), Shank3 (mouse, Neuromab, 75-109, 1:10),  $\alpha$ CaMKII (mouse, produced in house, 1:20),  $\beta$ CaMKII (mouse, Invitrogen 13-9800, 1:100), CaM (mouse, Upstate 05-173, 1:5), NR1 (mouse, Millipore, MAB363, 1:5), NR2b (mouse, Millipore, MAB5778, 1:20), RPT6 (mouse, Enzo Life Science, PW9265, 1:10). After incubation with the primary antibody, grids were rinsed three times by floating on top of 35  $\mu$ L drops of blocking buffer, blotting in between. Grids were then placed on 25  $\mu$ L drops of gold conjugated secondary antibody, diluted in blocking buffer, for 30 minutes. Secondary antibodies, summarized in Table 2.2, included 12nm Colloidal Gold-AffiniPure anti-mouse (goat, Jackson ImmunoResearch, 115-205-068, 1:5) or 12nm Colloidal Gold-AffiniPure anti-rabbit (goat, Jackson ImmunoResearch, 111-205-144, 1:5). Afterwards, grids were placed on a final 35  $\mu$ L drop of blocking buffer. Each grid was then negatively stained by rinsing twice with 5

$\mu\text{L}$  of MilliQ water, once briefly with 5  $\mu\text{L}$  NanoW (Nanoprobes) and afterwards with 5  $\mu\text{L}$  of NanoW for 30 seconds.

Grids were allowed to dry at room temperature for at least 30 minutes and then imaged on a JEOL 1400 electron microscope operated at 120 kV. Images were collected on an Orius camera (Gatan) at 32-64kx magnifications at the image plane. Labeling density was calculated as the total number of gold particles contained within the surface area of the PSD as measured in ImageJ (NIH). A representative immunogold labeled PSD is shown in Figure 2.4, alongside cross-sections through a final cryotomographic reconstruction of a representative immunogold labeled PSD illustrating gold labeling throughout the z-dimension of the PSD. The average labeling density was calculated by averaging 20 individual immunogold labeled PSDs for each region and antibody. Titrations for every primary and secondary antibody were done to ensure asymptotic labeling for a given target protein and Western blots were performed for each primary antibody to test specificity. Negative controls (no primary antibody) were run in each experiment and the number of background gold/surface area was subtracted from the average labeling density. Statistical significance was defined as a p-value  $< 0.05$ , as determined through two-tailed  $t$  tests in Excel.

Antibody	Species	Manufacturer	Catalog Number	WB Dilution	IG Dilution
$\alpha$ -actinin	mouse	Sigma	A5044	1:2500	1:20
actin	rabbit	Sigma	A2066	1:500	1:20
PSD-95	mouse	Thermo-Scientific	MA1-046	1:2000-5000	1:20
Homer	mouse	Santa Cruz	sc-17842	1:1000	1:50
SAP102	mouse	Neuromab	75-058	1:2500	1:10
Shank1	mouse	Neuromab	75-064	1:1000	1:20
Shank2	mouse	Neuromab	75-088	1:1000	1:50
Shank3	mouse	Neuromab	75-109	1:1000	1:10
$\alpha$ CaMKII	mouse	Waxham Lab	--	1:2000	1:20
$\beta$ CaMKII	mouse	Invitrogen	13-9800	1:2000	1:100
CaM	mouse	Upstate	05-173	1:1000	1:5
NR1	mouse	Millipore	MAB363	1:2500	1:5
NR2b	mouse	Millipore	MAB5778	1:2500	1:20
RPT6	mouse	Enzo Life Science	PW9265	1:2500	1:10
SV2	mouse	Developmental Studies Hybridoma Bank	AB 2315387	1:1000	--

**Table 2.1.** *Antibody Information for all Primary Antibodies Used.*

Information includes: the species in which antibody was raised, manufacturer, catalog number, Western blot dilution and immunogold labeling dilution.

Antibody	Species	Manufacturer	Catalog Number	WB Dilution	IG Dilution
HRP anti-mouse	goat	Pierce	31430	1:1250-5000	--
HRP anti-rabbit	goat	Pierce	31460	1:2000	--
Alexa 488	goat	Molecular Probes	A-11029	1:5000	--
12 nm Gold anti-mouse	goat	Jackson Immunoresearch	115-205-068	--	1:5
12 nm Gold anti-rabbit	goat	Jackson Immunoresearch	111-205-144	--	1:5

**Table 2.2.** *Antibody Information for all Secondary Antibodies Used.*

Information includes: the species in which antibody was raised, manufacturer, catalog number, Western blot dilution and immunogold labeling dilution.

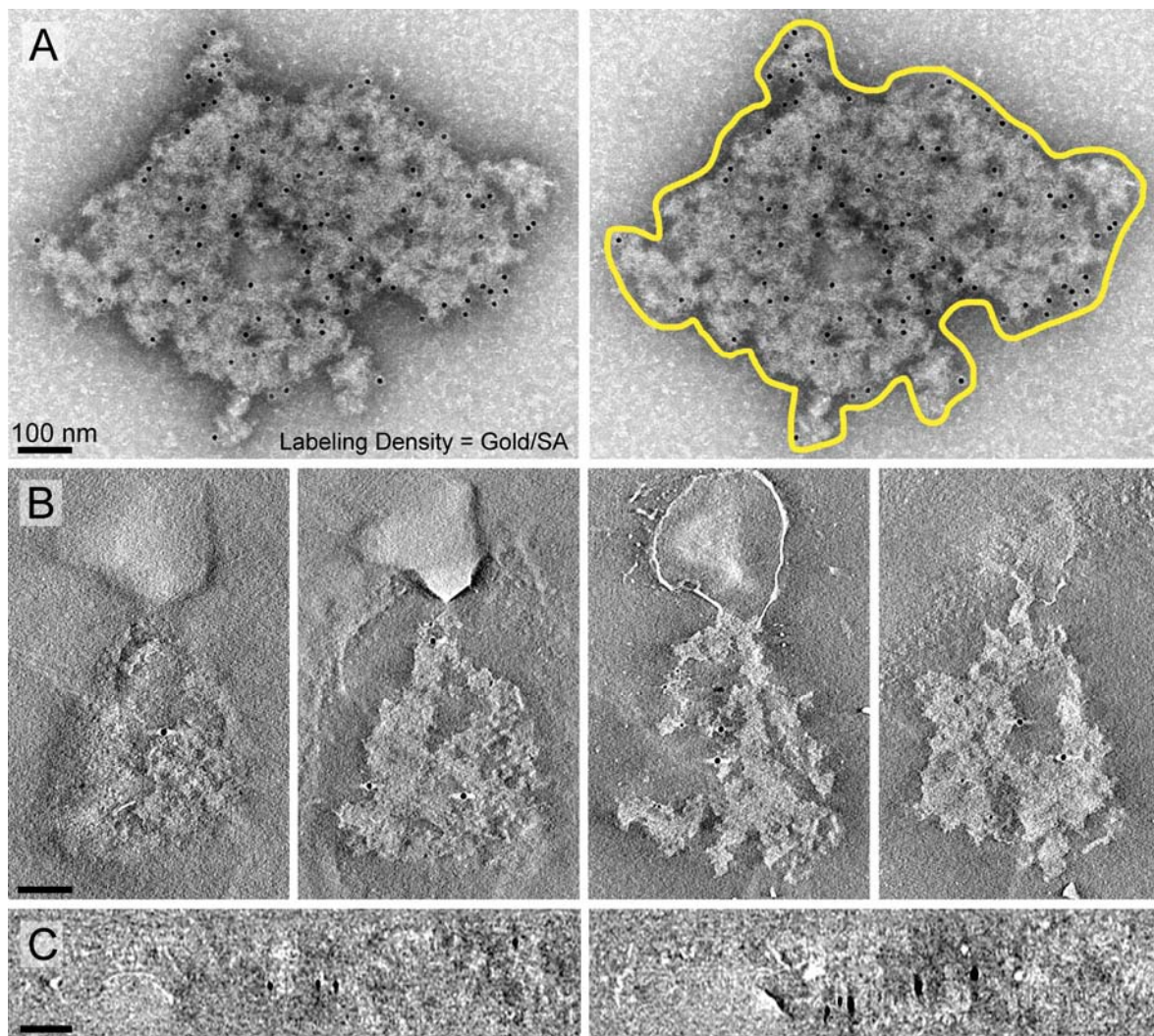


**Figure 2.4.** *Immunogold Labeling.*

A) Electron micrograph of cortical PSD immunogold labeled for  $\beta$ CaMKII. Labeling density is calculated as the number of gold divided by surface area. Surface area is calculated in ImageJ by measuring the number of pixels within a boundary freely drawn around the PSD, similar to left panel, and multiplying by the pixel size, which is reported by the Gatan software when imaging. Labeling density can also be reported as the number of gold per PSD. B) Ten-nanometer cross-sections through a final cryotomographic reconstruction of a representative hippocampal PSD immunogold labeled for the proteasome (6 nm gold) and  $\beta$ CaMKII (12 nm gold). The cross-sections illustrate gold labeling throughout the entire z-dimension of the PSD, suggesting that PSDs are permeable to gold conjugated secondary antibodies. C) Side views of the same immunogold labeled PSD, from B, illustrating gold labeling through the x-dimension (yz view). Scale bars = 100 nm.

#### *2.4. Spatial Analysis of Immunogold Labeling*

For 2D spatial analysis of gold labeling, I employed a Ripley's K-function based analysis to determine whether the gold distribution for a given PSD deviated from spatial randomness, as previously described (Swulius et al., 2010). Briefly, coordinates representing the boundary of the PSD and gold were recorded and a MATLAB (MathWorks) model was generated. The 2D spatial distribution of the gold was then compared to 1000 simulations of complete spatial randomness, within the same boundary given the same number of gold particles. This procedure was accomplished for every PSD where spatial analysis was employed.

For each immunogold labeled PSD, like the example shown in Figure 2.5.A, Photoshop (Adobe) was used to create a binary image of points outlining the PSD boundary and depicting gold distribution. To achieve this, a new layer was created for each image and the PSD border was defined in points using the paintbrush function at 15 pt and 100% hardness in as few points as needed to define the boundary. On the same layer, a point was created for each gold particle within the PSD boundary using the paintbrush function at 9 pt and 50% hardness. The layer was then saved as a grayscale image and opened in ImageJ. In ImageJ, the threshold function was used to select all of the points in the binary image. Using the analyze particles function, set to measure center of mass, the coordinates of each point were reported. For boundary points, the size entered into the analyze particle interface was 60-infinity, while for gold coordinates 1-50 was entered as the size. A text file was created for each image with boundary point coordinates ordered clockwise starting with the point closest to the top of the image and gold coordinates were listed below. All boundary coordinates were

denoted with a 1 before the x and y coordinates, while gold coordinates were denoted with a 2 prior to the x and y coordinates.

MATLAB (MathWorks) was then used to create coordinate models, like the example shown in Figure 2.5.B, for each PSD using the text files. The coordinate models were then used to create 1000 examples of complete spatial randomness (CSR) in MATLAB using the same boundary and same number of gold particles as the coordinate model. To determine whether the gold particle distribution deviates from random, the gold distribution was compared to the 1000 examples of CSR, using Ripley's K-function (Ripley, 1976, 1977, Kiskowski et al., 2009). Ripley's K-function uses concentric circles of various radii to calculate the average number of gold particles over distance from the center of each particle (Ripley, 1976, 1977). For example, Ripley's K-function analysis of clustered gold would show an increased number of gold particles at small radii as compared to examples of CSR. The example shown in Figure 2.4 C shows the H-function variant of Ripley's K-function, which is normalized so that the expected function is 0 (Loosmore and Ford, 2006). In the example shown in Figure 2.5, the experimental data from Figure 2.5.B is shown as a red line in Figure 2.5.C and CSR is the black line at 0. If the experimental data, red line, moves outside of the upper or lower envelopes, dashed lines, the data is said to deviate from random. In this example the data deviates at smaller radii from the upper envelope, indicating clustering and at larger radii drops below the envelope, indicating dispersion at larger distances (Figure 2.5).



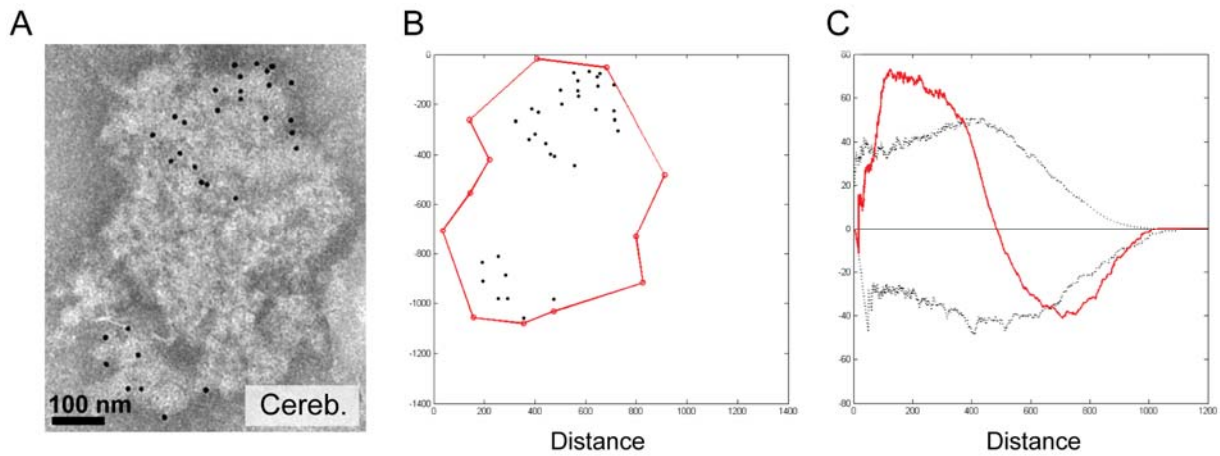


**Figure 2.5.** *Example Ripley's K-Function Analysis.*

Ripley's K-function analysis of a cerebellar PSD immunogold labeled for PSD-95. A) Negative stain electron micrograph of a PSD from cerebella immunogold labeled for PSD-95. B) Coordinate model for the PSD in A. The boundary is defined by red points, while the gold is represented in black points. C) H-function for example PSD. Simulated complete spatial randomness (black solid line) was normalized to zero and the Ripley's K-function of the experimental data is shown as a red line. Non-random distribution was determined by whether the red line crossed either the maximum and minimum envelopes (dashed lines), defined by 1000 simulations of complete spatial randomness. Scale bar = 100 nm.

## 2.5. Electron Tomography

Fiducial markers were prepared by adding 125  $\mu\text{L}$  of 5% BSA in HBS to 200  $\mu\text{L}$  of 10 nm colloidal gold for 5 min at RT. The gold was then spun at 14,000 x g for 18 min and resuspended in 5 mM HEPES, pH 7.4. PSDs were thawed, diluted in 5 mM HEPES, pH 7.4, spun down at 14,000 x g for 18 min, and resuspended in 5 mM HEPES buffer, pH 7.4 containing BSA coated colloidal gold as fiducial markers. For negative stain tomography, 5  $\mu\text{L}$  of PSDs with gold were applied to freshly glow-discharged formvar/carbon coated copper grids (Ted Pella) for 5 min. Grids were blotted, rinsed twice with 5  $\mu\text{L}$  MilliQ water and stained twice with 5  $\mu\text{L}$  NanoW (Nanoprobes), a 2% solution of methylamine tungstate. For electron cryotomography, 5  $\mu\text{L}$  of PSDs with gold were applied to 200 mesh copper 2/2 Quantifoil grids (EMS). Grids were blotted by hand and plunged into liquid ethane cooled with liquid nitrogen. The resulting grid preparations are modeled in Figure 2.6 in order to illustrate the differences between dehydrated negatively stained PSD samples and the non-stained hydrated cryo-preserved PSD samples. For all tomography, grids were imaged on a Technai F30 Polara, using FEI's Batch Tomography software at 2x binning with a Tietz 4K x 4K CCD. Negatively stained PSDs were imaged at 1° tilt angles from -60° to 60° at ~10  $\mu\text{m}$  defocus with a total dose less than 300  $\text{e}^-/\text{\AA}^2$  and a final pixel size of 0.9215 nm/pixel. For cryotomography, PSDs were imaged every 2° from -60° to 60° between 10 and 15  $\mu\text{m}$  defocus with a total dose less than 180  $\text{e}^-/\text{\AA}^2$  and a final pixel size of 1.193 nm/pixel. Individual PSDs were selected for tilt series collection based on gross morphologic criteria including diameter.

## *2.6. Tomographic Reconstruction and Image Processing*

The resulting image stacks were aligned to create three-dimensional reconstructions in ETomo within the IMOD suite of programs (Mastronarde, 1997) <http://bio3d.colorado.edu/imod/>. When aligning a new tomogram in ETomo, the file was selected, axis defined and header scanned for information. Missing header information was supplied, such as fiducial diameter, and com scripts were created. For pre-processing, a fixed stack was created and viewed. The cross correlation was then calculated for the fixed stack and a coarse aligned stack was created and viewed. Next the fiducial model was generated, at least 10 fiducial markers around the subject of interest were selected, and the seed model was tracked. Gaps in tracking were corrected and tracking was rerun. The alignment was then computed and if the residual error mean or standard deviation were above 0.5 and 0.3, respectively, residual vectors were examined, corrected and alignment recomputed. A 3x binned sample tomogram was created for positioning of the tomogram. The sample tomogram was opened, the X and Y dimensions flipped and 3 parallel lines created to define the orientation of the PSD throughout the Z dimension. Once the orientation was determined for the PSD, the final alignment could be created. Then, the default cubic interpolation was employed for negative stain tomography, while linear interpolation was selected for cryotomography, to reduce noise. The file was then binned to 1k and gold was erased. Low pass two-dimensional filtering was employed for cryotomograms to further reduce noise; cutoff and sigma values were 0.1 and 0.05, respectively. Once the full aligned stack was created, the full tomogram was generated, trimmed, pixels scaled and rotated around the x-axis.

Additional filtering steps were employed when reconstructing cryotomograms to increase the signal to noise ratio. Cryotomograms are inherently noisier than negative stain tomography and were collected at approximately half the dose, reducing the total signal. Increasing the signal to noise ratio was important for increasing the range between pixel intensities for buffer and protein in cryotomograms in order to calculate the protein-to-volume ratio of cryo-preserved PSDs. Figure 2.6 illustrates how additional filtering of the same cryotomogram can significantly increase visual contrast, although, at the cost of losing finer detail. Table 2.3 summarizes the average pixel intensity for buffer and for protein for each of the examples shown in Figure 2.6. The range between the average pixel intensities for buffer and for protein significantly increases with additional filtering, most intensely with the addition of low pass two-dimensional filtering (Table 2.3). For reconstruction of cryotomograms, linear interpolation and low pass two-dimensional filtering with a cutoff value of 0.1 was selected to be a part of the standard protocol, as this provided improved signal to noise ratio, while still maintaining finer detail. A description of the filtering options and suggested filtering conditions for tomographic reconstruction can be found online (<http://bio3d.colorado.edu/imod/doc/tomoguide.html#Filtering2D>).

To accomplish the protein-to-volume analysis, only PSDs that were centered within the holes of the quantifoil grids could be used to allow for the distinction between protein density and surrounding buffer. Because the PSDs had a tendency to attach to the carbon surface, the number of reconstructed images fitting this criterion was limited to 12 per group. Amira (v 5.3.3; Visage Imaging Inc. San Diego, CA) was used to calculate the protein-to-volume ratios of cryo-preserved PSDs from the final tomographic reconstructions using the following steps. For each individual tomogram,

the PSD boundary was defined in the XY dimensions every 5<sup>th</sup> slice through the z-dimension, enclosing the voxels representing both protein and open space within the PSD complex, and then the program interpolated the boundary enclosing the whole PSD volume. A pixel intensity threshold was then determined for each tomogram in order to distinguish between pixels representing protein and pixels representing buffer enclosed in the PSD volume. The threshold was set as the mid-point between the mean buffer and mean protein pixel intensities, as determined by calculating the statistical mean pixel intensity for 10x10x10 voxel cubes of only buffer and of PSD protein material, determined through the clip stats command in 3DMOD (IMOD). Using the threshold value, the voxels representing protein within the PSD boundary were segmented, quantified and the protein-to-volume ratio determined. Values are reported as the total number of voxels above the threshold value divided by the total number of voxels enclosed within the PSD boundary.

PSD thickness was determined by multiplying the number of tomographic slices that contained PSD protein density in the Z-dimension, determined in 3DMOD, by the pixel sizes of the reconstructions. Surface areas were determined by multiplying pixel size by the total number of pixels within the X-Y boundary of each PSD. The boundaries were set manually in ImageJ using the full projections of the tomograms created in 3DMOD. Differences were considered significant if  $P < 0.05$  in a 2-tailed t test.

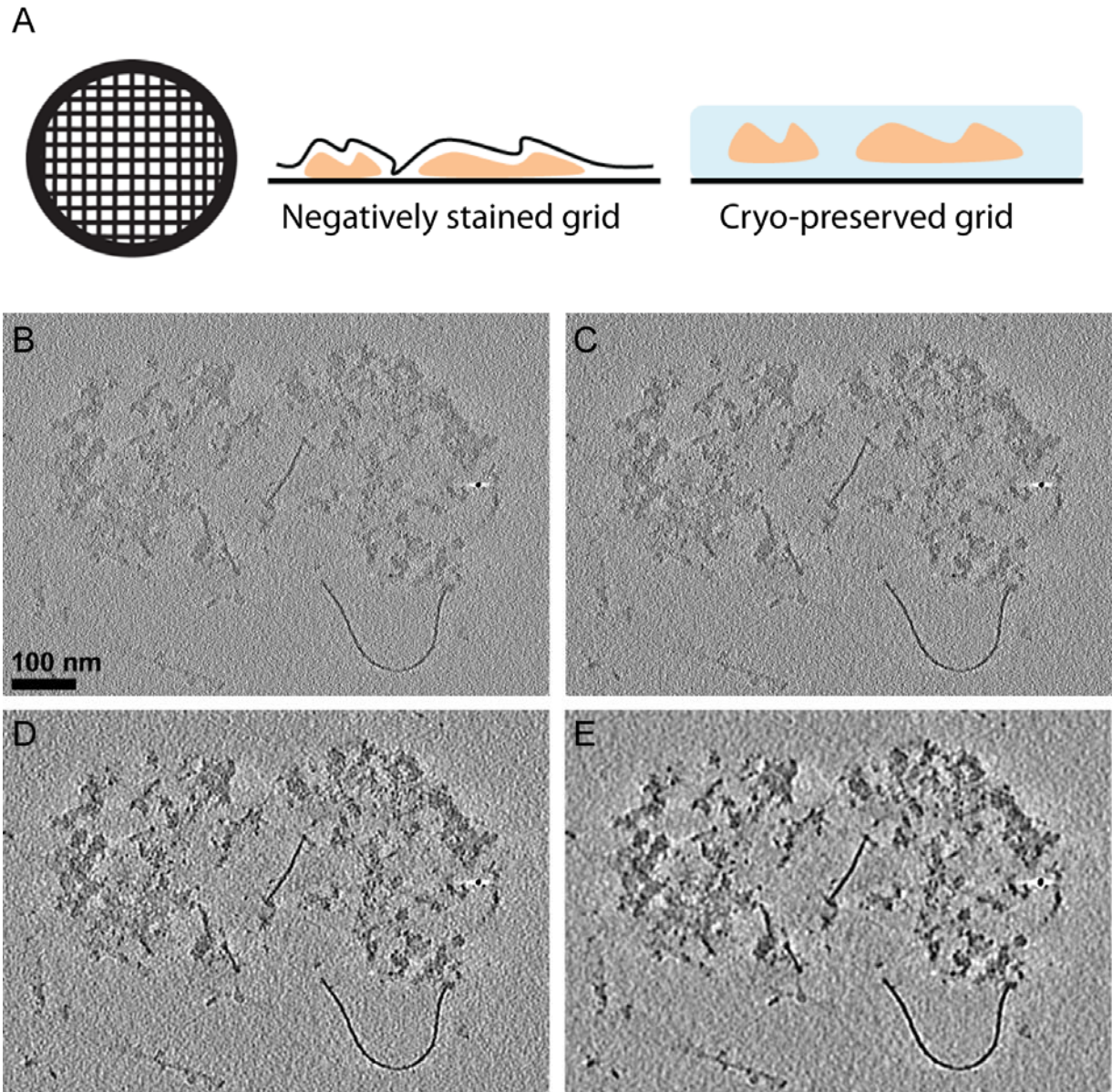


**Figure 2.6.** *Grid Preparation and Differential Filtering of a Tomographic Reconstruction.*

Shown for comparison in A) are cartoon models including a top down view of an EM grid as well as side views of both a dehydrated negatively stained PSD grid and a hydrated cryo-preserved PSD grid. Included in B-D) are 10 nm cross-sections through the same tomographic reconstruction of a cryo-preserved cortical PSD with differential filtering conditions employed throughout the reconstruction process. The reconstructions were identical until the creation of the final aligned stack. The example in B) was filtered only with the default cubic interpolation, while C) was filtered by linear interpolation. Examples D-E) were filtered by linear interpolation and low pass 2D filtering. The cutoff value for 2D filtering in D) was the default value, 0.1, while the value employed for E) was 0.05. Scale bar = 100 nm.

<b>Image</b>	<b>Filtering Conditions</b>	<b>Pixel Intensity for Buffer</b>	<b>Pixel Intensity for Protein</b>	<b>Range</b>
<b>A</b>	Default	150.3	130.4	20.7
<b>B</b>	Linear Interpolation	148.5	124.0	25.2
<b>C</b>	Linear + 2D filtering (0.1 cutoff)	147.6	106.2	41.6
<b>D</b>	Linear + 2D filtering (0.05 cutoff)	146.6	92.1	54.0

**Table 2.3.** *Differential Filtering of a Tomographic Reconstruction.*

The average pixel intensity for buffer and for protein was calculated for each reconstruction shown in Figure 2.5, to test the effect on differential filtering on the pixel intensity range between protein and buffer. This table lists the average pixel intensity for buffer, the average pixel intensity for protein and the difference between the two, termed range, for each example from Figure 2.5. Average pixel intensity was determined by measuring the mean pixel intensity for the same 10x10x10 voxel cubes of only buffer and of mostly protein for each reconstruction.

## **Chapter 3. Isolation of Postsynaptic Densities from Adult Rat Cerebral Cortices, Hippocampi, and Cerebella**

### *3.1. Enrichment of PSDs from Brain Tissue*

PSDs have been successfully biochemically isolated from synapses for decades (Cotman et al., 1974, Cohen et al., 1977), providing the ability to study the three-dimensional gross morphology of the synaptic organelle through electron microscopy (Cotman et al., 1974, Cohen et al., 1977, Carlin et al., 1980, Swulius et al., 2010, Fera et al., 2012, Swulius et al., 2012), and its protein composition through SDS-page (Blomberg et al., 1977, Carlin et al., 1980, Swulius et al., 2010), Western blotting (Petrallia et al., 2005, DeGiorgis et al., 2006), immunogold labeling (Petersen et al., 2003, DeGiorgis et al., 2006, Swulius et al., 2010) and more recently through proteomic approaches (Jordan et al., 2004, Li et al., 2004, Peng et al., 2004, Yoshimura et al., 2004, Cheng et al., 2006, Dosemeci et al., 2006, Dosemeci et al., 2007). However, there has not been a comprehensive comparison of morphologic structure and protein composition for PSDs from different brain regions. The work presented in this dissertation is the first use of negative stain and cryo electron tomography to directly compare the three-dimensional structure of PSDs isolated from cerebella, hippocampi, and cerebral cortices. It is also the first application of immunogold labeling to determine how the PSD protein composition and organization differs between individual morphologically identified PSDs from these brain regions.

PSDs were isolated from cerebral cortices, hippocampi, and cerebella, three brain areas amenable to straightforward isolation with unique population of neuronal cells. PSDs were isolated as described in the experimental procedures, adapted from



an established and widely used protocol (Cohen et al., 1977), similar to previously published protocols from the Waxham lab (Swulius et al., 2010, Swulius et al., 2012), and as briefly illustrated in Figure 3.1. Cerebella, hippocampi, and cortices from whole adult rat brains were rapidly dissected and separately homogenized. The homogenate fraction was refined through two low-speed centrifugations, prior to a medium-speed centrifugation, which produced a pellet enriched with pinched off nerve endings (synaptosomes) that were purified on a discontinuous sucrose gradient. Detergent treatment with TX-100 and centrifugation of synaptosomes lysed the pre- and postsynaptic elements, leaving synaptic junctions, which are composed of the PSD and residual presynaptic and postsynaptic plasma membranes. A high-speed centrifugation of a discontinuous sucrose gradient further refined the synaptic junction fraction. A second detergent treatment with TX-100 and centrifugation removed the remaining synaptic membranes providing the PSD fraction, which was purified with a final high-speed centrifugation of a discontinuous sucrose gradient.

Enrichment for PSDs through the steps of the isolation was monitored by Western blot (Figure 3.2). Eight total micrograms of the homogenate, synaptosome, synaptic junction and PSD fractions from each brain region were separated by SDS-PAGE and probed using antibodies against PSD-95 and SV2 (Figure 3.2). PSD-95 is a PSD scaffold protein, which served as a marker for PSDs, while SV2 is a synaptic vesicle protein, which served as a presynaptic marker. As anticipated, PSD-95 undergoes significant enrichment moving from the homogenate fraction (Hom.) to the PSD fraction, with a major enrichment coming at the step of synaptic junction (Syn. J.) enrichment (Figure 3.2). In contrast, SV2 becomes undetectable when synaptosomes (Syn.) are lysed with detergent to create the synaptic junction fraction (Figure 3.2), as

soluble presynaptic elements have been removed. Overall the enrichment and loss patterns of PSD-95 and SV2, respectively, were similar amongst the fractions from cerebella, hippocampi and cortices (Figure 3.2), confirming enrichment for PSD-95 rich material absent of presynaptic elements.

Representative electron micrographs of negatively stained synaptic junctions and PSDs from cerebella, hippocampi and cortices are shown in Figure 3.3. Negative stained synaptic junction fractions were lipid heavy, as expected since synaptic junctions are composed of the PSD and both presynaptic and postsynaptic membranes, and comparable to negative stain micrographs of isolated synaptic junctional complexes (Cotman et al., 1974, Matus and Taff-Jones, 1978) and isolated synaptosomal membrane fractions (Cohen et al., 1977). Most of the protein material appeared to bind directly to the grid with the lipid material resting on top, as shown in the left column of Figure 3.3. Synaptic junctions were circularly shaped, similar to isolated PSDs (right column Figure 3.3), with well-defined boundaries and diameters ranging from several hundred nanometers to well over a micron. The negative stained PSDs appeared to attach to the carbon surface with either their cytoplasmic or synaptic faces, giving them a general disc shape with irregular yet well-defined boundaries like the examples shown in the right column of Figure 3.3. PSDs were quite variable with respect to their diameters, which were typically several hundred nanometers, and displayed wide ranges of surface topology or texture like the examples in Figure 3.3.

To further characterize the enrichment of PSDs from cortices, hippocampi, and cerebella, the protein profiles for the homogenate, synaptic junction and PSD fractions were compared for each brain region (Figure 3.4). Three micrograms of total protein from each fraction were separated by SDS-PAGE and stained with deep purple stain;

the major bands in each lane are indicated with asterisks (Figure 3.4). For all regions, the protein profile is similar between the homogenate and synaptic junction fractions, while the profile differs for the PSD fraction (Figure 3.4), similar to previous comparisons of SDS-PAGE protein profiles between homogenates, synaptosomes and PSDs from adult rat forebrain PSDs (Swulius et al., 2010) and between synaptic membrane fractions and PSDs from canine cortices (Blomberg et al., 1977). The protein profiles are almost identical between cortical homogenate and synaptic junction fractions, as well as between hippocampal homogenate and synaptic junction fractions (Figure 3.4). The cerebellar synaptic junction fraction contains many but not all of the major bands present in the cerebellar homogenate fraction (Figure 3.4). For all brain regions, several of the protein bands are present in all fractions, but PSD fractions contain unique bands enriched from both the synaptic junction and homogenate fractions (Figure 3.4). Additionally, the intensity of some of the higher molecular weight bands is increased in the PSD fractions; these bands may represent PSD scaffolds like Shank proteins, which are enriched in the PSD fraction (Tao-Cheng et al., 2010). The protein patterns for the individual fractions are also similar when compared across the different regions, although there is some variety in the profiles of the PSD fractions (Figure 3.4), suggesting that PSDs from cerebella, hippocampi, and cortices have unique protein compositions which is consistent with previous SDS-PAGE protein profiles comparing cerebellar and cortical PSD fractions (Carlin et al., 1980, Cheng et al., 2006).

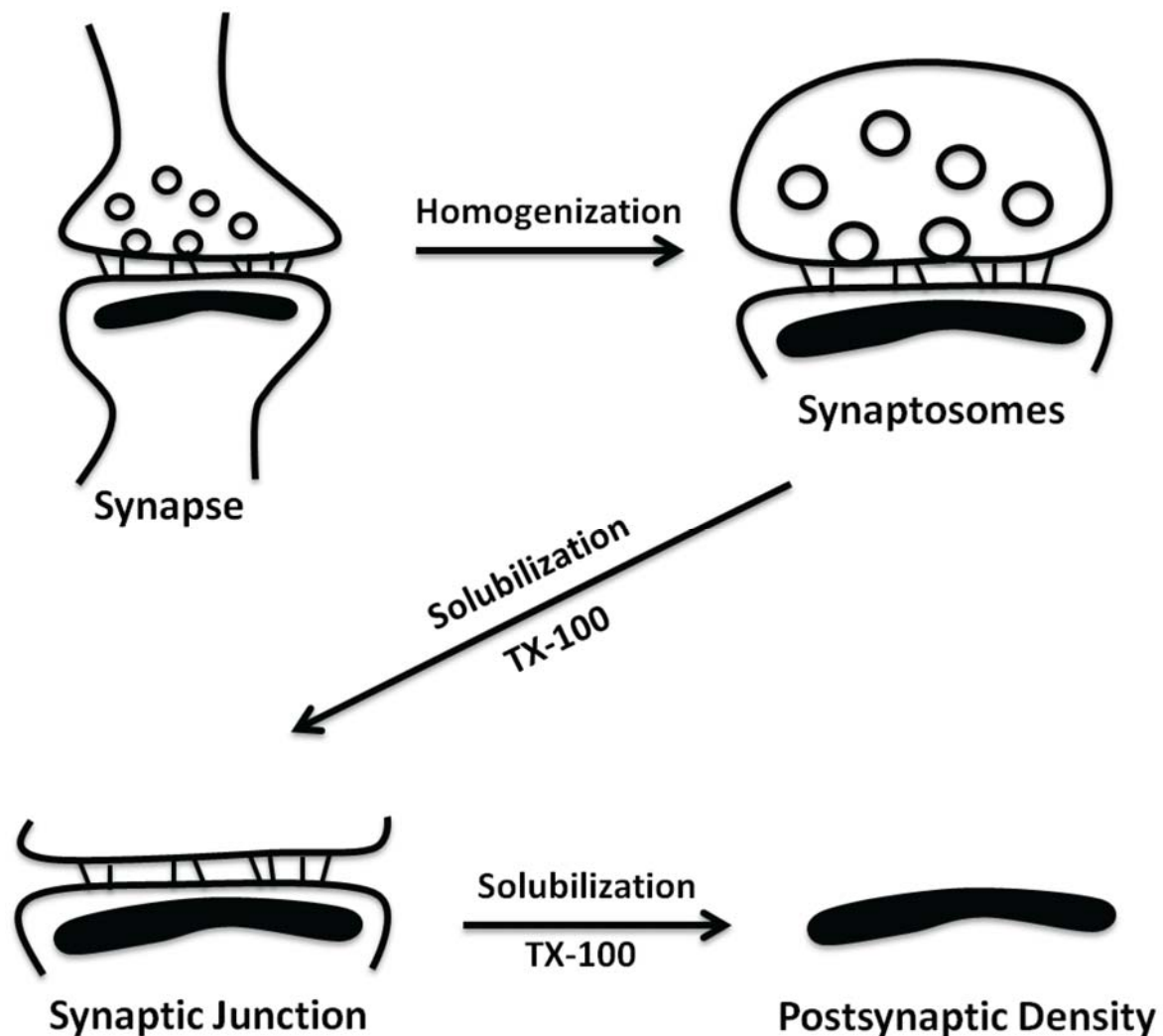


**Figure 3.1.** *Isolation of Postsynaptic Densities.*

Synapses are separated from homogenized whole brain tissue through centrifugation. Further homogenization and centrifugation produces fractions enriched for synaptosomes, which when solubilized with TX-100 produces synaptic junctions, composed of the presynaptic and postsynaptic plasma membranes and the PSD. Treatment of synaptic junctions with TX-100 further solubilizes the remaining synaptic membranes isolated PSDs.

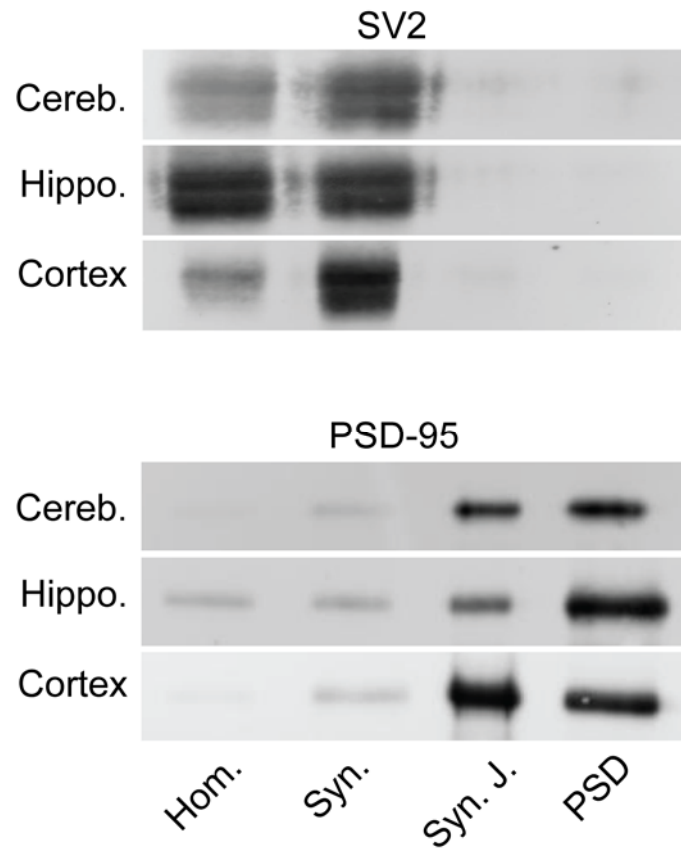


**Figure 3.2.** *Loss of Presynaptic Elements and Enrichment of Postsynaptic Elements.*

Western blots illustrating loss of synaptic vesicle protein, SV2, and enrichment of PSD scaffold, PSD-95, through the isolation of PSDs from cerebella, hippocampi, and cortices. SV2 loss is seen in synaptic junction (Syn. J) and PSD fractions in comparison to brain homogenate (Hom) and synaptosome (Syn) fractions. PSD-95 increases significantly from homogenate to PSD fraction. Eight micrograms of total protein were loaded into each lane and the secondary antibody was Alexa 488 goat anti-mouse (Molecular Probes).

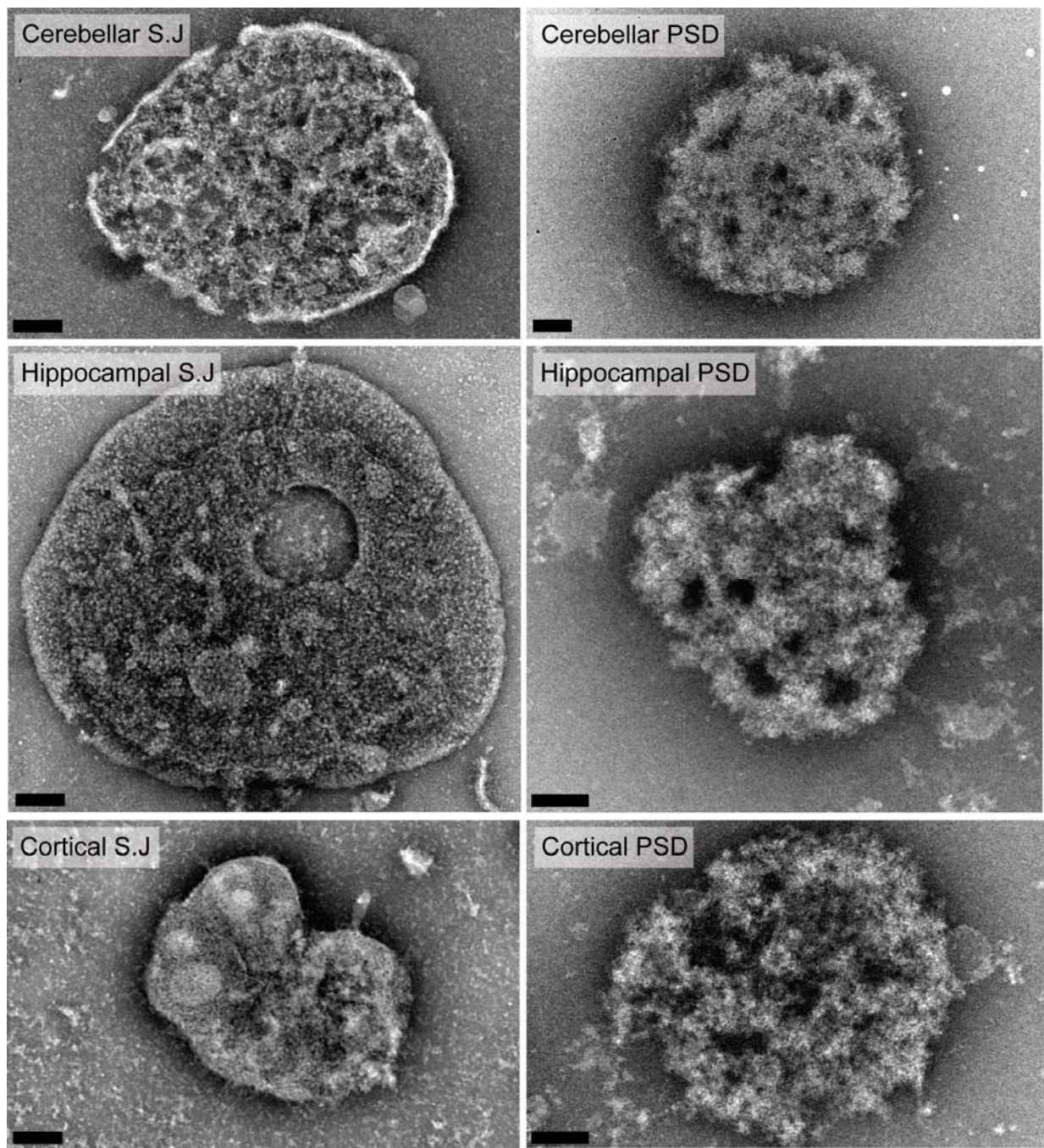


**Figure 3.3.** *Electron Micrographs of Synaptic Junctions and PSDs.*

Representative negative stain electron micrographs of synaptic junction material and isolated PSDs from cerebella, hippocampi, and cortices. Scale bars = 100 nm.



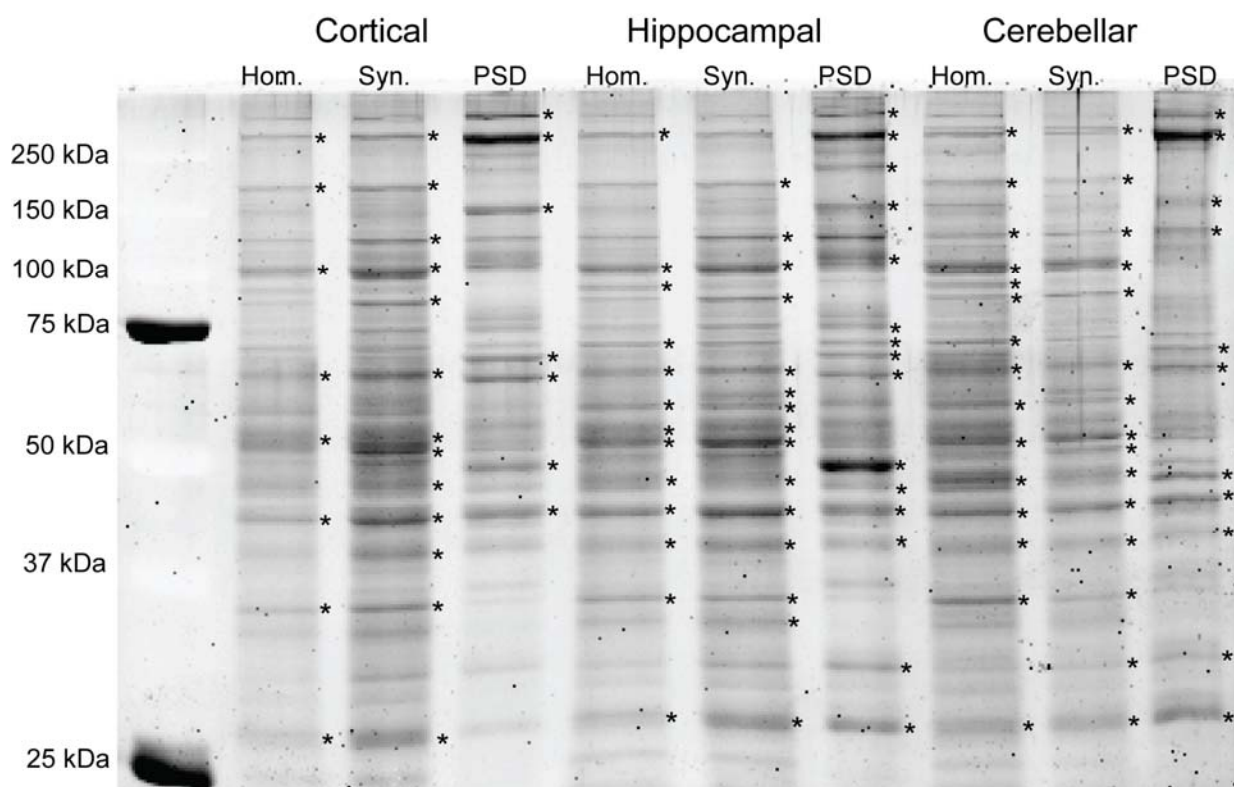


**Figure 3.4.** *Protein Profiles of Homogenate, Synaptosome and PSD fractions.*

Comparison of homogenate (Hom.), synaptosome (Syn.) and PSD protein profiles for cortical, hippocampal and cerebellar fractions, through deep purple staining of SDS-PAGE-separated proteins. Three micrograms of total protein were loaded into each lane. The major bands in each lane are indicated with asterisks. Molecular weights (kDa) are indicated to the left of the gel. Major bands were defined as bands whose intensities were at least twice the average band intensity within each sample as measured in ImageQuant.

### *3.2. Gross Morphology of Isolated PSDs from Negative Stain Micrographs*

For initial morphologic descriptions, isolated PSDs from each region were loaded onto glow discharged carbon formvar copper grids, stained with methylamine tungstate and then electron micrographs were collected. Low magnification micrographs shown in Figures 3.5-3.7 are representative fields of isolated PSDs from each region. Figure 3.5 is a low magnification micrograph of a typical field of negatively stained isolated cortical PSDs and three cortical PSDs, which are highlighted with arrows. Cortical preparations typically produced the best yield of isolated PSDs and this is well represented in Figure 3.5, as there is a high density of PSDs relative to the other regions. Detergent resistant lipids, described in more detail in Chapter 4, are also visible in the micrograph and the variability in PSD size is evident (Figure 3.5). Figure 3.6 is a low magnification micrograph of a field of negatively stained isolated hippocampal PSDs. The density of hippocampal PSDs is not as high as cortical PSDs, but this is representative of typical hippocampal PSD yields. Two well-defined hippocampal PSDs are highlighted with arrows (Figure 3.6). The filament in the top left of Figure 3.6 should be noted, as filaments are often seen in the PSD enriched fraction; it is likely the filament is composed of neurofilament proteins, which are known contaminants in PSD enriched fractions (Peng et al., 2004, Cheng et al., 2006, Dosemeci et al., 2006). Figure 3.7 is a low magnification micrograph of a field of isolated and negatively stained cerebellar PSDs. The density of cerebellar PSDs is more comparable to that of hippocampal PSDs and three well-defined cerebellar PSDs are highlighted with arrows (Figure 3.7).

Figures 3.5-3.7 also highlight the range of negative staining that naturally results from the staining protocol. The high density of material on the cortical PSD grid



plausibly helped to pool the stain providing sufficient and fairly even contrast between protein and the carbon background (Figure 3.5). The image in Figure 3.6, which has less PSD material on the grid, has areas of thicker stain around lipid and protein materials, like the highlighted hippocampal PSDs. Figure 3.7 is an example more similar to positive staining, where the protein is stained as opposed to the background, leaving the PSDs darker, or more electron dense, than the carbon surface.

Individual micrographs were collected of well-stained isolated PSDs from each region to assess the gross morphology of the different PSDs. Representative examples of individual PSDs from each region, imaged at high magnification, are shown in Figures 3.8-3.10. Figure 3.8 includes nine examples of cortical PSDs, and Figures 3.9 and 3.10 each include nine examples of hippocampal and cerebellar PSDs, respectively. From the negative stain micrographs collected and analyzed, cortical PSDs can be described as enormous protein complexes that are roughly disc-shaped. They had well-defined edges that were typically irregular in shape as seen in Figure 3.8. Cortical PSDs also varied greatly in diameter, as seen in Figure 3.8, where PSD diameters ranged from approximately 400 nm to a micron. Lipids were also often seen on and around individual PSDs and appeared attached to the protein density. Three PSDs in Figure 3.8 have intact detergent resistant lipid membranes clearly visible and the other PSDs appear to have remnants of lipid material. Texturally cortical PSDs were very similar amongst each other, composed of finely packed proteins forming a topology of ridges and valleys; ridges of lightly stained protein and dark valleys lacking in protein density, where stain has pooled.

Hippocampal PSDs were morphologically similar to cortical PSDs. Hippocampal PSDs, like the representative examples in Figure 3.9, were generally disc-shaped, with

irregular boundaries, some better defined than others. The hippocampal PSD in the middle of the bottom row and the example in the bottom right corner of Figure 3.9 have boundaries that are not as well-defined as the other examples. The example in the bottom right corner also has filaments near the upper left edge of the PSD, although it's unclear whether the filaments are interacting with the PSD from this example as they could have separately bound to the carbon surface of the grid. The diameter of hippocampal PSDs also greatly varied and the examples in Figure 3.9 range from approximately 400 nm to over a micron, similar to the cortical PSDs in Figure 3.8. Hippocampal PSDs also appear to have lipid membranes attached to the protein density and Figure 3.9 includes several PSDs with large lipid membranes, several with smaller lipid structures and two examples of what seems to be lipid remnants. Texturally hippocampal PSDs were also similar to cortical PSDs in that they appeared to be composed of finely compacted proteins organized into ridges of protein and valleys absent of protein where stain pooled, however, some of the material within hippocampal PSDs was not as crisp or finely resolved as in cortical PSDs. This could be due to the particular staining of the grids or perhaps some hippocampal PSDs have more lipid within their structure, which does not image as crisp as protein.

The texture of cerebellar PSDs ranged significantly; some cerebellar PSDs were composed of finely packed and crisply defined protein organized into ridges and valleys, although the areas absent of protein appeared smaller on average in cerebellar PSDs, like the representative cerebellar PSDs in the middle position of the top row and the left and right columns of the middle row in Figure 3.10. Some cerebellar PSDs, like the examples in left column of the top and bottom rows and the right column of the bottom row of Figure 3.10, were more cloudy in appearance, or not as crisp as others

and these structures appeared to have larger valleys or areas lacking in protein density, than the finer pack and more crisply imaged cerebellar PSDs, which more closely resembled hippocampal and cortical PSDs. Cerebellar PSDs were still generally describable as disc-shaped protein densities with irregularly shaped boundaries, which appeared to not be as well-defined as and more irregular than both hippocampal and cortical PSDs. Similar to hippocampal and cortical PSDs, lipids were often seen bound to cerebellar PSDs and the diameter of cerebellar PSDs was also quite variable, with the examples in Figure 3.10 ranging from 400 nm to over a micron.

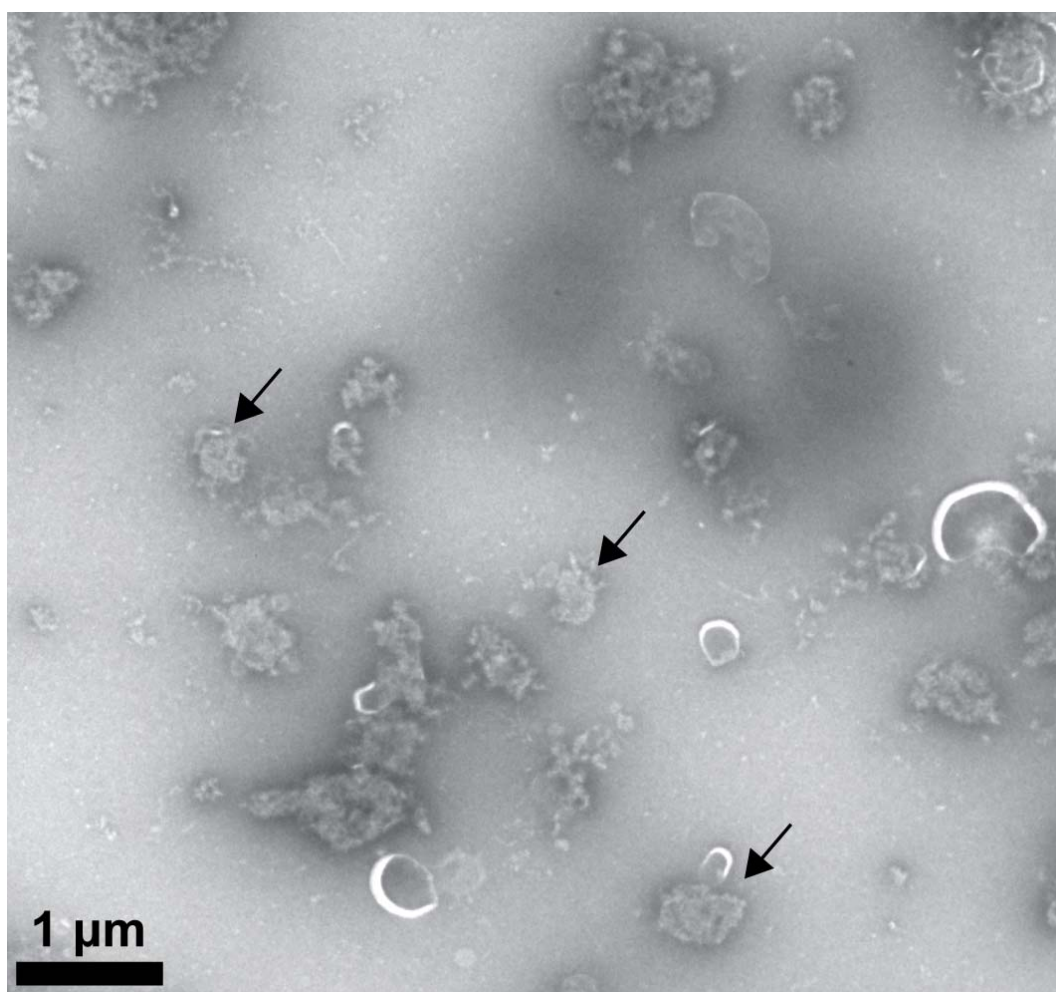


**Figure 3.5.** *Low Magnification Micrograph of Negatively Stained Cortical PSDs.*

Low magnification micrograph showing a typical field of isolated negatively stained cortical PSDs. Three well-defined cortical PSDs are highlighted with arrows. Scale bar = 1  $\mu\text{m}$ .

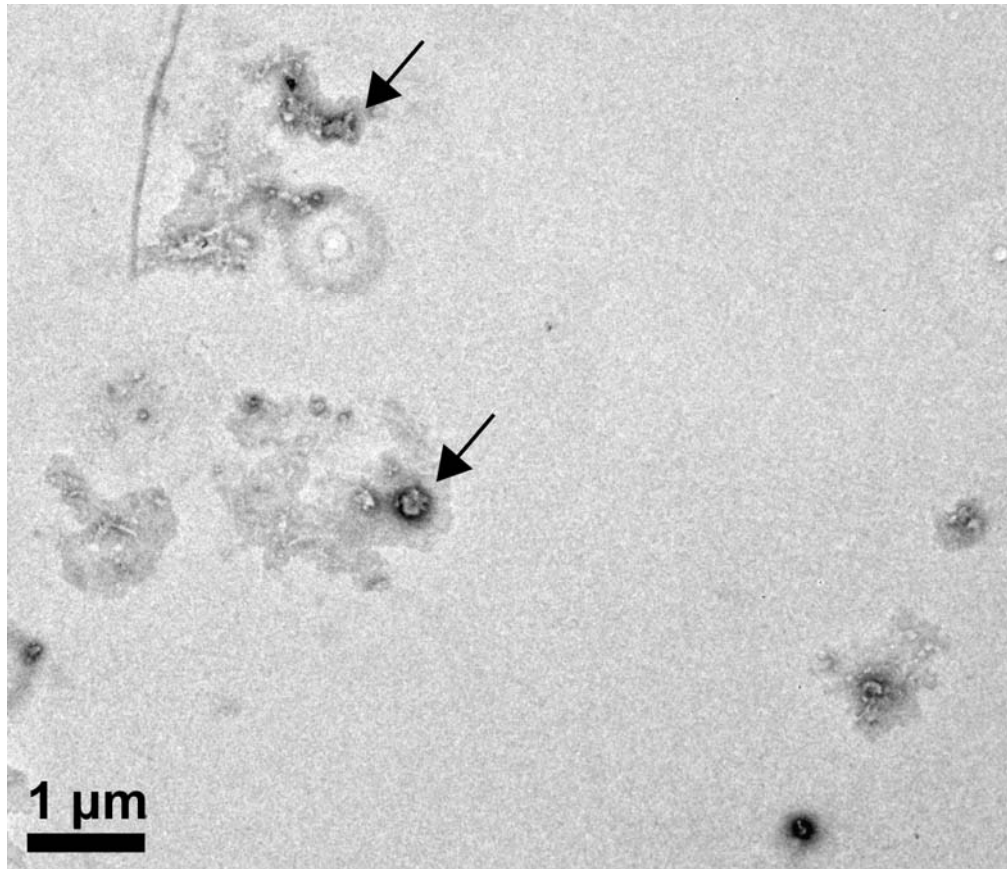


**Figure 3.6.** *Low Magnification Micrograph of Negatively Stained Hippocampal PSDs.*

Low magnification micrograph showing a typical field of isolated negatively stained hippocampal PSDs. Two well-defined hippocampal PSDs are highlighted with arrows. Scale bar = 1  $\mu\text{m}$ .

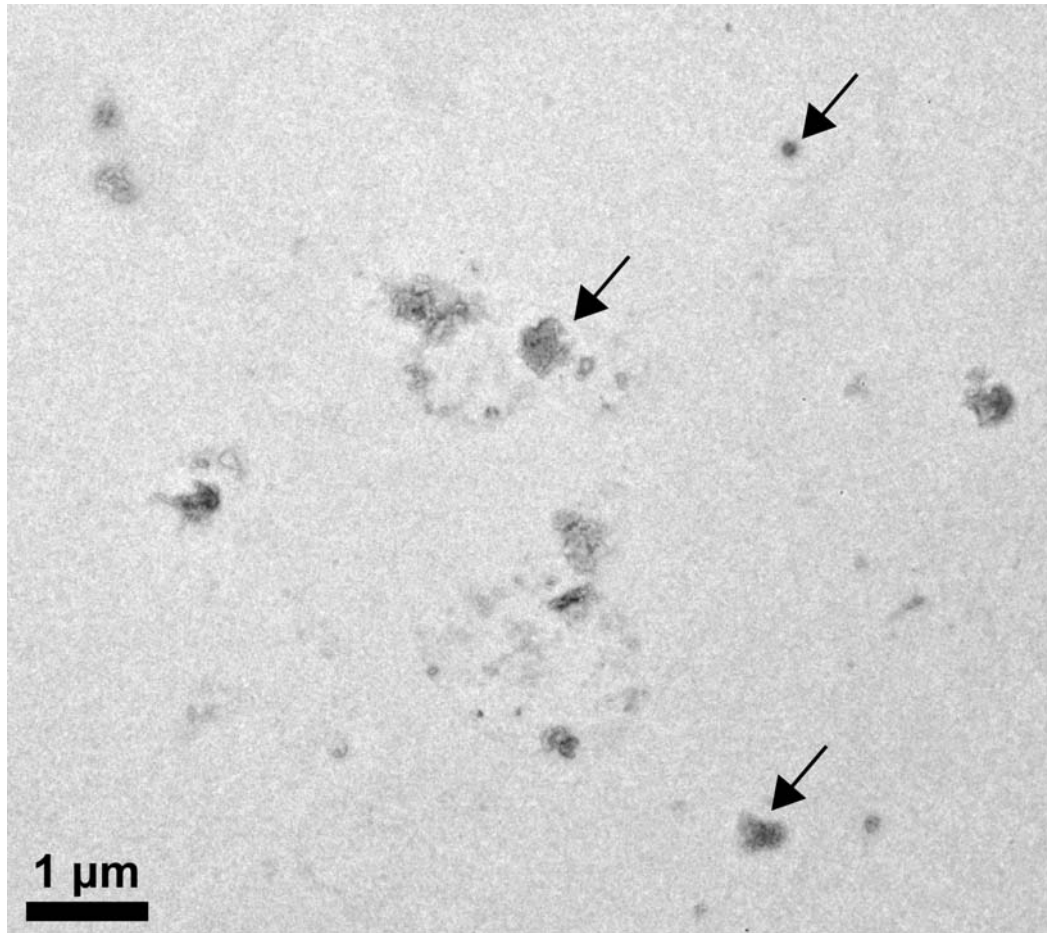


**Figure 3.7.** *Low Magnification Micrograph of Negatively Stained Cerebellar PSDs.*

Low magnification micrograph showing a typical field of isolated negatively stained cerebellar PSDs. Three well-defined cortical PSDs are highlighted with arrows. Scale bar = 1  $\mu\text{m}$ .

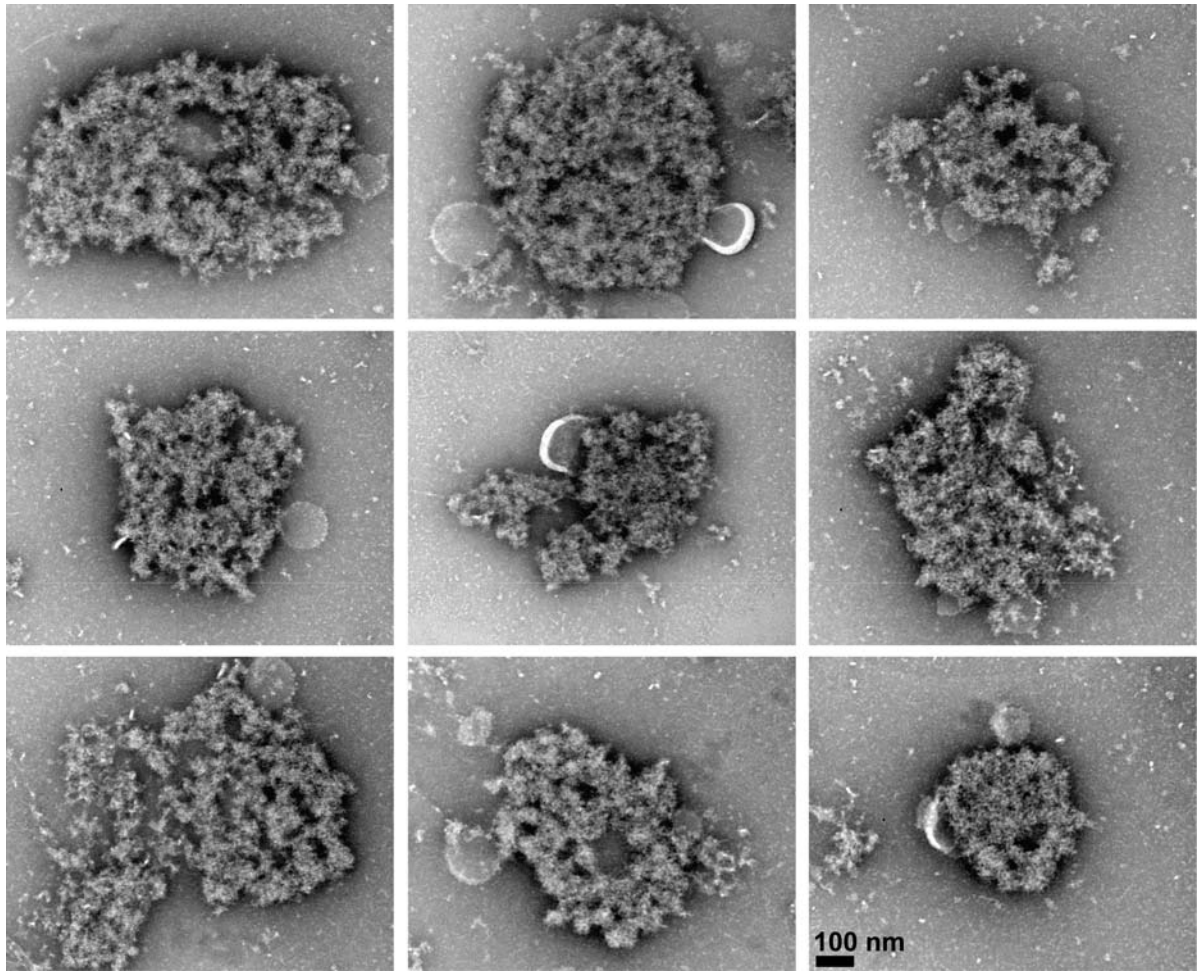


**Figure 3.8.** *High Magnification Micrographs of Negatively Stained Cortical PSDs.*

High magnification negative stain micrographs of representative isolated cortical PSDs. Scale bar = 100 nm.

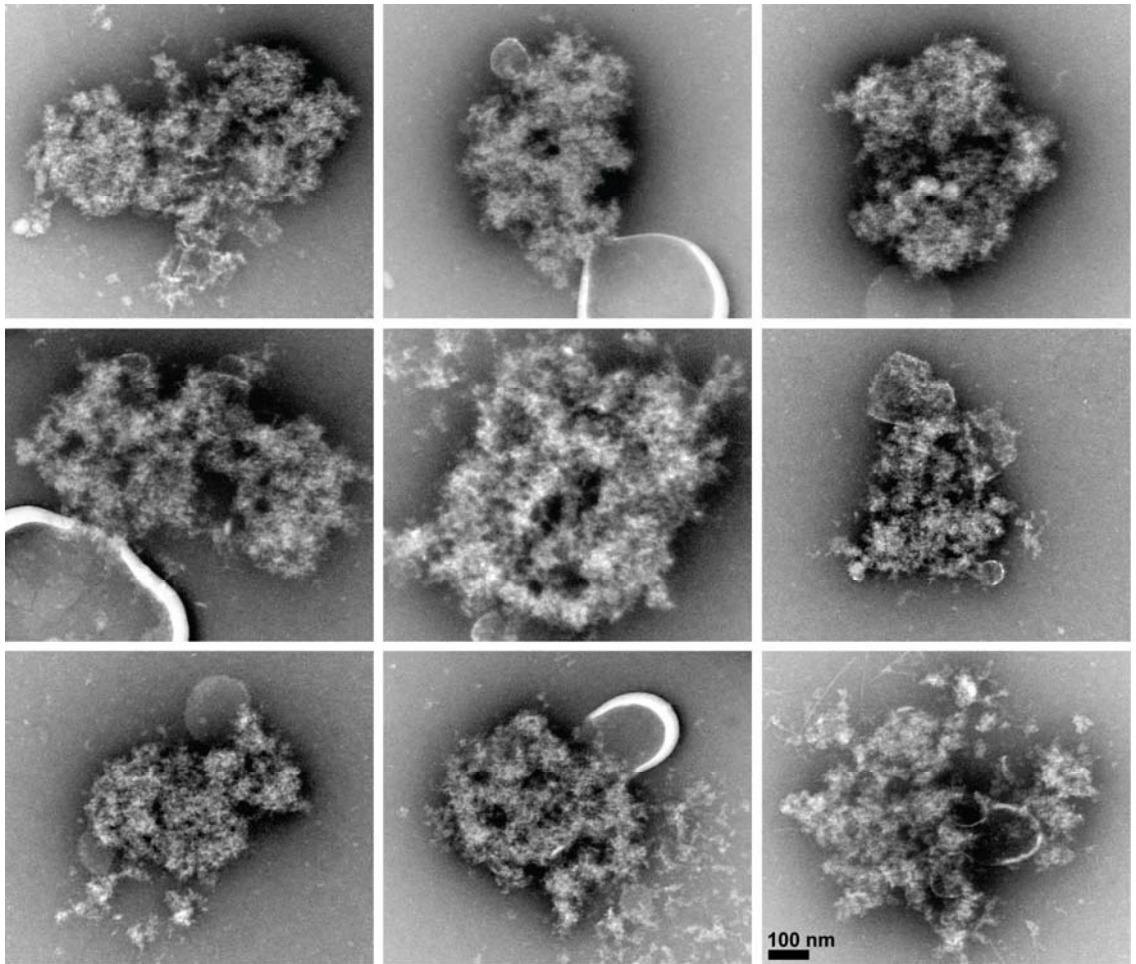


**Figure 3.9.** *High Magnification Micrographs of Negatively Stained Hippocampal PSDs.*  
High magnification negative stain micrographs of representative isolated hippocampal PSDs. Scale bar = 100 nm.



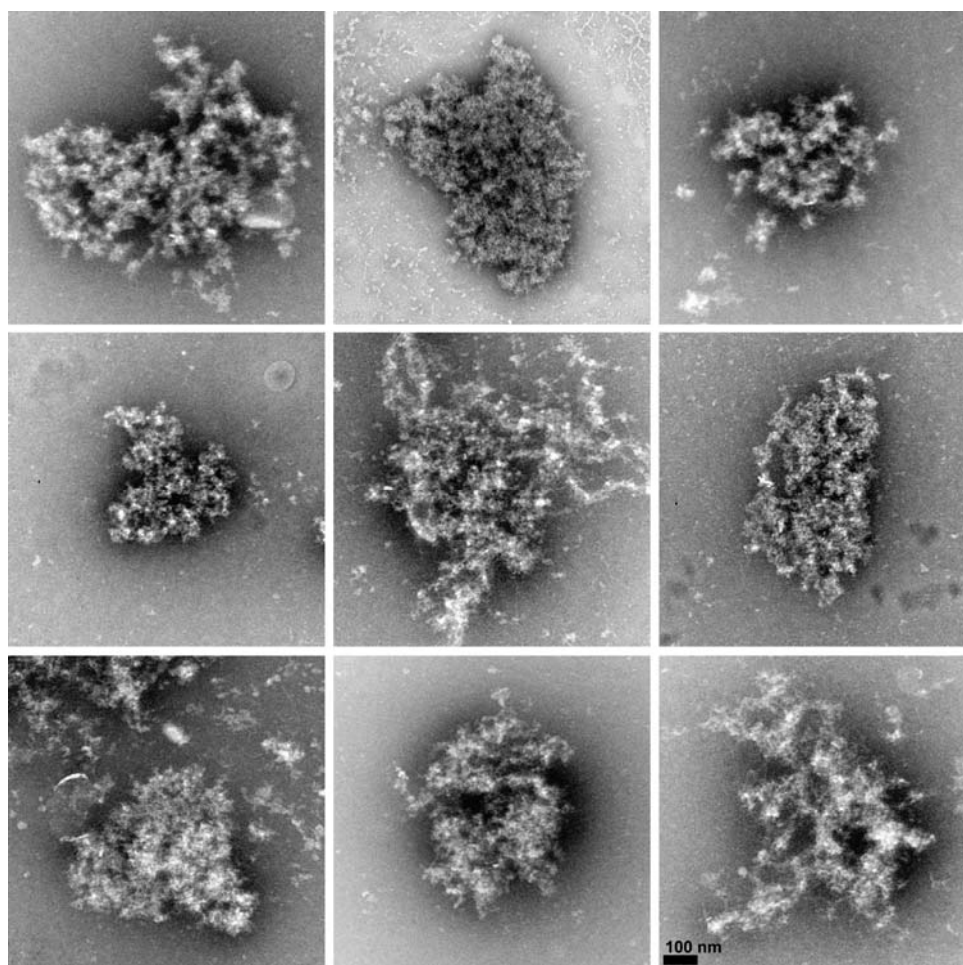


**Figure 3.10.** *High Magnification Micrographs of Negatively Stained Cerebellar PSDs.*

High magnification negative stain micrographs of representative isolated cerebellar PSDs. Scale bar = 100 nm.

### *3.3. Surface Area of Isolated PSDs from Negative Stain Micrographs*

Qualitative similarities and differences in gross morphologic characteristics were observed across PSDs from cortices, hippocampi, and cerebella, as well as within each PSD group. Most notable was the less densely packed protein arrangement in some cerebellar PSDs relative to those from either hippocampi or cortices (Figures 3.8-3.10). The detailed morphological characteristics as determined by electron tomography are described in Chapter 4, but a quantitative assessment of the relative surface area of PSDs was first accomplished by analyzing 120 randomly chosen PSDs from each preparation. Histograms of the binned surface areas (Figure 3.11) provide an assessment of the size distribution amongst PSDs and show the mode to be approximately  $0.2 \mu\text{m}^2$  for all PSD types, similar to the peak surface area of  $0.15 \mu\text{m}^2$  reported previously for PSDs isolated from adult rat forebrains, which contained PSDs from both the cerebral cortices and hippocampi (Swulius et al., 2010). The mean surface area of PSDs from cerebella, hippocampi and cortices were determined to be  $0.37$ ,  $0.34$  and  $0.35 \mu\text{m}^2$  (all  $\pm 0.02 \mu\text{m}^2$ ), respectively and were not significantly different from each other.

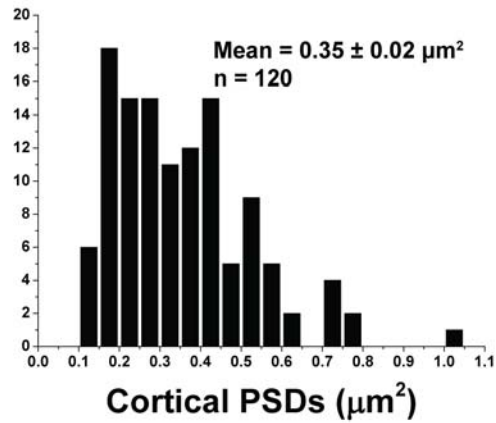
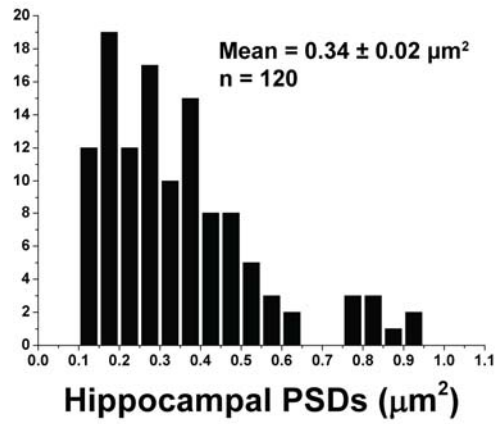
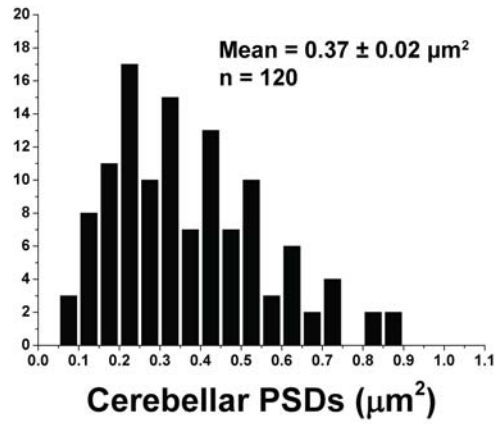


**Figure 3.11.** *Distribution of PSD Surface Areas.*

Histograms depicting surface area distribution for PSDs isolated from cerebella, hippocampi and cortices. The peak for all PSD types was approximately  $0.2 \mu\text{m}^2$ .

## **Chapter 4. Morphology of Postsynaptic Densities from Adult Rat Cerebella, Hippocampi, and Cerebral Cortices**

### *4.1. Morphology of Isolated PSDs from Negative Stain Electron Tomography*

Due to its potential to produce relatively high-resolution three-dimensional structural information, electron tomography is currently the best imaging option to reveal morphological details of individual macromolecular complexes like the PSD (Murphy and Jensen, 2007). Using this technique, a detailed comparative anatomical analysis of PSDs isolated from cerebella, hippocampi and cortices was accomplished using both negative stain and cryo electron tomography. Negative stain electron tomography provides increased contrast making visualization easier; however the application of stain and dehydration of the sample may distort the structure. These distortions are not a limitation with cryo electron tomography and the unique strengths of both of these techniques were utilized for the structural morphologic analysis. These distinct PSD preparations are modeled in Figure 2.6. A total of 49 tilt series of cerebellar PSDs (29 negative stained and 20 cryo-preserved), 37 of hippocampal PSDs (12 negative stained and 25 cryo-preserved) and 59 of cortical PSDs (14 negative stained and 45 cryo-preserved) were reconstructed for morphological and quantitative analyses.

Tilts series of negatively stained isolated PSDs from each region were collected and reconstructed in order to obtain higher resolution detail of the three-dimensional structure of each PSD. In Figure 4.1, full projection images of negatively stained PSDs from cerebral cortices, hippocampi, and cerebella are shown and compared to 10 nm cross-sections through the center of the final tomographic reconstructions for the same

PSDs to demonstrate the increased resolution available from the tomographic reconstructions.

From negative stain tomographic reconstructions, cortical PSDs were roughly disc-shaped, with well-defined boundaries as shown in the cross-sections through final tomographic reconstructions in Figure 4.2, consistent with the negative stain micrographs described in Chapter 3. It was also easily visible from the high contrast cross-sections that cortical PSDs were composed of tightly packed protein with few areas of low or absent protein density. In the representative examples in Figure 4.2 areas of dense protein packing are highlighted with black horizontal arrows and several examples of low protein density are indicated with black vertical arrows. As noted from the negative stain micrographs in Chapter 3, another prominent ultrastructural component was the presence of detergent resistant lipids intimately attached to the protein density of cortical PSDs, as seen in two of the tomographic examples in Figure 4.2. The lipids were well integrated into the PSD protein density around the PSD edges, as seen in Figure 4.2, and within the PSD volume as shown in the close-up cross-section of the cortical PSD in the right panel of Figure 4.7. Protein particles were often associated with the detergent resistant lipids membranes as in the tomographic cross-section through a cortical PSD shown in Figure 4.1.

From close-up views of the tomographic cross-sections, like shown in Figure 4.7, it was evident that cortical PSDs were composed of a variety of globular and filamentous proteins, highlighted by white vertical and horizontal arrows, respectively. Many of the globular proteins within cortical PSDs resembled the structure of CaMKII, which is barrel shaped and approximately 20 nm in diameter and height (Kolodziej et al., 2000, Swulius and Waxham, 2008). This was expected as CaMKII is the most

abundant protein in cortical PSDs (Dosemeci et al., 2007) and CaMKII has previously been identified in tomographic reconstructions of isolated PSDs (Fera et al., 2012, Swulius et al., 2012) through comparison with three-dimensional electron microscopic structures of purified CaMKII (Kolodziej et al., 2000, Gaertner et al., 2004a).

Negative stain tomographic reconstructions, like the examples shown in Figure 4.3, showed that hippocampal PSDs exhibited similar morphology to cortical PSDs. Hippocampal PSDs were disc-like in shape with irregular well-defined edges and were also composed of densely packed proteins with sparse areas absent of protein density (Figure 4.3). Black horizontal and vertical arrows highlight regions of tightly packed protein and areas of low protein density, respectively, within tomographic cross-sections of hippocampal PSDs. Figure 4.3 also shows examples of detergent lipid membranes (white asterisks) which were connected to proteins both on the edges and interior of PSDs. All of the lipid membranes associated with hippocampal PSDs in the negative stain tomographic reconstructions appeared to be studded with protein, as evident in Figure 4.3, similar to the cortical PSD in Figure 4.1. Also similar to cortical PSDs, hippocampal PSDs were composed of a combination of globular and filamentous proteins, as shown in Figure 4.7 where globular CaMKII-like proteins, easily visible within the tomographic reconstruction, are indicated with white vertical arrows and filamentous proteins are highlighted with white horizontal arrows.

In contrast to the relatively consistent architecture of cortical and hippocampal PSDs, three distinct morphological classes of PSDs isolated from cerebella were identified (Figures 4.4-4.6). Figure 4.4 includes three representative cross-sections through cerebellar PSDs that exhibit mostly densely packed protein with small areas absent of protein that closely resembles the morphology of cortical and hippocampal

PSDs. This type of dense cerebellar PSD was also disc-like with distinct protein boundaries (Figure 4.4) and had lipids associated with the protein density, as indicated with asterisks in Figure 4.4 and Figure 4.7.

Other cerebellar PSDs were identified that exhibited a more granular protein substructure (Figure 4.5) or a latticelike substructure (Figure 4.6), both which appeared to have smaller areas of dense protein packing. The granular-like cerebellar PSDs lacked larger regions of dense protein and instead had smaller regions of protein clusters about 40 nm in diameter with areas of low protein density between clusters (Figure 4.5), but were disc-shaped with distinct edges, similar to cortical, hippocampal and dense cerebellar PSDs. Three representative cross-sections through final tomographic reconstructions of granular cerebellar PSDs are shown in Figure 4.5, where black horizontal arrows highlight several small areas of protein clustering, black vertical arrows indicate areas lacking protein density and an asterisk highlights lipid material associated with one of the PSDs. The lacier cerebellar PSDs had a latticelike structure, with distinct filamentous proteins connecting regions of protein density (Figure 4.6). There also appeared to be significantly less protein density, evident as increased areas absent of protein density within the PSD boundaries, as highlighted by black vertical arrows within the representative tomographic cross-sections shown in Figure 4.6. The latticelike cerebellar PSDs were also roughly disc-shaped but in contrast to other PSD types their edges were more web-like, lacking a distinct boundary or perimeter.

In contrast to these larger scale differences, close examination of the fine structural details of PSDs isolated from cerebella indicated that they were all comprised of small filamentous and globular proteins (Figure 4.7), similar to hippocampal and

cortical PSDs. The larger scale differences for all PSD morphologies appeared to arise from the ratio and packing density of these smaller substructures as in the examples shown in Figure 4.7. Globular proteins resembling the structure of CaMKII were also evident in all cerebellar PSDs and examples are highlighted with white vertical arrows within a representative tomographic reconstruction for each cerebellar PSD morphologic class (Figure 4.7).



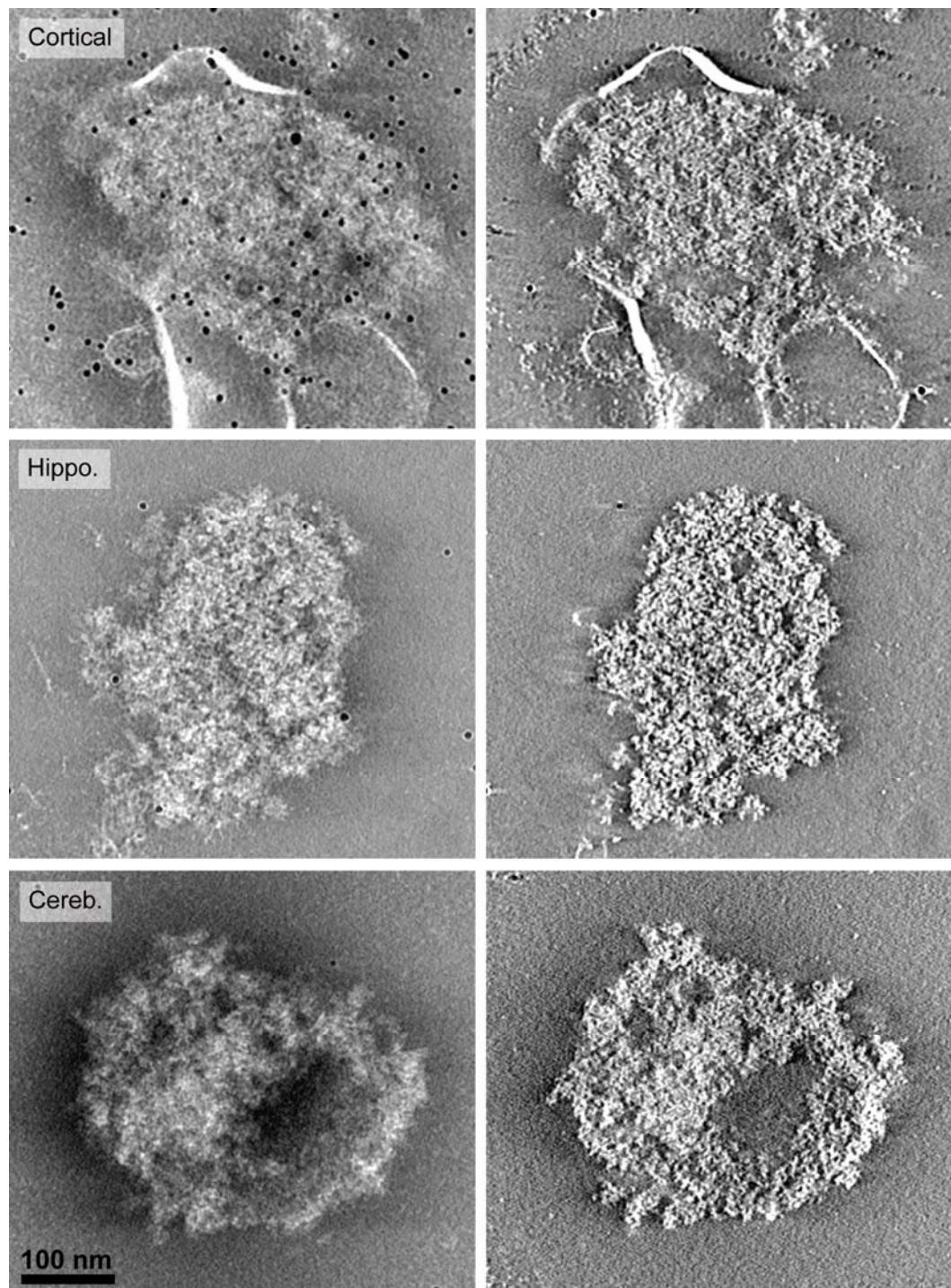


**Figure 4.1.** *Negative Stain Tomographic Reconstructions of PSDs Isolated from Adult Rat Cortices, Hippocampi, and Cerebella.*

Full projections of entire reconstructions are shown in the left panel while 10 nm cross-sections through the center of reconstructions are shown in the right panel for comparison. Gold is used as a fiducial marker to align image series during reconstruction. Scale bar = 100 nm.

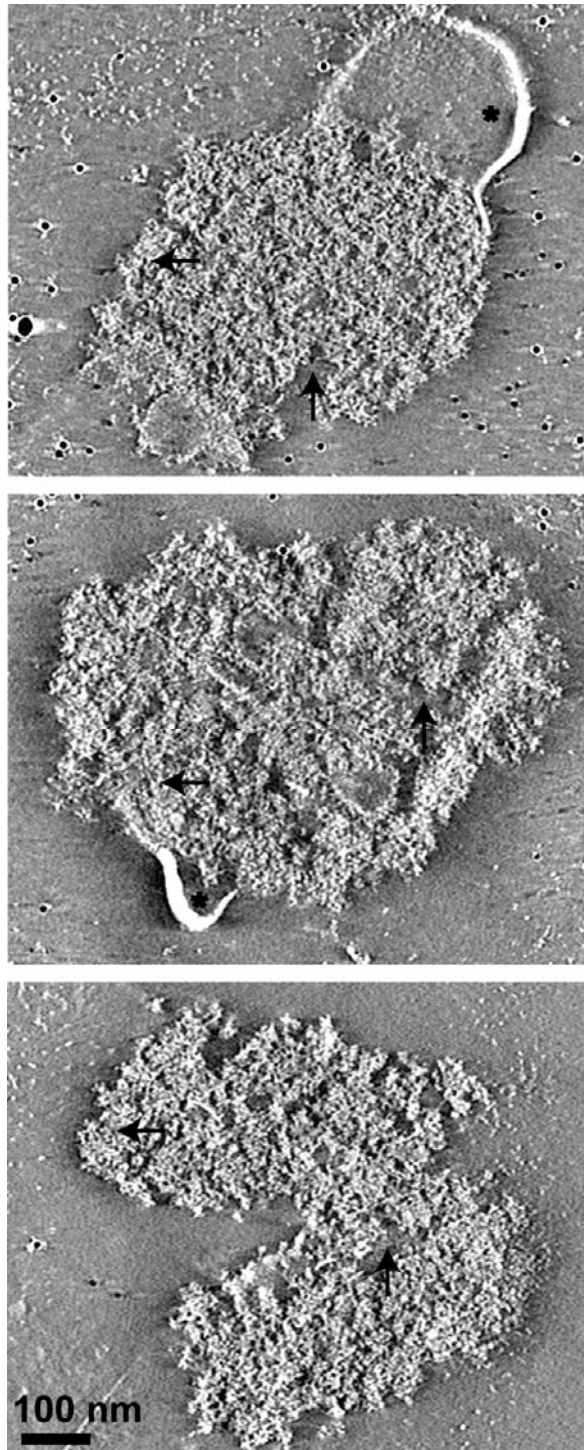


**Figure 4.2.** *Tomographic Reconstructions of Negatively Stained Cortical PSDs.*

Ten-nanometer cross-sections through final tomographic reconstruction of negatively stained cortical PSDs. Horizontal arrows indicate areas of dense protein, vertical arrows indicate areas without protein density and asterisks highlight detergent resistant membranes attached to the PSDs. Gold is used as a fiducial marker to align image series during reconstruction. Scale bar = 100 nm.

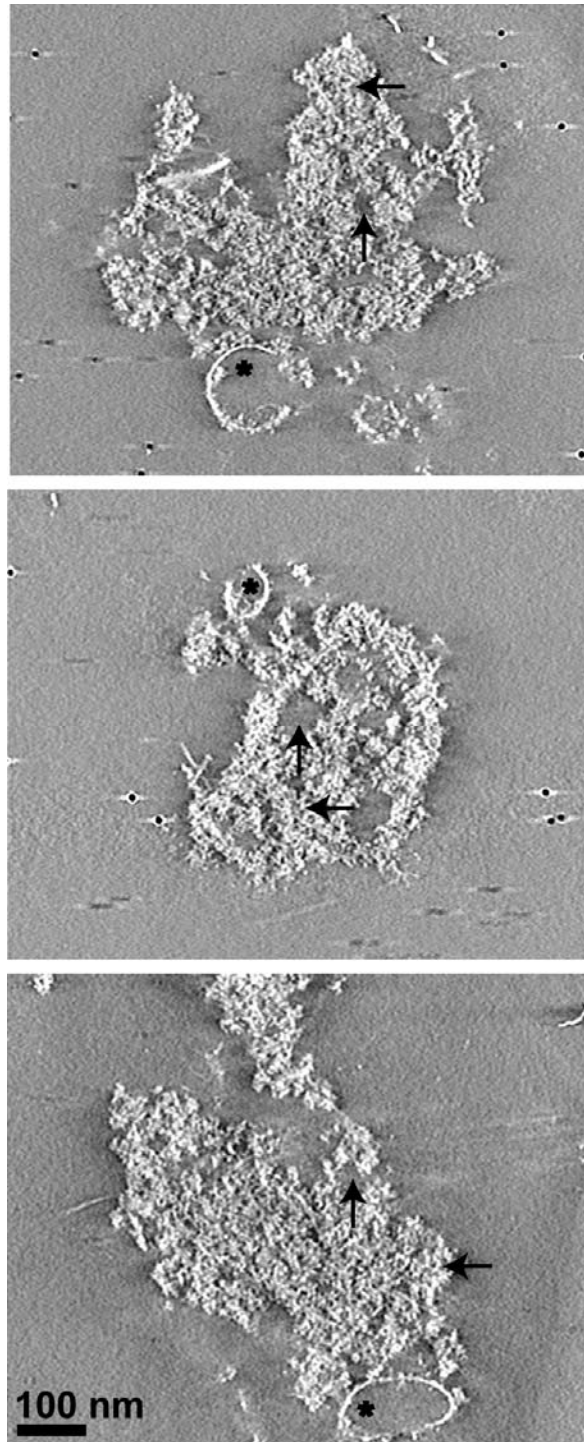


**Figure 4.3.** *Tomographic Reconstructions of Negatively Stained Hippocampal PSDs.*

Ten-nanometer cross-sections through final tomographic reconstruction of negatively stained hippocampal PSDs. Horizontal arrows indicate areas of dense protein, vertical arrows indicate areas without protein density and asterisks highlight detergent resistant membranes attached to the PSDs. Gold is used as a fiducial marker to align image series during reconstruction. Scale bar = 100 nm.

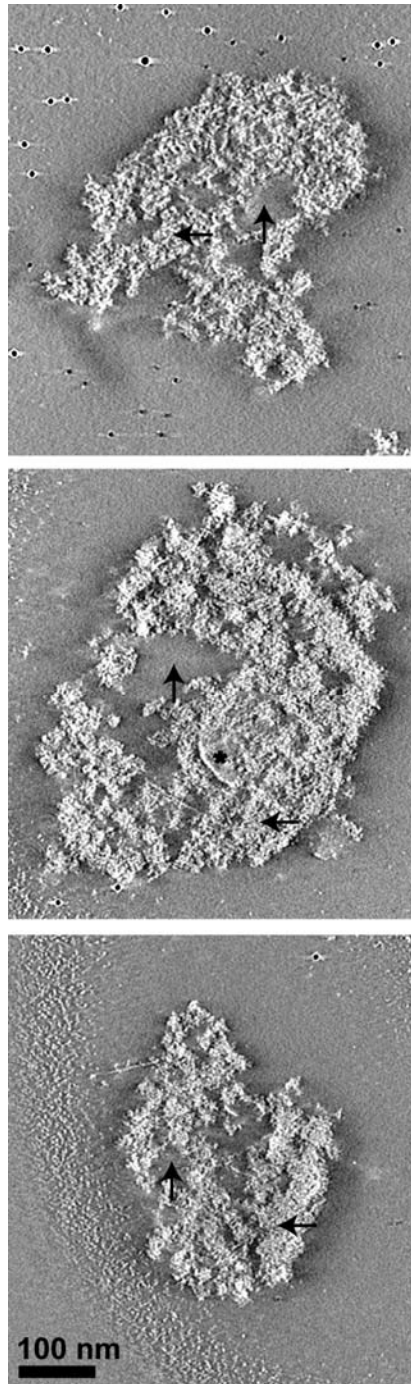


**Figure 4.4.** *Tomographic Reconstructions of Negatively Stained Cerebellar PSDs with Dense Morphology.*

Ten-nanometer cross-sections through final tomographic reconstruction of negatively stained cerebellar PSDs categorized as dense in morphology, similar to cortical and hippocampal PSDs. Horizontal arrows indicate areas of dense protein, vertical arrows indicate areas without protein density and asterisks highlight detergent resistant membranes attached to the PSDs. Gold is used as a fiducial marker to align image series during reconstruction. Scale bar = 100 nm.



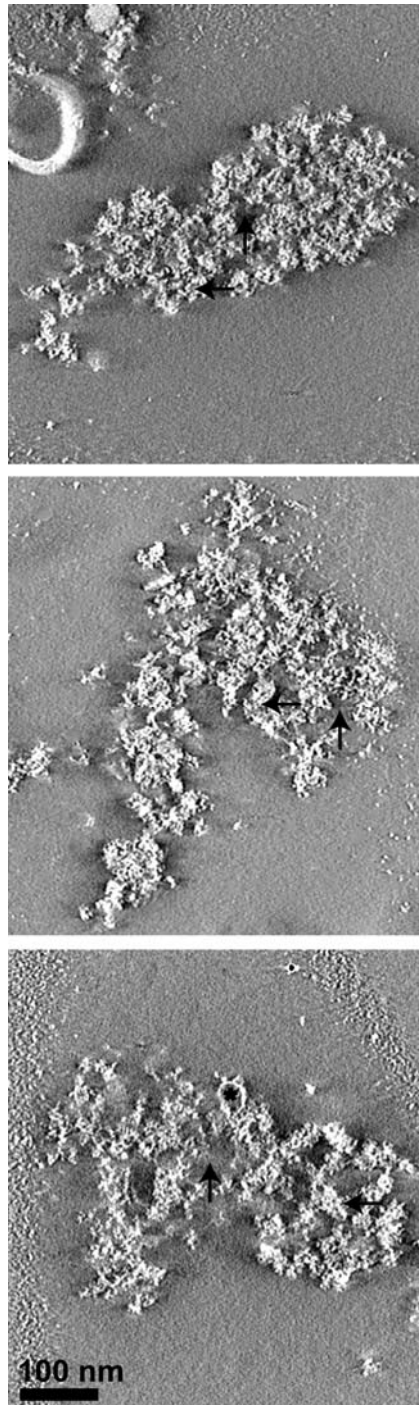


**Figure 4.5.** *Tomographic Reconstructions of Negatively Stained Cerebellar PSDs with Granular Morphology.*

Ten-nanometer cross-sections through final tomographic reconstruction of negatively stained cerebellar PSDs categorized as granular in morphology. Horizontal arrows indicate small areas of dense protein, approximately 40 nm in diameter, vertical arrows indicate areas without protein density and asterisks highlight detergent resistant membranes attached to the PSDs. Gold is used as a fiducial marker to align image series during reconstruction. Scale bar = 100 nm.

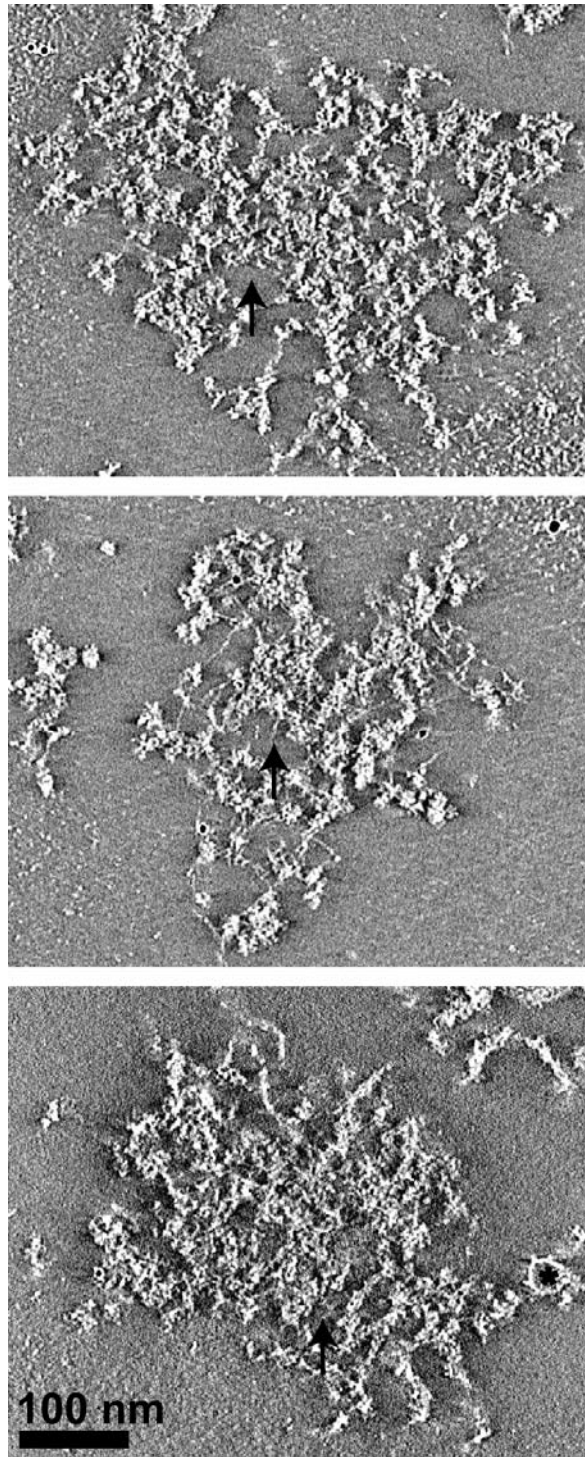


**Figure 4.6.** *Tomographic Reconstructions of Negatively Stained Cerebellar PSDs with Lacy Morphology.*

Ten-nanometer cross-sections through final tomographic reconstruction of negatively stained cerebellar PSDs categorized as lacy in morphology. Vertical arrows indicate areas without protein density and asterisks highlight detergent resistant membranes attached to the PSDs. Gold is used as a fiducial marker to align image series during reconstruction. Scale bar = 100 nm.

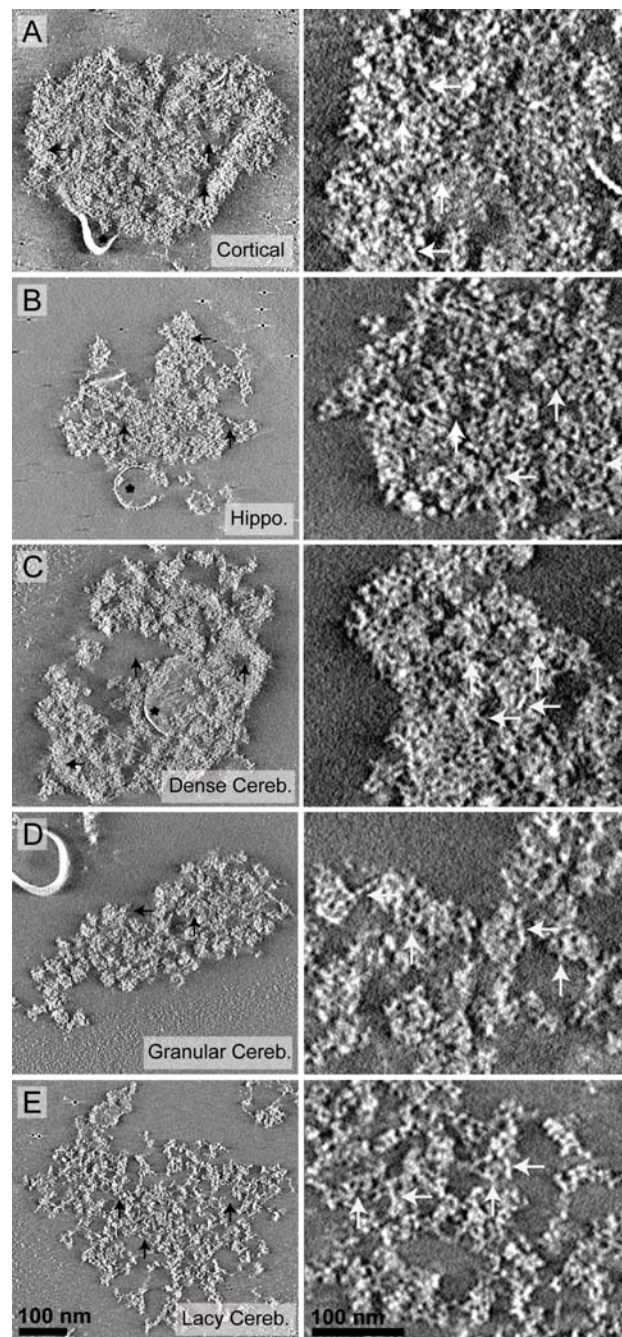


**Figure 4.7.** *Fine Morphology of Isolated PSDs from Negative Stain Tomographic Reconstructions.*

Ten-nanometer cross-sections through final tomographic reconstruction of negatively stained PSDs. The panels include the different morphologies observed among A) cortical, B) hippocampal, and C-D) cerebellar PSDs. Enlargements of each image are included, respectively, in the right column of panels illustrating the finer structural features of isolated PSDs. All PSDs were composed of filamentous and globular proteins, indicated with white horizontal and vertical arrows, respectively. Gold is used as a fiducial marker to align image series during reconstruction. Scale bar = 100 nm.

#### *4.2. Morphology of Isolated PSDs from Cryo Electron Tomography*

Tilt series were also collected for cryo-preserved PSDs from each region in order to assess their morphological structure without dehydration and negative stain. Since the PSDs were preserved in vitreous ice, rather than negatively stained, the contrast is reversed from the negative stain tomographic reconstruction and protein density is represented by darker voxel intensity in the final tomographic reconstructions, like the cross-sections shown in Figures 4.8-4.12. The morphology of PSDs as determined by cryo electron tomography confirmed and extended the findings from negative stain electron tomography.

Cortical PSDs were disc-like in shape with distinctive edges defining the protein density, and were composed of densely packed protein with occasional areas absent of protein, as shown in the representative cross-sections in Figure 4.8. Cortical PSDs also had lipid-structures attached to the protein density (Figure 4.8), as seen in the negative stain tomographic reconstructions (Figure 4.2). Figure 4.8 nicely illustrates the variable size of the associated lipids, indicated with asterisks, present within cortical PSDs. Hippocampal PSDs were morphologically similar to cortical PSDs, confirming the results from the negative stain tomography. As Figure 4.9 illustrates, hippocampal PSDs had well-defined boundaries and irregular but disc-like perimeters and were composed of dense layers of proteins with holes in the density as highlighted by vertical arrows. Detergent resistant lipids were also associated with the cryo-preserved hippocampal PSDs (Figure 4.9). It was also evident from the morphological analysis of cryo-preserved cerebellar PSDs that three separate classes of cerebellar PSDs existed with respect to protein texture or protein packing (Figures 4.10-4.12). The dense cerebellar PSDs, as shown in Figure 4.10, were also composed of large regions of



densely packed protein, with the occasional area absent of protein density within their well-defined perimeter, similar to the dense cerebellar PSDs from negative stain tomographic reconstructions (Figure 4.4). The cryo-preserved granular cerebellar PSDs (Figure 4.11) were also morphologically the same as the granular cerebellar PSDs imaged by negative stain electron tomography (Figure 4.5), lacking the larger regions of dense proteins which comprise cortical, hippocampal, and dense cerebellar PSDs and were instead composed of smaller areas of protein approximately 40 nm in diameter. These small protein granules are well represented in the example cross-sections through final tomographic reconstructions of cryo-preserved granular cerebellar PSDs shown in Figure 4.11, and several are highlighted with horizontal arrows. Three representative cross-sections through cryo-preserved lacy cerebellar PSDs are included in Figure 4.12. In these cross-sections, the latticelike structure is evident as filamentous proteins connecting much larger regions of densely packed protein, just as described from the negative stain tomographic examples (Figure 4.6). Lipid-like material was also associated with cryo-preserved cerebellar PSDs from all three morphologic classes, and examples of these are indicated with asterisks in Figures 4.10-4.12.

In total, dense cerebellar PSDs (Figures 4.4 and 4.10) represented 20 of 49 (41%) of the cerebellar PSDs analyzed by both negative stain and cryo electron tomography. Granular cerebellar PSDs (Figures 4.5 and 4.11) represented 12 of 49 (24%) of cerebellar PSDs, and 17 of 49 (35%) cerebellar PSDs were classified as latticelike in morphology (Figures 4.6 and 4.12). Cerebellar PSDs have previously been described as lacy or latticelike and it was postulated that they were from inhibitory synapses rather than excitatory synapses (Carlin et al., 1980). However, the results of

my immunogold labeling experiments, discussed further in Chapter 5, suggest that the PSDs isolated and described in this dissertation were only from excitatory synapses. Additionally, not all of the cerebellar PSDs isolated were lacy in morphology, suggesting isolation of differential PSD populations.

The presence of lipid-like structures obvious in the reconstructions was also quantified for each of the PSD types, from both the negative stain and cryo tomographic reconstructions. Lipids were associated with 78% (46 of 59) of cortical PSDs, while hippocampal PSDs had lipid present in 62% (21 of 37) and cerebellar PSDs in 63% (31 of 49). Within the cerebellar PSD group, lipid membrane structures were associated with 60% (12 of 20) of the dense cerebellar PSDs, 50% (6 of 12) of the granular cerebellar PSDs and 76% (13 of 17) of the lacy cerebellar PSDs. Lipid-like structures associated with PSDs have been described in previous publications (Cohen et al., 1977, Matus and Taff-Jones, 1978, Swulius et al., 2010, Swulius et al., 2012) and are hypothesized to be lipid raft-like (Suzuki et al., 2001, Swulius et al., 2012) as they are composed of raft-associated lipid GM1 in forebrain PSDs (Swulius et al., 2012).

#### *4.3. Protein-to-Volume Ratios of Isolated PSDs*

From the visual assessment of PSD morphology described above from both negative stain and cryo electron tomography, differences were evident in the packing density of structures within different cerebellar PSDs. Therefore subsets of cryo-preserved PSDs were chosen for analysis of protein-to-volume ratios, a measure of PSD protein occupancy, in the absence of stain/dehydration artifacts. Twelve

cryotomograms of PSDs from each region were selected for analysis and protein-to-volume ratios were calculated as described in the methodology, Chapter 2 section 2.6, and the results are shown in a whisker plot in Figure 4.13. The protein-to-volume ratios, which were calculated by taking the number of voxels representing protein and dividing by the total voxels within each PSD boundary, were more variable for cortical PSDs with a range from 0.19 to 0.53, than for hippocampal PSDs which ranged from just over 0.2 to 0.34 (Figure 4.13). As expected, cerebellar PSDs had the largest range of protein-to-volume ratios, ranging from 0.15 to over 0.5, and uniquely half (6 of 12) of the PSDs evaluated clustered near a protein-to-volume ratio of 0.175 while the others cerebellar PSDs ranged from approximately 0.25 to just over 0.5 (Figure 4.13). This suggests that a distinct group of less dense cerebellar PSDs existed with respect to protein volume, and consistent with the visual observations, the lower protein-to-volume ratios corresponded to the lacy cerebellar PSDs. Most hippocampal PSDs clustered around a protein-to-volume ratio of 0.325, while most cortical PSDs clustered around a ratio of 0.35 (Figure 4.13), and this was well represented by the calculated average protein-to-volume ratios, as reported in Table 4.2. Figure 4.13 also includes a surface rendering of a representative cryo-preserved hippocampal PSD to illustrate a PSD with a typical protein-to-volume ratio. Overall, the mean protein-to-volume ratios for cerebellar, hippocampal, and cortical PSDs were  $0.29 \pm 0.04$ ,  $0.31 \pm 0.01$ , and  $0.35 \pm 0.03$ , respectively but did not reach statistically significant differences (Table 4.2).

#### *4.4. PSD Thickness from Tomographic Reconstructions*

Average PSD thickness and surface area were also calculated for the same 12 cryo-preserved PSDs to assess PSD size in the absence of dehydration and staining

(Table 4.1). The mean surface areas were  $0.24 \pm 0.04 \mu\text{m}^2$ ,  $0.28 \pm 0.04 \mu\text{m}^2$ , and  $0.27 \pm 0.06 \mu\text{m}^2$  for cryo-preserved cerebellar, hippocampal and cortical PSDs, respectively (Table 4.1). These values were not statistically different from each other and were well within the distribution of surface areas measured from negative stain micrographs (Figure 3.11). The mean thickness of cryo-preserved hippocampal PSDs was calculated to be  $112 \pm 9 \text{ nm}$  and was statistically different than both cryo-preserved cortical and cerebellar PSDs, which had mean thicknesses of  $169 \pm 22 \text{ nm}$  and  $210 \pm 13 \text{ nm}$ , respectively (Table 4.2). This finding cannot be ascribed to differences in the isolation procedure as the samples from all three regions were processed simultaneously and were imaged under identical conditions, suggesting that cortical and cerebellar PSDs are significantly thicker than hippocampal PSDs. However, these thicknesses are significantly larger than historically reported for PSDs (Cohen et al., 1977, Carlin et al., 1980, Harris et al., 1992), and it is plausible that the discrepancy in PSD thickness could be the result of the negative stain and dehydration employed in the earlier studies.

For a direct comparison, I measured the thickness and surface area of PSDs from negative stain tomographic reconstructions using the identical procedure to that described for the cryo-preserved PSDs, and the values are reported in comparison to the measurements of cryo-preserved PSDs in Table 4.2. The mean surface areas calculated for the PSDs imaged by negative stain tomography were statistically the same as the average surface areas for cryo-preserved PSDs (Table 4.2), suggesting that dehydration and stain do not significantly affect PSD surface area. In contrast, the mean thicknesses for negatively stained cerebellar and cortical PSDs ( $115 \pm 11 \text{ nm}$  and  $94 \pm 5 \text{ nm}$ , respectively, were significantly thinner, approximately 2-fold, than for

cryo-preserved PSDs from the same brain regions ( $210 \pm 13$  nm and  $169 \pm 22$  nm, respectively) (Table 4.2). However, negatively stained hippocampal PSDs had a mean thickness of  $94 \pm 7$  nm, which was not statistically different than cryo-preserved hippocampal PSDs ( $112 \pm 9$  nm) (Table 4.2). These results provide evidence that the application of stain and dehydration causes collapse of cortical and cerebellar PSDs along their Z dimension, and that PSDs from these brain regions are significantly thicker than hippocampal PSDs, extending further into the synaptic compartment. The impact of dehydration and stain on hippocampal PSDs was not significant, suggesting that the molecular organization of hippocampal PSDs prevents the structure from collapsing under negative stain conditions.

Morphologic analysis of PSDs by negative stain and cryo electron tomography established that there were significant differences in PSD morphology among cerebellar PSDs and in the variability of protein-to-volume ratios between PSD types, as well as in PSD thickness. The described differences in PSD structure were believed to be most likely due to differences in the molecular composition of the PSDs from the different brain regions. In fact, proteomic approaches already provided evidence to support this conclusion (Cheng et al., 2006). To directly assess whether PSD protein composition and organization of specific proteins within individual PSDs was different for PSDs from each region, immunogold labeling and EM localization was employed, using antibodies to different functional classes of PSD associated proteins and is discussed in Chapter 5.

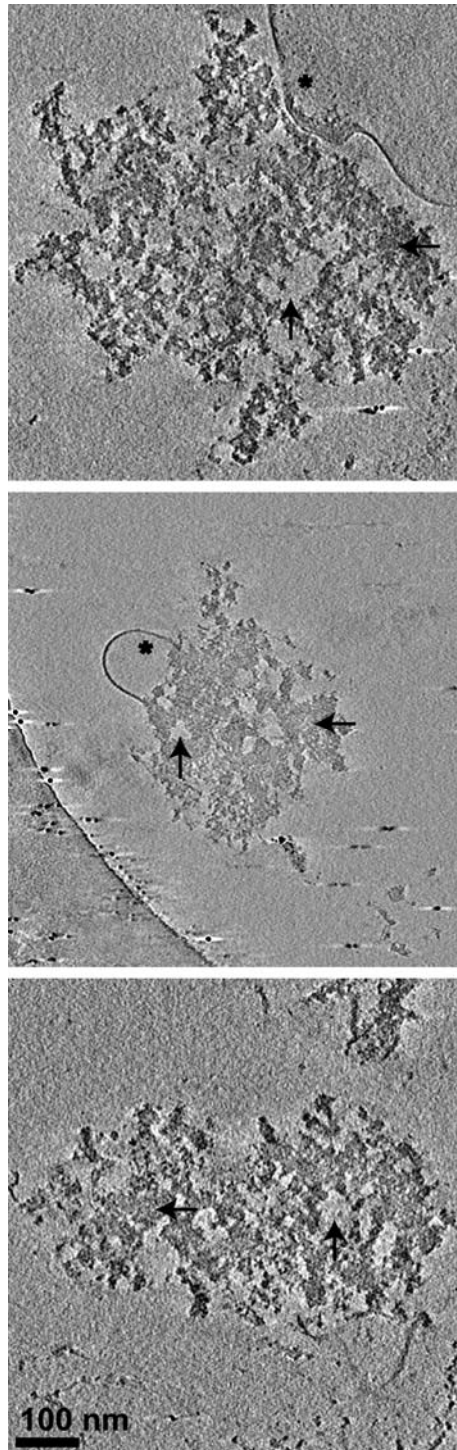


**Figure 4.8.** *Tomographic Reconstructions of Cryo-Preserved Cortical PSDs.*

Ten-nanometer cross-sections through final tomographic reconstruction of cryo-preserved cortical PSDs. Horizontal arrows indicate areas of dense protein, vertical arrows indicate areas without protein density and asterisks highlight detergent resistant membranes attached to the PSDs. Gold is used as a fiducial marker to align image series during reconstruction. Scale bar = 100 nm.

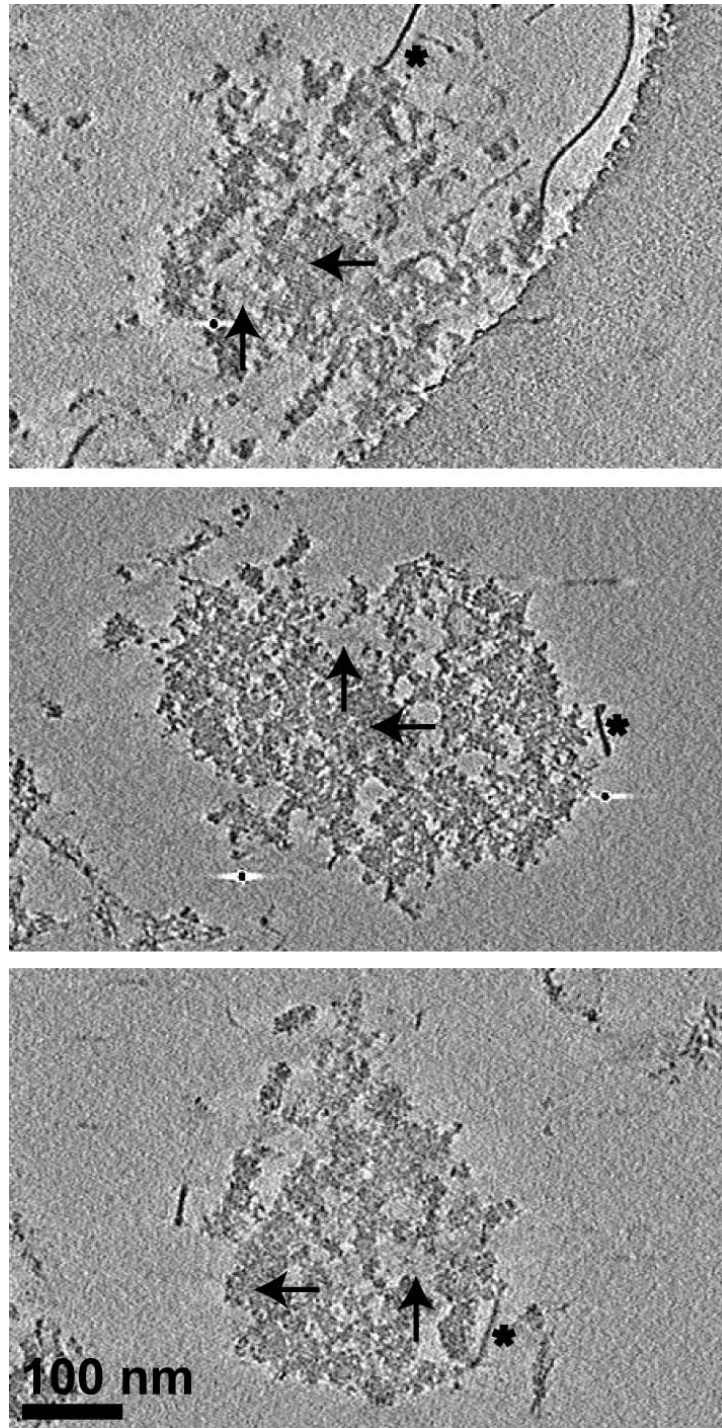


**Figure 4.9.** *Tomographic Reconstructions of Cryo-Preserved Hippocampal PSDs.*

Ten-nanometer cross-sections through final tomographic reconstruction of cryo-preserved hippocampal PSDs. Horizontal arrows indicate areas of dense protein, vertical arrows indicate areas without protein density and asterisks highlight detergent resistant membranes attached to the PSDs. Gold is used as a fiducial marker to align image series during reconstruction. Scale bar = 100 nm.

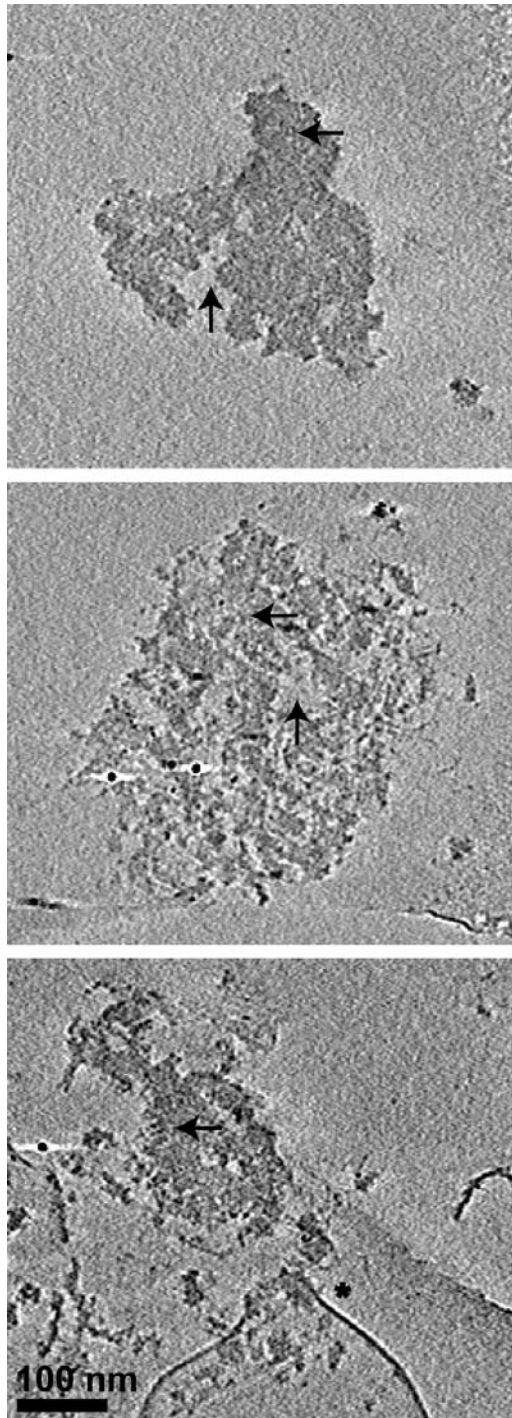


**Figure 4.10.** *Tomographic Reconstructions of Cryo-Preserved Cerebellar PSDs with Dense Morphology.*

Ten-nanometer cross-sections through final tomographic reconstruction of cryo-preserved cerebellar PSDs categorized as dense in morphology, similar to cortical and hippocampal PSDs. Horizontal arrows indicate areas of dense protein, vertical arrows indicate areas without protein density and asterisks highlight detergent resistant membranes attached to the PSDs. Gold is used as a fiducial marker to align image series during reconstruction. Scale bar = 100 nm.



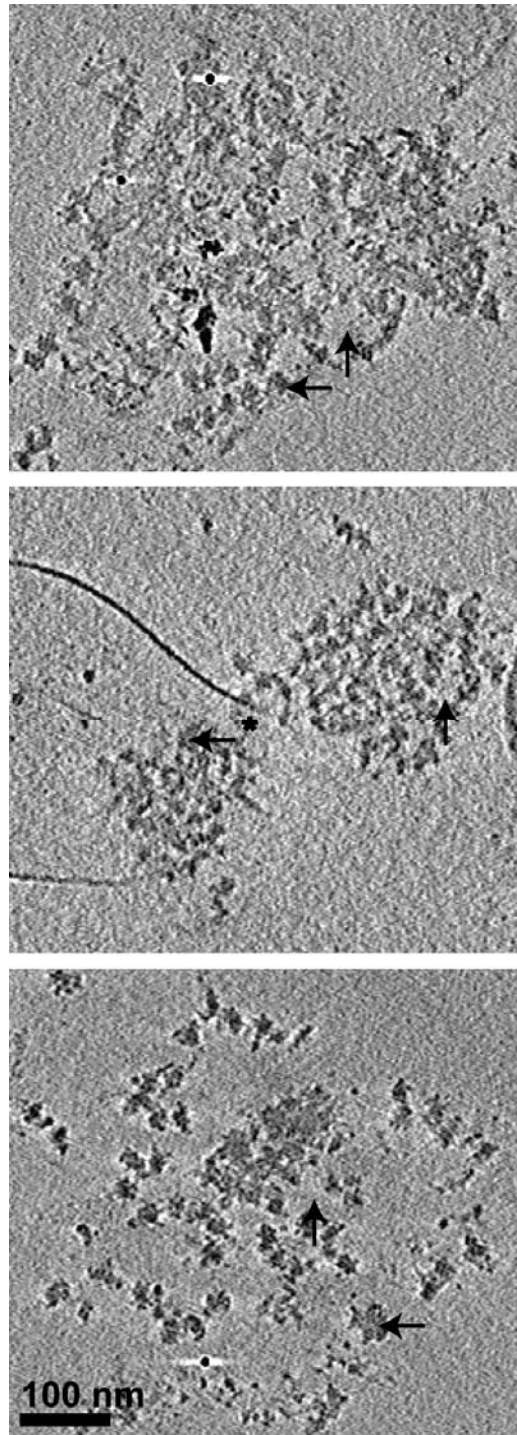


**Figure 4.11.** *Tomographic Reconstructions of Cryo-Preserved Cerebellar PSDs with Granular Morphology.*

Ten-nanometer cross-sections through final tomographic reconstruction of cryo-preserved cerebellar PSDs categorized as granular in morphology. Horizontal arrows indicate small areas of dense protein, approximately 40 nm in diameter, vertical arrows indicate areas without protein density and asterisks highlight detergent resistant membranes attached to the PSDs. Gold is used as a fiducial marker to align image series during reconstruction. Scale bar = 100 nm.

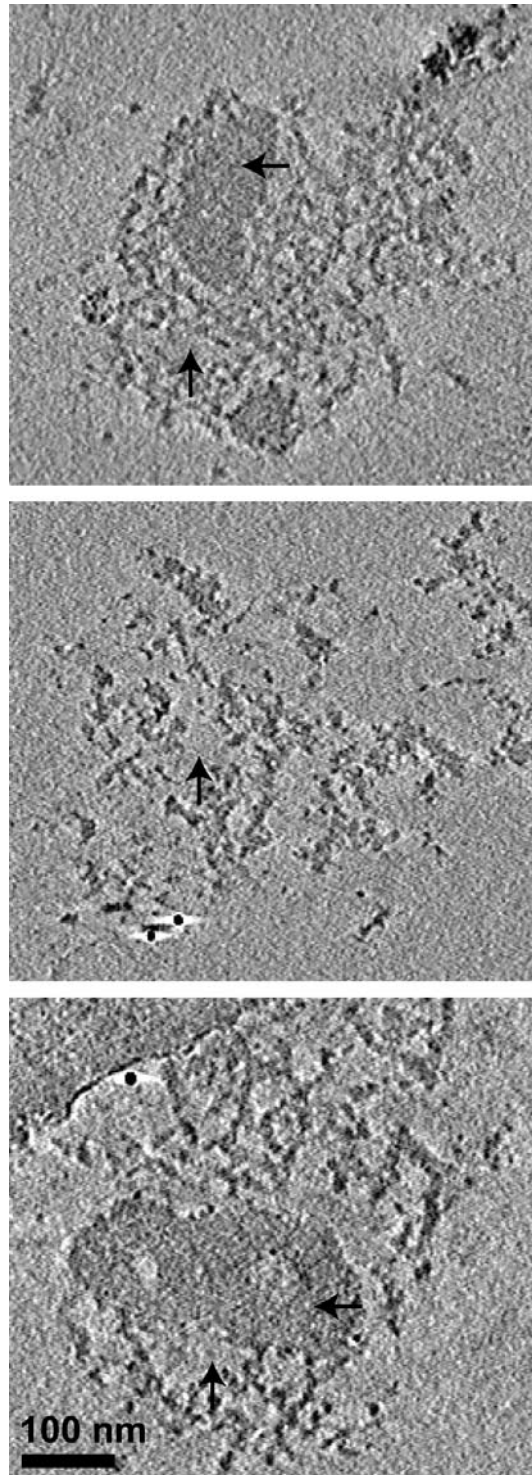


**Figure 4.12.** *Tomographic Reconstructions of Cryo-Preserved Cerebellar PSDs with Lacy Morphology.*

Ten-nanometer cross-sections through final tomographic reconstruction of cryo-preserved cerebellar PSDs categorized as lacy in morphology. Vertical arrows indicate areas without protein density and asterisks highlight detergent resistant membranes attached to the PSDs. Gold is used as a fiducial marker to align image series during reconstruction. Scale bar = 100 nm.

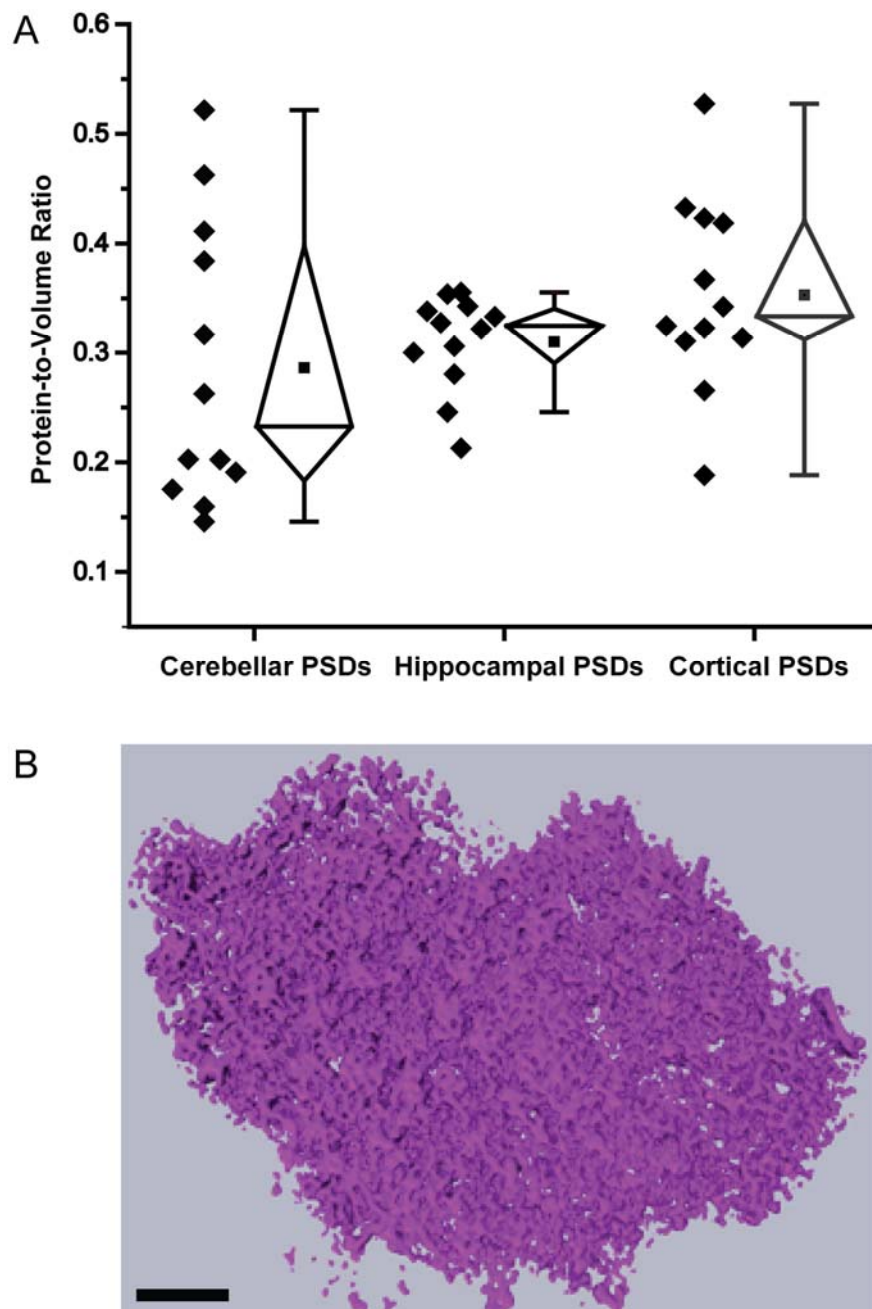


**Figure 4.13.** *PSD Protein-to-Volume Ratios Measured from Cryo Tomographic Reconstructions.*

A) Histogram of protein-to-volume ratios for PSDs isolated from each region as measured from tomographic reconstructions of cryo-preserved PSDs. N = 12. B) Surface rendering of representative cryo-preserved hippocampal PSD created in Amira. Scale bar = 100 nm.

	Surface Area $\pm$ SEM ( $\mu\text{m}^2$ )	Thickness $\pm$ SEM (nm)	P-to-V Ratio $\pm$ SEM
Cerebellar PSDs	$0.24 \pm 0.04$	$210 \pm 13$	$0.29 \pm 0.04$
Hippocampal PSDs	$0.28 \pm 0.04$	$112 \pm 9$	$0.31 \pm 0.01$
Cortical PSDs	$0.27 \pm 0.06$	$169 \pm 22$	$0.35 \pm 0.03$

**Table 4.1.** PSD Surface Area, Thickness and Protein-to-Volume Ratio Measured from Cryo Tomographic Reconstructions.

Surface Area, Thickness and PSD Protein-to-Volume Ratios (P-to-V) for PSDs isolated from each region as measured from tomographic reconstructions of cryo-preserved PSDs. N = 12.

	Surface Area $\pm$ SEM ( $\mu\text{m}^2$ )	
	Cryo-Preserved	Negative Stain
Cerebellar PSDs	$0.24 \pm 0.04$	$0.32 \pm 0.09$
Hippocampal PSDs	$0.28 \pm 0.04$	$0.21 \pm 0.04$
Cortical PSDs	$0.27 \pm 0.06$	$0.37 \pm 0.06$

	Thickness $\pm$ SEM (nm)	
	Cryo-Preserved	Negative Stain
Cerebellar PSDs	$210 \pm 13$	$115 \pm 11$
Hippocampal PSDs	$112 \pm 9$	$94 \pm 7$
Cortical PSDs	$169 \pm 22$	$93 \pm 5$

**Table 4.2.** *PSD Surface Area and Thickness Compared from Cryo and Negative Stain Tomographic Reconstructions.*

Surface area and thickness for PSDs isolated from each region as measured from tomographic reconstructions of cryo-preserved and negatively stained PSDs. N = 12.

## **Chapter 5. Protein Composition of Postsynaptic Densities from Adult Rat Cerebella, Hippocampi, and Cerebral Cortices**

### *5.1. PSD Protein Staining Patterns*

In order to determine whether PSD protein composition differs across the brain, the global protein staining pattern was first compared between PSDs isolated from adult rat cortices, hippocampi, and cerebella. PSD fractions from each region were separated by SDS-PAGE and stained using Amersham Deep Purple Stain (GE Healthcare) following SDS-PAGE (Figure 5.1). The PSD protein profiles exhibit similar overall staining patterns; however, there were specific differences in band intensity between the PSD types, confirming that PSD protein composition does vary across the brain. In Figure 5.1, the protein bands whose intensities were at least twice the average band intensity within each sample were considered major bands and are identified with asterisks. A band just above 250 kDa is highlighted for all PSD types, while a band at approximately 100 kDa is only highlighted in cortical and hippocampal PSDs. The band above 250 kDa could represent Shank scaffolds which are typically between 190 kDa and 220 kDa, while the band around 100 kDa could represent scaffold PSD-95, which is abundant in cortical (Cheng et al., 2006) and hippocampal PSDs (Dosemeci et al., 2007). The band at approximately 100 kDa is present in the cerebellar PSD fraction; however it was not determined to be a major band within the cerebellar PSD fraction. Cortical and hippocampal PSDs share an additional intense band highlighted at 45 kDa, which is the approximate molecular weight of PSD scaffold Homer. There are also unique and intensely stained bands within each individual sample; 70 kDa in cortical PSDs, 50 kDa in hippocampal PSDs, and 27 kDa and 47 kDa in cerebellar PSDs. These results confirm previous studies which have shown

compositional differences in PSD fractions from different brain regions identifiable by SDS-PAGE (Carlin et al., 1980) and are consistent with more recent proteomic approaches (Cheng et al., 2006). These approaches have been successful in determining and quantifying the protein composition of PSD fractions, but not of individual PSDs, which as described before are unique heterogeneous structures.

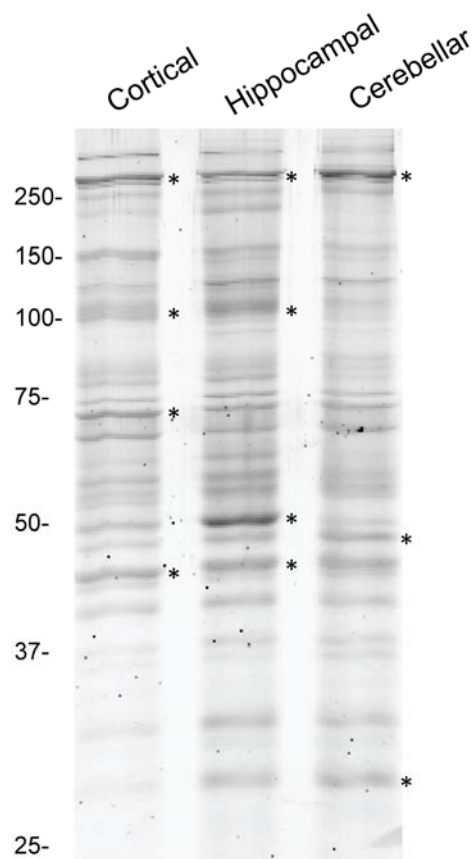


**Figure 5.1.** *Comparison of Isolated PSD Protein Profiles.*

Amersham Deep Purple stained gel of SDS-PAGE-separated proteins from PSDs isolated from cortices, hippocampi, and cerebella. The major bands in each lane are indicated with asterisks and molecular weights (kDa) are indicated to the left of the gel. Three micrograms of total protein were loaded into each lane.



## *5.2. Immunogold Labeling of Major PSD Proteins*

To further refine our understanding of PSD composition and structure, and to determine how PSD protein composition and organization differ across the brain, immunogold labeling was employed. Immunogold labeling, described in detail in Chapter 2.4, combines antibody specific identification of proteins and electron microscopy through the use of electron dense gold-conjugated secondary antibodies. Briefly, PSDs are applied to grids, proteins of interest are tagged with a protein specific primary antibody and gold-conjugated secondary antibody, PSD are then negatively stained and individually imaged. From the resulting micrographs I can measure the labeling density and distribution for the protein of interest and determine if there are differences across and within PSD groups. Three distinct protein classes were investigated: scaffolds, signaling proteins, and neurotransmitter receptors and the results are described in the following sections. Representative examples of the primary data generated from the immunogold labeling protocol are shown in Figures 5.2-5.6.

The first group of proteins targeted through immunogold labeling were PSD scaffolds, which form the core structure of the PSD and serve to anchor neurotransmitter receptors and organize signaling proteins (Okabe, 2007). Antibodies against eight major PSD scaffolds were employed, including  $\alpha$ -actinin, actin, PSD-95, Homer, SAP102, Shank1, Shank2, and Shank3 to test whether the composition and organization of the PSD scaffold network differs across brain regions. PSDs isolated from cerebella, hippocampi, and cortices immunogold labeled for scaffolds  $\alpha$ -actinin, actin, PSD-95, and Homer are shown in Figure 5.2. PSDs labeled for additional scaffolds SAP102, Shank1, Shank2, and Shank3 are shown in Figure 5.3.

The second group of proteins targeted in immunogold labeling experiments included calcium signaling proteins  $\alpha$ CaMKII,  $\beta$ CaMKII, and calmodulin, CaM. CaM is the calcium-transducing molecule of the synapse, which has many targets including  $\alpha$ CaMKII and  $\beta$ CaMKII. The  $\alpha$ CaMKII and  $\beta$ CaMKII isoforms of CaMKII are the neuronal isoforms of the protein, which when activated phosphorylate a variety of synaptic and PSD proteins (Dosemeci and Jaffe) and are crucial for learning and memory (Lisman et al., 2012).  $\beta$ CaMKII also binds both monomeric and F-actin, regulating actin polymerization in response to calcium influxes. This suggests that  $\beta$ CaMKII plays a role in regulating molecular transport and synaptic architecture (Swulius and Waxham, 2008, Sanabria et al., 2009, Hoffman et al., 2013). Cerebellar, hippocampal and cortical PSDs immunogold labeled for  $\alpha$ CaMKII,  $\beta$ CaMKII, and CaM are presented in Figure 5.4.

Neurotransmitter receptors were the third group of proteins targeted through immunogold labeling experiments. Antibodies against several postsynaptic neurotransmitter receptors, including glutamate receptors: NR1, NR2a, NR2b, GluR1, GluR2, GluR1/5, and GluR $\delta$ 2, and a GABA receptor antibody, were used in an attempt to determine labeling densities for these proteins in the PSDs isolated from each brain region. However, I did not detect labeling above background for NR2a, GluR1, GluR2, GluR1/5, GluR $\delta$ 2, or GABA; only the antibodies against NR1 and NR2b positively labeled PSDs. These results may lead one to conclude that these receptors are not present in the isolated PSDs due to the two detergent treatments which remove the plasma membranes; however, it is also plausible that the epitopes to which the antibodies were raised are masked when these proteins are incorporated into the native PSD structure, preventing labeling under my experimental conditions. Figure 5.5

includes PSDs isolated from each region immunogold labeled for NMDA receptors subunits NR1 and NR2b.

Lastly, PSDs were also immunogold labeled for the proteasome, which in response to synaptic activity, is activated and recruited to synapses (Ehlers, 2003, Bingol and Schuman, 2006, Djakovic et al., 2009, Bingol et al., 2010) where it can degrade PSD scaffolds PSD-95 (Colledge et al., 2003), GKAP and Shank (Ehlers, 2003). This suggests that the ubiquitin proteasome system provides a role in the activity-dependent structural reorganization of PSDs underlying synaptic plasticity. An antibody against a subunit of the proteasome lid was used to immunogold PSDs from each region (Fig 5.6).

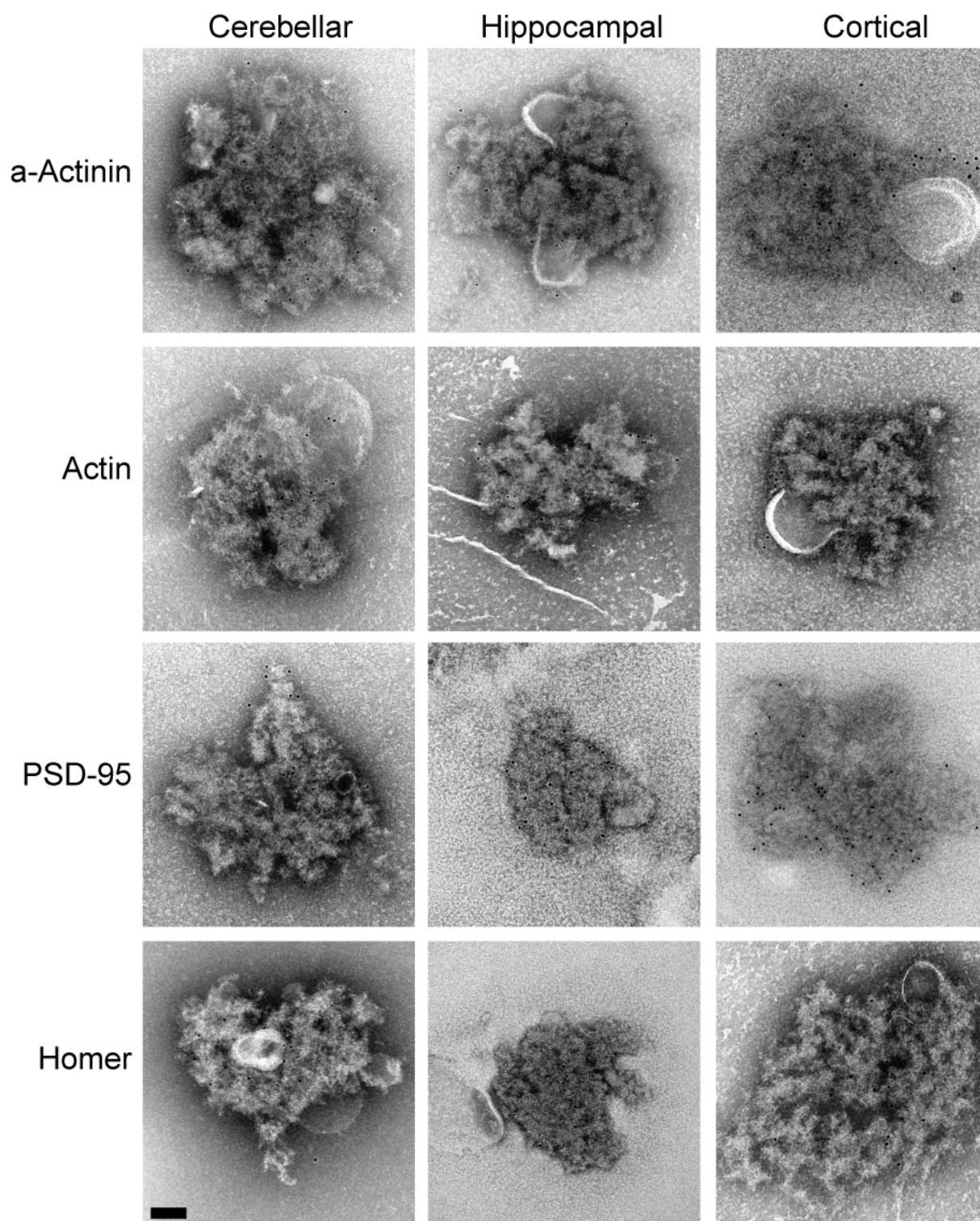


**Figure 5.2.** PSDs Immunogold Labeled for Scaffolds:  $\alpha$ -Actinin, Actin, PSD-95 and Homer.

Representative negative stain electron micrographs of PSDs isolated from cerebella, hippocampi, or cortices immunogold labeled for PSD scaffolds:  $\alpha$ -actinin, actin, PSD-95 and Homer. Gold = 12 nm. Scale bar = 100 nm.



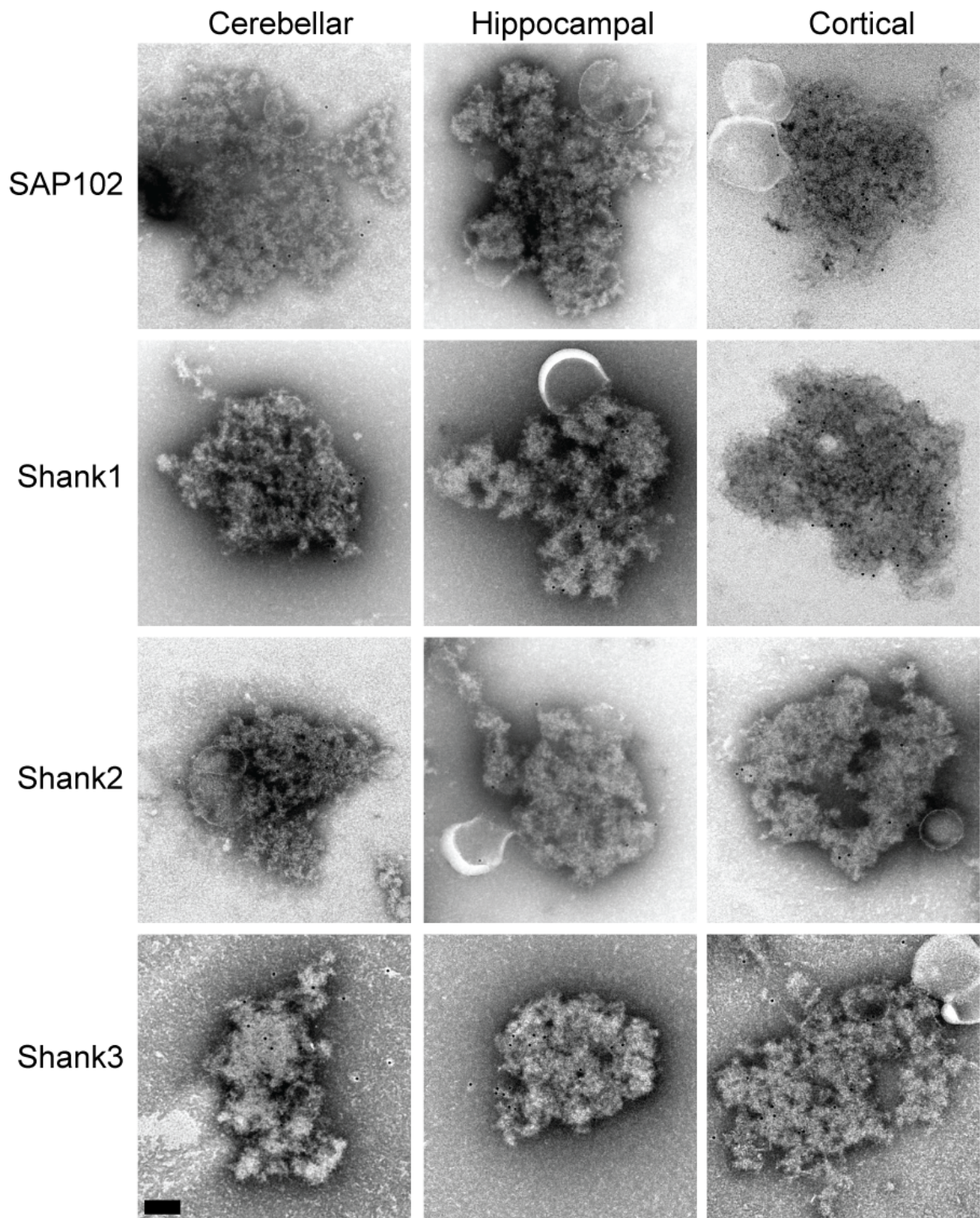


**Figure 5.3.** *PSDs Immunogold Labeled for Scaffolds: SAP102, Shank1, Shank2, and Shank3.*

Representative negative stain electron micrographs of PSDs isolated from cerebella, hippocampi, or cortices immunogold labeled for PSD scaffolds: SAP102, Shank1, Shank2, and Shank3. Gold = 12 nm. Scale bar = 100 nm.

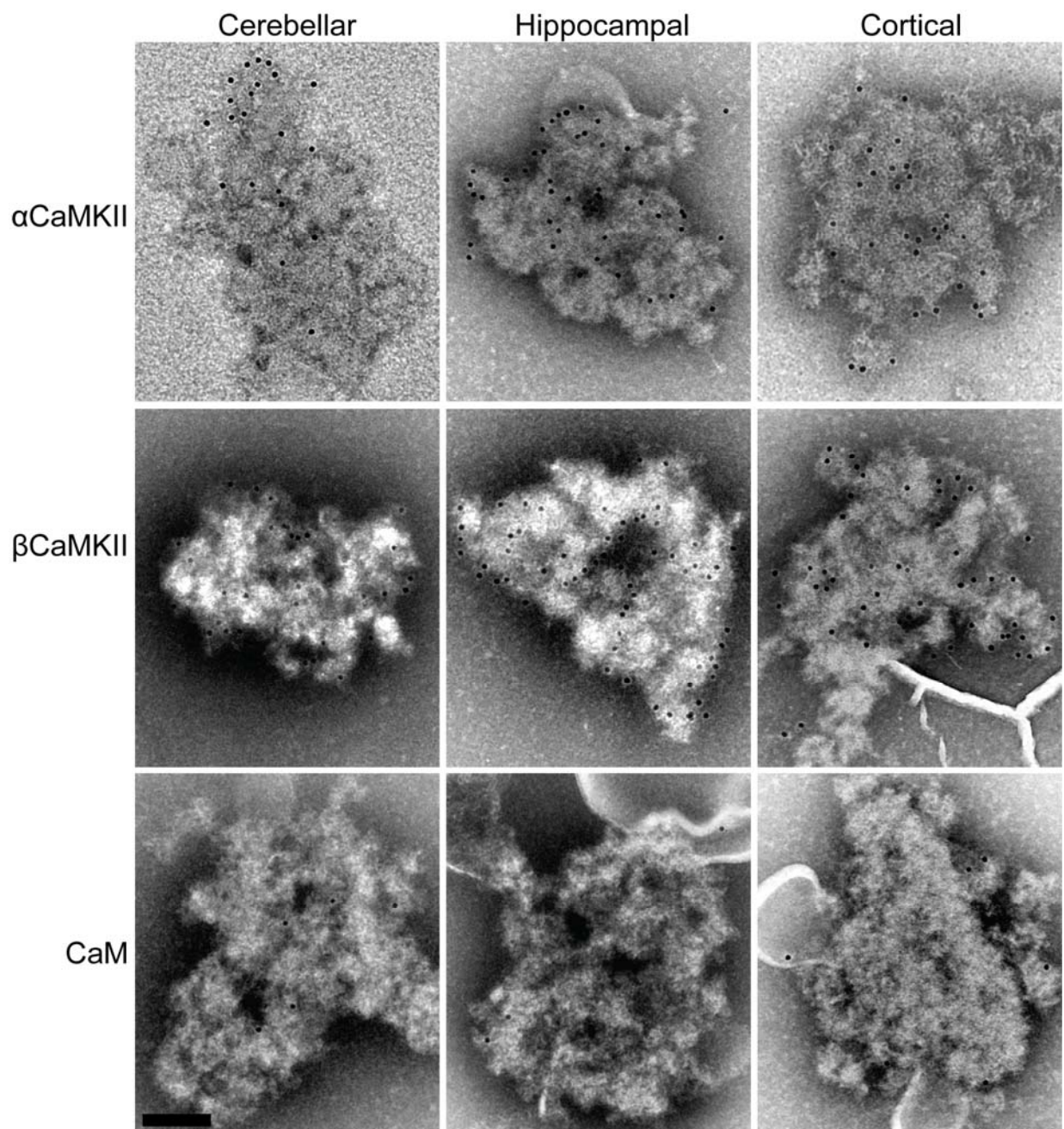


**Figure 5.4.** *PSDs Immunogold Labeled for  $\text{Ca}^{2+}$  Signaling Proteins.*

Representative negative stain electron micrographs of PSDs isolated from cerebella, hippocampi, or cortices immunogold labeled for calcium signaling proteins:  $\alpha$ CaMKII,  $\beta$ CaMKII, and CaM. Gold = 12 nm. Scale bar = 100 nm.



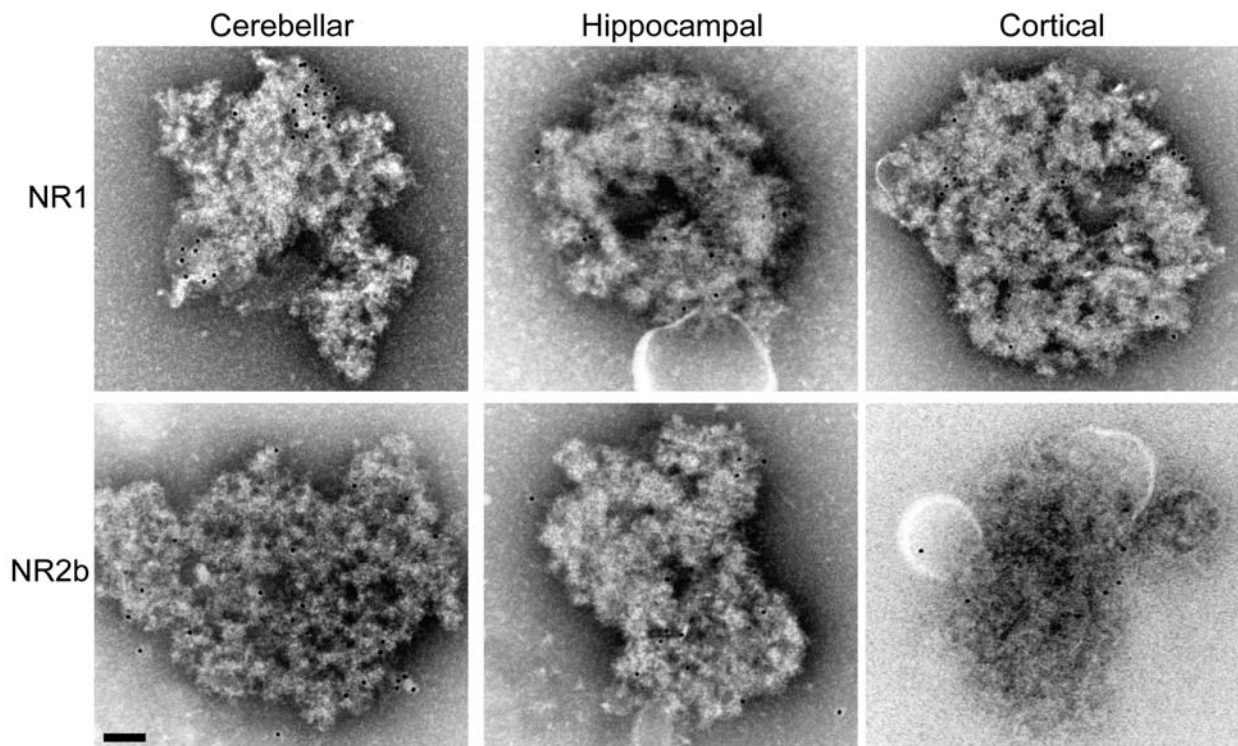


**Figure 5.5.** *PSDs Immunogold Labeled for Neurotransmitter Receptors.*

Representative negative stain electron micrographs of PSDs isolated from cerebella, hippocampi, or cortices immunogold labeled for neurotransmitter receptor subunits NR1 and NR2b. Gold = 12 nm. Scale bar = 100 nm.

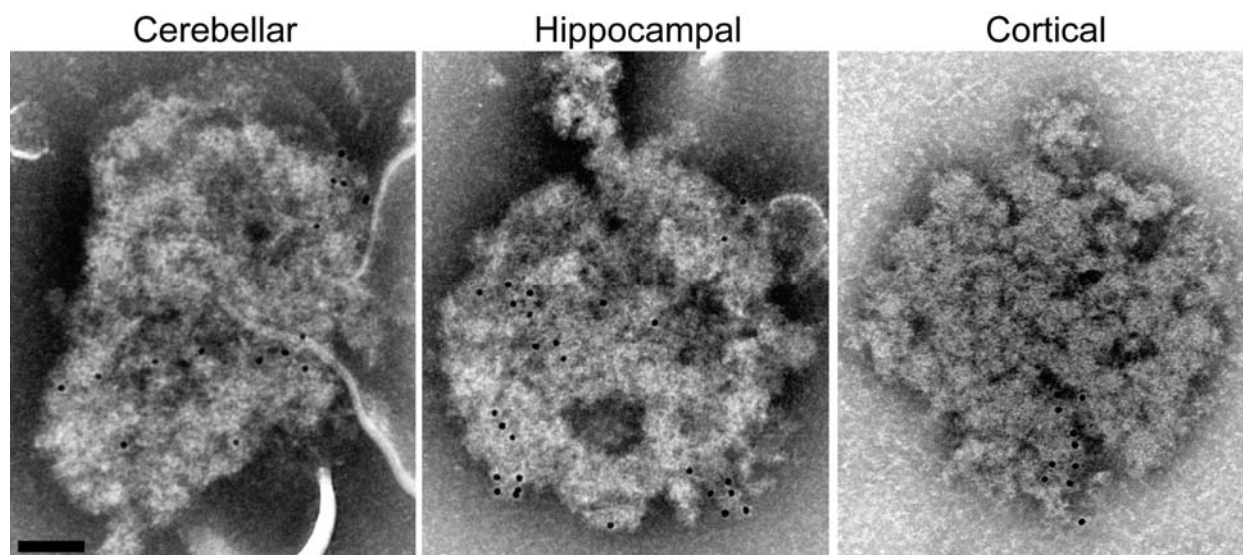


**Figure 5.6.** *PSDs Immunogold Labeled for the Proteasome.*

Representative negative stain electron micrographs of PSDs isolated from cerebella, hippocampi, or cortices immunogold labeled for the RPT6 subunit of the proteasome lid. Gold = 12 nm. Scale bar = 100 nm.



The results of the immunogold labeling experiments are presented in Tables 5.1-5.3 as well as Figures 5.7 and 5.8. Table 5.1 reports the average labeling density for each antibody and each PSD group as the average number of gold per unit of area and as the average number of gold per PSD. Table 5.2 compares the average labeling density, measured as gold per unit of area, across the different PSD groups for each antibody to assess trends in protein composition. Each column in Table 5.2 compares labeling densities of one PSD group directly to another and reports the ratio of the labeling densities. Table 5.3 reports the percentage of PSDs from each experiment with gold labeling density above secondary background control experiments. Typically at least 90% of PSDs from each experiment were measured to have gold labeling well above background, however this was not always the case and Table 5.3 provides some unique information about the diversity of PSD protein composition within brain regions. Figure 5.7 illustrates the data from Table 5.1 in graphical form to provide visualization for the average labeling densities, reported as gold per unit area. Figure 5.8 presents three graphs which report labeling for each antibody as the percentage of total labeling for that PSD group, giving a better picture for individual protein representation within PSDs.

#### *5.2.1. Scaffold Proteins within and across PSD Groups*

As mentioned previously, scaffolds form the core substructure of the PSD, anchoring neurotransmitter receptors, and organizing signaling proteins (Okabe, 2007). Antibodies against  $\alpha$ -actinin, actin, PSD-95, Homer, SAP102, Shank1, Shank2, and Shank3 were employed to test whether the composition and organization of the PSD

scaffold network differs in PSDs across the brain. In PSDs isolated from adult rat cortices, the most abundant scaffold was PSD-95 which demonstrated a significantly greater average labeling density than all other scaffold proteins analyzed (Table 5.1 and Figure 5.7). In cerebellar PSDs, labeling densities for  $\alpha$ -actinin, Shank1, Shank3, and actin were approximately equally abundant, and they were significantly greater than the average labeling for PSD-95, Homer, SAP102, and Shank2 (Table 5.1 and Figure 5.7). Labeling for  $\alpha$ -actinin was the most abundant of all the scaffolds tested in hippocampal PSDs, while actin, Shank1, PSD-95, Shank3, and Homer were moderately abundant (Table 5.1 and Figure 5.7). Labeling for shank2 and SAP102 was found to be the least abundant of the scaffolds in each PSD group (Table 5.1 and Figure 5.8), which was consistent with previous observations that SAP102 is replaced with scaffold PSD-95 as PSDs developmentally mature (Sans et al., 2000, Petralia et al., 2005, Zheng et al., 2011).

Labeling densities for each scaffold were also compared across the different PSD groups (Table 5.2). Of the scaffold proteins evaluated, Shank1 was the only scaffold that did not change significantly in labeling density between PSDs isolated from cerebella, hippocampi and cortices, suggesting a fundamental role for Shank1 in PSDs across the brain. In contrast, PSD-95 and Homer were found to differ significantly between all groups (Table 5.2), which was surprising given that PSD-95 is thought of as the primary PSD scaffold supporting both NMDA and AMPA receptors in the synaptic plasma membrane (Zheng et al., 2011). Labeling for PSD-95 and Homer was most abundant in cortical PSDs and least abundant in cerebellar PSDs (Table 5.1 and 5.2). Cortical PSDs also had significantly increased labeling for actin and Shank3 as compared to hippocampal and cerebellar PSDs (Table 5.2). Labeling densities for

Shank2 and  $\alpha$ -actinin in hippocampal and cortical PSDs were significantly increased in comparison to cerebellar PSDs (Table 5.2).

Of the cortical and hippocampal PSDs imaged in scaffold immunogold labeling experiments, at least 85% were measured with gold labeling densities above background (Table 5.3). With several exceptions, 95% of cerebellar PSDs were found to have positive labeling for the scaffolds analyzed (Table 5.3). Only 45% of cerebellar PSDs had positive labeling for Homer, 70% for PSD-95 and 75% for Shank2 (Table 5.3). Given the low labeling densities for cerebellar PSDs labeled for Homer, PSD-95 and Shank2, these percentages were not entirely surprising. However, labeling for SAP102 was the second lowest within cerebellar PSDs and yet 100% of cerebellar PSDs positively labeled for SAP102 (Table 5.3). The differential labeling densities for scaffolds across the PSD groups and the variability of labeling for scaffolds within cerebellar PSDs, compared to both cortical and hippocampal PSDs, suggest that the PSD scaffold network changes across the brain even within specific brain areas such as the cerebellum. It is also of interest to note that while scaffolds were targeted by 8 of the 13 (62%) antibodies used in this analysis, labeling for scaffolds only represented 47% of total gold labeling for cortical PSDs, 36% for cerebellar PSDs and 27% for hippocampal PSDs (Figure 5.8), suggesting that there are other proteins that comprise the hippocampal and cerebellar scaffold networks that were not targeted in this analysis or it is plausible that PSDs from hippocampi and cerebella have less scaffolding than cortical PSDs.

#### *5.2.2. Signaling Molecules within and across PSD Groups*

Antibodies against the  $\alpha$  and  $\beta$  isoforms of CaMKII, the most abundant proteins in PSDs, and CaM, the calcium signal transducing activator, were used to determine labeling densities in the region specific PSDs. In PSDs isolated from cerebral cortices, the average labeling density for  $\alpha$ CaMKII was significantly greater than labeling for  $\beta$ CaMKII, while in PSDs isolated from cerebella and hippocampi the average labeling densities were reversed with labeling significantly greater for  $\beta$ CaMKII than  $\alpha$ CaMKII (Table 5.1 and Figure 5.7). The ratio of  $\alpha$ CaMKII to  $\beta$ CaMKII was approximately 3:2 for cortical PSDs, 2:3 for hippocampal PSDs and 1:4 for cerebellar PSDs (Table 5.1 and Figure 5.7).  $\beta$ CaMKII was present in PSDs at higher concentrations than expected, suggesting stronger interactions between PSDs and the actin network as  $\beta$ CaMKII can uniquely bind monomeric and F-actin unlike  $\alpha$ CaMKII (Swulius and Waxham, 2008, Sanabria et al., 2009, Hoffman et al., 2013).

Labeling for CaM was present in all PSD groups, although the average labeling densities were significantly lower than labeling densities for  $\alpha$ CaMKII and  $\beta$ CaMKII (Table 5.1 and Figure 5.7) and labeling for CaM was not statistically different between the PSD groups (Table 5.2). Labeling densities for  $\beta$ CaMKII were different between all PSD groups, with labeling ratios between PSD types ranging from 1.6 to 2.9 (Table 5.2). Cortical and hippocampal PSDs had significantly increased labeling, 11x and 8.4x respectively, for  $\alpha$ CaMKII as compared to cerebellar PSDs (Table 5.2). Interestingly, 40% of cerebellar PSDs did not show labeling for  $\alpha$ CaMKII over background, while labeling for  $\alpha$ CaMKII was above background in 100% of cortical and hippocampal PSDs immunogold labeled, further supporting the heterogeneity of PSDs isolated from the cerebellum (Table 5.3).

Together the average gold labeling densities for both isoforms of CaMKII represented 41% of the total labeling within cortical PSDs (Figure 5.8). Cerebellar PSDs had the lowest labeling densities for both  $\alpha$ CaMKII and  $\beta$ CaMKII, which together represented 26% of the total gold labeling for all proteins targeted within cerebellar PSDs (Figure 5.8). Hippocampal PSDs had the greatest labeling for  $\beta$ CaMKII and the labeling for CaMKII represented 50% of the total gold labeling for all proteins targeted within hippocampal PSDs (Figure 5.8). When combined, labeling for  $\alpha$ CaMKII and  $\beta$ CaMKII was 2-4 times greater than for all other proteins evaluated, consistent with a major role for CaMKII in establishing the structure of PSDs from the three regions evaluated.

#### *5.2.3. Neurotransmitter Receptors within and across PSD Groups*

Immunogold labeling for NMDA receptor subunit NR1 was statistically greater than the labeling for the NR2b subunit in both cortical and hippocampal PSDs (Table 5.1 and Figure 5.7), while labeling densities for NR1 and NR2b were not different in PSDs isolated from cerebella (Table 5.1 and Figure 5.7). NR1 is the necessary subunit to form ion conducting NMDA receptors (Kumar and Mayer, 2013), therefore these results suggest that NR subunits other than NR2b are likely present in cortical and hippocampal PSDs to form the obligate heteromeric complexes. In contrast, the majority of NMDA receptors in the cerebellum associated with PSDs may be largely composed of NR1/NR2b subunits. Given that at least 90% of all PSDs labeled above background for NR1 and 100% of all PSDs labeled for NR2b, it is likely that the majority of the PSDs analyzed in the immunogold analysis were from glutamatergic synapses.

Comparing the average labeling densities across PSD types, there were no significant differences in NR1 or NR2b labeling with the exception that hippocampal PSDs had 1.5x more labeling for NR2b when compared to cortical PSDs (Table 5.3). It is also of interest to note that while the labeling densities of NR1 and NR2b did not change significantly between most PSD groups, the labeling for both subunits represented 19% of total labeling for cerebellar PSDs while only representing 12% and 9% of the total labeling for hippocampal and cortical PSDs, respectively.

#### *5.2.4. Proteasome within and across PSD Groups*

Given recent evidence suggesting that the ubiquitin proteasome system (UPS) plays a crucial role in activity-dependent plasticity (Ehlers, 2003, Bingol and Schuman, 2006, Djakovic et al., 2009), I performed immunogold labeling experiments on each PSD group with an antibody against the proteasome. Labeling for the proteasome was present in all PSD types (Table 5.1 and Figure 5.7), but the labeling density was significantly increased in hippocampal and cerebellar PSDs compared to cortical PSDs (Table 5.2). Interestingly, only 65% of cortical PSDs labeled for the proteasome (Table 5.3) and labeling for the proteasome represented only 2% of total labeling in cortical PSDs as compared to 7% in hippocampal PSDs and 12% in cerebellar PSDs (Figure 5.8). These results confirm that proteasomes are present within PSDs across the brain and imply that synapses from different regions of the brain may differentially engage the UPS for structural modification of the PSD scaffold.

#### *5.2.5. Additional Trends across PSD Groups*

Figure 5.8 illustrates the percentage each antibody represents of the total immunogold labeling for each PSD group, allowing visualization of the protein composition of each PSD type. In order to further compare the protein composition of the PSDs isolated from cortices, hippocampi and cerebella, the four most abundant proteins in each PSD group, as determined by Figure 5.8, were compared. The most abundant proteins in cortical PSDs were  $\alpha$ CaMKII,  $\beta$ CaMKII, PSD-95 and actin (Figure 5.8 and Table 5.1), which was consistent with previous work ranking proteins in PSD fractions isolated from cerebral cortices (Dosemeci et al., 2007). The most abundant proteins within hippocampal PSDs were  $\beta$ CaMKII,  $\alpha$ CaMKII, NR1, and the proteasome, while  $\beta$ CaMKII, the proteasome, NR1, and NR2b were the most abundant components of cerebellar PSDs (Figure 5.8 and Table 5.1). Interestingly PSD-95 was not one of the four most abundant proteins within hippocampal and cerebellar PSDs, but no other scaffolds were within the most abundant proteins either for these PSD types. The proteasome, however, was included in hippocampal and cerebellar PSDs as a major component, further suggesting that synapses from these brain areas may differentially utilize proteasomal degradation.

	Gold/ $\mu\text{m}^2 \pm \text{SEM}$			Gold/PSD $\pm \text{SEM}$		
	Cereb.	Hippo.	Cortical	Cereb.	Hippo.	Cortical
$\alpha$ -actinin	27 $\pm$ 4	45 $\pm$ 7	52 $\pm$ 8	10 $\pm$ 2	18 $\pm$ 4	21 $\pm$ 4
Actin	24 $\pm$ 3	30 $\pm$ 3	66 $\pm$ 11	18 $\pm$ 2	18 $\pm$ 3	31 $\pm$ 7
PSD-95	12 $\pm$ 4	27 $\pm$ 5	87 $\pm$ 11	4 $\pm$ 1	9 $\pm$ 3	32 $\pm$ 4
Homer	9 $\pm$ 3	24 $\pm$ 5	49 $\pm$ 7	2 $\pm$ 1	5 $\pm$ 1	14 $\pm$ 3
SAP102	8 $\pm$ 2	17 $\pm$ 3	10 $\pm$ 2	3 $\pm$ 1	6 $\pm$ 2	4 $\pm$ 1
Shank1	25 $\pm$ 5	30 $\pm$ 5	33 $\pm$ 6	10 $\pm$ 2	9 $\pm$ 2	11 $\pm$ 2
Shank2	5 $\pm$ 2	13 $\pm$ 3	16 $\pm$ 4	1 $\pm$ 1	3 $\pm$ 1	3 $\pm$ 1
Shank3	25 $\pm$ 4	26 $\pm$ 5	59 $\pm$ 11	9 $\pm$ 2	8 $\pm$ 2	17 $\pm$ 4
$\alpha$ CaMKII	18 $\pm$ 7	153 $\pm$ 17	199 $\pm$ 21	5 $\pm$ 2	41 $\pm$ 10	52 $\pm$ 9
$\beta$ CaMKII	80 $\pm$ 17	232 $\pm$ 21	127 $\pm$ 12	18 $\pm$ 3	59 $\pm$ 8	39 $\pm$ 6
CaM	12 $\pm$ 3	17 $\pm$ 3	9 $\pm$ 3	3 $\pm$ 1	8 $\pm$ 3	3 $\pm$ 2
NR1	39 $\pm$ 8	56 $\pm$ 5	45 $\pm$ 8	11 $\pm$ 2	23 $\pm$ 4	14 $\pm$ 3
NR2b	32 $\pm$ 4	40 $\pm$ 4	26 $\pm$ 3	9 $\pm$ 2	13 $\pm$ 2	11 $\pm$ 2
Proteasome	46 $\pm$ 9	54 $\pm$ 9	13 $\pm$ 7	15 $\pm$ 3	20 $\pm$ 5	4 $\pm$ 2

**Table 5.1.** *Summary of Immunogold labeling Experiments.*

Average labeling densities reported as gold/ $\mu\text{m}^2$  and gold/PSD for all immunogold labeling experiments. Antibodies were used against a subset of PSD scaffolds, calcium signaling proteins, neurotransmitters and the proteasome. N = 20 for each PSD group and antibody combination.



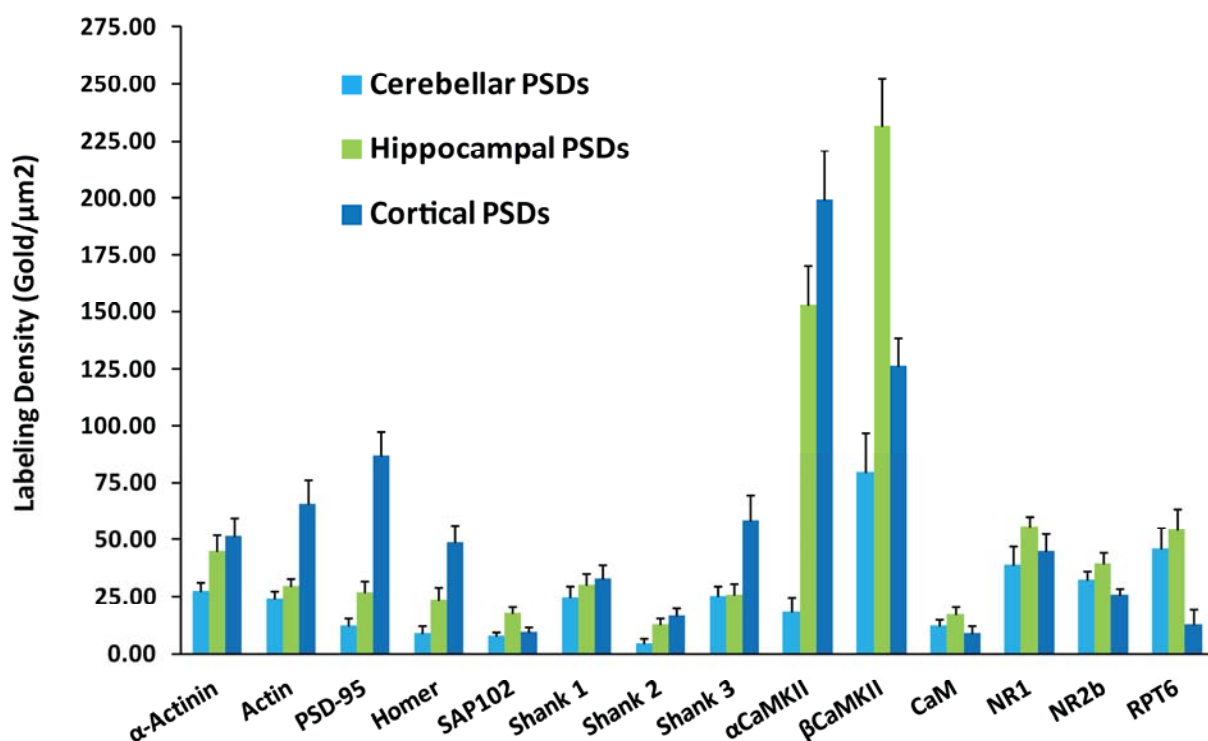


**Figure 5.7.** *Bar Graph of Immunogold Labeling Results.*

Bar graph illustrating the average labeling densities reported as gold/μm<sup>2</sup> ± SEM for all immunogold labeling experiments. Antibodies were used against a subset of PSD scaffolds, calcium signaling proteins, neurotransmitters and the proteasome. N = 20 for each PSD group and antibody combination.

	CX vs. CB	CX vs. Hippo	Hippo vs. CB
	Labeling Density (CX ÷ CB)	Labeling Density (CX ÷ H)	Labeling Density (H ÷ CB)
α-actinin	1.9 ↑*	1.1	1.7 ↑*
Actin	<b>2.7</b> ↑**	2.2 ↑*	1.2
PSD-95	<b>7.3</b> ↑**	<b>3.2</b> ↑**	<b>2.3</b> ↑**
Homer	<b>5.6</b> ↑**	2.1 ↑*	2.7 ↑*
SAP102	1.2	0.6	2.3 ↑*
Shank1	1.3	1.1	1.2
Shank2	3.5 ↑*	1.3	2.8 ↑*
Shank3	2.3 ↑*	2.3 ↑*	1
αCaMKII	<b>11</b> ↑**	1.3	<b>8.4</b> ↑**
βCaMKII	1.6 ↑*	<b>0.6</b> ↓**	<b>2.9</b> ↑**
CaM	0.7	0.5	1.4
NR1	1.2	0.8	1.4
NR2b	0.8	0.7 ↓*	1.2
Proteasome	0.3 ↓*	0.2 ↓*	1.2

**Table 5.2.** *Immunogold Labeling Densities Compared Across Regions.*

Comparisons of immunogold labeling across PSD groups. Ratios were considered significant if  $P < 0.05$  in a 2-tailed t test, indicated with a single asterisk (\*); boldface and double asterisks (\*\*) indicated a  $P \leq 0.001$ . Arrows indicated whether the ratios represented increased (↑) or decreased (↓) immunogold labeling. N = 20 for each PSD group and antibody combination.

	PSDs with Gold above Background		
	Cerebellar PSDs	Hippocampal PSDs	Cortical PSDs
$\alpha$ -actinin	100%	100%	100%
Actin	95%	100%	100%
PSD-95	70%	95%	100%
Homer	45%	85%	100%
SAP102	100%	90%	90%
Shank1	95%	95%	95%
Shank2	75%	90%	85%
Shank3	100%	100%	100%
2D5	60%	100%	100%
CB $\beta$ 1	95%	100%	100%
CaM	85%	95%	80%
NR1	90%	100%	100%
NR2b	100%	100%	100%
RPT6	90%	100%	65%

**Table 5.3.** *Fractions of PSDs with Gold Labeling above Background.*

Percentage of PSDs included in the immunogold labeling experiments with gold labeling above background gold measurements. N = 20 for each PSD group and antibody combination.

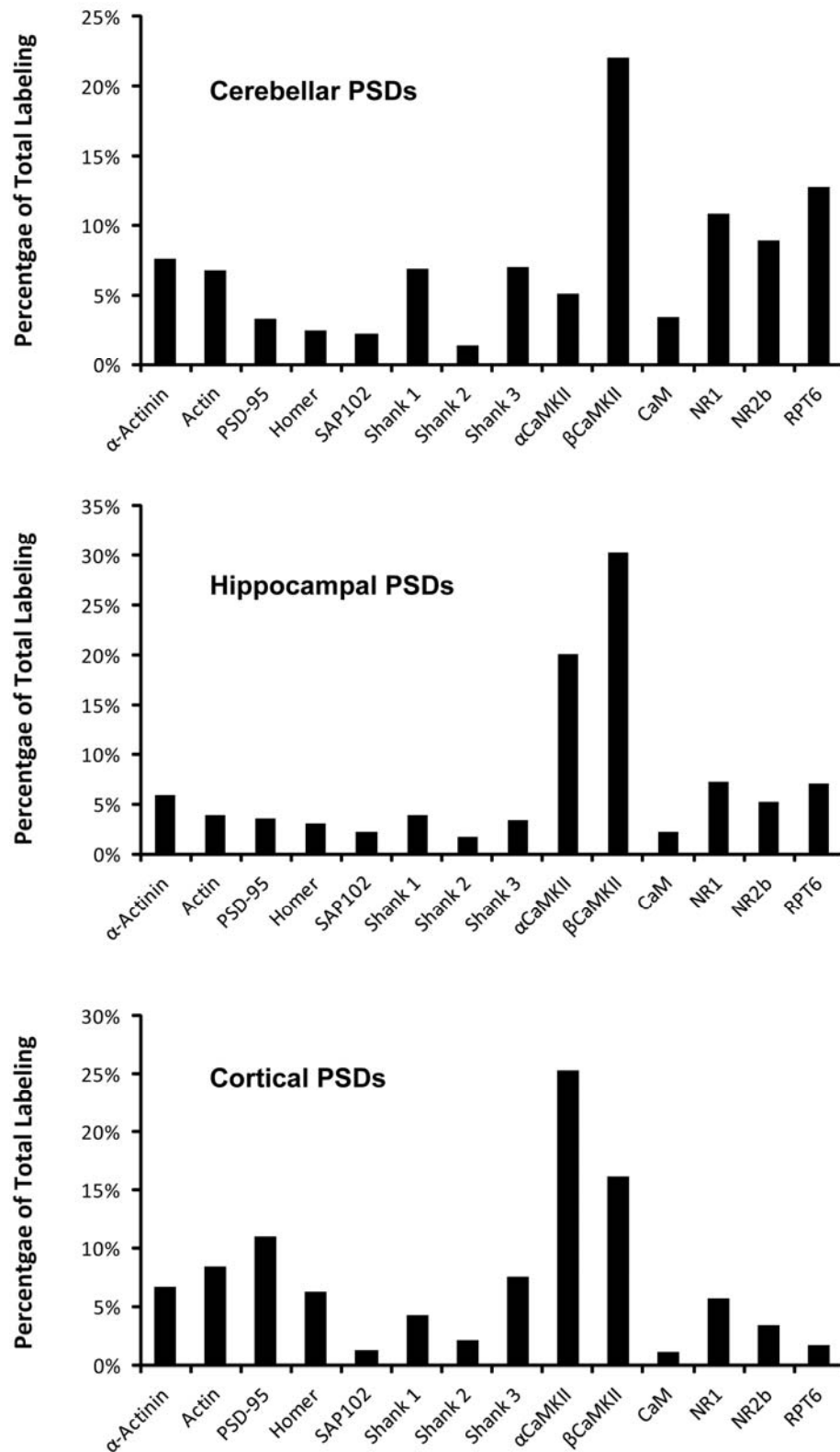


**Figure 5.8.** *Percentage of Total Immunogold Labeling.*

Bar graphs illustrating the percentage of total immunogold labeling each antibody represented for the different PSD groups.

### 5.3. *Spatial Analysis of Gold Labeling*

While measuring labeling densities for PSDs immunogold labeled for scaffold PSD-95, it was observed that gold appeared clustered on cerebellar PSDs, a pattern not observed with cortical or hippocampal PSDs (Fig. 5.9). A Ripley's K-function based spatial analysis was employed to test whether the spatial distribution of PSD-95 in cerebellar PSDs was statistically non-random. A description of the analysis can be found in Chapter 2, section 2.4, and examples of random and non-random gold labeling are illustrated in Figure 5.10. Included in Figure 5.10 are two micrographs of immunogold labeled PSDs (Fig. 5.10.A), one with random gold distribution and the other with non-random distribution, the 2D models of the same PSDs (Fig. 5.10.B) and the H-functions which result from the Ripley's K-function analysis (Fig. 5.10.C). In Figure 5.10.C, the horizontal black lines through 0 on the y-axis represents complete spatial randomness, the black traces represent the minimum and maximum envelopes for random distribution based on the simulated data of complete spatial randomness, and the red traces represent the distribution of the gold from the data. If the red trace falls outside of the minimum or maximum envelope, the distribution is non-random, as shown in the right column of Figure 5.10. If the red trace stays within the min and max envelopes, the gold is distribution is considered random as shown in the left column of Figure 5.10. The PSD with non-random distribution in Figure 5.10 is a cerebellar PSD immunogold labeled for PSD-95, and the distribution of PSD-95 labeling is clearly non-random at both short (~ 200 nm) and long (~ 800 nm) distances, consistent with statistically significant clustering.

Spatial analysis for PSD-95 labeling was assessed for 21 cerebellar PSDs, of which 20 PSDs (95%) were determined to have non-random distribution for gold

labeling PSD-95 (Table 5.4). Seventeen of the cerebellar PSDs with non-random distribution deviated from random at larger distances suggesting clustering (Table 5.4) as opposed to non-random dispersed points, indicating that PSD-95 is typically organized in clusters within cerebellar PSDs, when present, as labeling for PSD-95 was below controls in approximately 30% of cerebellar PSDs. For comparison, spatial analysis of the gold labeling of PSD-95 in hippocampal and cortical PSDs was also determined (Table 5.4). In total, 71% (12 of 17) of hippocampal PSDs and only 54% (13 of 24) of cortical PSDs were categorized as having non-random gold distribution compared to the 95% (20 of 21) of cerebellar (Table 5.4). The number of hippocampal (7 of 17, 41%) and cortical PSDs (11 of 24, 46%) with gold distribution categorized as clustering was also significantly less than cerebellar PSDs (17 of 21, 81%) (Table 5.4), confirming the visual observation that gold labeling PSD-95 clustered more often in cerebellar PSDs.

Spatial analysis was also performed on cerebellar, hippocampal, and cortical PSDs immunogold labeled against  $\beta$ CaMKII, to determine if cerebellar PSDs display increased non-random distribution for proteins other than PSD-95 as compared to other PSD types (Table 5.4). Gold distribution for  $\beta$ CaMKII, which was the most abundant protein in cerebellar and hippocampal PSDs and the second most abundant in cortical PSDs (Table 5.1), was found to have similar levels of non-random distribution between the different PSD groups, approximately 64%. Hippocampal PSDs had the highest percentage of PSDs with clustering of gold targeting  $\beta$ CaMKII (11 of 25, 44%), followed by cerebellar PSDs (7 of 20, 35%) and cortical (10 of 25, 25%), suggesting that increased non-random distribution and clustering in cerebellar PSDs is possibly limited to PSD-95 (Table 5.4). To test this, the spatial distribution of gold targeting the NR1

subunit of the NMDA receptor complex, which is anchored in the synaptic plasma membrane by PSD-95, was also analyzed by Ripley's K-function analysis. Interestingly, the level of non-random distribution for NR1 followed the same trend as PSD-95, with 70% (7 of 10) of cerebellar PSDs having gold distribution categorized as non-random, while only 53% (8 of 15) of hippocampal PSDs and 45% (5 of 11) of cortical PSDs were categorized as having non-random gold distribution (Table 5.4). The same trend was also evident for gold distribution consistent with clustering; gold distribution for NR1 was clustered in 50% of cerebellar PSDs, 33% of hippocampal and only 18% of cortical PSDs (Table 5.4). These results first illustrate that a threshold exists for non-random distribution and second suggest that organization of proteins within cerebellar PSDs deviates from random more often than the organization of proteins from cortical and hippocampal PSDs. Future work will be required to determine the full functional significance of non-random distribution and clustered distribution. However, given that the trend for both non-random and clustered NR1 gold distribution was consistent with although not as robust as PSD-95, it is plausible that NR1 clustering may be in part the result of interactions between the NMDA receptor complex and PSD-95.

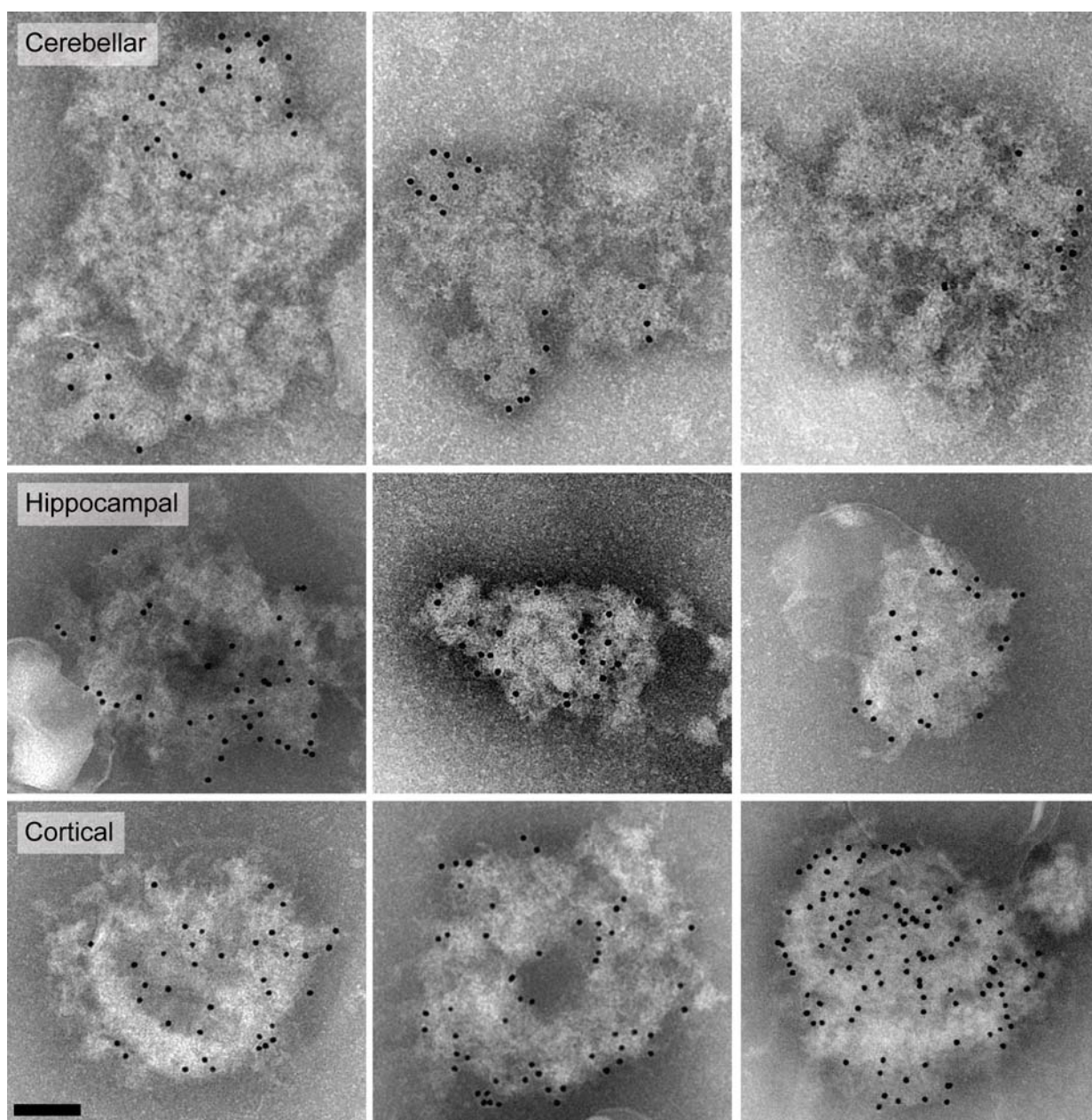


**Figure 5.9.** *PSDs Immunogold Labeled for PSD-95.*

Representative electron micrographs of negatively stained cerebellar, hippocampal and cortical PSDs immunogold labeled for PSD scaffold PSD-95. Gold = 12 nm. Scale Bar = 100 nm.



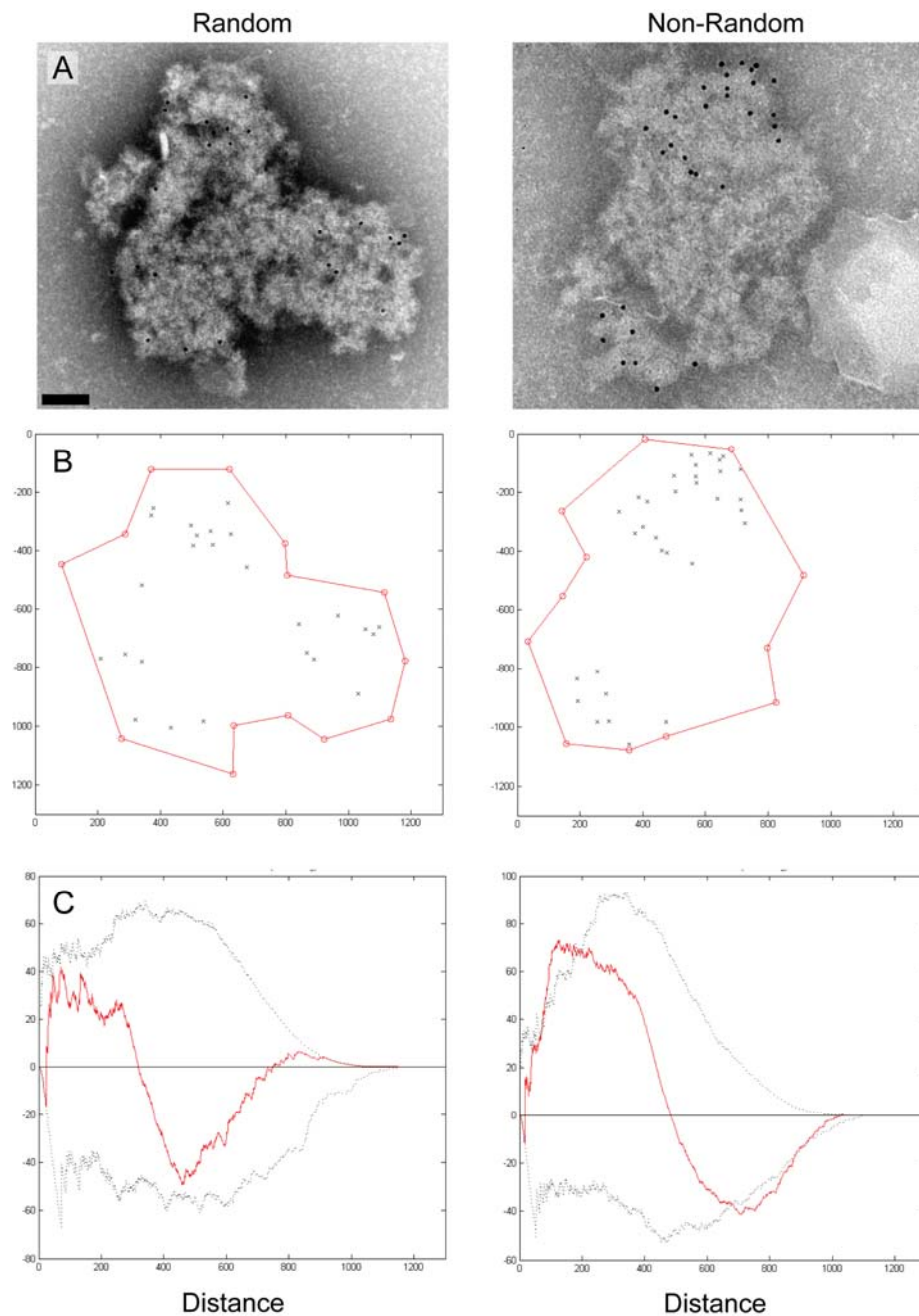


**Figure 5.10.** *Ripley's K-Function Analysis of Random and Non-Random Gold Distribution.*

A) Electron micrographs are representative immunogold labeled and negatively stained PSDs with either random or non-random gold distribution. B) Corresponding coordinate models for the PSD boundary and gold distribution from the micrographs in A. C) The H-functions are the result of the Ripley's K-function analysis comparing examples of complete spatial randomness to the actual gold distribution. When the red trace, which represents the distribution of gold from A, deviates outside of the minimum or maximum envelopes, the black traces, the distribution deviates from random. See Chapter 2.5 for more information. Scale bar = 100 nm.

<b>Number of PSDs with Non-Random Gold Distribution</b>			
	$\beta$ CaMKII	PSD-95	NR1
Cerebellar	13 of 20 (65%)	20 of 21 (95%)	7 of 10 (70%)
Hippocampal	16 of 25 (64%)	12 of 17 (71%)	8 of 15 (53%)
Cortical	16 of 25 (64%)	13 of 24 (54%)	5 of 11 (45%)

<b>Number of PSDs with Gold Clustering</b>			
	$\beta$ CaMKII	PSD-95	NR1
Cerebellar	7 of 20 (35%)	17 of 21 (81%)	5 of 10 (50%)
Hippocampal	11 of 25 (44%)	7 of 17 (41%)	5 of 15 (33%)
Cortical	10 of 25 (25%)	11 of 24 (46%)	2 of 11 (18%)

**Table 5.4.** *Summary of Gold Distribution Data by Ripley's K-Function Analysis.*

## Chapter 6. Discussion

For decades, numerous studies have focused on unraveling the composition and structure of PSDs, as they play an essential role in establishing and modulating synaptic transmission (Okabe, 2007, Sheng and Hoogenraad, 2007). Despite these efforts, there remain significant gaps in the understanding of the detailed anatomical structure of the PSD and the spatial distribution of the proteins from which it is composed. This dissertation presents the first study to employ stain and cryo electron tomography to directly compare PSDs isolated from cerebella, hippocampi and cortices and couple that analysis with immunogold labeling to advance the understanding of the fine morphology and protein composition of the PSD.

Biochemical isolation of PSDs, as first established in the 1970's (Cotman et al., 1974, Cohen et al., 1977), produces an enriched PSD fraction, that is morphologically and compositionally similar to PSDs *in situ* (Kennedy, 1997) and allows for analysis of individual PSDs which is crucial given that PSDs are heterogeneous in nature (Petersen et al., 2003, Swulius et al., 2012). PSDs were isolated from adult rat cerebella, hippocampi and cortices because these brain regions contain unique populations of neuronal cells and are amenable to straightforward isolation. Neuronal cells within cerebral cortices and hippocampi are primarily pyramidal cells, while purkinje cells and granule cells are the major neuronal cells of the cerebellum (Cotman et al., 1974, Rollenhagen and Lubke, 2006). Therefore, it is believed that the vast majorities of PSDs isolated were derived from these neuronal cell types and are from excitatory glutamatergic synapses as confirmed by immunogold labeling experiments. However, it is possible that PSDs from other neuronal cell populations were enriched during the PSD isolation procedure, although they are likely a minor contribution.

Final PSD fractions, produced by first enriching for synaptosomes and then removing all detergent soluble membrane and presynaptic material through detergent treatments and centrifugations on discontinuous sucrose gradients, were all enriched for PSD scaffold PSD-95 and depleted of synaptic marker SV2 (Figure 3.2) as previously shown by Western blot analysis (Swulius et al., 2010). Enrichment of PSD-95 was expected as PSD-95 is a known component of forebrain (Dosemeci et al., 2007) and hippocampal PSDs (Dosemeci et al., 2006). Depletion of SV2 was also anticipated since presynaptic terminals are removed in the isolation procedure as shown in the negative stain micrographs of synaptic junctions (Figure 3.3), which were morphologically similar to synaptic junction fractions previously described (Cotman et al., 1974, Matus and Taff-Jones, 1978). For each region, SDS-PAGE protein profiles were similar between homogenate and synaptosome fractions (Figure 3.4) as previously reported for forebrain tissue (Swulius et al., 2010). PSD protein profiles also shared many of the same bands as homogenate and synaptosomal fractions but contained protein bands significantly enriched from previous fractions, especially in the higher molecular weight range (Figure 3.4) which likely represent PSD scaffolds including PSD-95 (100 kDa) and Shank (~120-240 kDa) (Sheng and Kim, 2011). The protein profiles for the individual PSD fractions from cerebella, hippocampi and cortices were also different (Figure 3.4) confirming that the protein composition of PSDs is varied across brain regions (Carlin et al., 1980, Cheng et al., 2006).

Initial morphologic comparisons of PSDs from negative stain micrographs revealed both similarities and differences (Figures 3.8-3.10). Overall, they appeared similar in dimensions and texture, yet some cerebellar PSDs qualitatively appeared to have less protein density than other cerebellar PSDs and were distinct from both

hippocampal and cortical PSDs. A quantitative assessment of surface area determined that PSDs from cerebella, hippocampi and cortices are similar in size with the average surface areas equivalent at approximately  $0.35 \mu\text{m}^2$  with a peak surface area of  $0.2 \mu\text{m}^2$  (Figure 3.11), comparable to surface areas measured for isolated forebrain PSDs (Swulius et al., 2010). This was unexpected as PSD areas have been reported to vary greatly, as measured through serial electron microscopy of fixed tissue sections, between adult rat hippocampi,  $0.069 \mu\text{m}^2$ , (Harris and Stevens, 1989) and cerebella,  $0.15 \mu\text{m}^2$ , (Harris and Stevens, 1988), reviewed in (Harris and Weinberg, 2012). Note that the average PSD areas reported in this dissertation, similar to previously published PSD areas from this lab (Swulius et al., 2010), are larger than the values reported from serial sectioning of fixed tissue (Harris and Stevens, 1988, 1989, Harris and Weinberg, 2012) and this will be discussed in more detail later in the discussion.

Negative stain and cryo electron tomographic reconstructions of isolated PSDs were used to resolve the morphologic structures of PSDs isolated from cerebella, hippocampi and cortices, and revealed both similarities and differences (Figures 4.2-4.12). Overall, the majority of PSDs were similar in texture but there were clear distinctions in the organization of protein modules within PSDs from the different regions. Cortical and hippocampal PSDs were disc-shaped and generally displayed densely packed areas of protein with occasional areas of low or absent protein density. These morphological features are consistent with previous descriptions of PSDs isolated from hippocampi (Wu and Siekevitz, 1988) and cerebral cortices (Cohen et al., 1977, Carlin et al., 1980) where the authors noted the cup or disc-shaped morphology and also described PSD substructure as being composed of both particles (13-28 nm) and filaments. Areas of less protein density in the PSD center (Cohen et al., 1977,

Cohen and Siekevitz, 1978, Carlin et al., 1980) or openings in the PSD mesh (Petersen et al., 2003) have also been described previously and are consistent with the findings reported here.

Most striking was comparison of PSDs from the cerebellum. Three distinct types of morphology were apparent, which could be categorized by the packing and organization of protein substructures. One type, similar to the morphological features of PSDs from cortices and hippocampi, showed a relatively high protein packing density obscuring some of the fine detail. This dense type of cerebellar PSD represented ~ 41% of cerebellar PSDs. Cerebellar PSDs more granular in texture represented ~ 24% of cerebellar PSDs and were composed of smaller (~ 40nm) protein regions than dense cerebellar PSDs, while latticelike cerebellar PSDs composed ~ 35% of all cerebellar PSDs and exhibited less dense packing of the protein substructure. My description of the latticelike cerebellar PSDs is mostly consistent with a previous morphologic description of cerebellar PSDs as disc-shaped and latticelike (Carlin et al., 1980). The previously described latticelike cerebellar PSDs were postulated to be inhibitory PSDs (Carlin et al., 1980), however the immunogold labeling experiments presented here indicate that the vast majority of PSDs isolated using our protocol were from glutamatergic synapses. Future work will be required to relate these morphologically distinct PSDs to both their neuronal type of origin and the functional significance of their structural differences.

I also determined that a high proportion, 62%, 63% and 78% respectively, of hippocampal, cerebellar and cortical PSDs had tightly associated lipids. The presence of lipids associated with PSDs was previously noted (Cohen et al., 1977, Petersen et al., 2003, Swulius et al., 2010, Swulius et al., 2012). These tightly associated lipids are

hypothesized to be lipid raft-like (Suzuki, 2002, Petersen et al., 2003, Swulius et al., 2012) as they are composed of GM1, a raft-associated lipid, in forebrain PSD fractions (Swulius et al., 2012) and therefore may well play an important role in organizing the overlying synaptic plasma membrane. Interestingly, immunogold labeling of synaptic membranes found a significant fraction of AMPARs co-localized with GM1 (Cole et al., 2010), while another study concluded that ~ 40% of synaptic NMDARs are associated with synaptic lipid rafts (Delint-Ramirez et al., 2010). These results suggest that synaptic lipid rafts are crucial for synaptic organization of glutamate receptors and therefore synaptic transmission. Additionally, PSD-95, a PSD scaffold, is a known component of synaptic lipid rafts (Delint-Ramirez et al., 2010) which associates with cell membranes when palmitoylated (Topinka and Bredt, 1998). Ring-like structures, approximately 15-20 nm in diameter resembling CaMKII, were also evident in tomographic reconstructions of PSDs from all brain regions. This was expected, as CaMKII holoenzymes have previously been visually identified in tomographic reconstructions of PSDs (Fera et al., 2012) and as my immunogold labeling results (Table 5.1), discussed in further detail later, confirm that CaMKII is the most abundant protein in PSDs from cerebella, hippocampi, and cortices.

Additional insights into the morphology of regional PSDs was provided by quantifying the protein-to-volume ratios and thickness of PSDs imaged through electron cryotomography. As expected based on cerebellar PSD morphology, cerebellar PSDs had the largest range of protein-to-volume ratios with half of the PSDs evaluated uniquely clustered near a ratio much smaller than the calculated average (Figure 4.13). This suggested that a distinct group of less dense cerebellar PSDs exist with respect to protein volume, consistent with the visual observations. I expect that increasing the

pool of cerebellar PSDs analyzed for protein-to-volume ratios to allow separation by morphologic type would confirm that separate populations of cerebellar PSDs exist with respect to protein packing, with the lower protein ratios corresponding to the latticelike cerebellar PSDs. With respect to PSD thickness, hippocampal PSDs were determined to be significantly thinner (~ 110 nm) than cerebellar (~ 170 nm) and cortical PSDs (~ 210 nm) from cryo-preserved tomographic reconstruction. This lab has previously reported a disparity in thickness between traditionally prepared and cryo-preserved forebrain PSDs (Swulius et al., 2012) and a similar increase in thickness was found in PSDs across the three brain regions analyzed in this dissertation. Cerebellar, hippocampal and cortical PSDs were six, two and three times thicker than those reported previously in serial sections of fixed and plastic embedded isolated PSDs (Carlin et al., 1980, Wu and Siekevitz, 1988) or from thin sections of fixed, plastic embedded neuropil isolated from the same brain regions (Harris et al., 1992). Interestingly, the thickness of PSDs from these earlier studies (~60-80 nm) was quite similar even though the studies analyzed PSDs prepared in different ways. Two studies (Carlin et al., 1980, Wu and Siekevitz, 1988) used isolated PSDs prepared using a nearly identical protocol to that employed in the present study, while the other (Harris et al., 1992) analyzed PSD thickness in serial sections of fixed neuropil. Therefore, isolating the PSDs from the brain does not appear to cause significant distortions in their overall morphology.

I favor the explanation that the discrepancy in thickness is due to differences in methods employed to preserve and image the PSDs. The use of electron cryotomography to assess the dimensions and morphology of PSDs does not require dehydration, fixation or heavy metal staining and has advantages in retaining a more



accurate representation of the structure of macromolecular assemblies (Murphy and Jensen, 2007, Koning and Koster, 2009). Consistent with this idea, I showed that negatively stained PSDs, from cerebella and cerebral cortices, were approximately half as thick as when cryo-preserved and significantly closer to the values historically reported for thickness of fixed or negative stained PSDs. Additionally PSD surface areas were consistent between negative stain and cryotomography suggesting that staining and dehydrating isolated PSDs selectively compresses the structure in the z-dimension. Fixation embedding of tissue may cause underestimation of PSD size in all three dimensions, and this could account for the differences in surface area mentioned previously between this work and published studies reporting PSD surface area from serial sectioned fixed neuronal tissue (Harris and Stevens, 1988, 1989). For these reasons, I conclude that PSDs may be significantly thicker and extend farther into the spine compartment than previously recognized, potentially facilitating interactions with the cytoskeleton and/or spine apparatus that reside more deeply in the spine head. This idea is supported by tomographic reconstructions of sectioned neuronal tissue where filamentous structures appear to be directly contacting the PSD bridging it with the cytoskeletal network (Rostaing et al., 2006). Additionally, another group investigated the laminar organization of PSD proteins through immunogold labeling of sectioned neuronal tissue (Tao-Cheng et al., 2010, Yang et al., 2011) and defined the core of the PSD to be the area approximately 40 nm under the postsynaptic membrane and the area 40-120 nm under the postsynaptic membrane to be the PSD contiguous network which labels for the PSD proteins synGAP and Shank (Tao-Cheng et al., 2010, Yang et al., 2011). Together, these results strongly suggest that PSDs extend significantly farther into the spine compartment, presumably interacting directly with the

cytoskeletal network through Shank and cortactin. The difference in hippocampal PSD thickness, compared to cortical and cerebellar PSDs, is also intriguing and suggests that differences exist in the interactions between integral PSD components that maintain their three-dimensional architecture.

To compliment the morphological analyses, I investigated the composition and spatial organization of a set of the major PSD associated proteins within individual morphologically identified PSD by employing immunogold labeling. Such an approach has been strategically used in past studies to analyze the presence and distribution of PSD associated proteins (Dosemeci et al., 2001, Valtschanoff and Weinberg, 2001, Petersen et al., 2003, DeGiorgis et al., 2006, Swulius et al., 2010). In interpreting the previous work and the results presented here, it is important to acknowledge that antibodies to individual proteins each bind with a different affinity and epitopes could be inaccessible within the PSD structure. Nevertheless, the amount and patterns of distribution of labeling in PSDs across the different regions provided unique comparative insights into the roles played by each protein.

PSD-95 was the most abundant scaffold in cortical PSDs, consistent with earlier studies (Cheng 2006, Dosemeci 2007), but interestingly was found to differ significantly between all groups and was not the most abundant scaffold in hippocampal or cerebellar PSDs. This is surprising given that PSD-95 is thought of as the primary scaffold supporting glutamate receptors in the synaptic plasma membrane (Zheng et al., 2011). In fact, 30% of cerebellar showed no significant labeling for PSD-95 and when present, spatial analysis showed PSD-95 was clustered. PSD-95 clustering was not prominent in either hippocampal or cortical PSDs, consistent with previous descriptions of homogenous labeling for PSD-95 within forebrain PSDs (Petersen et al.,

2003, DeGiorgis et al., 2006). This suggests that PSD-95 plays a unique role in forming structural/functional subdomains in cerebellar PSDs. Perhaps the PSD-95 rich domains function to cluster AMPA receptors as it has been shown by super resolution fluorescence microscopy that PSD-95 rich domains were associated with increased AMPA receptor presence, rather than NMDA receptors in hippocampal neurons (MacGillavry et al., 2013). However, this idea conflicts with my conclusions from the Ripley's K-function analysis of cerebellar PSDs. Future experiments will be required to determine the function of PSD-95 clusters in cerebellar PSDs. Additionally, the antibody used against PSD-95 is known to cross-react with PSD-93 (Sans et al., 2000), thus it is plausible that PSD-93 represents a portion of the labeling seen with the PSD-95 antibody. Unfortunately, labeling experiments with a specific PSD-93 antibody did not yield labeling above background, which was somewhat surprising since PSD-93 is believed to be the only member of the PSD-95 family in cerebellar purkinje cells, as determined by immunohistochemistry (McGee et al., 2001). This could well be the result of the epitope this antibody recognizes being inaccessible for labeling. Ultimately, the differential labeling for PSD-95 across each PSD group indicates that PSD-95 may play distinct roles in the synapses from each of these regions.

Interestingly, the most abundant scaffolds in cerebellar PSDs:  $\alpha$ -actinin, Shank1, Shank3, and actin, all suggested that cerebellar PSDs are integrally connected with the actin cytoskeletal network, as both  $\alpha$ -actinin and Shanks bind actin (Sheng and Kim, 2011), confirming the conclusions from the morphologic analysis. Cerebellar PSDs were also quite variable in scaffold composition; only 45% of cerebellar PSDs had positive labeling for Homer, 70% for PSD-95 and 75% for Shank2. Given this variability within cerebellar PSDs and the differential labeling densities for scaffolds across the

PSD groups, my findings indicate that the PSD scaffold network changes across the brain even within specific brain areas such as the cerebellum. Figure 6.1 includes my hypothesized models for the core organization of PSDs from each region based on my immunogold labeling results and known protein-interactions. The cortical organization is similar to the “traditional” model of PSD organization as others have predicted (Sheng and Kim, 2011), while the models of hippocampal and cerebellar PSD organization rely more heavily on  $\beta$ CaMKII and actin binding proteins (Figure 6.1). It is also of interest to note that while scaffolds were targeted by 62% of the antibodies used in this analysis, labeling for scaffolds represented 47% of total gold labeling for cortical PSDs, and only represented 36% for cerebellar PSDs and 27% for hippocampal PSDs. This suggests that there are other proteins that make up the hippocampal and cerebellar scaffold networks that were not targeted in this analysis and it is also plausible that PSDs from hippocampi and cerebella have less traditional PSD scaffolding than cortical PSDs.

I hypothesize that the core structure of hippocampal PSDs is composed primarily of  $\beta$ CaMKII, the most abundant molecule measured in hippocampal PSDs, and  $\alpha$ -actinin, the most abundant scaffold measured in hippocampal PSDs which interacts with  $\beta$ CaMKII. Through its interactions with actin,  $\beta$ CaMKII is thought to act more as a structural molecule within PSDs, and given that  $\beta$ CaMKII,  $\alpha$ -actinin and actin can all bind one another to form a multi-protein assembly. It is easy to visualize this complex functioning as the primary core of hippocampal PSDs (Figure 6.1). Supporting this idea, hippocampal PSDs had the least labeling for scaffold molecules and were significantly thinner than cortical and cerebellar PSDs when measured from cryo tomographic reconstructions; hippocampal PSDs were also resistant to collapse by

negative staining, perhaps through stabilization by the  $\beta$ CaMKII,  $\alpha$ -actinin and actin complex. I think it would be of interest to further investigate this possibility by treating hippocampal PSDs with detergents known to strip away additional PSD proteins (Matus and Taff-Jones, 1978) to visualize and determine through dual immunogold labeling the composition of hippocampal PSD substructure. Labeling for scaffolds and CaMKII molecules within cerebellar PSDs was also much lower than in cortical PSDs, and I suspect that given that cerebellar PSDs are thicker, there are cerebellar scaffolds not yet identified. One study employed a proteomic approach to quantify the proteins in cerebellar PSD and cortical PSD fractions and, of the 287 proteins identified, 43 proteins differed in quantity between the two samples and several novel proteins were identified within cerebellar PSDs relating to the protein kinase C pathway (Cheng et al., 2006). Close inspection of such proteomic studies should provide insights into the most likely candidates for additional scaffold molecules that would be priorities for future investigations.

Shank1 was the only scaffold for which immunogold labeling did not differ significantly across all PSD groups in either amount or spatial distribution, suggesting that it might play a functionally similar role fundamental to all PSDs. Shank1 interacts with the actin cytoskeleton and ionotropic and metabotropic glutamate receptors through scaffolds GKAP and Homer (Naisbitt et al., 1999, Tu et al., 1999, Grubruker et al., 2011c). Furthermore, Shank1 is also known to bind to neuroligin, an adhesion molecule involved in aligning the presynaptic and postsynaptic membranes (Meyer et al., 2004). These results are consistent with a ubiquitous role for Shank1 as a scaffold to create local domains of glutamate receptors as well as bridging the PSD scaffold to the cytoskeletal network.

CaMKII is the most abundant protein in the PSD (Kennedy et al., 1983, Cheng et al., 2006, Dosemeci et al., 2007) and is an important molecule regulating synaptic plasticity (Lisman et al., 2002, Colbran and Brown, 2004). From the immunogold labeling experiments, I calculated the ratio of  $\alpha$ CaMKII and  $\beta$ CaMKII isoforms to be 3:2 in cortical PSDs, which is relatively consistent with previous findings from forebrain PSDs (ranging from 3:1-6:1) (McGuinness et al., 1985, Miller and Kennedy, 1985, Cheng et al., 2006). The smaller  $\alpha/\beta$  CaMKII ratio calculated in this study is likely due in part to the fact that I determined the amounts of CaMKII in morphologically identified PSDs and not the bulk PSD fraction, which includes variable amounts of non-PSD material. Additionally, great care was taken to ensure rapid isolation and cooling of the brains in order to minimize  $\alpha$ CaMKII aggregation (Hudmon et al., 2005) and recruitment to the PSD (Aronowski et al., 1992, Suzuki et al., 1994, Kolb et al., 1995). This is a known consequence of ischemia unavoidable during brain isolation and  $\alpha$ CaMKII enriched aggregates could contribute to the increased ratio of  $\alpha$ CaMKII to  $\beta$ CaMKII in fractions analyzed previously by Western blot (McGuinness et al., 1985, Miller and Kennedy, 1985) and proteomics (Cheng et al., 2006). Interestingly, my results showed an even greater amount of  $\alpha$ CaMKII vs.  $\beta$ CaMKII in hippocampal PSDs (2:3  $\alpha/\beta$  ratio), so discrepancies with past reports and those presented here cannot be explained by the fact that separate analyses on hippocampal and cortical PSDs were performed. My ratio for cerebellar PSDs also favored  $\beta$ CaMKII over  $\alpha$ CaMKII (4:1) and was consistent with previous work (Miller and Kennedy, 1985). Interestingly, when analyzed by immunocytochemistry  $\alpha$ CaMKII was only present within purkinje cells of the cerebellum, with  $\beta$ CaMKII being present throughout the cerebellum (Walaas et al., 1988). From my immunogold labeling experiments, approximately 60% of the isolated

cerebellar PSDs were labeled for  $\alpha$ CaMKII. It is possible that the subset of isolated cerebellar PSDs that labeled for  $\alpha$ CaMKII were PSDs from purkinje cells while the PSDs that did not label for  $\alpha$ CaMKII were from other cells types, such as granule cells (Voogd and Glickstein, 1998, Rollenhagen and Lubke, 2006). Overall, the  $\alpha/\beta$ -CaMKII ratios, which are presumably representative of the isoform composition of the average PSD CaMKII holoenzyme, suggested that  $\beta$ CaMKII subunit plays a more integral role in the PSD and is present at higher concentration in cortical and hippocampal PSDs than previously appreciated. One possibility for the increased amount of  $\beta$ CaMKII over  $\alpha$ CaMKII in hippocampal and cerebellar PSDs is to provide additional interactions with the spine actin network.  $\beta$ CaMKII can bind actin and actin filaments in a  $\text{Ca}^{2+}$ /CaM reversible manner (Shen et al., 1998, Colbran and Brown, 2004, Sanabria et al., 2009) and has proposed structural roles as a scaffold to integrate  $\text{Ca}^{2+}$  signals with modifications of actin associated with PSDs and the actin cytoskeleton in spines. Additionally,  $\alpha$ CaMKII and  $\beta$ CaMKII have different affinities for  $\text{Ca}^{2+}$ /CaM (Miller and Kennedy, 1985, Gaertner et al., 2004a) and different frequency-dependent activation curves (De Koninck and Schulman, 1998). The results showing that PSDs from different regions vary in their CaMKII holoenzyme subunit ratios suggests that differential recruitment of the enzyme could help distinctively tune the ability of a synapse to respond to the varying frequencies of  $\text{Ca}^{2+}$  signals. The high relative concentration of  $\beta$ CaMKII compared to  $\alpha$ CaMKII in cerebellar PSDs also further confirms conclusions drawn by the morphologic descriptions and scaffold composition of cerebellar PSDs in that cerebellar PSDs are likely well-connected to the actin network. Additionally, labeling for  $\alpha$ CaMKII and  $\beta$ CaMKII was 2-4 times greater than for all other proteins evaluated in all PSD types, consistent with a major role for CaMKII

in establishing the structure of PSDs from the three regions evaluated. Supporting this idea, labeling for both  $\alpha$ CaMKII and  $\beta$ CaMKII represented 50% of the total labeling for hippocampal PSD, further suggesting that CaMKII may act as both the major signaling molecule and as the major scaffold within hippocampal PSDs.

AMPA, NMDA and metabotropic glutamate receptor subunits have been identified in proteomic studies of forebrain (Jordan et al., 2004, Li et al., 2004, Peng et al., 2004, Yoshimura et al., 2004, Cheng et al., 2006) and cerebellar PSD fractions (Cheng et al., 2006), and I expected to detect these receptors in the immunogold analysis. Additionally I expected to detect GluR $\delta$ 2, which is thought to be present at cerebellar parallel fiber-purkinje cell synapses (Takumi et al., 1999) and has been detected in isolated cerebellar PSDs (Cheng et al., 2006). In the analyses of morphologically identified PSDs, significant immunogold labeling was detected for only the NMDA receptor (NR1 and NR2b subunits) whose levels were consistent between cerebellar, hippocampal and cortical PSDs. Perhaps there were minor subcellular contaminants in the fractions used for the proteomic analyses that contained AMPA and metabotropic receptors that were avoided in this analysis of morphologically identified PSDs. Alternatively, these negative results could be due to epitopes on the receptors being obscured from antibody labeling by their incorporation into PSDs. Remarkably, despite the double Triton X-100 extraction during PSD isolation, the NMDA receptor remains tightly anchored, presumably through interactions with scaffold and signaling proteins. Along with PSD-95, NR2b also binds CaMKII and both NR1 and NR2b can bind  $\alpha$ -actinin, creating a multi-protein complex that likely stabilizes the NMDA receptor in the PSD and prevents its extraction (Strack and Colbran, 1998, Inoue and Okabe, 2003, Robison et al., 2005, Okabe, 2007, Sheng and Hoogenraad,



2007). These results suggest that the mobility of the NMDA receptor is restricted, consistent with work that has demonstrated that a portion (~50%) of NMDA receptors are immobile at synapses (Groc et al., 2004, Triller and Choquet, 2005).

Finally, I determined that the proteasome is a component of isolated PSDs and while all cerebellar and hippocampal PSDs were positively labeled, only 65% of cortical PSDs were labeled. Since the proteasome plays a role in activity-dependent changes to PSD composition (Ehlers, 2003), it is interesting to propose that some PSDs might utilize the proteasome pathway while others do not. In response to synaptic activity, the proteasome was found to be recruited into hippocampal dendritic spines (Bingol and Schuman, 2006) where it can bind to and be phosphorylated by  $\alpha$ CaMKII, thereby increasing proteasomal activity, (Djakovic et al., 2009, Bingol et al., 2010, Djakovic et al., 2012). Once activated, several PSD proteins are targeted for degradation, including PSD-95 (Colledge et al., 2003), Shank, and GKAP (Ehlers, 2003). From these results, one can speculate that the increased labeling of hippocampal and cerebellar PSDs for the proteasome indicates that a higher percentage of synapses in these brain areas are undergoing active proteasomal remodeling than in cortex. This finding raises the additional possibility that a population of cortical PSDs is not susceptible to proteasome-mediated plasticity, although activity-dependent changes in cortical PSD composition, as determined by Western blot, have been shown to be mediated by proteasomal activity (Ehlers, 2003). This is an excellent example of the type of unique information that comes from analyzing individual PSDs. If proteasomal degradation is a hallmark of plasticity at synapses, one can speculate that a population of synapses in the cortex are resistant to plasticity and perhaps are the specific sites of long-term memory storage, as has recently been proposed (Osada et al., 2008, Fuster, 2009,

Hasan et al., 2013). Future experiments focusing on the proteasomal remodeling of individual PSDs will be required to determine if there is a population of cortical PSDs resistant to proteasomal degradation. It is also intriguing that cortical PSDs with the greatest abundance of  $\alpha$ CaMKII, which is the presumed proteasome scaffold within PSDs, had the lowest labeling for the proteasome, while hippocampal and cerebellar PSDs, with more  $\beta$ CaMKII than  $\alpha$ CaMKII, had significant labeling for the proteasome; cerebellar PSDs labeled for twice as much proteasome as  $\alpha$ CaMKII. While it is possible that in response to synaptic activity the additional  $\alpha$ CaMKII molecules which translocate to PSDs act as scaffolds for incoming proteasome molecules, this suggests that the proteasome may also be binding to other PSD proteins within hippocampal and cerebellar PSDs. Dual labeling experiments should be employed in the future to determine the fraction of CaMKII molecules co-localizing with the proteasome.

Future work will be required to unfold the mechanism of proteasomal degradation of PSD scaffolds and preliminary work addressing this is presented in Appendix 1. To begin to understand the level of proteasomal remodeling in PSDs isolated from hippocampi, cerebella, and cortices, western blotting should be employed to assess the level of ubiquitin and ubiquitin specific for proteasomal degradation. Dual labeling experiments or dual Western blotting between ubiquitin and PSD scaffolds could determine whether PSD scaffolds are being tagged for proteasomal degradation. Additionally, proteasome activity assays could also be performed to test whether the proteasomes present in the different PSD fractions are functional. It is also interesting that PSD populations with lower labeling for two of the proteasome-targeted PSD scaffolds, PSD-95 and shank, were the PSDs with the most labeling for the proteasome. While it is plausible that PSD-95 and Shank family members are just less

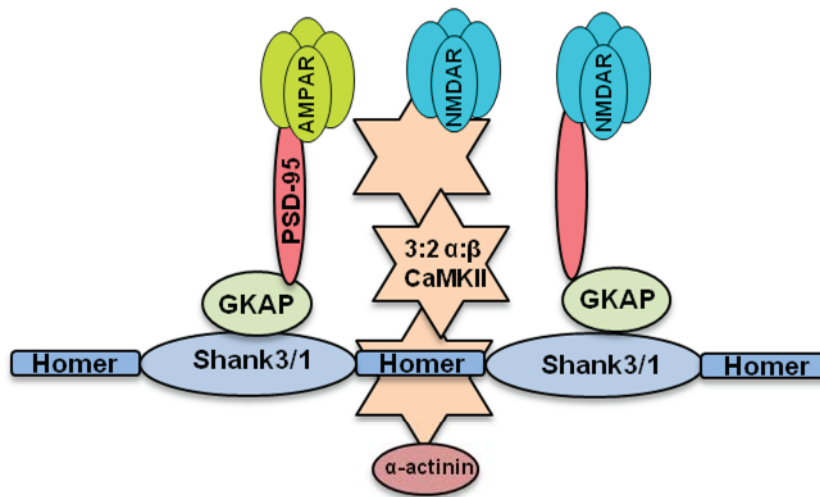
abundant in hippocampal and cerebellar derived PSDs, it is interesting to speculate that their concentration at PSDs is more heavily regulated by proteasomal degradation in hippocampal and cerebellar PSDs.

Future work will also be required to relate the morphologically distinct cerebellar PSDs to both their neuronal type of origin and the functional significance of their structural differences. Intriguingly, from my immunogold labeling results, 75% of cerebellar PSDs immunogold labeled positively for Shank2, which is thought to be specific for purkinje cells, as determined by *in situ* hybridization (Boeckers et al., 1999b), and 60% of cerebellar PSDs labeled for  $\alpha$ CaMKII, the dominant CaMKII isoform in purkinje cells as determined by immunocytochemistry (Walaas et al., 1988). These results suggested that 60-75% of the cerebellar PSDs were isolated from purkinje cells. However, 100% of cerebellar PSDs labeled for shank3, which is believed to be specific for granule cells as determined by *in situ* hybridization (Boeckers et al., 1999b), and only 45% of cerebellar PSDs labeled positively for scaffold homer, which is enriched selectively in purkinje cells as determined by immunohistochemistry (Xiao et al., 1998, Okabe, 2007), thereby confusing the issue. These conflicting results suggest that expression of these proteins, especially specific isoforms of the same protein, may not be as distinctly separate within cerebellar tissue. Future experiments will be required to further clarify the synaptic molecular composition of the different populations of cerebellar cells. I also suggest that antibodies specific against PSD-93 and PSD-95, which successfully label PSDs and do not cross-react, be acquired in order to parse out PSDs from specific cerebellar neurons, as PSD-93 is believed to be the only member of the PSD-95 family within purkinje cells as previously determined by immunohistochemistry (McGee et al., 2001). Once a pattern of labeling is consistent

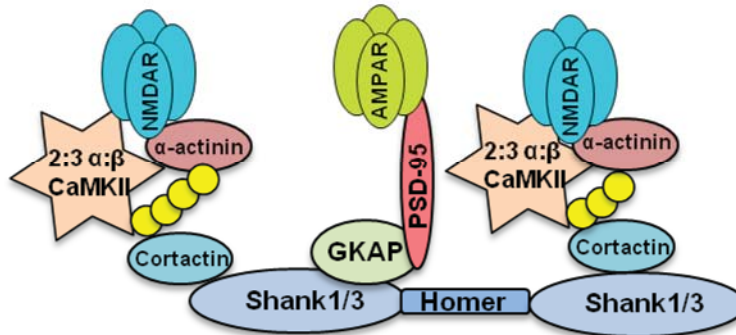
and suggests that separate identifiable populations of cerebellar PSDs exist, it would be fascinating to combine immunogold labeling and electron tomography to connect differences in protein composition to detailed morphologic distinctions in cerebellar PSD texture. Additionally cerebellar synaptic junction fractions (a fraction one step preceding the final PSD fraction) could be immunogold labeled for GluR $\delta$ 2, as the postsynaptic membrane and presumably neurotransmitter receptors are still attached to PSDs within this fraction and GluR $\delta$ 2 is again believed to only be present within purkinje cells of the cerebellum (Takumi et al., 1999).

Tomographic analysis of synaptic junctions could also prove to be a fruitful endeavor. Synaptic junctions are composed of PSDs with residual presynaptic and postsynaptic membranes still attached, as they have only been once treated with detergent. Tomographic analysis of synaptic junctions combined with immunogold labeling could provide valuable information about the organization of proteins in individual morphologically identified PSDs with respect to the postsynaptic plasma membrane. For example, synaptic junctions could be dual immunogold labeled with antibodies against palmitate or scaffold PSD-95 and other markers of lipids rafts in order to determine how synaptic lipid rafts and the PSD might interact, addressing the hypothesis that PSDs play a role in organizing the synaptic membrane. Additionally, to more specifically address PSD dynamics, synaptic junctions could be isolated from chemically activated hippocampal slices, as the yield is also greater for synaptic junctions than for PSDs, and the fine morphologic and compositional changes associated with synaptic activity could be addressed with a combined tomographic and immunogold approach.

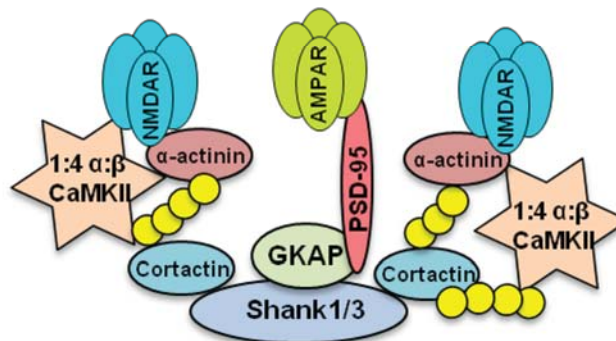
Overall, my results indicate that there are unique structural and compositional differences between PSDs isolated from different brain regions. Despite sharing similar morphology, PSDs were diverse in molecular composition, implying functional distinctions. The differential labeling for PSD scaffolds and clustering of PSD-95, suggested that the underlying PSD scaffold varies across the brain, even within brain regions, a question I am actively investigating. It is quite remarkable to me that PSDs of similar morphology can have such variable protein compositions and that within the cerebellum similar protein composition is observed across PSDs with such varying morphologies. I speculate that the overall structure of the PSD depends more heavily on protein organization than on protein composition, meaning that the PSD structure is largely determined by assembling similar smaller modules of proteins in unique ways. These issues will need to be addressed by identifying the structure of individual modules within the PSD along with higher resolution structural information about their organization and binding interactions within PSDs. Lastly, I propose that the differential ratios of CaMKII isoforms and varying presence of the proteasome suggest that the regulation of synaptic plasticity might vary significantly at different synapses across the brain, thereby increasing the complexity of the rules for how specific synapse types respond to synaptic activity.



**Cortical PSD**



**Hippocampal PSD**



**Cerebellar PSD**

**Figure 6.1.** *Proposed Organization of PSD Scaffolds from Cortical, Hippocampal and Cerebellar PSDs.*

## **Appendix 1: Insights into the Dynamic PSD Structure**

### *A.1.1. Introduction*

Investigations into the PSD have determined that the protein composition and structure of PSDs change through development (Petrulia et al., 2005, Swulius et al., 2010, Swulius et al., 2012) and with synaptic activity (Ehlers, 2003, Tao-Cheng et al., 2010, Yang et al., 2011). The activity-dependent changes to the molecular composition and organization of the PSD are postulated to mediate the long-term changes in synaptic strength underlying learning and memory (Swulius et al., Tao-Cheng et al., Yang et al., Swulius et al., 2012), although the exact molecular organization of the PSD as well as how synaptic activity alters PSD organization and architecture remain unclear. It is reasonable to hypothesize that regulated degradation of key organizing molecules within PSDs could lead to remodeling, and the ubiquitin proteasome system (UPS) has recently been shown to mediate activity-dependent changes in PSD composition (Ehlers, 2003, Sheng and Hoogenraad, 2007). Whether these changes in PSD composition result in structural changes to the PSD is unknown, as are the mechanisms in which the UPS alters PSD composition.

The UPS is a highly regulated protein degradation system, where proteins tagged with polyubiquitin lysine-48 chains are specifically targeted by the proteasome and degraded (Miller and Gordon, 2005). In 2003, it was demonstrated that several PSD scaffold proteins are ubiquitinated in response to activity, including Shank, GKAP (Ehlers, 2003) and PSD-95 (Colledge et al., 2003). Other groups have shown that in response to activity the level of both ubiquitinated proteins and the proteasome increases in dendritic spines (Bingol and Schuman, 2006, Djakovic et al., 2009). Additionally, the activity-induced recruitment of the proteasome to spines was

dependent on prior translocation of CaMKII (Djakovic et al., 2009, Bingol et al., 2010). It is also of interest to note that mutations in and/or dysregulation of PSD-95 (Roselli et al., 2005) and Shank (Roselli et al., 2009, Grabrucker et al., 2011c, Grabrucker et al., 2011d) have been associated with neurologic disorders and diseases, characterized by synaptic dysfunction, such as Autism, the Autism Spectrum Disorders and Alzheimer's Disease. These findings strengthen the idea that the structure of the PSD plays an important role in synaptic function and developing a dynamic molecular model of the PSD will be crucial in understanding mechanisms underlying synaptic function.

My hypothesis for activity-induced structural reorganization of the PSD by the ubiquitin proteasome system is modeled in Figure A.1.1., where in response to synaptic activation, there is initial recruitment of CaMKII into the spine and to the PSD (Dosemeci et al., 2001, Sheng and Hoogenraad, 2007), along with increased ubiquitination of PSD scaffolds (Ehlers, 2003). The 12 subunit CaMKII holoenzyme is known to phosphorylate the proteasome (Djakovic et al., 2009), and act as a target providing binding sites for the proteasome within the PSD (Figure A.1.1.). The arrival of the proteasome at the PSD allows for targeted degradation of ubiquitinated PSD scaffold proteins including Shank, GKAP and PSD-95 (Figure A.1.1.). Loss of these scaffold proteins allows for molecular rearrangement within the PSD as Shank, GKAP and PSD-95 have multiple protein-interaction domains forming multiprotein complexes (Kennedy, 2000, Kim and Sheng, 2004).

Shank molecules can interact with themselves and are hypothesized to construct the frame of the PSD (Kim and Sheng, 2004) (Figure A.1.1.). Shank and PSD-95 form receptor modules as Shank is believed to indirectly support metabotropic glutamate receptors in the membrane, whereas PSD-95 is believed to support both



NMDA and AMPA receptors in the postsynaptic membrane (Kennedy, 2000, Colledge et al., 2003, Kim and Sheng, 2004). Interestingly, GKAP binds both PSD-95 and Shank bringing the two scaffold modules together (Kennedy, 2000), and loss of GKAP could directly impact the organization of synaptic receptors. Therefore targeted proteasomal degradation of PSD scaffolds could result in the removal of receptors from the synapse or could rearrange the PSD scaffold in order to support the recruitment of additional receptors, altering the physiological properties of the synapse. To begin to test this hypothesis, preliminary experiments were performed in order to investigate how the composition of PSDs change in response to activity and whether the proteasome plays a role in PSD structural remodeling throughout development.

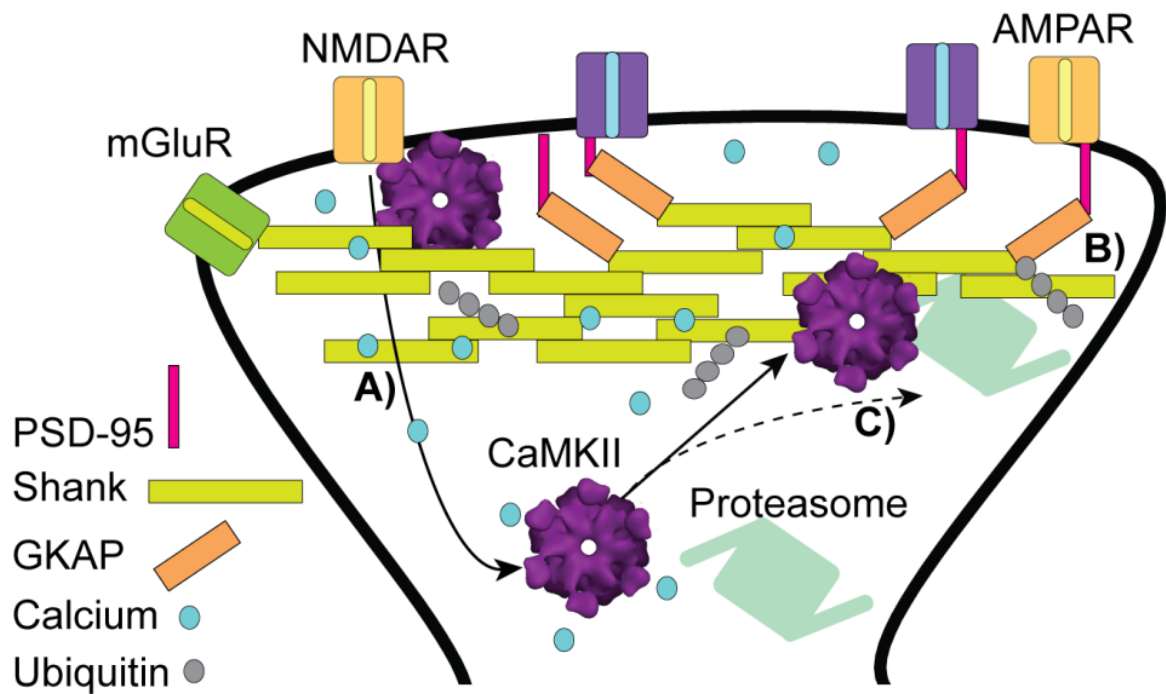


**Figure A.1.1.** *Model for Activity-Induced Structural Reorganization of the PSD by the Ubiquitin Proteasome System*

A) Calcium influx through NMDA receptors triggers immediate activation and translocation of CaMKII into the PSD. B) Ubiquitination of PSD scaffold proteins increases. C) In the PSD, CaMKII acts as a scaffold recruiting proteasome molecules localizing proteasomal degradation within the PSD.

### *A.1.2. Additional Methodology*

#### *A.1.2.1. Preparation of Hippocampal Slices and Chemical Induction of Neuronal Activity*

To prepare hippocampal slices, adult Sprague-Dawley rats were decapitated immediately after being anesthetized with isoflurane. Brains were removed, placed in oxygenated ringer's solution, and hemisected. Hippocampi were isolated and transverse 400  $\mu\text{m}$  slices were prepared with a McIlwain tissue chopper. Slices were then placed in continuously oxygenated ringer's solution at room temperature to recover for 1 hr. Since the goal of this proposal was to study the activity-induced changes to PSD structure, hippocampal slices were synaptically activated with the potassium channel blocker TEA (Enzo Life Sciences). After the recovery period, slices were incubated for 10 min in modified oxygenated ringer's solution either with or without 25 mM TEA (Lengyel et al., 2004) and returned to ringer's solution to allow activity-induced changes to develop, before being immediately frozen in liquid nitrogen and then homogenized for PSD isolation. PSDs were isolated from hippocampal slices following the PSD isolation protocol described in Chapter 2, section 2.1, scaled for starting material.

#### *A.1.2.2. Isolation of Postsynaptic Densities from Forebrains at Postnatal Days 2, 7, 14, 21, and 60*

The protocol to isolate forebrain PSDs from Sprague-Dawley rats at postnatal days 2, 7, 14, 21, and 60 (denoted as P2, P7, P14, P21, and P60 respectively) was adapted from a widely used PSD enrichment procedure (Cohen et al., 1977) modified to increase PSD yield (Figure A.1.2). Forebrains were removed within 30 seconds of decapitation and placed in ice-cold buffer A. For each preparation, a total of 9

forebrains from P60, 12 from P21, 14 from P14, 30 from P7, or 40 from P2 were homogenized in 108 ml of buffer A with a motor-driven glass/Teflon homogenizer (0.2 mm clearance). All steps of the following protocol were accomplished at 4°C. Homogenates were spun at 3600 g for 10 minutes in a RTH-750 rotor, supernatants saved. Pellets were resuspended in original volume of buffer A, hand homogenized, and spun again at 3600 x g for 10 minutes in a RTH-750 rotor. Supernatants were combined and spun at 10,000 x g in a JA-20 rotor for 10 minutes. Pellets were resuspended in original volume of buffer A by hand homogenizing and spun again at 10,000 x g for 10 minutes in a JA-20 rotor. Pellets were resuspended in 28 ml of buffer B and applied to a sucrose gradient (7 ml sample, 9.5 ml 0.85 M sucrose, 10.5 ml 1.0 M sucrose, 10.5 ml 1.4 M sucrose) which was spun for 2 hours at 125,800 x g in a SW32 rotor. The band between 1.0 M and 1.4 M sucrose, containing the synaptosome fraction, was collected and diluted in half with buffer B. An equal volume of triton extraction buffer was added and the samples rotated for 15 minutes prior to being spun at 30,000 x g for 20 minutes in the SW32 rotor. Pellets were resuspended in 2.5 ml of buffer B and applied to a second sucrose gradient (2.5 ml sample, 5 ml 1.0 M sucrose, 5 ml 1.2 M sucrose). The gradient was spun at 167,000 x g for 2 hours in a SW41 rotor. The pellet was resuspended in 1 ml 5 mM HEPES/KOH pH 7.4, 1 ml triton extraction buffer was added, and the sample was mixed on ice for 15 minutes. Finally the sample was spun at 38,000 x g for 15 minutes in a SW55 rotor and the resulting pellet was suspended in 300-500 µl of 20% glycerol in 5 mM HEPES/KOH pH 7.4 and stored as aliquots at -80°C. Spins were performed in a Sorvall® RT7 plus centrifuge, Avanti® J-E Centrifuge and Optima XPN-80 Ultracentrifuge. Gradients were spun with

acceleration and deceleration program 1, resulting in a 2 minute acceleration to and deceleration from 170 RPM, respectively.

#### *A.1.2.3. Western Blotting and Immunogold Labeling*

Western blotting and immunogold labeling were performed as previously described in Chapter 2, sections 2.2 and 2.3. Additional primary antibodies included: pan-Shank (mouse, Neuromab, 75-089), GKAP (mouse, Neuromab, 75-156), CaMKII (rabbit, Millipore, 04-1079), pT286 (Rabbit, Phosphosolutions, p1005-286), pT286 (mouse, Thermo, MA1-047), pT305 (rabbit, produced in house), and 20S (mouse, Enzo Life Sciences, PW8195). Antibody information including Western blot and immunogold labeling dilutions not included in Table 2.1 are listed in Table A.1.1.

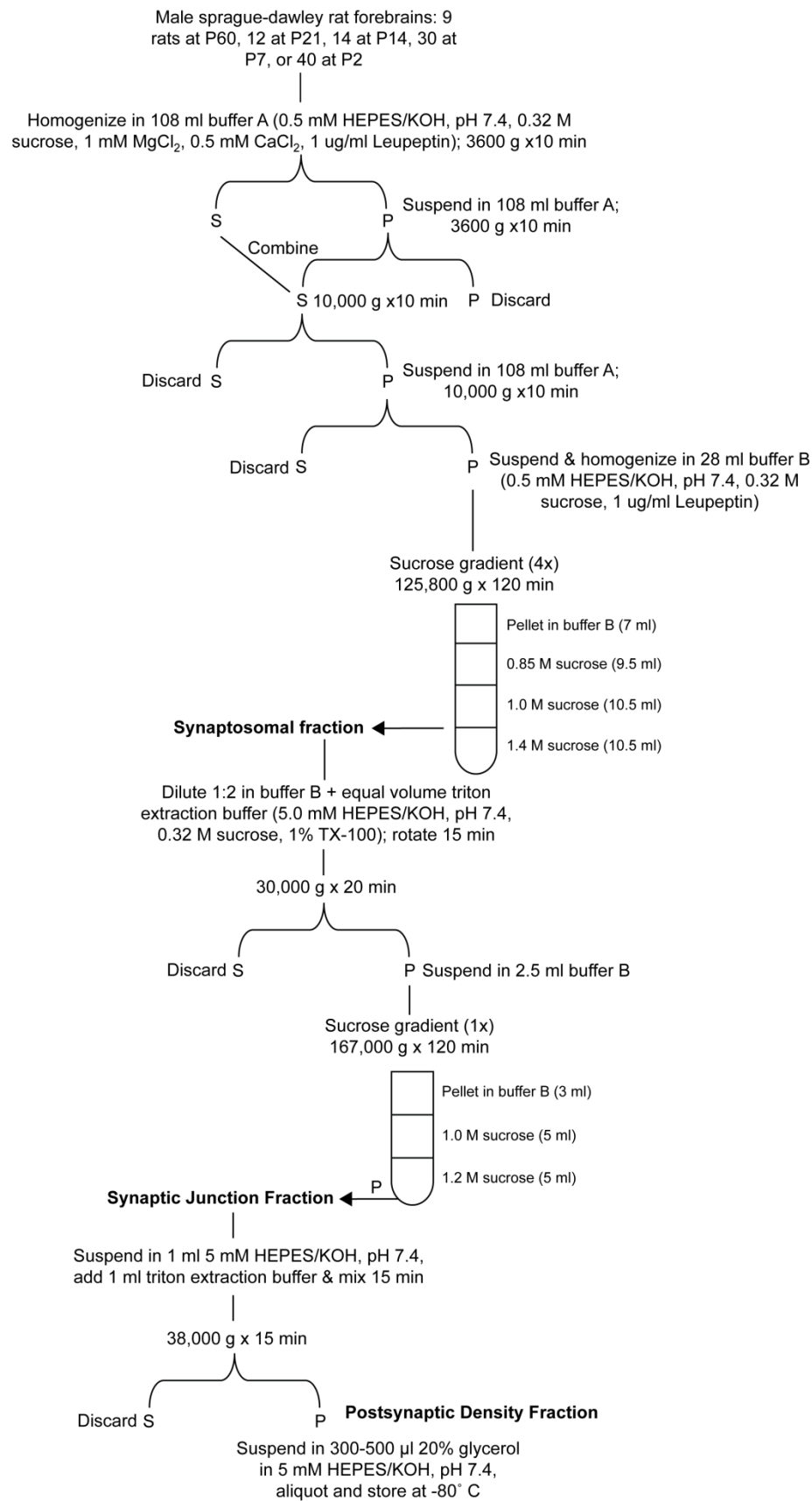


**Figure A.1.2. Isolation of PSDs from Forebrains throughout Development.**

Antibody	Species	Manufacturer	Catalog Number	WB Dilution	IG Dilution
pan-Shank	mouse	Neuromab	75-089	1:2500	1:20
GKAP	mouse	Neuromab	75-156	1:2500	1:20
CaMKII	rabbit	Millipore	04-1079	1:1000	1:20
pT286	rabbit	Phosphosolutions	p1005-386	1:1000	1:20
pT286	mouse	Thermo	MA1-047	1:2000	1:20
pT305	rabbit	Waxham Lab	--	1:1000	1:20
20S	mouse	Enzo Life Science	PW8195	1:1000	1:20

**Table A.1.1.** *Antibody Information for all Primary Antibodies Used.*

Information includes: the species in which antibody was raised, manufacturer, catalog number, Western blot dilution and immunogold labeling dilution.

### *A.1.3. Results*

#### *A.1.3.1. Hippocampal Slice PSDs*

In preliminary experiments to address activity-induced changes in PSD composition and structure, hippocampal slices were prepared, activated with potassium channel blocker TEA, and PSDs isolated, as described in the methodology section A.1.2.3. Hippocampal slices were frozen with liquid nitrogen immediately after the 10 min TEA treatment or control treatment, homogenized and PSDs isolated. Negative stain micrographs of control and TEA treated PSDs were collected to determine if there were gross morphologic differences associated with activation. As no obvious differences were evident in the gross morphology, the surface area was measured for 120 control and TEA treated hippocampal PSDs and average surface area calculated (Figure A.1.3). The mean surface area was  $0.27 \pm 0.02 \mu\text{m}^2$  for control hippocampal PSDs and  $0.18 \pm 0.01 \mu\text{m}^2$  for TEA treated, which was a statistically significant difference from the control PSDs. The peak surface areas, or mode, were also different with control hippocampal PSD surface area peaking at  $0.15 \mu\text{m}^2$  while the surface area for TEA treated hippocampal PSDs peaked at  $0.10 \mu\text{m}^2$  (Figure A.1.3). This trend is evident in the histograms of PSD surface area shown in Figure A.1.3, where the surface areas for TEA treated hippocampal PSDs were less variable, tending toward smaller surface areas. These results suggested that PSDs are smaller as a result of inducing neuronal activity, further supporting the idea that structural remodeling of PSDs underlies synaptic plasticity.

Immunogold labeling experiments were performed on the TEA treated and control hippocampal slice PSDs to directly test how PSD protein composition changes



in response to synaptic activity. Antibodies against  $\alpha$ CaMKII,  $\beta$ CaMKII, CaMKII phosphorylated at T286 (pT286), CaMKII phosphorylated at T305 (pT305), and a pan antibody against the Shank isoforms (pan-Shank) were employed in immunogold labeling experiments. The results of the immunogold labeling experiments are shown as gold/ $\mu\text{m}^2$  and gold/PSD in Table A.1.2. Secondary controls were included for the  $\alpha$ CaMKII immunogold labeling experiment. Sample size was 20 PSDs for each experiment, with the exception of pan-Shank, where 15 non-TEA treated PSDs and 8 TEA treated PSDs were imaged. There were no significant differences in labeling density when results were reported as gold over surface area; however when labeling densities were reported as gold per PSD there were statistical differences (Table A.1.2). These results are easily explained as the average surface areas of TEA treated PSDs were smaller than controls (Figure A.1.3).

Labeling densities for  $\beta$ CaMKII and pT305 were significantly different and greater for control non-treated PSDs than for TEA-treated PSDs (Table A.1.2). These results, while preliminary, were in part not expected; it is known that activation of synapses results in translocation of CaMKII to PSDs (Strack et al., 1997, Shen and Meyer, 1999, Dosemeci et al., 2001) and yet there was lower labeling for  $\beta$ CaMKII in TEA treated hippocampal slice PSDs compared to control and there was no difference in the level of  $\alpha$ CaMKII between groups (Table A.1.2). Additionally, it was expected that TEA treatment of hippocampal slices would result in increased phosphorylation of CaMKII at T286, suggesting activation of CaMKII (Miller and Kennedy, 1986), and yet the labeling densities for pT286 were the same in the control and TEA treated groups, while phosphorylation at T305 was increased in control PSDs (Table A.1.2). Phosphorylation of CaMKII at T305 is inhibitory autophosphorylation which prevents

CaMKII activation by  $\text{Ca}^{2+}$ /CaM (Hanson and Schulman, 1992) and is believed to be important in targeting CaMKII to the PSD (Elgersma et al., 2002). Therefore, while less inhibitory CaMKII phosphorylation was evident in PSDs which had been treated with potassium channel blocking TEA, translocation and activation of CaMKII was not evident as expected. The scaffold Shank is also thought to translocate to PSDs in an activity-dependent manner (Tao-Cheng et al., 2010), although the labeling of Shank between TEA treated PSDs and control PSDs was the same.

Additional PSDs were isolated from TEA treated hippocampal slices and control hippocampal slices, in order to assess the time course of molecular events occurring after TEA treatment. Hippocampal slices were homogenized either immediately after or 20 minutes after TEA or control treatment, and PSDs were then isolated and immunogold labeled (Table A.1.3). The first PSD preparation, termed A, was prepared 20 min after TEA treatment following the same isolation procedure as the hippocampal slice PSDs previously discussed, to test whether CaMKII translocation and recruitment of the proteasome could be detected 20 minute after synaptic activation. The results of the immunogold labeling experiments are shown in Table A.1.3. There were no differences in labeling densities of the proteasome between TEA-treated and control PSDs, however there was significantly more gold targeting  $\beta$ CaMKII per PSD in the TEA-treated group as compared to the control group (Table A.1.3), suggesting that activity-dependent CaMKII recruitment to the PSD can be detected within 20 min of activity induction.

Due to low PSD yields when isolating hippocampal slice PSD through three separate discontinuous sucrose gradients, the PSD isolation protocol for hippocampal slices was changed to a two sucrose gradient protocol, as described in section A.1.2.2.

Hippocampal slice PSD preps B and C were isolated through the two sucrose gradient protocol to increase yield and thus increasing the number of preliminary experiments possible. Slices from prep B were homogenized immediately after TEA treatment, while slices for prep C were homogenized 20 minutes after treatment. Preliminary immunogold assessment of protein density in the resulting PSDs is shown in Table A.1.3. Labeling for the lid of the proteasome was determined to be the same in control and TEA-treated hippocampal slice PSDs from prep B, the immediate time point. However, labeling for the proteasome lid was increased in TEA-treated hippocampal slice PSDs, as compared to control PSDs, isolated 20 minutes after activity induction (Table A.1.3). This result contradicts the proteasome labeling densities calculated for prep A which was also isolated 20 minutes after TEA-treatment, although the sample size for prep C was double the sample size for prep A (Table A.1.3). Labeling densities for  $\alpha$ CaMKII were calculated for preps B and C to test whether recruitment of CaMKII could be detected immediately after or 20 minutes after activity induction, and surprisingly there were no statistical differences in labeling for  $\alpha$ CaMKII between control and TEA-treated PSDs at either time point, also contradicting the increased labeling for  $\beta$ CaMKII measured in TEA-treated PSDs from prep A (Table A.1.3). Two immediate issues should be addressed before continuing this line of investigation. First, activity induction in hippocampal slices by TEA, although well documented (Lengyel et al., 2004), will need to be verified by electrophysiology, to ensure the efficacy of TEA-induced activity. Second, protocols will need adapted/optimized in order to increase the PSD yield. This is presently the major factor limiting this potentially revealing line of investigation. By increasing the yields, the time course of

molecular events related to activity-dependent PSD modification can be assessed by Western blots analysis in addition to immunogold labeling experiments.

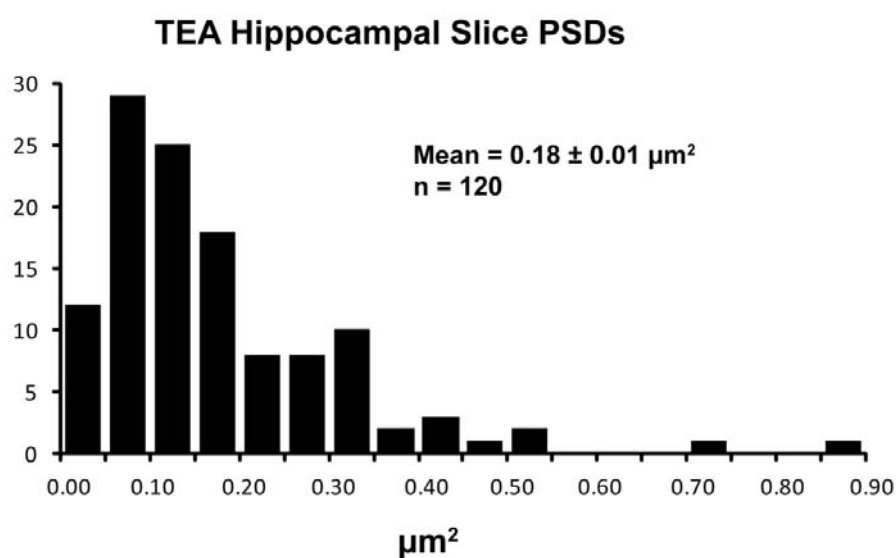
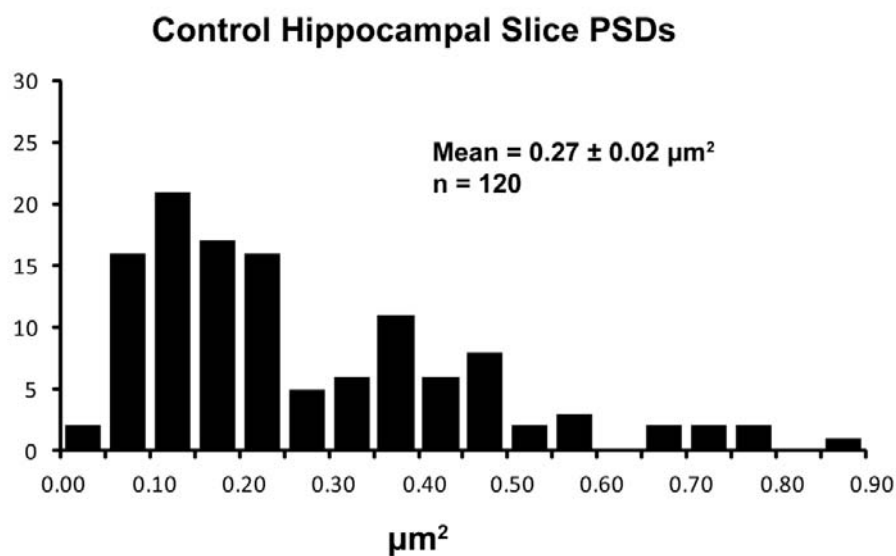


**Figure A.1.3.** *Histograms of Control and TEA Treated Hippocampal Slice PSD Surface Areas.*

The mean surface area for TEA PSDs was statistically smaller than control PSDs as determined if  $P < 0.05$  in two-tailed  $t$  tests. The peak surface areas for control and TEA treated PSDs were also different,  $0.15 \mu\text{m}^2$  and  $0.10 \mu\text{m}^2$  respectively.

	Gold/ $\mu\text{m}^2$		Gold/PSD	
	Control	TEA	Control	TEA
$\alpha\text{CaMKII}$	446 $\pm$ 45	472 $\pm$ 48	113 $\pm$ 18	103 $\pm$ 13
$\beta\text{CaMKII}$	238 $\pm$ 36	257 $\pm$ 57	<b>71 <math>\pm</math> 13</b>	31 $\pm$ 9
pT286	188 $\pm$ 32	227 $\pm$ 49	62 $\pm$ 12	35 $\pm$ 8
pT305	283 $\pm$ 35	346 $\pm$ 91	<b>93 <math>\pm</math> 15</b>	47 $\pm$ 13
pan-Shank	41 $\pm$ 7	45 $\pm$ 5	13 $\pm$ 3	12 $\pm$ 1

**Table A.1.2.** *Preliminary Immunogold Labeling for Hippocampal Slice PSDs treated with TEA and Controls.*

Secondary controls were only included for  $\alpha\text{CaMKII}$  experiment. Sample size was 20 PSDs for each experiment, with the exception of pan-Shank, where 15 non-TEA treated PSDs and 8 TEA treated PSDs were imaged.

	Slice Prep	PSD Group	Gold/ $\mu\text{m}^2$	Gold/PSD	Sample Size
<b>RPT6</b>	A (20 min)	Control	56 $\pm$ 6	23 $\pm$ 4	10
		TEA	55 $\pm$ 3	15 $\pm$ 3	10
	B (0 min)	Control	54 $\pm$ 8	14 $\pm$ 2	20
		TEA	60 $\pm$ 8	15 $\pm$ 2	20
	C (20 min)	Control	55 $\pm$ 9	9 $\pm$ 4	20
		TEA	69 $\pm$ 12	<b>22 <math>\pm</math> 4</b>	20
<b><math>\alpha</math>CaMKII</b>	B (0 min)	Control	126 $\pm$ 21	35 $\pm$ 8	20
		TEA	174 $\pm$ 21	59 $\pm$ 20	20
	C (20 min)	Control	134 $\pm$ 13	28 $\pm$ 4	20
		TEA	127 $\pm$ 11	29 $\pm$ 4	20
<b><math>\beta</math>CaMKII</b>	A (20 min)	Control	65 $\pm$ 9	25 $\pm$ 4	5
		TEA	121 $\pm$ 29	<b>47 <math>\pm</math> 7</b>	5

**Table A.1.3.** *Preliminary Immunogold Labeling for Control and TEA Treated PSDs Isolated from Hippocampal Slices.*

Statistical significance, indicated in bold, was defined as a p-value < 0.05, as determined through two-tailed *t* tests in Excel. TEA treatment was 10 minutes long for each preparation. Hippocampal Slices were homogenized 20 min after TEA treatment for preparations A and C while slices were homogenized immediately following TEA treatment for preparation B. Preparation A included the typical 3 gradients, while preps B and C were shortened to 2 gradients to increase PSD yield.

#### *A.1.3.2. PSDs during Development*

To continue investigating how the composition of PSDs changes and to investigate the potential role of the proteasome in PSD modifications, a developmental model was employed as the Waxham Lab has previously done (Swulius et al., 2010, Swulius et al., 2012). As a preliminary experiment PSDs isolated from rat forebrain at embryonic day 19 (E19), postnatal day 2 (P2), postnatal day 21 (P21) and postnatal day 60 (P60) were immunogold labeled for the lid of the proteasome to assess for its presence and differences in amount over development (Table A.1.4). A bar graph of the immunogold labeling results from Table A.1.4 is shown in Figure A.1.4 and developmental regulation of the proteasome at PSDs is clearly evident. Not only was the proteasome present within PSDs from all ages, labeling densities for the proteasome were significantly higher in PSDs from early development, peaking at P2, compared to PSDs isolated from P21 and adult, P60 animals, where the labeling was lowest.

Given this preliminary result, PSDs were also isolated from rat forebrains at two additional time points: P7 and P14, in order to further investigate the developmental profile of the proteasome system. Initial experiments focused on Western blotting to examine the developmental profile of CaMKII, the proteasome, and scaffolds targeted by the proteasome (Figure A.1.5). Western blots illustrated that PSD-95 increases in concentration as PSDs matured (Figure A.1.5), as previously shown by Western blot (Petrulia et al., 2005) and immunogold labeling (Swulius et al., 2010). Scaffolds Shank and GKAP were also determined to increase in concentration within PSDs through development (Figure A.1.5) confirming published work (Petrulia et al., 2005). However a subunit of the proteasome lid, RPT6, decreased in concentration within PSDs



throughout development (Figure A.1.5), confirming the preliminary immunogold labeling results (Table A.1.4). PSDs isolated at P2 contained 315% more proteasome lid subunits than PSDs isolated at P60, as quantified in ImageQuant (GE Healthcare). The 20S proteasome core was also found to be developmentally regulated in PSDs, and decreased in amount from P2 to P60 similar to RPT6 (Figure A.1.5). These results confirm that the proteasome is present in PSDs and that the presence of the proteasome within PSDs is developmentally regulated, supporting that the ubiquitin proteasome system plays a role in structural remodeling of the PSD during development and plausibly in response to synaptic activity.

CaMKII, the hypothesized target for the proteasome in PSDs, was also probed by Western blot and both  $\alpha$ CaMKII and  $\beta$ CaMKII increased from P2 to P60, with  $\beta$ CaMKII as the dominant isoform until P60, as previously reported (Sahyoun et al., 1985, Swulius et al., 2010). The blots in Figure A.1.5 demonstrate that at P2, phosphorylation of T286 is mainly on  $\beta$ CaMKII (the abundant isoform at that age), and interestingly decreases from P2 to P60, even though the abundance of  $\beta$ CaMKII increases through this time frame. Phosphorylation of  $\alpha$ CaMKII at Thr286 increases from P2 to P60, as does abundance of  $\alpha$ CaMKII (Figure A.1.5). Of all the known PSD associated proteins, the only ones identified to decrease through development are NR2B, SAP102 (Petrulia et al., 2005), and CaM (Swulius et al., 2010). Therefore the decreases seen by Western blot for the proteasome lid (RPT6), core (20s), and phosphorylation of  $\beta$ CaMKII at T286 is novel and suggests that the proteasome and phosphorylation of  $\beta$ CaMKII are correlated with the structural maturation of PSD.

	Gold/ $\mu\text{m}^2 \pm \text{SEM}$	Gold/PSD $\pm \text{SEM}$
<b>E19</b>	56 $\pm$ 17	29 $\pm$ 9
<b>P2</b>	86 $\pm$ 15	52 $\pm$ 11
<b>P21</b>	<b>19 <math>\pm</math> 3</b>	<b>10 <math>\pm</math> 2</b>
<b>P60</b>	<b>10 <math>\pm</math> 3</b>	5 $\pm$ 1

**Table A.1.4.** *Preliminary Immunogold Labeling for RPT6 on Developmental PSDs.*

Labeling densities for the proteasome significantly drop between P2 and P21. Statistical significance, indicated in bold, was defined as a p-value < 0.05, as determined through two-tailed t tests in Excel. N = 10. No secondary controls were performed.

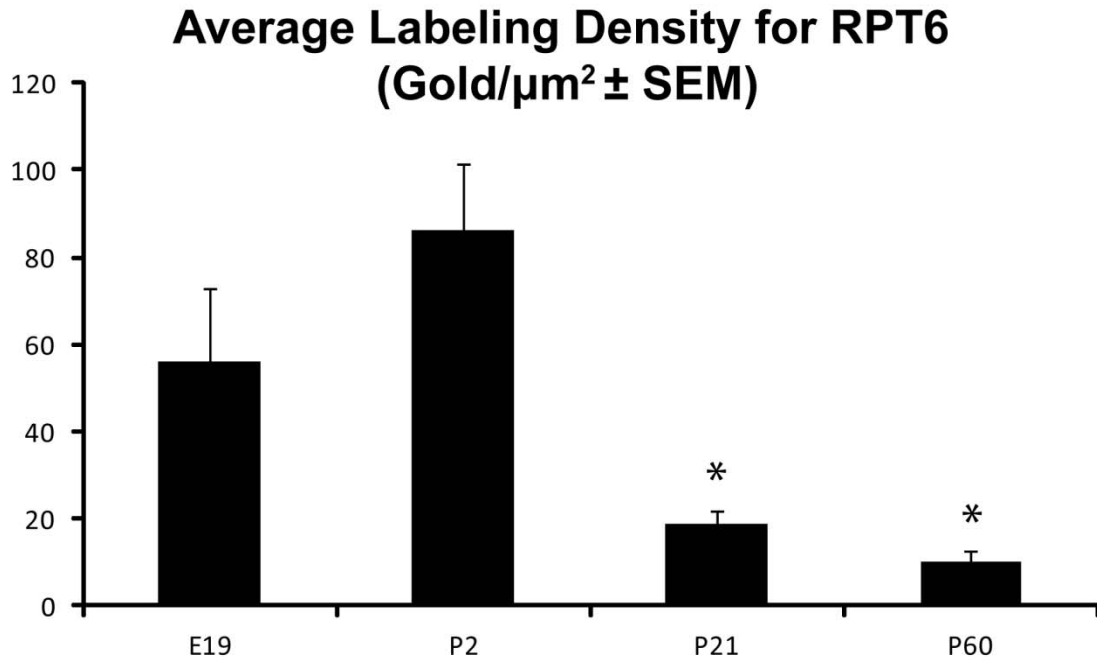


**Figure A.1.4.** *Preliminary Average Labeling Densities for RPT6 on Developmental PSDs.*

No secondary controls were performed. Labeling densities for the proteasome significantly drop between P2 and P21. Statistical significance, indicated with asterisks, was defined as a p-value < 0.05, as determined through two-tailed *t* tests in Excel. N = 10.

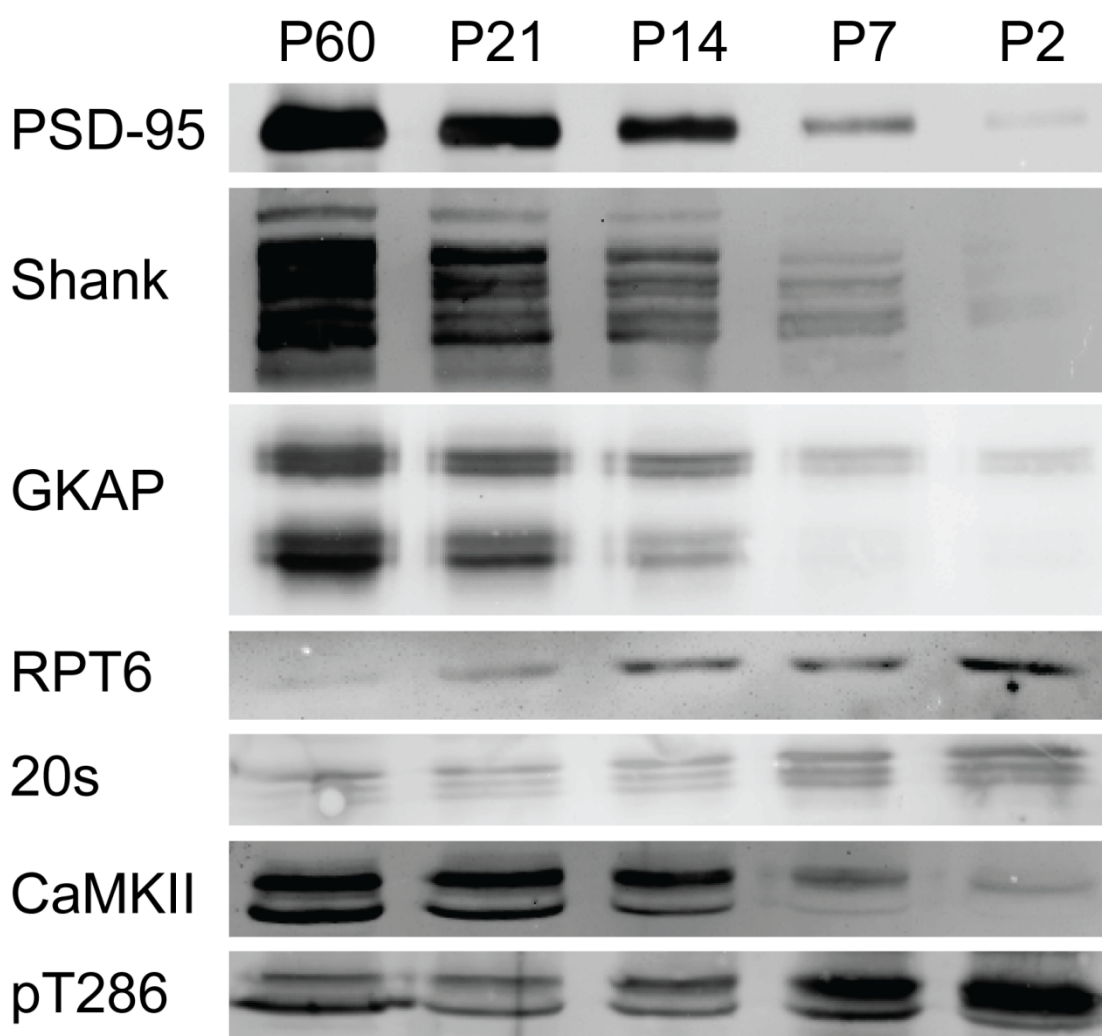


**Figure A.1.5.** *Western Blots Illustrating the Developmental Profiles for Select PSD Proteins.*

Lanes for each blot were loaded with equal protein, between 5 and 10  $\mu$ g, using 8%, 10% or 15% polyacrylamide gels. Multiple bands are expected to be detected by the primary antibodies against Shank, GKAP, 20S, CaMKII and pT286. The pan-Shank antibody recognizes the entire family of Shank proteins which range in from 120-240 kDa (Sheng and Kim, 2000). The GKAP antibody also recognizes multiple isoforms of the protein at 110 kDa and 120 kDa; others have reported this as well (Petrulia et al., 2005). The 20S antibody against the core of the proteasome recognizes multiple subunits which compose the 2000 kDa catalytic core of the proteasome, as shown by others (Djakovic et al., 2012). The CaMKII antibody and the pT286 antibody recognize both  $\alpha$ CaMKII (55 kDa) and  $\beta$ CaMKII (60 kDa).

#### *A.1.4. Discussion*

While some of the preliminary experiments described above were inconclusive, they have contributed forward progress toward the goal of building a dynamic structural model for the PSD. PSDs were isolated from chemically activated hippocampal slices to investigate how PSD composition changes in response to activity and whether the proteasome is recruited to PSDs in an activity-dependent manner. The ubiquitin proteasome system is predicted to degrade PSD proteins in response to activity providing structural flexibility for reorganization within PSDs supporting synaptic plasticity. The results of the preliminary hippocampal slice work are inconclusive; while there were some statistically significant differences between TEA-treated hippocampal slice PSDs and control hippocampal PSDs, activity induction by TEA requires verification and a consistent PSD isolation protocol that produces sufficient PSD yield for Western blotting.

As an alternative preparation to assess the potential role of the UPS in PSD structural remodeling, PSDs were isolated from different developmental time points. Western blots showed that both the proteasome lid and core were present at highest concentrations in PSDs isolated early in development and decreased as PSDs matured. This suggests that the proteasome plays an important role in the structural maturation of PSDs early in development, but its role diminishes as synapses mature. Interestingly the PSD scaffolds targeted by the proteasome including; PSD-95 (Colledge et al., 2003), Shank and GKAP (Ehlers, 2003), increase in concentration within PSDs through development, as shown here and as previously published (Sans et al., 2000, Petralia et al., 2005, Swulius et al., 2010) while the proteasome decreases in concentration. While it is possible that these trends are unrelated, it is interesting to

speculate that early in postnatal development while the concentrations of PSD scaffolds Shank, GKAP and PSD-95 are increasing there is steady proteasomal turnover of the scaffolds providing flexibility for the maturing PSD structure. To begin to test this hypothesis proteasome activity assays could be performed on PSD fractions from each developmental age to determine the level of proteasome activity in PSDs throughout development. Western blotting of PSD fractions could also be probed for monomeric ubiquitin and polyubiquitin chains specific for proteasomal degradation to test whether a subset of PSD components are being tagged for proteasomal degradation. Western blots dually probed for polyubiquitin K48, specific for proteasomal degradation (Miller and Gordon, 2005), and Shank, GKAP or PSD-95 could also determine which scaffolds are specifically targeted by the ubiquitin chains.

Phosphorylation of  $\beta$ CaMKII at T286 decreased within PSDs as animals matured, in contrast to the increasing concentration of  $\beta$ CaMKII. This is a novel result suggesting that the activation of  $\beta$ CaMKII is crucial for the structural maturation of PSD. This result makes sense in that early in development  $\beta$ CaMKII is the primary isoform of CaMKII expressed (Sahyoun et al., 1985), therefore the majority of phosphorylated CaMKII would be on  $\beta$ CaMKII. However the intensities of the pT286 band for  $\beta$ CaMKII at postnatal day 2 and 7 were significantly more intense than the pT286 bands for both  $\alpha$ CaMKII and  $\beta$ CaMKII together at any other age. This suggested that the majority of the CaMKII present within PSDs at P2 and P7 are in the autophosphorylated form. It is intriguing at such early postnatal time points that the majority of  $\beta$ CaMKII is active and very little  $\alpha$ CaMKII is present in PSDs, especially when translocation of  $\alpha$ CaMKII, not  $\beta$ CaMKII, is proposed to be required for activity-dependent recruitment of the proteasome to the PSD (Djakovic et al., 2009, Bingol et al., 2010). Additionally it is

believed that  $\alpha$ CaMKII acts as the anchoring protein for the proteasome into PSDs (Bingol et al., 2010) and phosphorylation of RPT6 by  $\alpha$ CaMKII increases proteasomal activity (Djakovic et al., 2012). Likely, the noted  $\beta$ CaMKII activation is crucial for other synaptic functions at these stages in development through its interactions with F-actin (Lin and Redmond, 2008, Sanabria et al., 2009, Hoffman et al., 2013), such as the formation and expansion of neurites (Fink et al., 2003) although these results suggest a further investigation of phosphorylated  $\beta$ CaMKII and the proteasome may be warranted. However, the low levels of  $\alpha$ CaMKII measured at P2 and P7 and the idea that  $\beta$ CaMKII is not acting as the proteasome scaffold suggests that CaMKII is plausibly not the primary proteasome scaffold molecule early in development. It would be of interest to affinity-purify proteasomes out of PSDs isolated from P2 and P7 rats and determine what PSD proteins precipitate alongside the proteasome.

In the future it will also be of interest to investigate the postsynaptic developmental profiles of deubiquitinases CLYD and UCH-L1. CLYD accumulates in PSDs in a manner that is dependent on synaptic translocation of CaMKII (Thein et al., 2014), similar to the proteasome. CaMKII can also phosphorylate CYLD promoting CYLD's deubiquitinase activity which preferentially removes ubiquitin from polyubiquitin lysine-63 chains, which target proteins for non-proteasomal pathways (Thein et al., 2014). The additional free ubiquitin is then available to form lysine-48 chains, specific for proteasomal degradation (Miller and Gordon, 2005). It is easy to visualize a model where in response to synaptic activity CaMKII enzymes translocate to PSDs, followed by the proteasome and CYLD, active CaMKII then phosphorylates CYLD, resulting in deubiquitination of lysine-63 chains, providing additionally ubiquitin for formation of lysine-48 chains, which are specific for proteasomal degradation. CaMKII also

phosphorylates proteasomes, increasing their activity, which then degrade PSD scaffolds tagged with lysine-48 chains. Ubiquitin carboxyl-terminal hydrolase L1, UCH-L1 also increases levels of free ubiquitin in response to synaptic activation (Cartier et al., 2009). Inhibition of UCH-L1 resulted in decreased free ubiquitin, changes in spine morphology and density (Cartier et al., 2009), and increased levels of PSD-95 (Xie et al., 2014). Additionally it is believed that  $\alpha$ -synuclein accumulation results from oxidative damage of UCH-L1 in both Alzheimer's disease and Parkinson's disease (Liu et al., 2002, Choi et al., 2004). A more thorough understanding of how these deubiquitinases are organized within PSDs, as well how they may influence PSD structure and function in response to activity and through development is warranted.



## **Appendix 2. *CaMKII Isoforms Differentially Impact the Structure of Actin Cytoskeleton***

### *A.2.1. Introduction*

This chapter of the appendix is based on previously published work which I contributed to. The methods, figures and figure legends, pertaining to my contribution, were taken directly, with permission, from the published work (Hoffman et al., 2013). The introduction, results and discussion are rewritten and focused on experiments to which I contributed.

$\alpha$ CaMKII and  $\beta$ CaMKII, the major PSD proteins, are well known for their role converting variable synaptic calcium signals into enzymatic activity crucial for learning and memory (Lisman et al., 2002, Colbran and Brown, 2004, Swulius and Waxham, 2008). There are four isoforms of the enzyme, produced from four separate genes (Hudmon and Schulman, 2002). The  $\alpha$  and  $\beta$  isoforms are present within neuronal tissue, comprising 1-2% of the total protein in the brain (Erondy and Kennedy, 1985), while the other isoforms of CaMKII,  $\gamma$  and  $\delta$  are present alongside the  $\alpha$  and  $\beta$  isoforms in cells across the body (Tobimatsu and Fujisawa, 1989, Swulius and Waxham, 2008). The structures of the isoforms are highly conserved with exception of a variable linker region, located on the C-terminal side of the shared regulatory domain (Gaertner et al., 2004a, Swulius and Waxham, 2008), as shown in Figure A.2.1.

This variable region is hypothesized to provide  $\beta$ CaMKII the unique ability to bind actin and regulate actin polymerization (Fink and Meyer, 2002, O'Leary et al., 2006, Okamoto et al., 2007, Lin and Redmond, 2009), which is important for molecular transport throughout cells and establishing cellular structure (Pollard and Cooper, 2009,

Michelot and Drubin, 2011, Schoenenberger et al., 2011).  $\beta$ CaMKII, unlike  $\alpha$ CaMKII, can bind monomeric G-actin, polymerized F-actin, and can bundle F-actin filaments due to the dodecameric structure (Ohta et al., 1986, Shen and Meyer, 1999, O'Leary et al., 2006, Okamoto et al., 2007, Sanabria et al., 2009). CaMKII exists as a mixed holoenzyme composed of 12 subunits of CaMKII isoforms in two stacked rings of 6 subunits each (Kolb et al., 1998, Brocke et al., 1999, Gaertner et al., 2004a). Therefore a holoenzyme composed entirely of  $\beta$ CaMKII could presumably bind up to 12 actin molecules, allowing the kinase to simultaneously bind F-actin and sequester G-actin, both regulating the rate of polymerization and providing a pool of G-actin available for polymerization (Hoffman et al., 2013). While many studies have analyzed the interactions of  $\beta$ CaMKII and actin (O'Leary et al., 2006, Okamoto et al., 2007, Sanabria et al., 2009), not much work has evaluated the interactions of the other CaMKII isoforms and actin. This is an important step in understanding how mixed CaMKII holoenzymes in neural and non-neural cells interact with and regulate the actin network.

The goal of the work, which is summarized in this appendix, was to investigate CaMKII isoform specific interactions with actin (for a full description see Hoffman et al., 2013). As described in the paper and performed by Dr. Laurel Hoffman, cosedimentation experiments between CaMKII isoforms and F-actin suggested that binding of F-actin is isoform specific with  $\beta$ CaMKII most avidly binding actin followed by  $\delta$ ,  $\gamma$ , and  $\alpha$  (Hoffman et al., 2013). All isoforms also inhibited actin polymerization and  $\text{Ca}^{2+}$ /CaM activation of each isoforms resulted in increased polymerization by freeing monomeric actin from binding to the kinase (Hoffman et al., 2013). In order to visualize

the interaction of each isoform with actin, I produced negative stain tomographic tilt series of the actin/CaMKII complexes and these results are described in this appendix.

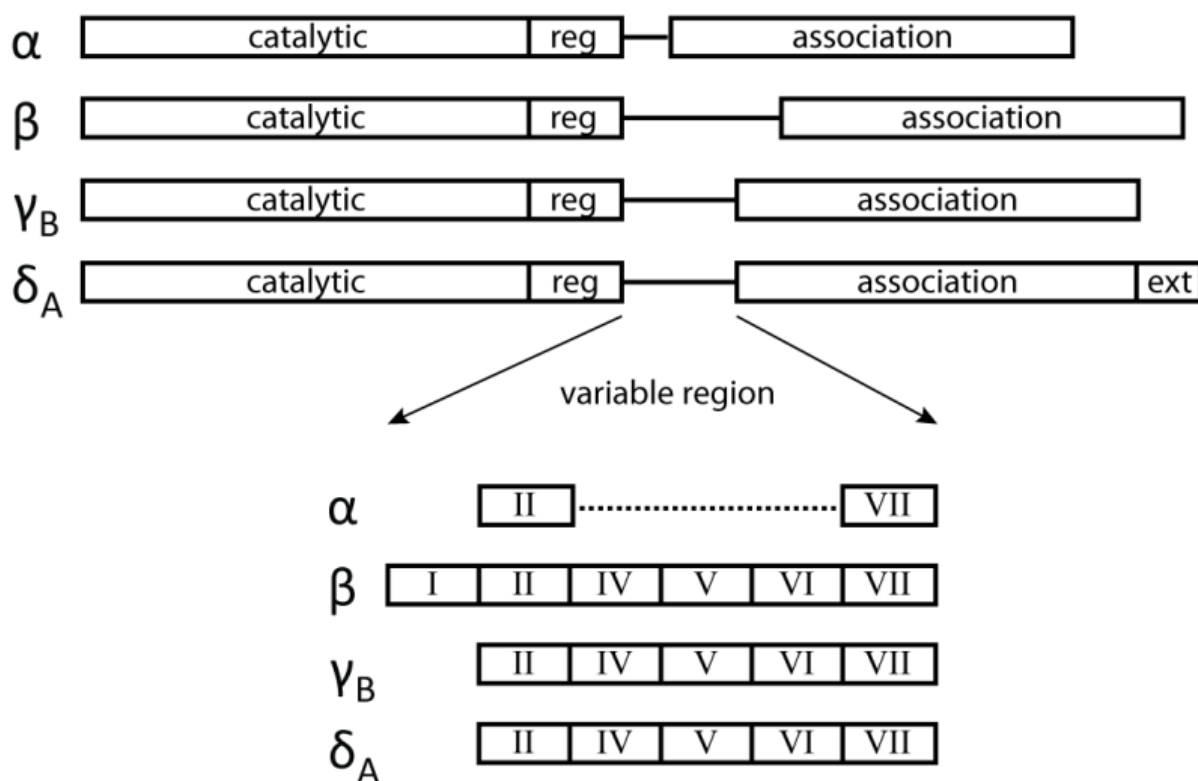


**Figure A.2.1.** Domain map of CaMKII isoforms

The domain structures of all CaMKII isoforms used in these studies are highly conserved in sequence in the catalytic, regulatory, and association domains. The only noteworthy differences are found in the variable linker region where alternative splicing results in inclusion or omission of various exons denoted by Roman numerals. Figure adapted from (Hoffman et al., 2013).

### *A.2.2. Methodology*

Tomographic tilt series were collected on a 300 kV FEI Polara F30 electron microscope equipped with a 4000 × 4000 pixel Tietz CCD camera. Series were collected at 39000x magnification with a 5 to 10  $\mu\text{m}$  defocus under a dose of  $\sim 400$  electrons/ $\text{\AA}^2$ . Images were collected at 2° tilt increments from  $-60^\circ$  to  $60^\circ$  with 2x binning that generated a final pixel size of 4.6  $\text{\AA}$ . Tilt series were aligned and tomographic reconstructions produced using Etomo, part of the IMOD software package (Mastronarde, 1997). Protein preparation, F-actin–CaMKII binding reactions, and grid preparation were completed by Dr. Laurel Hoffman, as published (Hoffman et al., 2013).

### *A.2.3. Results*

#### *A.2.3.1. Actin Filaments are Bundled Similarly by $\delta\text{CaMKII}$ and $\beta\text{CaMKII}$*

From negative stain micrographs it was evident that there were differences in the interaction of the CaMKII isoforms and F-actin (Figure A.2.2.A and Figure A.2.3.A), however the F-actin bundles formed by  $\delta\text{CaMKII}$  were structurally indistinguishable from those formed by  $\beta\text{CaMKII}$  (Figure A.2.2.A), which have been described previously (Okamoto et al., 2007, Sanabria et al., 2009). The F-actin bundles produced by both  $\delta\text{CaMKII}$  and  $\beta\text{CaMKII}$  were approximately 100 nm wide and composed of tightly packed slightly twisting parallel actin filaments (Figure A.2.2.A). The bundles were also quite variable in length with some extending up to 15  $\mu\text{m}$  in length.

Negative stain electron tomography was employed to further investigate the structure of the F-actin bundles. Cross-sections, approximately 10 nm thick, through final tomographic reconstructions of actin bundles are shown for  $\beta$ CaMKII and  $\delta$ CaMKII in Figure A.2.2.B, and individual holoenzymes are easily visible within the tightly packed actin bundles. For both  $\beta$ CaMKII and  $\delta$ CaMKII, the actin filaments were organized in a fairly parallel manner, with some twisting, and bundles were approximately 50-100 nm thick. Close-up views of the same reconstructions shown in Figure A.2.2.B are shown in C of Figure A.2.2 to highlight individual CaMKII holoenzymes bridging actin filaments. Interestingly, bundles formed by both  $\beta$ CaMKII and  $\delta$ CaMKII also appeared to have blunt ends rather than tapered ends (Figure A.2.2.D), suggesting that the manner of packing produced by both isoforms did not support extension of individual filaments beyond a certain length. Presumably the kinase provided stability for the individual filaments; therefore the individual filaments could only extend so far past the last kinase, although it is possible that filaments extending past the end of the bundle were severed during grid preparation.

#### *A.2.3.2. $\gamma$ CaMKII Uniquely Bundles Actin Filaments*

The F-actin bundles formed by  $\gamma$ CaMKII deviated in structure from the bundles produced by both  $\delta$ CaMKII and  $\beta$ CaMKII (Figure A.2.2.A and Figure A.2.3.A). The left panel in Figure A.2.3.A shows a negative stain micrograph of a typical  $\gamma$ CaMKII actin bundle, which were less consistent in width and 2-3 times wider than the  $\beta$ CaMKII and  $\delta$ CaMKII bundles. The  $\gamma$ CaMKII bundles were wide and flat with branching in both the x and y dimensions (Figure A.2.3.), and a layered structure was evident from the

tomographic reconstructions (Figure A.2.3). Individual holoenzymes were visibly interacting with actin (Figure A.2.3.A right panel) in the  $\gamma$ CaMKII bundles, which appeared to be composed of a single layer of filamentous actin sandwiched between two layers of CaMKII (Figure A.2.3), roughly 40 nm thick compared to the 50-100 nm thickness of the  $\beta$ CaMKII and  $\delta$ CaMKII bundles. Representative tomographic slices through the layers of one bundle are shown in Figure A.2.3.C and a cartoon illustration comparing the layered  $\gamma$ CaMKII bundle to the rod-like  $\delta$  and  $\beta$ CaMKII is included in Figure A.2.3.B.

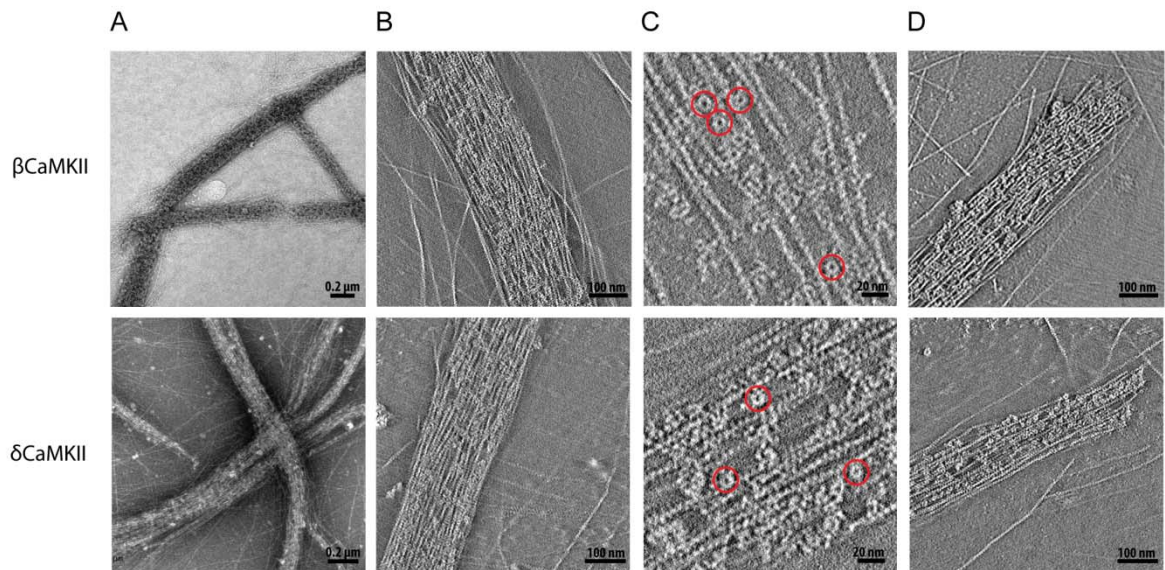


**Figure A.2.2.** *Structural Analysis of Actin Bundles Formed in the Presence of the  $\beta$  and  $\delta$  Isoforms of CaMKII (Hoffman et al., 2013).*

A) Left panels illustrate representative 2D projections of low power electron micrographs of negative stained F-actin in the presence of  $\beta$  (upper) and  $\delta$  (lower) isoforms ( $n > 5$ ). B) Panels show  $\sim 10$  nm thick slices of two tomographic reconstructions to illustrate packing of  $\beta$  and  $\delta$  CaMKII holoenzyme molecules within bundles. C) Several CaMKII holoenzyme molecules are highlighted by red circles in a zoomed in region of a representative slice from the same reconstructions shown in Panel B. D) The right panels show  $\sim 10$  nm slices through two different tomographic reconstructions that illustrate examples of blunt ended bundles formed with  $\beta$  or  $\delta$  CaMKII (Hoffman et al., 2013).



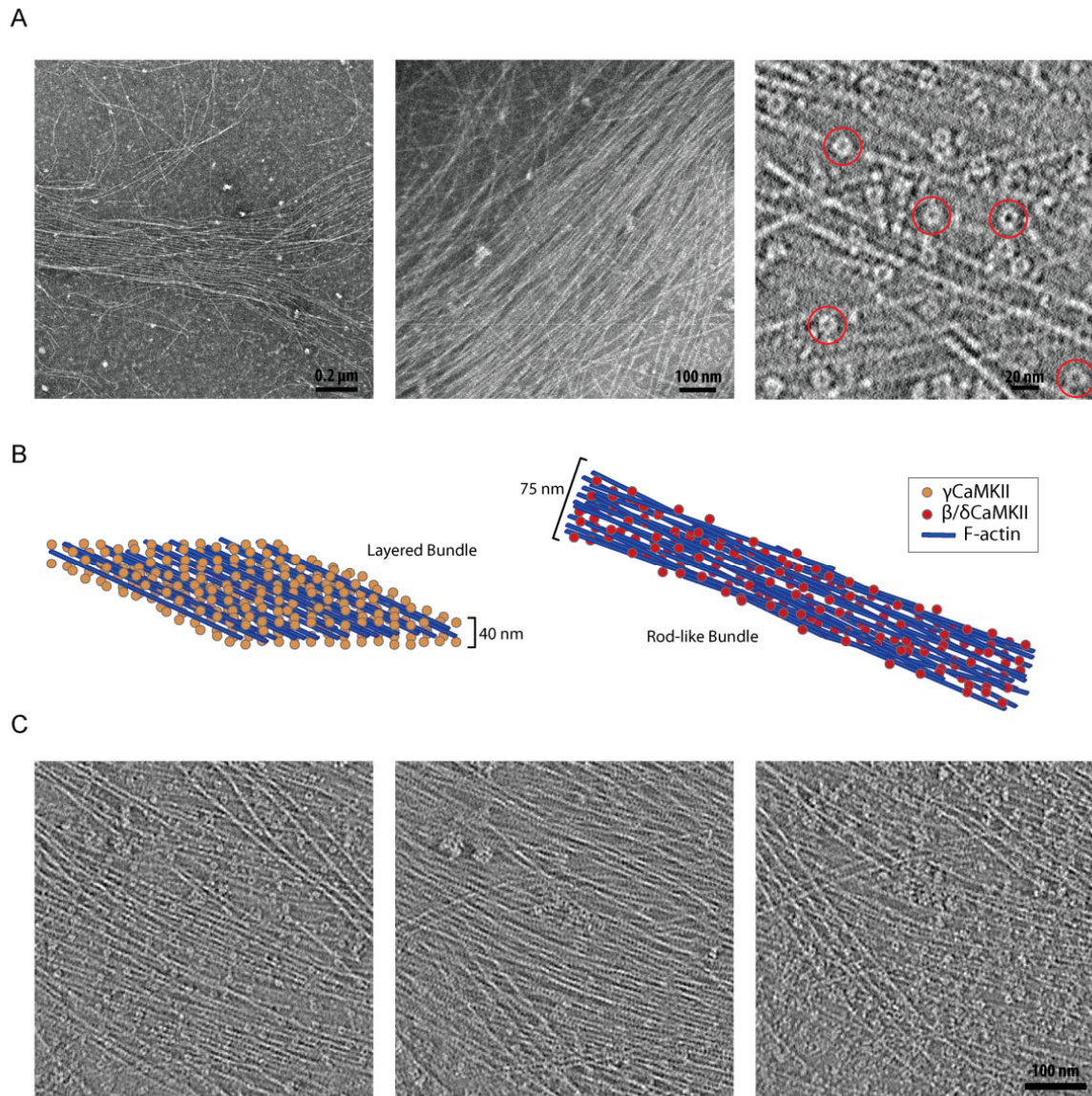


**Figure A.2.3.** *Structure of Layered  $\gamma$ CaMKII Bundle (Hoffman et al., 2013).*

A) Left and center panels show representative electron micrographs of F-actin bundles in the presence of  $\gamma$ CaMKII ( $n = 6$ ). The right panel illustrates a  $\sim 10$  nm slice from a tomographic reconstruction where several CaMKII holoenzyme molecules are highlighted in red circles. B) A cartoon illustrates structural differences between the layered bundles observed in the presence of the  $\gamma$  isoform (orange spheres) and the rod-like bundles observed in the presence of the  $\beta$  or  $\delta$  isoforms (red spheres). C)  $\sim 10$  nm slices from tomograms illustrate the top, center, and bottom z sections of the layered bundle in the left, center, and right panels, respectively (Hoffman et al., 2013).

#### *A.2.4. Discussion*

The low resolution structure of the different CaMKII isoforms was similar as previously published (Gaertner et al., 2004a), however the differential actin bundle structures indicate that there are isoform-specific differences in the interactions between CaMKII and actin. The electron microscopic and cosedimentation results suggest that there is a correlation between actin bundle structure and actin binding capacity. Each of the CaMKII isoforms did indeed bind actin, with the  $\beta$ ,  $\delta$ , and  $\gamma$  isoforms forming higher ordered structures with F-actin.  $\alpha$ CaMKII showed the lowest actin binding capacity and did not form detectable actin bundles. Interestingly, the bundles formed by F-actin and  $\gamma$ CaMKII structurally diverged from the bundles formed by  $\beta$ CaMKII and  $\delta$ CaMKII. The wide and flat bundles produced by  $\gamma$ CaMKII appeared limited in the z dimension, while the bundles formed by  $\beta$ CaMKII and  $\delta$ CaMKII bundles appeared limited in the x and y dimensions, as they were very consistent in width and thickness. It is plausible that flexibility of the variable linker region constrains the three-dimensional organization of the actin bundles and identification of the actin binding domain will be crucial for fully understanding the isoform specific differences in actin binding and bundling. These results are significant step toward our understanding the complex multifaceted regulation of the actin network by CaMKII holoenzymes composed of varying ratios of CaMKII isoforms.

## Bibliography

- Al-Hallaq RA, Yasuda RP, Wolfe BB (2001) Enrichment of N-methyl-D-aspartate NR1 splice variants and synaptic proteins in rat postsynaptic densities. *J Neurochem* 77:110-119.
- Allison DW, Gelfand VI, Spector I, Craig AM (1998) Role of actin in anchoring postsynaptic receptors in cultured hippocampal neurons: differential attachment of NMDA versus AMPA receptors. *J Neurosci* 18:2423-2436.
- Aronowski J, Grotta JC, Waxham MN (1992) Ischemia-induced translocation of  $\text{Ca}^{2+}$ /calmodulin-dependent protein kinase II: potential role in neuronal damage. *J Neurochem* 58:1743-1753.
- Arons MH, Thynne CJ, Grabrucker AM, Li D, Schoen M, Cheyne JE, Boeckers TM, Montgomery JM, Garner CC (2012) Autism-Associated Mutations in ProSAP2/Shank3 Impair Synaptic Transmission and Neurexin-Neuroligin-Mediated Transsynaptic Signaling. *J Neurosci* 32:14966-14978.
- Baron MK, Boeckers TM, Vaida B, Faham S, Gingery M, Sawaya MR, Salyer D, Gundelfinger ED, Bowie JU (2006) An architectural framework that may lie at the core of the postsynaptic density. *Science* 311:531-535.
- Berkel S, Marshall CR, Weiss B, Howe J, Roeth R, Moog U, Endris V, Roberts W, Szatmari P, Pinto D, Bonin M, Riess A, Engels H, Sprengel R, Scherer SW, Rappold GA (2010) Mutations in the SHANK2 synaptic scaffolding gene in autism spectrum disorder and mental retardation. *Nature genetics* 42:489-491.
- Bingol B, Schuman EM (2006) Activity-dependent dynamics and sequestration of proteasomes in dendritic spines. *Nature* 441:1144-1148.

- Bingol B, Wang CF, Arnott D, Cheng D, Peng J, Sheng M (2010) Autophosphorylated CaMKIIalpha acts as a scaffold to recruit proteasomes to dendritic spines. *Cell* 140:567-578.
- Blanpied TA, Kerr JM, Ehlers MD (2008) Structural plasticity with preserved topology in the postsynaptic protein network. *Proc Natl Acad Sci U S A* 105:12587-12592.
- Blomberg F, Cohen RS, Siekevitz P (1977) The structure of postsynaptic densities isolated from dog cerebral cortex. II. Characterization and arrangement of some of the major proteins within the structure. *J Cell Biol* 74:204-225.
- Boeckers TM, Kreutz MR, Winter C, Zuschratter W, Smalla KH, Sanmarti-Vila L, Wex H, Langnaese K, Bockmann J, Garner CC, Gundelfinger ED (1999a) Proline-rich synapse-associated protein-1/cortactin binding protein 1 (ProSAP1/CortBP1) is a PDZ-domain protein highly enriched in the postsynaptic density. *J Neurosci* 19:6506-6518.
- Boeckers TM, Winter C, Smalla KH, Kreutz MR, Bockmann J, Seidenbecher C, Garner CC, Gundelfinger ED (1999b) Proline-rich synapse-associated proteins ProSAP1 and ProSAP2 interact with synaptic proteins of the SAPAP/GKAP family. *Biochem Biophys Res Commun* 264:247-252.
- Brocke L, Chiang LW, Wagner PD, Schulman H (1999) Functional implications of the subunit composition of neuronal CaM kinase II. *J Biol Chem* 274:22713-22722.
- Carlin RK, Grab DJ, Cohen RS, Siekevitz P (1980) Isolation and characterization of postsynaptic densities from various brain regions: enrichment of different types of postsynaptic densities. *J Cell Biol* 86:831-845.

- Cartier AE, Djakovic SN, Salehi A, Wilson SM, Masliah E, Patrick GN (2009) Regulation of synaptic structure by ubiquitin C-terminal hydrolase L1. *J Neurosci* 29:7857-7868.
- Chen X, Nelson CD, Li X, Winters CA, Azzam R, Sousa AA, Leapman RD, Gainer H, Sheng M, Reese TS (2011) PSD-95 is required to sustain the molecular organization of the postsynaptic density. *J Neurosci* 31:6329-6338.
- Chen X, Vinade L, Leapman RD, Petersen JD, Nakagawa T, Phillips TM, Sheng M, Reese TS (2005) Mass of the postsynaptic density and enumeration of three key molecules. *Proc Natl Acad Sci U S A* 102:11551-11556.
- Chen X, Winters C, Azzam R, Li X, Galbraith JA, Leapman RD, Reese TS (2008) Organization of the core structure of the postsynaptic density. *Proc Natl Acad Sci U S A* 105:4453-4458.
- Cheng D, Hoogenraad CC, Rush J, Ramm E, Schlager MA, Duong DM, Xu P, Wijayawardana SR, Hanfelt J, Nakagawa T, Sheng M, Peng J (2006) Relative and absolute quantification of postsynaptic density proteome isolated from rat forebrain and cerebellum. *Mol Cell Proteomics* 5:1158-1170.
- Chklovskii DB, Mel BW, Svoboda K (2004) Cortical rewiring and information storage. *Nature* 431:782-788.
- Choi J, Levey AI, Weintraub ST, Rees HD, Gearing M, Chin LS, Li L (2004) Oxidative modifications and down-regulation of ubiquitin carboxyl-terminal hydrolase L1 associated with idiopathic Parkinson's and Alzheimer's diseases. *J Biol Chem* 279:13256-13264.
- Cingolani LA, Goda Y (2008) Actin in action: the interplay between the actin cytoskeleton and synaptic efficacy. *Nat Rev Neurosci* 9:344-356.

- Coba MP, Pocklington AJ, Collins MO, Kopanitsa MV, Uren RT, Swamy S, Croning MD, Choudhary JS, Grant SG (2009) Neurotransmitters drive combinatorial multistate postsynaptic density networks. *Science signaling* 2:ra19.
- Cohen RS, Blomberg F, Berzins K, Siekevitz P (1977) The structure of postsynaptic densities isolated from dog cerebral cortex. I. Overall morphology and protein composition. *J Cell Biol* 74:181-203.
- Cohen RS, Siekevitz P (1978) Form of the postsynaptic density. A serial section study. *J Cell Biol* 78:36-46.
- Colbran RJ (2004) Targeting of calcium/calmodulin-dependent protein kinase II. *Biochem J* 378:1-16.
- Colbran RJ, Brown AM (2004) Calcium/calmodulin-dependent protein kinase II and synaptic plasticity. *Curr Opin Neurobiol* 14:318-327.
- Cole AA, Dosemeci A, Reese TS (2010) Co-segregation of AMPA receptors with G(M1) ganglioside in synaptosomal membrane subfractions. *Biochem J* 427:535-540.
- Colledge M, Snyder EM, Crozier RA, Soderling JA, Jin Y, Langeberg LK, Lu H, Bear MF, Scott JD (2003) Ubiquitination regulates PSD-95 degradation and AMPA receptor surface expression. *Neuron* 40:595-607.
- Collins MO, Husi H, Yu L, Brandon JM, Anderson CN, Blackstock WP, Choudhary JS, Grant SG (2006) Molecular characterization and comparison of the components and multiprotein complexes in the postsynaptic proteome. *J Neurochem* 97 Suppl 1:16-23.

- Collins MO, Yu L, Coba MP, Husi H, Campuzano I, Blackstock WP, Choudhary JS, Grant SG (2005) Proteomic analysis of in vivo phosphorylated synaptic proteins. *J Biol Chem* 280:5972-5982.
- Cotman CW, Banker G, Churchill L, Taylor D (1974) Isolation of postsynaptic densities from rat brain. *J Cell Biol* 63:441-455.
- Craven SE, El-Husseini AE, Brecht DS (1999) Synaptic targeting of the postsynaptic density protein PSD-95 mediated by lipid and protein motifs. *Neuron* 22:497-509.
- De Koninck P, Schulman H (1998) Sensitivity of CaM kinase II to the frequency of  $\text{Ca}^{2+}$  oscillations. *Science* 279:227-230.
- DeGiorgis JA, Galbraith JA, Dosemeci A, Chen X, Reese TS (2006) Distribution of the scaffolding proteins PSD-95, PSD-93, and SAP97 in isolated PSDs. *Brain Cell Biol* 35:239-250.
- Delint-Ramirez I, Fernandez E, Bayes A, Kicsi E, Komiyama NH, Grant SG (2010) In vivo composition of NMDA receptor signaling complexes differs between membrane subdomains and is modulated by PSD-95 and PSD-93. *J Neurosci* 30:8162-8170.
- Djakovic SN, Marquez-Lona EM, Jakawich SK, Wright R, Chu C, Sutton MA, Patrick GN (2012) Phosphorylation of Rpt6 regulates synaptic strength in hippocampal neurons. *J Neurosci* 32:5126-5131.
- Djakovic SN, Schwarz LA, Barylko B, DeMartino GN, Patrick GN (2009) Regulation of the proteasome by neuronal activity and calcium/calmodulin-dependent protein kinase II. *J Biol Chem* 284:26655-26665.

- Dosemeci A, Jaffe H Regulation of phosphorylation at the postsynaptic density during different activity states of Ca<sup>2+</sup>/calmodulin-dependent protein kinase II. *Biochem Biophys Res Commun* 391:78-84.
- Dosemeci A, Makusky AJ, Jankowska-Stephens E, Yang X, Slotta DJ, Markey SP (2007) Composition of the synaptic PSD-95 complex. *Mol Cell Proteomics* 6:1749-1760.
- Dosemeci A, Tao-Cheng JH, Vinade L, Jaffe H (2006) Preparation of postsynaptic density fraction from hippocampal slices and proteomic analysis. *Biochem Biophys Res Commun* 339:687-694.
- Dosemeci A, Tao-Cheng JH, Vinade L, Winters CA, Pozzo-Miller L, Reese TS (2001) Glutamate-induced transient modification of the postsynaptic density. *Proc Natl Acad Sci U S A* 98:10428-10432.
- Du Y, Weed SA, Xiong WC, Marshall TD, Parsons JT (1998) Identification of a novel cortactin SH3 domain-binding protein and its localization to growth cones of cultured neurons. *Molecular and cellular biology* 18:5838-5851.
- Durand CM, Betancur C, Boeckers TM, Bockmann J, Chaste P, Fauchereau F, Nygren G, Rastam M, Gillberg IC, Anckarsater H, Sponheim E, Goubran-Botros H, Delorme R, Chabane N, Mouren-Simeoni MC, de Mas P, Bieth E, Roge B, Heron D, Burglen L, Gillberg C, Leboyer M, Bourgeron T (2007) Mutations in the gene encoding the synaptic scaffolding protein SHANK3 are associated with autism spectrum disorders. *Nature genetics* 39:25-27.
- Ehlers MD (2003) Activity level controls postsynaptic composition and signaling via the ubiquitin-proteasome system. *Nat Neurosci* 6:231-242.



- El-Husseini AE, Schnell E, Chetkovich DM, Nicoll RA, Brecht DS (2000) PSD-95 involvement in maturation of excitatory synapses. *Science* 290:1364-1368.
- El-Husseini AE, Schnell E, Dakoji S, Sweeney N, Zhou Q, Prange O, Gauthier-Campbell C, Aguilera-Moreno A, Nicoll RA, Brecht DS (2002) Synaptic strength regulated by palmitate cycling on PSD-95. *Cell* 108:849-863.
- Elgersma Y, Fedorov NB, Ikonen S, Choi ES, Elgersma M, Carvalho OM, Giese KP, Silva AJ (2002) Inhibitory autophosphorylation of CaMKII controls PSD association, plasticity, and learning. *Neuron* 36:493-505.
- Erondy NE, Kennedy MB (1985) Regional distribution of type II Ca<sup>2+</sup>/calmodulin-dependent protein kinase in rat brain. *J Neurosci* 5:3270-3277.
- Fera A, Dosemeci A, Sousa AA, Yang C, Leapman RD, Reese TS (2012) Direct visualization of CaMKII at postsynaptic densities by electron microscopy tomography. *J Comp Neurol* 520:4218-4225.
- Fink CC, Bayer KU, Myers JW, Ferrell JE, Jr., Schulman H, Meyer T (2003) Selective regulation of neurite extension and synapse formation by the beta but not the alpha isoform of CaMKII. *Neuron* 39:283-297.
- Fink CC, Meyer T (2002) Molecular mechanisms of CaMKII activation in neuronal plasticity. *Curr Opin Neurobiol* 12:293-299.
- Foa L, Gasperini R (2009) Developmental roles for Homer: more than just a pretty scaffold. *J Neurochem* 108:1-10.
- Fuster JM (2009) Cortex and memory: emergence of a new paradigm. *Journal of cognitive neuroscience* 21:2047-2072.
- Gaertner TR, Kolodziej SJ, Wang D, Kobayashi R, Koomen JM, Stoops JK, Waxham MN (2004a) Comparative analyses of the three-dimensional structures and

- enzymatic properties of alpha, beta, gamma and delta isoforms of Ca<sup>2+</sup>-calmodulin-dependent protein kinase II. *J Biol Chem* 279:12484-12494.
- Gaertner TR, Putkey JA, Waxham MN (2004b) RC3/Neurogranin and Ca<sup>2+</sup>/calmodulin-dependent protein kinase II produce opposing effects on the affinity of calmodulin for calcium. *J Biol Chem* 279:39374-39382.
- Gauthier J, Spiegelman D, Piton A, Lafreniere RG, Laurent S, St-Onge J, Lapointe L, Hamdan FF, Cossette P, Mottron L, Fombonne E, Joober R, Marineau C, Drapeau P, Rouleau GA (2009) Novel de novo SHANK3 mutation in autistic patients. *American journal of medical genetics Part B, Neuropsychiatric genetics : the official publication of the International Society of Psychiatric Genetics* 150B:421-424.
- Gong Y, Lippa CF, Zhu J, Lin Q, Rosso AL (2009) Disruption of glutamate receptors at Shank-postsynaptic platform in Alzheimer's disease. *Brain research* 1292:191-198.
- Grabrucker AM, Knight MJ, Proepper C, Bockmann J, Joubert M, Rowan M, Nienhaus GU, Garner CC, Bowie JU, Kreutz MR, Gundelfinger ED, Boeckers TM (2011a) Concerted action of zinc and ProSAP/Shank in synaptogenesis and synapse maturation. *The EMBO journal* 30:569-581.
- Grabrucker AM, Rowan M, Garner CC (2011b) Brain-Delivery of Zinc-Ions as Potential Treatment for Neurological Diseases: Mini Review. *Drug delivery letters* 1:13-23.
- Grabrucker AM, Schmeisser MJ, Schoen M, Boeckers TM (2011c) Postsynaptic ProSAP/Shank scaffolds in the cross-hair of synaptopathies. *Trends in cell biology* 21:594-603.

- Grabrucker AM, Schmeisser MJ, Udvardi PT, Arons M, Schoen M, Woodling NS, Andreasson KI, Hof PR, Buxbaum JD, Garner CC, Boeckers TM (2011d) Amyloid beta protein-induced zinc sequestration leads to synaptic loss via dysregulation of the ProSAP2/Shank3 scaffold. *Molecular neurodegeneration* 6:65.
- Gray EG (1959a) Axo-somatic and axo-dendritic synapses of the cerebral cortex: an electron microscope study. *Journal of anatomy* 93:420-433.
- Gray EG (1959b) Electron microscopy of synaptic contacts on dendrite spines of the cerebral cortex. *Nature* 183:1592-1593.
- Gray EG (1961) The granule cells, mossy synapses and Purkinje spine synapses of the cerebellum: light and electron microscope observations. *Journal of anatomy* 95:345-356.
- Groc L, Heine M, Cognet L, Brickley K, Stephenson FA, Lounis B, Choquet D (2004) Differential activity-dependent regulation of the lateral mobilities of AMPA and NMDA receptors. *Nat Neurosci* 7:695-696.
- Hanson PI, Schulman H (1992) Inhibitory autophosphorylation of multifunctional  $\text{Ca}^{2+}$ /calmodulin-dependent protein kinase analyzed by site-directed mutagenesis. *J Biol Chem* 267:17216-17224.
- Harris KM, Jensen FE, Tsao B (1992) Three-dimensional structure of dendritic spines and synapses in rat hippocampus (CA1) at postnatal day 15 and adult ages: implications for the maturation of synaptic physiology and long-term potentiation. *J Neurosci* 12:2685-2705.

- Harris KM, Stevens JK (1988) Dendritic spines of rat cerebellar Purkinje cells: serial electron microscopy with reference to their biophysical characteristics. *J Neurosci* 8:4455-4469.
- Harris KM, Stevens JK (1989) Dendritic spines of CA 1 pyramidal cells in the rat hippocampus: serial electron microscopy with reference to their biophysical characteristics. *J Neurosci* 9:2982-2997.
- Harris KM, Weinberg RJ (2012) Ultrastructure of synapses in the mammalian brain. *Cold Spring Harbor perspectives in biology* 4.
- Hasan MT, Hernandez-Gonzalez S, Dogbevia G, Trevino M, Bertocchi I, Gruart A, Delgado-Garcia JM (2013) Role of motor cortex NMDA receptors in learning-dependent synaptic plasticity of behaving mice. *Nature communications* 4:2258.
- Hayashi MK, Tang C, Verpelli C, Narayanan R, Stearns MH, Xu RM, Li H, Sala C, Hayashi Y (2009) The postsynaptic density proteins Homer and Shank form a polymeric network structure. *Cell* 137:159-171.
- Hell JW (2014) CaMKII: claiming center stage in postsynaptic function and organization. *Neuron* 81:249-265.
- Hoffman L, Farley MM, Waxham MN (2013) Calcium-calmodulin-dependent protein kinase II isoforms differentially impact the dynamics and structure of the actin cytoskeleton. *Biochemistry* 52:1198-1207.
- Hudmon A, Lebel E, Roy H, Sik A, Schulman H, Waxham MN, De Koninck P (2005) A mechanism for  $\text{Ca}^{2+}$ /calmodulin-dependent protein kinase II clustering at synaptic and nonsynaptic sites based on self-association. *J Neurosci* 25:6971-6983.

- Hudmon A, Schulman H (2002) Neuronal CA<sup>2+</sup>/calmodulin-dependent protein kinase II: the role of structure and autoregulation in cellular function. *Annu Rev Biochem* 71:473-510.
- Inoue A, Okabe S (2003) The dynamic organization of postsynaptic proteins: translocating molecules regulate synaptic function. *Curr Opin Neurobiol* 13:332-340.
- Inoue N, Nakao H, Migishima R, Hino T, Matsui M, Hayashi F, Nakao K, Manabe T, Aiba A, Inokuchi K (2009) Requirement of the immediate early gene vesl-1S/homer-1a for fear memory formation. *Mol Brain* 2:7.
- Jordan BA, Fernholz BD, Boussac M, Xu C, Grigorean G, Ziff EB, Neubert TA (2004) Identification and verification of novel rodent postsynaptic density proteins. *Mol Cell Proteomics* 3:857-871.
- Kennedy MB (1997) The postsynaptic density at glutamatergic synapses. *Trends in neurosciences* 20:264-268.
- Kennedy MB (2000) Signal-processing machines at the postsynaptic density. *Science* 290:750-754.
- Kennedy MB, Bennett MK, Erondur NE (1983) Biochemical and immunochemical evidence that the "major postsynaptic density protein" is a subunit of a calmodulin-dependent protein kinase. *Proc Natl Acad Sci U S A* 80:7357-7361.
- Kerr JM, Blanpied TA (2012) Subsynaptic AMPA receptor distribution is acutely regulated by actin-driven reorganization of the postsynaptic density. *J Neurosci* 32:658-673.
- Kim E, Sheng M (2004) PDZ domain proteins of synapses. *Nat Rev Neurosci* 5:771-781.

- Kiskowski MA, Hancock JF, Kenworthy AK (2009) On the use of Ripley's K-function and its derivatives to analyze domain size. *Biophys J* 97:1095-1103.
- Kolb SJ, Hudmon A, Ginsberg TR, Waxham MN (1998) Identification of domains essential for the assembly of calcium/calmodulin-dependent protein kinase II holoenzymes. *J Biol Chem* 273:31555-31564.
- Kolb SJ, Hudmon A, Waxham MN (1995)  $\text{Ca}^{2+}$ /calmodulin kinase II translocates in a hippocampal slice model of ischemia. *J Neurochem* 64:2147-2156.
- Kolodziej SJ, Hudmon A, Waxham MN, Stoops JK (2000) Three-dimensional reconstructions of calcium/calmodulin-dependent (CaM) kinase II $\alpha$  and truncated CaM kinase II $\alpha$  reveal a unique organization for its structural core and functional domains. *J Biol Chem* 275:14354-14359.
- Koning RI, Koster AJ (2009) Cryo-electron tomography in biology and medicine. *Annals of anatomy = Anatomischer Anzeiger : official organ of the Anatomische Gesellschaft* 191:427-445.
- Kumar J, Mayer ML (2013) Functional insights from glutamate receptor ion channel structures. *Annual review of physiology* 75:313-337.
- Kumar RA, Christian SL (2009) Genetics of autism spectrum disorders. *Current neurology and neuroscience reports* 9:188-197.
- Kuriu T, Inoue A, Bito H, Sobue K, Okabe S (2006) Differential control of postsynaptic density scaffolds via actin-dependent and -independent mechanisms. *J Neurosci* 26:7693-7706.
- Lee SH, Valtschanoff JG, Kharazia VN, Weinberg R, Sheng M (2001) Biochemical and morphological characterization of an intracellular membrane compartment containing AMPA receptors. *Neuropharmacology* 41:680-692.

- Lengyel I, Voss K, Cammarota M, Bradshaw K, Brent V, Murphy KP, Giese KP, Rostas JA, Bliss TV (2004) Autonomous activity of CaMKII is only transiently increased following the induction of long-term potentiation in the rat hippocampus. *Eur J Neurosci* 20:3063-3072.
- Li KW, Hornshaw MP, Van Der Schors RC, Watson R, Tate S, Casetta B, Jimenez CR, Gouwenberg Y, Gundelfinger ED, Smalla KH, Smit AB (2004) Proteomics analysis of rat brain postsynaptic density. Implications of the diverse protein functional groups for the integration of synaptic physiology. *J Biol Chem* 279:987-1002.
- Lim S, Naisbitt S, Yoon J, Hwang JI, Suh PG, Sheng M, Kim E (1999) Characterization of the Shank family of synaptic proteins. Multiple genes, alternative splicing, and differential expression in brain and development. *J Biol Chem* 274:29510-29518.
- Lin YC, Redmond L (2008) CaMKII $\beta$  binding to stable F-actin in vivo regulates F-actin filament stability. *Proc Natl Acad Sci U S A* 105:15791-15796.
- Lin YC, Redmond L (2009) Neuronal CaMKII acts as a structural kinase. *Commun Integr Biol* 2:40-41.
- Lisman J, Schulman H, Cline H (2002) The molecular basis of CaMKII function in synaptic and behavioural memory. *Nat Rev Neurosci* 3:175-190.
- Lisman J, Yasuda R, Raghavachari S (2012) Mechanisms of CaMKII action in long-term potentiation. *Nat Rev Neurosci* 13:169-182.
- Liu Y, Fallon L, Lashuel HA, Liu Z, Lansbury PT, Jr. (2002) The UCH-L1 gene encodes two opposing enzymatic activities that affect alpha-synuclein degradation and Parkinson's disease susceptibility. *Cell* 111:209-218.

- Loosmore NB, Ford ED (2006) Statistical inference using the g or K point pattern spatial statistics. *Ecology* 87:1925-1931.
- MacGillavry HD, Song Y, Raghavachari S, Blanpied TA (2013) Nanoscale scaffolding domains within the postsynaptic density concentrate synaptic AMPA receptors. *Neuron* 78:615-622.
- Malenka RC, Bear MF (2004) LTP and LTD: an embarrassment of riches. *Neuron* 44:5-21.
- Malenka RC, Kauer JA, Perkel DJ, Mauk MD, Kelly PT, Nicoll RA, Waxham MN (1989) An essential role for postsynaptic calmodulin and protein kinase activity in long-term potentiation. *Nature* 340:554-557.
- Mastronarde DN (1997) Dual-axis tomography: an approach with alignment methods that preserve resolution. *Journal of structural biology* 120:343-352.
- Matus AI, Taff-Jones DH (1978) Morphology and molecular composition of isolated postsynaptic junctional structures. *Proceedings of the Royal Society of London Series B, Containing papers of a Biological character Royal Society* 203:135-151.
- McGee AW, Topinka JR, Hashimoto K, Petralia RS, Kakizawa S, Kauer FW, Aguilera-Moreno A, Wenthold RJ, Kano M, Brecht DS (2001) PSD-93 knock-out mice reveal that neuronal MAGUKs are not required for development or function of parallel fiber synapses in cerebellum. *J Neurosci* 21:3085-3091.
- McGuinness TL, Lai Y, Greengard P (1985) Ca<sup>2+</sup>/calmodulin-dependent protein kinase II. Isozymic forms from rat forebrain and cerebellum. *J Biol Chem* 260:1696-1704.



- Meyer G, Varoqueaux F, Neeb A, Oschlies M, Brose N (2004) The complexity of PDZ domain-mediated interactions at glutamatergic synapses: a case study on neuroligin. *Neuropharmacology* 47:724-733.
- Michelot A, Drubin DG (2011) Building distinct actin filament networks in a common cytoplasm. *Current biology* : CB 21:R560-569.
- Migaud M, Charlesworth P, Dempster M, Webster LC, Watabe AM, Makhinson M, He Y, Ramsay MF, Morris RG, Morrison JH, O'Dell TJ, Grant SG (1998) Enhanced long-term potentiation and impaired learning in mice with mutant postsynaptic density-95 protein. *Nature* 396:433-439.
- Miller J, Gordon C (2005) The regulation of proteasome degradation by multi-ubiquitin chain binding proteins. *FEBS letters* 579:3224-3230.
- Miller SG, Kennedy MB (1985) Distinct forebrain and cerebellar isozymes of type II  $\text{Ca}^{2+}$ /calmodulin-dependent protein kinase associate differently with the postsynaptic density fraction. *J Biol Chem* 260:9039-9046.
- Miller SG, Kennedy MB (1986) Regulation of brain type II  $\text{Ca}^{2+}$ /calmodulin-dependent protein kinase by autophosphorylation: a  $\text{Ca}^{2+}$ -triggered molecular switch. *Cell* 44:861-870.
- Moessner R, Marshall CR, Sutcliffe JS, Skaug J, Pinto D, Vincent J, Zwaigenbaum L, Fernandez B, Roberts W, Szatmari P, Scherer SW (2007) Contribution of SHANK3 mutations to autism spectrum disorder. *American journal of human genetics* 81:1289-1297.
- Murphy GE, Jensen GJ (2007) Electron cryotomography. *BioTechniques* 43:413, 415, 417 passim.

- Naisbitt S, Kim E, Tu JC, Xiao B, Sala C, Valtschanoff J, Weinberg RJ, Worley PF, Sheng M (1999) Shank, a novel family of postsynaptic density proteins that binds to the NMDA receptor/PSD-95/GKAP complex and cortactin. *Neuron* 23:569-582.
- O'Leary H, Lasda E, Bayer KU (2006) CaMKII $\beta$  association with the actin cytoskeleton is regulated by alternative splicing. *Mol Biol Cell* 17:4656-4665.
- Oh JS, Manzerra P, Kennedy MB (2004) Regulation of the neuron-specific Ras GTPase-activating protein, synGAP, by Ca<sup>2+</sup>/calmodulin-dependent protein kinase II. *J Biol Chem* 279:17980-17988.
- Ohta Y, Nishida E, Sakai H (1986) Type II Ca<sup>2+</sup>/calmodulin-dependent protein kinase binds to actin filaments in a calmodulin-sensitive manner. *FEBS letters* 208:423-426.
- Okabe S (2007) Molecular anatomy of the postsynaptic density. *Molecular and cellular neurosciences* 34:503-518.
- Okamoto K, Narayanan R, Lee SH, Murata K, Hayashi Y (2007) The role of CaMKII as an F-actin-bundling protein crucial for maintenance of dendritic spine structure. *Proc Natl Acad Sci U S A* 104:6418-6423.
- Omkumar RV, Kiely MJ, Rosenstein AJ, Min KT, Kennedy MB (1996) Identification of a phosphorylation site for calcium/calmodulin-independent protein kinase II in the NR2B subunit of the N-methyl-D-aspartate receptor. *J Biol Chem* 271:31670-31678.
- Osada T, Adachi Y, Kimura HM, Miyashita Y (2008) Towards understanding of the cortical network underlying associative memory. *Philosophical transactions of the Royal Society of London Series B, Biological sciences* 363:2187-2199.

- Palay SL (1956) Synapses in the central nervous system. *J Biophys Biochem Cytol* 2:193-202.
- Peng J, Kim MJ, Cheng D, Duong DM, Gygi SP, Sheng M (2004) Semiquantitative proteomic analysis of rat forebrain postsynaptic density fractions by mass spectrometry. *J Biol Chem* 279:21003-21011.
- Petersen JD, Chen X, Vinade L, Dosemeci A, Lisman JE, Reese TS (2003) Distribution of postsynaptic density (PSD)-95 and  $\text{Ca}^{2+}$ /calmodulin-dependent protein kinase II at the PSD. *J Neurosci* 23:11270-11278.
- Petralia RS, Sans N, Wang YX, Wenthold RJ (2005) Ontogeny of postsynaptic density proteins at glutamatergic synapses. *Molecular and cellular neurosciences* 29:436-452.
- Pham E, Crews L, Ubhi K, Hansen L, Adame A, Cartier A, Salmon D, Galasko D, Michael S, Savas JN, Yates JR, Glabe C, Masliah E (2010) Progressive accumulation of amyloid-beta oligomers in Alzheimer's disease and in amyloid precursor protein transgenic mice is accompanied by selective alterations in synaptic scaffold proteins. *The FEBS journal* 277:3051-3067.
- Picconi B, Gardoni F, Centonze D, Mauceri D, Cenci MA, Bernardi G, Calabresi P, Di Luca M (2004) Abnormal  $\text{Ca}^{2+}$ -calmodulin-dependent protein kinase II function mediates synaptic and motor deficits in experimental parkinsonism. *J Neurosci* 24:5283-5291.
- Pollard TD, Cooper JA (2009) Actin, a central player in cell shape and movement. *Science* 326:1208-1212.

- Racca C, Stephenson FA, Streit P, Roberts JD, Somogyi P (2000) NMDA receptor content of synapses in stratum radiatum of the hippocampal CA1 area. *J Neurosci* 20:2512-2522.
- Ripley BD (1976) The Second-Order Analysis of Stationary Point Processes *Journal of Applied Probability* 13:11.
- Ripley BD (1977) Modelling spatial patterns. *Journal of the Royal Statistical Society Series B Methodological* 39:50.
- Robison AJ, Bass MA, Jiao Y, MacMillan LB, Carmody LC, Bartlett RK, Colbran RJ (2005) Multivalent interactions of calcium/calmodulin-dependent protein kinase II with the postsynaptic density proteins NR2B, densin-180, and alpha-actinin-2. *J Biol Chem* 280:35329-35336.
- Rollenhagen A, Lubke JH (2006) The morphology of excitatory central synapses: from structure to function. *Cell and tissue research* 326:221-237.
- Roselli F, Hutzler P, Wegerich Y, Livrea P, Almeida OF (2009) Disassembly of shank and homer synaptic clusters is driven by soluble beta-amyloid(1-40) through divergent NMDAR-dependent signalling pathways. *PloS one* 4:e6011.
- Roselli F, Tirard M, Lu J, Hutzler P, Lamberti P, Livrea P, Morabito M, Almeida OF (2005) Soluble beta-amyloid1-40 induces NMDA-dependent degradation of postsynaptic density-95 at glutamatergic synapses. *J Neurosci* 25:11061-11070.
- Rostaing P, Real E, Siksou L, Lechère JP, Boudier T, Boeckers TM, Gertler F, Gundelfinger ED, Triller A, Marty S (2006) Analysis of synaptic ultrastructure without fixative using high-pressure freezing and tomography. *Eur J Neurosci* 24:3463-3474.

- Sahyoun N, LeVine H, 3rd, Burgess SK, Blanchard S, Chang KJ, Cuatrecasas P (1985) Early postnatal development of calmodulin-dependent protein kinase II in rat brain. *Biochem Biophys Res Commun* 132:878-884.
- Sala C, Piech V, Wilson NR, Passafaro M, Liu G, Sheng M (2001) Regulation of dendritic spine morphology and synaptic function by Shank and Homer. *Neuron* 31:115-130.
- Sanabria H, Swulius MT, Kolodziej SJ, Liu J, Waxham MN (2009)  $\beta$ CaMKII regulates actin assembly and structure. *J Biol Chem* 284:9770-9780.
- Sans N, Petralia RS, Wang YX, Blahos J, 2nd, Hell JW, Wenthold RJ (2000) A developmental change in NMDA receptor-associated proteins at hippocampal synapses. *J Neurosci* 20:1260-1271.
- Sato D, Lionel AC, Leblond CS, Prasad A, Pinto D, Walker S, O'Connor I, Russell C, Drmic IE, Hamdan FF, Michaud JL, Endris V, Roeth R, Delorme R, Huguet G, Leboyer M, Rastam M, Gillberg C, Lathrop M, Stavropoulos DJ, Anagnostou E, Weksberg R, Fombonne E, Zwaigenbaum L, Fernandez BA, Roberts W, Rappold GA, Marshall CR, Bourgeron T, Szatmari P, Scherer SW (2012) SHANK1 Deletions in Males with Autism Spectrum Disorder. *American journal of human genetics* 90:879-887.
- Schoenenberger CA, Mannherz HG, Jockusch BM (2011) Actin: from structural plasticity to functional diversity. *European journal of cell biology* 90:797-804.
- Schuman EM, Dynes JL, Steward O (2006) Synaptic regulation of translation of dendritic mRNAs. *J Neurosci* 26:7143-7146.
- Shen K, Meyer T (1999) Dynamic control of CaMKII translocation and localization in hippocampal neurons by NMDA receptor stimulation. *Science* 284:162-166.

- Shen K, Teruel MN, Subramanian K, Meyer T (1998) CaMKII $\beta$  functions as an F-actin targeting module that localizes CaMKII $\alpha/\beta$  heterooligomers to dendritic spines. *Neuron* 21:593-606.
- Sheng M, Hoogenraad CC (2007) The postsynaptic architecture of excitatory synapses: a more quantitative view. *Annu Rev Biochem* 76:823-847.
- Sheng M, Kim E (2000) The Shank family of scaffold proteins. *Journal of cell science* 113 ( Pt 11):1851-1856.
- Sheng M, Kim E (2011) The postsynaptic organization of synapses. *Cold Spring Harbor perspectives in biology* 3.
- Sheng M, Kim MJ (2002) Postsynaptic signaling and plasticity mechanisms. *Science* 298:776-780.
- Sorokina O, Sorokin A, Armstrong JD (2011) Towards a quantitative model of the post-synaptic proteome. *Molecular bioSystems* 7:2813-2823.
- Steward O, Schuman EM (2003) Compartmentalized synthesis and degradation of proteins in neurons. *Neuron* 40:347-359.
- Strack S, Choi S, Lovinger DM, Colbran RJ (1997) Translocation of autophosphorylated calcium/calmodulin-dependent protein kinase II to the postsynaptic density. *J Biol Chem* 272:13467-13470.
- Strack S, Colbran RJ (1998) Autophosphorylation-dependent targeting of calcium/calmodulin-dependent protein kinase II by the NR2B subunit of the N-methyl- D-aspartate receptor. *J Biol Chem* 273:20689-20692.
- Suh SW, Jensen KB, Jensen MS, Silva DS, Kesslak PJ, Danscher G, Frederickson CJ (2000) Histochemically-reactive zinc in amyloid plaques, angiopathy, and

- degenerating neurons of Alzheimer's diseased brains. Brain research 852:274-278.
- Suzuki T (2002) Lipid rafts at postsynaptic sites: distribution, function and linkage to postsynaptic density. Neuroscience research 44:1-9.
- Suzuki T, Ito J, Takagi H, Saitoh F, Nawa H, Shimizu H (2001) Biochemical evidence for localization of AMPA-type glutamate receptor subunits in the dendritic raft. Brain research Molecular brain research 89:20-28.
- Suzuki T, Okumura-Noji K, Tanaka R, Tada T (1994) Rapid translocation of cytosolic Ca<sup>2+</sup>/calmodulin-dependent protein kinase II into postsynaptic density after decapitation. J Neurochem 63:1529-1537.
- Swulius MT, Farley MM, Bryant MA, Waxham MN (2012) Electron cryotomography of postsynaptic densities during development reveals a mechanism of assembly. Neuroscience 212:19-29.
- Swulius MT, Kubota Y, Forest A, Waxham MN Structure and composition of the postsynaptic density during development. J Comp Neurol 518:4243-4260.
- Swulius MT, Kubota Y, Forest A, Waxham MN (2010) Structure and composition of the postsynaptic density during development. J Comp Neurol 518:4243-4260.
- Swulius MT, Waxham MN (2008) Ca(2+)/calmodulin-dependent protein kinases. Cell Mol Life Sci 65:2637-2657.
- Takeda A (2000) Movement of zinc and its functional significance in the brain. Brain research Brain research reviews 34:137-148.
- Takumi Y, Matsubara A, Rinvik E, Ottersen OP (1999) The arrangement of glutamate receptors in excitatory synapses. Annals of the New York Academy of Sciences 868:474-482.

- Tao-Cheng JH, Dosemeci A, Gallant PE, Smith C, Reese T Activity induced changes in the distribution of Shanks at hippocampal synapses. Neuroscience.
- Tao-Cheng JH, Dosemeci A, Gallant PE, Smith C, Reese T (2010) Activity induced changes in the distribution of Shanks at hippocampal synapses. Neuroscience 168:11-17.
- Thein S, Tao-Cheng JH, Li Y, Bayer KU, Reese TS, Dosemeci A (2014) CaMKII mediates recruitment and activation of the deubiquitinase CYLD at the postsynaptic density. PloS one 9:e91312.
- Thiagarajan TC, Piedras-Renteria ES, Tsien RW (2002) alpha- and betaCaMKII. Inverse regulation by neuronal activity and opposing effects on synaptic strength. Neuron 36:1103-1114.
- Tobimatsu T, Fujisawa H (1989) Tissue-specific expression of four types of rat calmodulin-dependent protein kinase II mRNAs. J Biol Chem 264:17907-17912.
- Topinka JR, Bredt DS (1998) N-terminal palmitoylation of PSD-95 regulates association with cell membranes and interaction with K<sup>+</sup> channel Kv1.4. Neuron 20:125-134.
- Triller A, Choquet D (2005) Surface trafficking of receptors between synaptic and extrasynaptic membranes: and yet they do move! Trends in neurosciences 28:133-139.
- Tu JC, Xiao B, Naisbitt S, Yuan JP, Petralia RS, Brakeman P, Doan A, Aakalu VK, Lanahan AA, Sheng M, Worley PF (1999) Coupling of mGluR/Homer and PSD-95 complexes by the Shank family of postsynaptic density proteins. Neuron 23:583-592.



- Tu JC, Xiao B, Yuan JP, Lanahan AA, Leoffert K, Li M, Linden DJ, Worley PF (1998) Homer binds a novel proline-rich motif and links group 1 metabotropic glutamate receptors with IP3 receptors. *Neuron* 21:717-726.
- Valtschanoff JG, Weinberg RJ (2001) Laminar organization of the NMDA receptor complex within the postsynaptic density. *J Neurosci* 21:1211-1217.
- van Woerden GM, Harris KD, Hojjati MR, Gustin RM, Qiu S, de Avila Freire R, Jiang YH, Elgersma Y, Weeber EJ (2007) Rescue of neurological deficits in a mouse model for Angelman syndrome by reduction of alphaCaMKII inhibitory phosphorylation. *Nat Neurosci* 10:280-282.
- Voogd J, Glickstein M (1998) The anatomy of the cerebellum. *Trends in cognitive sciences* 2:307-313.
- Walaas SI, Lai Y, Gorelick FS, DeCamilli P, Moretti M, Greengard P (1988) Cell-specific localization of the alpha-subunit of calcium/calmodulin-dependent protein kinase II in Purkinje cells in rodent cerebellum. *Brain research* 464:233-242.
- Weeber EJ, Jiang YH, Elgersma Y, Varga AW, Carrasquillo Y, Brown SE, Christian JM, Mirnikjoo B, Silva A, Beaudet AL, Sweatt JD (2003) Derangements of hippocampal calcium/calmodulin-dependent protein kinase II in a mouse model for Angelman mental retardation syndrome. *J Neurosci* 23:2634-2644.
- Wu K, Siekevitz P (1988) Neurochemical characteristics of a postsynaptic density fraction isolated from adult canine hippocampus. *Brain research* 457:98-112.
- Wyszynski M, Lin J, Rao A, Nigh E, Beggs AH, Craig AM, Sheng M (1997) Competitive binding of alpha-actinin and calmodulin to the NMDA receptor. *Nature* 385:439-442.

- Xiao B, Tu JC, Petralia RS, Yuan JP, Doan A, Breder CD, Ruggiero A, Lanahan AA, Wenthold RJ, Worley PF (1998) Homer regulates the association of group 1 metabotropic glutamate receptors with multivalent complexes of homer-related, synaptic proteins. *Neuron* 21:707-716.
- Xie M, Wang SH, Lu ZM, Pan Y, Chen QC, Liao XM (2014) UCH-L1 inhibition involved in CREB dephosphorylation in hippocampal slices. *Journal of molecular neuroscience* : MN 53:59-68.
- Yang Y, Tao-Cheng JH, Reese TS, Dosemeci A SynGAP moves out of the core of the postsynaptic density upon depolarization. *Neuroscience* 192:132-139.
- Yang Y, Tao-Cheng JH, Reese TS, Dosemeci A (2011) SynGAP moves out of the core of the postsynaptic density upon depolarization. *Neuroscience* 192:132-139.
- Yi JJ, Ehlers MD (2005) Ubiquitin and protein turnover in synapse function. *Neuron* 47:629-632.
- Yoshimura Y, Shinkawa T, Taoka M, Kobayashi K, Isobe T, Yamauchi T (2002) Identification of protein substrates of Ca(2+)/calmodulin-dependent protein kinase II in the postsynaptic density by protein sequencing and mass spectrometry. *Biochem Biophys Res Commun* 290:948-954.
- Yoshimura Y, Yamauchi Y, Shinkawa T, Taoka M, Donai H, Takahashi N, Isobe T, Yamauchi T (2004) Molecular constituents of the postsynaptic density fraction revealed by proteomic analysis using multidimensional liquid chromatography-tandem mass spectrometry. *J Neurochem* 88:759-768.
- Zheng CY, Petralia RS, Wang YX, Kachar B, Wenthold RJ (2010) SAP102 is a highly mobile MAGUK in spines. *J Neurosci* 30:4757-4766.

Zheng CY, Seabold GK, Horak M, Petralia RS (2011) MAGUKs, synaptic development, and synaptic plasticity. *The Neuroscientist : a review journal bringing neurobiology, neurology and psychiatry* 17:493-512.

## **Vita**

Madeline Marie Farley was born in Royal Oak, Michigan on March 18, 1987, the daughter of Kimberly Lynn Hardman and David Edward Burgoyne. After completing her work at Louisiana School for Math, Science and the Arts High School, Natchitoches, Louisiana in 2005, she entered Centenary College of Louisiana in Shreveport, Louisiana. She received the degree of Bachelor of Science with a major in Biochemistry and a minor in Mathematics from Centenary in May, 2009. In September of 2009 she entered The University of Texas Graduate School of Biomedical Sciences at Houston.

Permanent address:

7575 Cambridge St. Unit 3305

Houston, Texas 77054